# Developments toward a Silicon Strip Tracker for the $\overline{\text{P}}$ANDA Experiment

Dissertation

zur

Erlangung des Doktorgrades (Dr. rer. nat.)

der

Mathematisch-Naturwissenschaftlichen Fakultät

der

Rheinischen Friedrich-Wilhelms-Universität Bonn

vorgelegt von

HANS-GEORG ZAUNICK

aus Radebeul

Bonn 2012

Angefertigt mit Genehmigung der Mathematisch-Naturwissenschaftlichen Fakultät der Rheinischen Friedrich-Wilhelms-Universität Bonn

1. Gutachter : Prof. Dr. K.-Th. Brinkmann

2. Gutachter : Prof. Dr. R. Beck

Tag der Promotion : 12.04.2013

Erscheinungsjahr   : 2013

## Kurzdarstellung

Der $\overline{P}$ANDA Detektor im zukünftigen FAIR-Beschleunigerkomplex in Darmstadt wird ein Schlüsselexperiment im Verständnis der starken Wechselwirkung bei mittleren Energien, bei denen kein Zugang über perturbative Methoden zur Quark-Quark Interaktion existiert, sein. Eine wichtige Eigenschaft des Detektorsystems, die Ortsrekonstruktion sekundärer Zerfallsvertizes kurzlebiger Zwischenzustände, wird dabei durch ein Spurverfolgungssystem mit dem Mikro-Vertex Detektor (MVD) als wichtigstem Element zur hochauflösenden Charmonium- und Open-Charm Spektroskopie garantiert. Der MVD ist konzipiert als leichtgewichtiges, geteiltes Silizium-Detektorsystem mit Pixeldetektoren im inneren Bereich und doppelseitigen Streifendetektoren (DSSD) in den äußeren Regionen. Das $\overline{P}$ANDA Detektorsystem soll in einem selbstgetriggertem Regime Daten breitbandig und ohne Totzeitverluste verarbeiten können. Die sich daraus ergebenden Implikationen auf den Aufbau der Ausleseelektronik und der Front-end-Baugruppen werden analysiert und es werden Ergebnisse von Messungen an DSSD-Prototypen im Hinblick auf Signal-zu-Rausch-Verhältnis, Rauscheigenschaften, Ladungsteilungsverhalten, Ortsauflösung und Bestrahlungstoleranz diskutiert. Methoden zur elektrischen Charakterisierung von Sensoren werden untersucht, die bei zukünftigen großangelegten QA-Untersuchungen nützlich eingesetzt werden können. Ein neuartiger Cluster-Korrelationsalgorithmus, welcher mehrfach entartete Clusterhit-Muster zu erkennen vermag wird ebenso vorgestellt wie eine mögliche Architektur des noch zu entwickelnden Module-Data-Concentrator ASIC (MDC), welcher die Datenströme der Front-end Chips auf Modulebene zusammenfassen soll. Ein erstes integratives Konzept für Konstruktion und Zusammenbau von DSSD-Modulen des Barrel-Bereichs des MVD wird im Abschluss der Dissertation vorgestellt. Darüber hinaus wird eine detaillierte Beschreibung einer vereinfachten Vorschrift zur Berechnung des Versetzungsschadens durch Neutronen in zusammengesetzten Stoffen angegeben, welche sich als nützlich für die Ableitung des nicht-ionisierenden Energieverlustes in Materialien neben Silizium erwiesen hat.

## Abstract

The $\overline{\text{P}}$ANDA detector at the future FAIR facility in Darmstadt will be a key experiment in the understanding of the strong interaction at medium energies where perturbative models fail to describe the quark-quark interaction. An important feature of the detector system is the ability to reconstruct secondary decay vertices of short-lived intermediate states by means of a powerful particle tracking system with the the Micro-Vertex Detector (MVD) as central element to perform high-resolution charmonium and open-charm spectroscopy. The MVD is conceived with pixel detectors in the inner parts and double-sided silicon strip detectors at the outer half in a very lightweight design. The $\overline{\text{P}}$ANDA detector system shall be operated in a self-triggering broadband acquisition mode. Implications on the read-out electronics and the construction of the front-end assemblies are analyzed and evaluation of prototype DSSD-detectors wrt. signal-to-noise ratio, noise figures, charge sharing behavior, spacial resolution and radiation degradation discussed. Methods of electrical sensor characterization with different measurement setups are investigated which may be useful for future large-scale QA procedures. A novel algorithm for recovering multiple degenerate cluster hit patterns of double-sided strip sensors is introduced and a possible architecture of a Module Data Concentrator ASIC (MDC) aggregating multiple front-end data streams conceived. A first integrative concept for the construction and assembly of DSSD modules for the barrel part of the MVD is introduced as a conclusion of the thesis. Furthermore, a detailed description of a simplified procedure for the calculation of displacement damage in compound materials is given as reference which was found useful for the retrieval of non-ionizing energy loss for materials other than silicon.

# Preface

With this thesis I want to accommodate the work done in the past years with the objective of the development of an expedient silicon strip detector system for the Micro-Vertex Detector (MVD) of the $\overline{\mathsf{P}}$ANDA experiment and present a documentation about achieved progress with the focus on the hardware of sensors and front-end electronics. The document thus lines up with the theses of R. Jäkel and Th. Würschig drawn up earlier and the one of R. Kliemt under preparation, all of them covering complementary parts on the first development stage towards the final detector system as is reported in the *Technical Design Report for the* $\overline{\mathsf{P}}$ANDA MVD (Ref. [35]). It shall evenly be conceived as a reference documentation for further works on the subject. Therefore, I put an emphasis on the description of reproducible methods which are thought to be useful for the future evaluation of sensor parameters (Section 4.2), performance of front-end electronics (Section 4.3) and of sensor–front-end systems (Chapter 3), particularly with respect to signal-to-noise ratio (SNR), noise characterization, charge sharing behavior and spacial resolution as well as a simplified procedure for the calculation of displacement damage in arbitrary compound materials (Appendix B). Furthermore, a novel cluster-charge correlation algorithm for double-sided strip detectors (DSSD) capable of recovering degenerate hit patterns with unequal cluster counts on either sensor plane is documented in Section 3.4. Finally, a first integrative concept for the construction, layout, powering scheme and assembly of double-sided silicon strip module-entities for the barrel part of the $\overline{\mathsf{P}}$ANDA MVD is introduced throughout Chapter 4.

The treatment of charged particle tracking and an appropriate description of the silicon strip tracking telescope constructed on the basis of the DSSD modules discussed in Chapter 3 and all related issues such as alignment, tracking algorithms, measurement results etc. are intentionally excluded from this thesis since it would go beyond the circumference imposed by volume and thematical constraints. A proper and rather detailed write-up can be obtained from Refs. [205, 206] instead.

For readers not familiar to the field in which this thesis is settled the following books are recommended to grasp the basic principles, concepts and idiomatic specifica of experimental high energy physics implicitly taken reference to throughout this work. A decent introduction on general particle physics is available from Ref. [29]. For further reading the excellent overviews on the standard model of particle physics and hadron as well as nuclear physics given in [30] and [26] are recommended which convey an insight into e.g. the quark model that is merely touched superficially in Chapter 1. Experimental concepts in nuclear and high energy physics are reviewed in [112] while a very good comprehension of instrumental aspects of high energy particle physics is given in [93].

Finally, I want to convey my gratitude to Prof. Dr. Brinkmann who supported my work beyond mere supervision.

<div align="right">Bonn, April 15, 2013</div>

# Contents

*"Among themselves all things*
*Have order; and from hence the form, which makes*
*The universe resemble God. In this*
*The higher creatures see the printed steps*
*Of that eternal worth, which is the end*
*Whither the line is drawn. All natures lean,*
*In this their order, diversely, some more,*
*Some less approaching to their primal source"*
         — Dante Alighieri ( ca. 1265 - 1321)

# Chapter 1.

# Introduction

One century ago, *Rutherford* discovered a remarkable feature in the structure of atoms. By scattering $\alpha$ particles on thin gold foils he noticed rare but strong deflections of the projectiles which were reconcilable only with an ultra-compact nucleus that confines protons to several femtometers within the center of the atom while a certain number of electrons was thought to be closely bound to the nucleus to avoid electromagnetic repulsion between the protons [1–3]. A few years later *Bothe & Becker* discovered a penetrating neutral radiation emanating from beryllium when this was targeted by $\alpha$ particles [4,5]. *I. & F. Joliot-Curie* and others concluded for the time being the generation of high-energetic $\gamma$-radiation until *Chadwick* (Nobel laureate 1935), in reluctance of this interpretation, reevaluated *Bothe's* experiment under the assumption of a massive neutral particle in 1932. He was able to identify this, as already by *Rutherford* christened "neutron" particle by mass which he found to be slightly heavier than the proton [6,7]. Thus, the atomic nucleus was consequently understood as a compact object composed of protons and neutrons surrounded by a dispersed cloud of electrons. Past the introduction of the quantum-mechanical spin algebra by *Pauli* (1927), *Heisenberg* suggested right after the discovery of the neutron to perceive proton ($p$) and neutron ($n$) as two different manifestations of one and the same state in "isobaric" spin space, the "nucleon", with a value of $I{=}\frac{1}{2}$. These sub-states are realized when the isobaric spin, or more conveniently isospin, assumes values of $-\frac{1}{2}$ (neutron) or $+\frac{1}{2}$ (proton) [8,9].

## 1.1. The Strong Interaction

The interaction between the particles inside the nucleus, which is not described by electrodynamics gave rise to the assumption of the existence of a "nuclear force". To all what was empirically known then, this force must be insensitive to electrical charge and active within very short range scales in the order of the nucleon size ($\approx 1\,\mathrm{fm}$). Furthermore, a mass change of nuclei of ca. $8.5\,\mathrm{MeV}$[1] per nucleon was observed in nuclear decays and fission experiments which could eventually be attributed to the binding of the constituents to the nuclear potential. *Weizsäcker & Bethe* were able to calculate the small mass differences with the macroscopically

---

[1] Mass and energy are used here in a convertible manner according to *Einstein's* mass-energy equivalence relation $E = mc^2$. An energy is indicated in units of J or, more conveniently in particle-physical notation eV while masses are stated in units of $\mathrm{eV}/c^2$ with the velocity of light $c$. The binding between nucleons is measured as an energy of $8.5\,\mathrm{MeV}$ but is manifest as an additional mass of $8.5\,\mathrm{MeV}/c^2$ in bound nuclei. Therefore, an indication for the mass-difference measured as liberated energy of $8.5\,\mathrm{MeV}$ per nucleon in the above case is justified.

inspired liquid drop model [10]. For the force exchange carrier[2], *Yukawa* (1934) proposed a light particle mediating the attraction between the nucleons which was eventually discovered in high-energetic cosmic radiation by means of balloon-borne experiments by *Powell et al.* and named $\pi$ particle or more conveniently "pion" with a mass of $140\,\text{MeV}/c^2$ [11–13]. About the same time investigations to the nature of the proton's magnetic moment undertaken by *Frisch & Stern* and later to that of the neutron[3] by *Alvarez, Bloch* and others yielded a rather puzzling picture which gave a first glimpse of a possible substructure of the nucleon itself [14, 15].

Systematic studies of the then known hadrons (8 baryons and 7 mesons known in 1961) stimulated the search for a common reference system generating all possible hadronic states from a set of conservation laws. Identification of the quantum numbers isospin, strangeness and baryon number as the symmetries of the strong interaction, the subsequent application of *Lie*-group algebra and the ingenious idea of fractional charged eigenstates (*Gell-Mann & Zweig*) in SU(3)-representations of the strong interaction led to the present understanding of the hadrons as compound objects composed of "quarks"[4] [16–22]. Those constituents could be shown to not only generate all known hadrons (mesons: $q\bar{q}$, baryons: $qqq$) at that time but also predictions for new particles were made which were eventually found, e.g. the $\eta$-meson or the $\Omega^-$-baryon. All possible combinations predicted by this model for $u$,$d$ and $s$ quark flavors are depicted in Figure 1.1 (mesons) and Figure 1.2 (baryons). The mass differences between the particles can be explained with quark content of different flavor and, in complete analogy to atomic physics and QED, with spin-spin and spin-orbit interactions between the quarks.
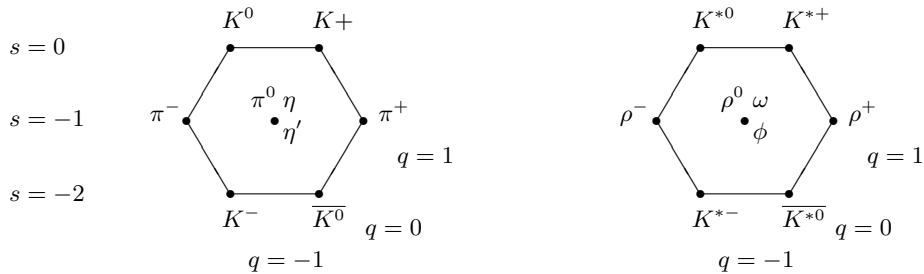


**Figure 1.1.:** Meson multiplets in SU(3). Nonets of pseudoscalar mesons with spin $J^P{=}0^-$ (left) and vector mesons with $J^P{=}1^-$ (right).

Isoscalar states with the same set of quantum numbers $J^{PC}$ can mix (manifest a particle as a superposition of different flavor eigenstates) when the quark eigenstates have comparable masses. In case of the isospin-flavors ($u$,$d$) mixing occurs with the strange flavor states resulting

---

[2] Every physical interaction ("force") is mediated by exchange of specific particles, the gauge bosons in the view of quantum physics. The electromagnetic force for example is carried by exchange of $\gamma$ particles (photons) in the framework of Quantum-Electrodynamics (QED).

[3] It was referred to as "anomalous magnetic moment" soon after its discovery since neither the proton's nor the neutron's magnetic moment were found to be integral multiples of the nuclear magnetic moment $\mu_N$.

[4] Denoted as $q$. Quarks may assume any of the six "flavors" ($u,d,s,c,b,t$) or their respective anti-flavors ($\bar{u},\bar{d},\bar{s},\bar{c},\bar{b},\bar{t}$).
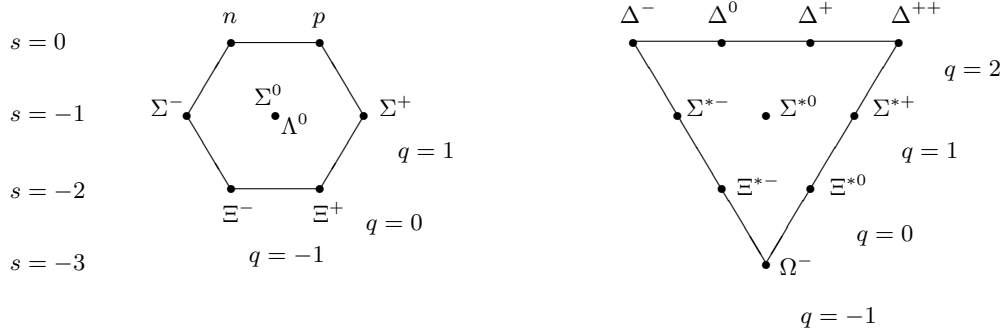
**Figure 1.2.:** Baryon multiplets in SU(3). Octet of baryons with spin $J^P{=}\frac{1}{2}^+$ (left) and decuplet for $J^P{=}\frac{3}{2}^+$ (right).

in the $\omega$ and $\phi$ isoscalars with close to ideal mixing such that the $\phi(1020)$ carries nearly pure $s\bar{s}$ content and the $\omega(782)$ consists of nearly pure $u\bar{u}$ and $d\bar{d}$ flavor [23].

The introduction of the quarks as constituents of hadrons, however, brought up another important statement about the nature of the strong interaction in order to provide matching for symmetry requirements of the hadron wave functions. Quarks come along in states described by another SU(3) symmetry group, the "color charge"[5] introduced by *Fritzsch, Gell-Mann* and *Bardeen* [24, 25]. Hadrons are thought to be composed of quarks appearing in a color singlet, i.e. with vanishing net color charge ("white"), which is accomplished e.g. in the simplest combinations of quarks with color charges red, green and blue ($rgb$) or also in combinations of two quarks carrying opposite colors ($r\bar{r}$, $g\bar{g}$ or $b\bar{b}$). So far, no evidence for non-neutrally charged (non-white) objects is found. However, the associated gauge particle of the strong interaction, called "gluon", postulated along with the introduction of the concept of color charge, binds two adjacent quarks tightly together through color exchange[6]. Gluons are, like the photon, massless and carry a spin of 1, but are themselves subject to the strong interaction. A consequence of this self-interaction is a steady increase of potential energy between two strongly interacting particles ($qq$, $qg$ or even $gg$) when the mutual distance increases. The strong potential between two quarks is illustrated in Figure 1.3 and compared to the harmonic *Coulomb*-like potential of the electromagnetic interaction due to the quark charges. A linear term $\sim r$ causes the confinement of the binding partners to close distances. Forcing them to increased distances increases the binding force. A flux-tube of gluonic exchange between the particles emerges which breaks up eventually when the stored potential energy suffices to materialize light quarks as binding partners for the initial constituents from the vacuum. This process is referred to as hadronization. Scrutinizing the strong potential at different length scales by probes of different energies[7] revealed a further significant difference to the electromagnetic interaction [26]: the severe energy-scale dependence of the coupling constant $\alpha_s$ of the strong interaction (cf. Figure 1.4). While the coupling asymptotically vanishes at

---

[5] The property of "color charge" (or more conveniently "color") is a quantum-physical degree of freedom and merely intuitively referring to the macroscopic phenomenon.

[6] Gluons ($g$) carry an octet of color charge in an $SU(3)_C$ representation. The interaction between e.g. a green and a blue quark is accomplished by exchange of a gluon with blue-antigreen charge.

[7] The kinetic energy of the probe particles determines the visible length scale. This can be seen in direct analogy to the resolution-wavelength dependence of optical systems, e.g. microscopes.
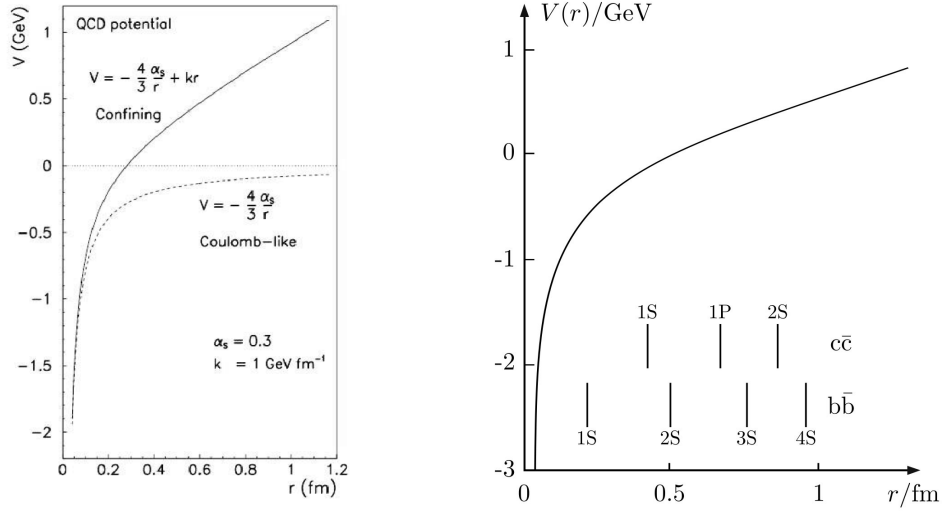
**Figure 1.3.:** $q\bar{q}$ confinement potential and comparison to *Coulomb*-like potential (left, from [26]). Position of discrete energy eigenstates (in atomic spectroscopic notation) for charmonium and bottonium systems (right, from [27]).

sufficiently large energies (small characteristic distances) which is also known as "asymptotic freedom", it increases steeply toward lower energies (large distances). As a consequence, theoretical calculations based on perturbative QCD methods deliver a rather precise picture of the strong interaction while they fail in the low energy regime due to non-vanishing higher orders. Alternative methods, as the lattice-QCD (LQCD) are in principle subject to the same limitation, but successfully applied in the domain of light-quark baryon confinement and deliver precise results e.g. of the proton mass [28].



**Figure 1.4.:** Coupling constant of the strong interaction $\alpha_s$ [23].

An overview of the known zoo of elementary particles within the standard model is given in Figure 1.5. Beside the already known light quarks $u$,$d$ and $s$ further massive quarks could

be identified in the subsequent years. The current picture of the standard model contains three lepton and quark families, latter with electric charges of $q = \frac{2}{3}$ for the upper gender ($u$,$c$,$t$) and $q = -\frac{1}{3}$ for the lower one ($d$,$s$,$b$).

| | | Particles | | | Antiparticles | | | | |
|---|---|---|---|---|---|---|---|---|---|
| Leptons | $q=-1$ | $e^-$ | $\mu^-$ | $\tau^-$ | $e^+$ | $\mu^+$ | $\tau^+$ | | $q=1$ |
| | $q=0$ | $\nu_e$ | $\nu_\mu$ | $\nu_\tau$ | $\overline{\nu}_e$ | $\overline{\nu}_\mu$ | $\overline{\nu}_\tau$ | | $q=0$ |
| Quarks | $q=\frac{2}{3}$ | $u$ | $c$ | $t$ | $\overline{u}$ | $\overline{c}$ | $\overline{t}$ | | $q=-\frac{2}{3}$ |
| | $q=-\frac{1}{3}$ | $d$ | $s$ | $b$ | $\overline{d}$ | $\overline{s}$ | $\overline{b}$ | | $q=\frac{1}{3}$ |
| Elementary Bosons | | | $\gamma$ | $W^\pm, Z^0$ | $g$ | $H^0$ | | | |

**Figure 1.5.:** Overview of the elementary particle zoo within the standard model of particle physics.

The systematic construction of hadrons from spontaneous symmetry breaking in SU(3) as discussed above can be equally extended to the remaining quark flavors. Taking just the charm flavor into account, additional mesons appear as a result of this SU(4)-representation with all possible combinations of a charm quark (or antiquark) and all the other flavors as illustrated in Figure 1.6. The isoscalar particle with a pure $c\bar{c}$ content is known as $\eta_c$ and $J/\Psi$ for the pseudoscalar and vector meson, respectively. It is a tightly bound state of a quark-antiquark pair inside the mutual strong potential. In analogy to the electromagnetic harmonic *Coulomb* potential of an entangled electron-positron pair which exhibits a spectrum of discrete eigenstates exactly described by the quantum field-theory of the electromagnetic interaction (QED), a bound quark-antiquark system manifests itself in the ground state ($\eta_c$ for charmonium) or in a discrete excited state. The comparison between both the bound $e^+e^-$ system and a bound $c\bar{c}$ system is illustrated in Figure 1.7. As shown in Figure 1.3, the



**Figure 1.6.:** Multiplets for SU(4) symmetry group showing all possible mesons including charm flavor for antisymmetric spin coupling $J^P{=}0^-$ (a) and the symmetrically coupled vector mesons with $J^P{=}1^-$ (b). Note that the isoscalars are enhanced by the pure $c\bar{c}$ quarkonia $\eta_c$ and $J/\Psi$ while no mixing between charm and lighter flavors occurs. Illustration taken from [23].

strong potential resembles the harmonic $\propto \frac{1}{r}$ characteristic at low excitation energies near the

ground state which results in a similar configuration of states in this domain while for higher excitations substantial differences are expected due to the linear confinement term $\propto r$ of the strong potential. The designation of quarkonium states, however, follows the spectroscopic notation $N^{2S+1}L_J$ known from atomic physics.
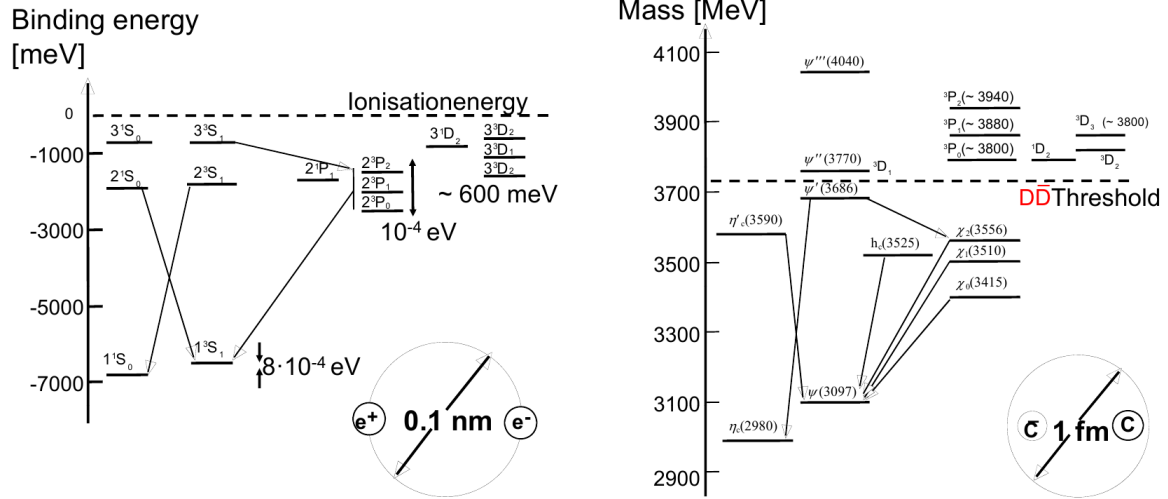


**Figure 1.7.:** Bound excitations in the positronium system (left) and charmonium (right) [26].

## 1.2. Charmonium Spectroscopy

As briefly demonstrated in Figure 1.7, the strong potential, as approached with proven methods based on the QED, exhibits a striking similarity to bound electromagnetic states like the hydrogen atom or, even simpler in description, the positronium in the domain of asymptotic freedom. Due to the confinement, on the other hand, no threshold of bound-to-free excitations such as the ionization limit exists in strongly bound systems. Infinite excited states are generally conceivable. However, since strong potential energies range in the order of typically GeV, hadronization affects the occurrence of highly excited levels. Above the $D\bar{D}$ threshold the charmonium system breaks up and the quark-antiquark pair separates by binding to lighter quarks to e.g. one $D^+$-meson ($c\bar{d}$) and one $D^-$-meson ($\bar{c}d$) which decay themselves via flavor-changing reactions into kaons:

$$\bar{p}p \rightarrow \Psi(3770) \rightarrow D^+D^- \rightarrow K^-\pi^+\pi^+K^+\pi^-\pi^-$$

the kaons in turn decay again via pions and muons until only stable particles remain eventually (electrons or positrons and neutrinos). The decay time of the $D^\pm$ accounts in average to merely $\tau \approx 1\,\text{ps}$. At a velocity close to the speed of light these particles traverse a distance of ca. $300\,\mu\text{m}$ before they decay (cf. Figure 1.8). The precise measurement of the displacement of the $D$-decay vertex from the interaction point (IP) at which the $c\bar{c}$ system was generated is of significant importance since such a dislocated secondary decay is a characteristic signature for the presence of the $D$-mesons. Evidence through detection of the decay products (kaons and pions) alone is not entirely unique. Consider e.g. following possible non-resonant production channel:

$$\bar{p}p \rightarrow K^-\pi^+\pi^+K^+\pi^-\pi^-$$
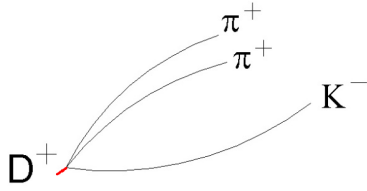
**Figure 1.8.:** Decay of a charged $D$-meson into a prominent final state (BR=24%) of charged kaon and pions. The $D$-meson traverses an average distance of $c\tau \approx 300\,\mu\text{m}$ before it decays (red trajectory). The tracks exhibit a curvature due to the *Lorentz*-force acting on the charged particles in magnetic fields.

which has the same particle signature in the final state but this time no intermediate charmonium resonance was excited.

The briefly described mechanism of the break-up of higher excited states in charmonium and in quarkonia in general prevents the development of stable resonances above such thresholds. The expected spectrum in this region thus should exhibit very broad resonances mixing with other excitations and is therefore more difficult to observe than low lying or ground states in charmonium [31].

## 1.3. The $\overline{P}$ANDA–Detector at FAIR

Proton-antiproton annihilation processes for the study of hadronic excitations have been successfully utilized extensively by the LEAR experimental facilities at CERN from 1983 until 1996 with beam momenta up to $1.94\,\text{GeV}/c$. Many aspects of baryonic and mesonic channels were investigated and first evidences for hybrid and gluonic states could be found [32]. In order to extend these studies to hadrons with charm content, the idea emerged to use $\overline{p}p$ collisions at higher beam energies [33]. Since the charm quark is the lightest of the three heavy quarks but with a mass of $1.275 \pm 0.025\,\text{GeV}/c^2$ [23], sufficiently heavy to exclude mixing with the lighter flavors, resonances should be narrow and exotic states are more likely to be found. Furthermore, charmed hadrons can be described by effective models like Heavy Quark Effective Theory (HQET) and non-relativistic QCD (NRQCD) [23] which provide a theoretical base to be validated (or falsified) by experimental observations of hadronic states. The advantage of using $\overline{p}p$ processes lies in the possibility of direct formation of the targeted state in opposite to $e^+e^-$ experiments which populate only states with photon quantum numbers. Other resonances e.g. in charmonia are then only populated through production of the vector meson states yielding poor statistics. In $\overline{p}p$ formation experiments, the energy resolution of reconstructed resonances is merely limited by the beam momentum uncertainty. The latter can be minimized by beam cooling (electron and stochastic cooling) to be much better than the experimental detector resolution [34].

The proposed $\overline{P}$ANDA[8] experiment is planned as part of the future FAIR (Facility for Antiproton and Ion Research) accelerator complex as an extension of the current GSI (Gesellschaft für Schwerionenforschung) facility. An overview of the FAIR complex is shown in Figure 1.9. The $\overline{P}$ANDA compound detector system will be located inside the High-Energy Storage Ring (HESR). Latter accelerates antiprotons which are injected into it in regular intervals from the SIS100 storage ring to beam momenta in a range of $1.5 \ldots 15\,\text{GeV}/c$. This medium energy range is of special interest to the research into the strong interaction since it covers the transition between perturbative and non-perturbative regimes of the QCD as seen in Figure 1.4. A high luminosity can be achieved with the proposed setup. Interaction between beam and

---

[8] (Anti)-Proton Annihilations at Darmstadt
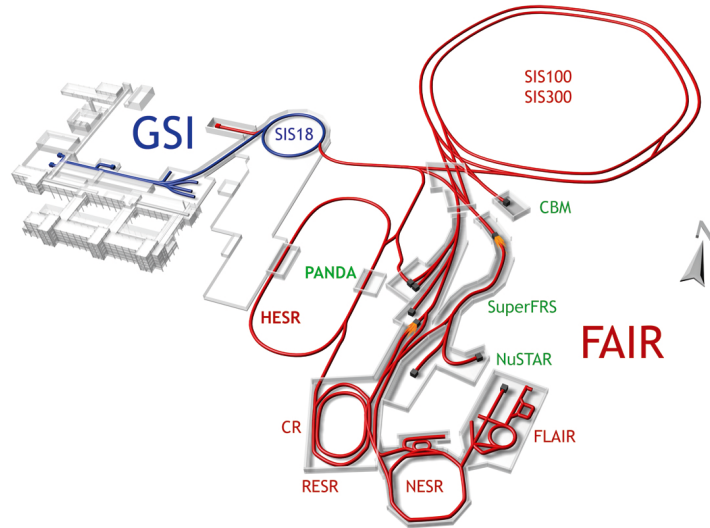
**Figure 1.9.:** The planned FAIR facility at GSI in Darmstadt [35].

target leads to losses which decrease the beam lifetime. Therefore two operation modes are foreseen, which comprise optimal experimental conditions depending on the actual application, a high luminosity mode with up to $L = 2 \cdot 10^{32}\,\mathrm{cm}^{-2}\,\mathrm{s}^{-1}$ and a beam momentum uncertainty of $\Delta p/p = 10^{-4}$ and a high resolution mode with $10$-fold lower luminosity and a superior momentum spread of $\Delta p/p = 10^{-5}$. Former would be utilized in survey scans while the latter is useful in precision measurements such as the determination of resonance widths.

The $\overline{\mathsf{P}}$ANDA physics program intends to address following topics[9] [36–48]:

- **high resolution charmonium spectroscopy**
  The determination of masses and widths of excited states of the bound $c\bar{c}$ system allows inference about the properties of the quark-antiquark confinement potential (cf. Figure 1.7). Specifically a large set of newly discovered states above the $D\bar{D}$ threshold of $3.77\,\mathrm{GeV}$ which do not agree with predictions from lattice QCD calculations raise the need for more and statistically more pronounced experimental data. The experimentally found X,Y,Z-states shown superimposed to a predicted charmonium spectrum in Figure 1.10 are not or partly explained yet, some of these states also show remarkable narrow resonances [50,51]. On the other hand, predicted states with higher radial excitations have not been seen yet.

- **search for evidence of exotic hadronic states**
  Exotic states and excitations, which are characterized by quantum numbers that are not occupied by mesons or baryons, are generally not forbidden by the QCD. Thus any combination of quarks not violating the demanded wave-function symmetry and color neutrality is conceivable. Moreover, even gluonic excitations are allowed since gluons are known to carry color charge and spin which may result in stable hadronic configurations. Hadrons with exotic quantum numbers searched for are:

---

[9] The highlighted objectives are merely an incomplete selection. An exhaustive write-up rendering the $\overline{\mathsf{P}}$ANDA physics program is found in Ref. [36].
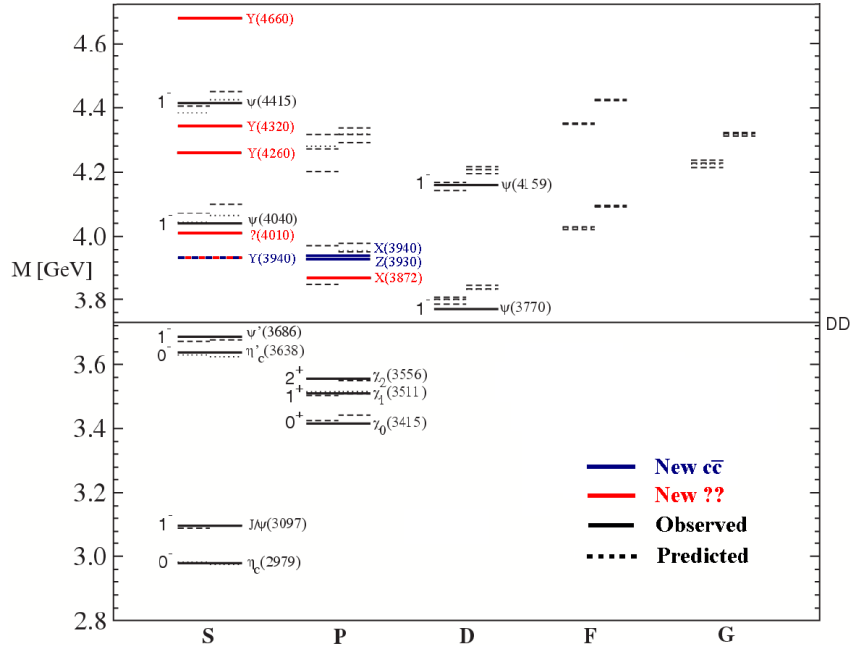
**Figure 1.10.:** Predicted and observed bound excitations in the charmonium system, adopted from [49].

**Dibaryons**  Six-quark system that is predicted in the bag model as two baryons loosely bound to each other. The existence of such a state (specifically *udsuds*) would have implications for astrophysical models of neutron star configurations [52–54].

**Multi-Mesons, Mesic Mulecules**  Similar to the dibaryon, a multiple mesonic state $q\bar{q}q\bar{q}$ is not excluded by any theory. Such a system could provide an independent approach to sample the strong potential.

**Hybrids and Glueballs**  Beside exclusive combinations of quarks in the classical hadrons a mixed configuration of quarks and gluon excitations is possible as long as the compound object remains colorless. Those hybrid hadrons are thought to be better separated from $q\bar{q}$ states in the charm sector than is the case for quarkonia of other flavors [55] and thus easier to find. The quantum numbers of such a $q\bar{q}g$ system ($J^{PC}=0^{+-},1^{-+},2^{+-}\dots$) are clearly distinguishable from mesonic quantum numbers. A color-neutral bound state of pure gluons ($ggg$) confined by the color self-interaction might exist as well [56,57]. Such an exotic entity could shed light on the effect of gluonic angular momentum to the confinement potential [58].

- **measurement of in-medium-modification of meson masses**
  The masses of light mesons are expected to be modified inside the nuclear matter which is thought to be a consequence of partial restoration of chiral symmetry. In the theory of chiral symmetry, its spontaneous breaking imparts mass to the mesons [59]. Figure 1.11 illustrates the expected mass shift and split-off in charge-symmetric states. Experimental evidence for the in-medium modification was found in several experiments for the light isoscalar $\pi$, $\omega$, $\rho$ and $\phi$ mesons [60]. In the $\overline{P}$ANDA experiment a large set of analyses will
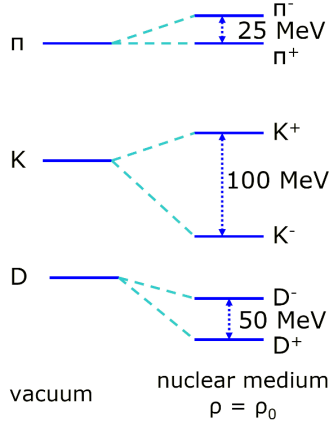
**Figure 1.11.:** Expected meson mass modification due to partial restoration of chiral symmetry and split-off of charged symmetry partners in nuclear matter.

be dedicated to finding further experimental evidence for this phenomenon and mesons with heavy flavor content are accessible for measurements of their properties in nuclear matter as well [61–63].

- **production and analysis of hyperons**
  By substitution of a light quark inside the nucleon through a heavier one, hyperons are formed such as $\Sigma^{\pm/0}$, $\Lambda$, $\Xi^{-/0}$, $\Omega^-$ (with strangeness $\neq 0$) or $\Lambda_c^+$, $\Sigma_c^+$, $\Sigma_c^{++}$, $\Sigma_c^0$ (with charm $\neq 0$) or even baryons exhibiting a combination of $s$- and $c$ quarks. The production of large quantities of these hyperons is intended in $\overline{\mathrm{P}}$ANDA in order to study their integration into heavy nuclei and the emerging binding configuration inside nuclear matter [64].

A large set of further points to be investigated by the $\overline{\mathrm{P}}$ANDA experiment is mentioned in the following just by headwords and without significance in priority. For more detailed descriptions of the $\overline{\mathrm{P}}$ANDA physics goals it is referred once more to [36, 37, 47, 48]. Following further topics are intended to be addressed through the $\overline{\mathrm{P}}$ANDA experiment:

- open-charm spectroscopy [65]

- $\mathcal{CP}$-violation in $D\bar{D}$- and $\Lambda\bar{\Lambda}$-systems

- precision spectroscopy of new $D_s$ states

- precision measurements of $D$ decay channels with small branching ratios

- hadronic structure functions through deep inelastic virtual *Compton* scattering [66]

- transversity and analyses of *Drell-Yan* processes with high statistical significance [67]

- measurement of complex time-like form factors in a wide kinematic range up to momentum transfers of $q^2 \approx 20\,\mathrm{GeV}^2$ and first-time independent determination of $G_E$ and $G_M$ [68–70]

### 1.3.1. Configuration of the $\overline{\mathrm{P}}$ANDA Detector

The $\overline{\mathrm{P}}$ANDA detector will be placed inside the HESR as depicted in Figure 1.9 which features a unidirectionally circulating quasi-DC beam of antiprotons with very high luminosities. The interaction point (IP) is defined by a beam of frozen hydrogen droplets which represent the
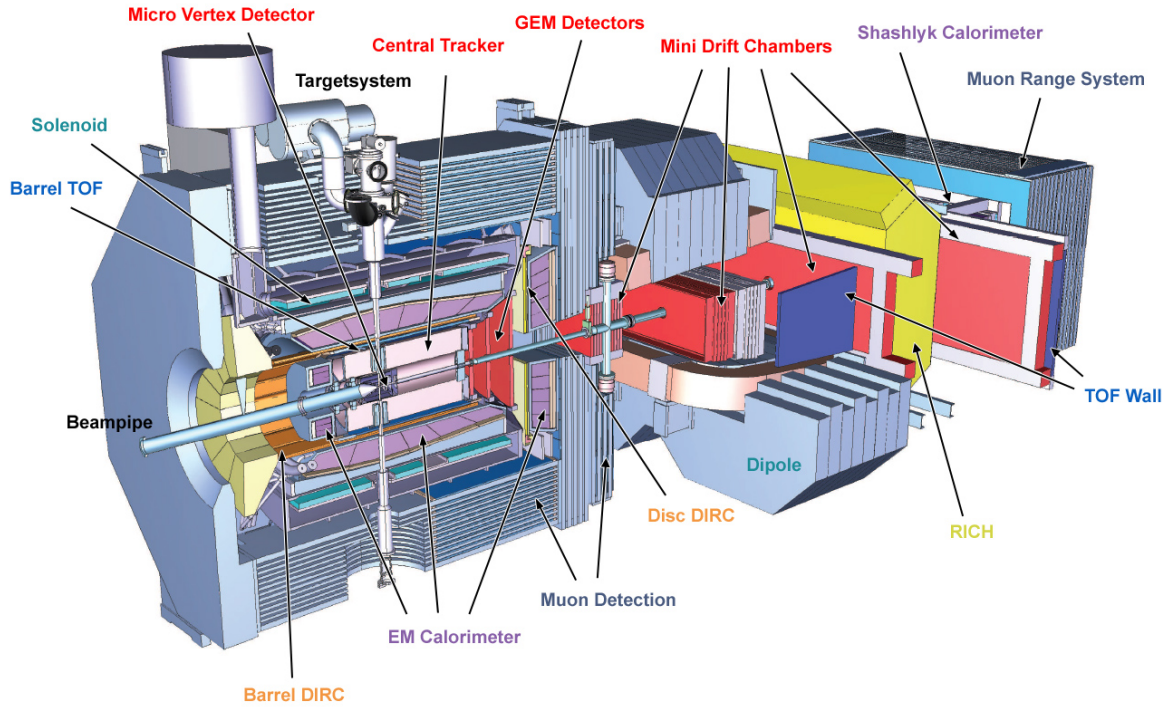
**Figure 1.12.:** Artist's view of the $\overline{\mathrm{P}}$ANDA detector system [71].

target crossing the $\bar{p}$ beam orthogonally [72]. This fixed-target layout yields higher luminosities over collider experiments but exhibits an asymmetric acceptance pattern. The detector is therefore divided into two separate parts, the target spectrometer (TS) and the forward spectrometer (FS) to achieve full angular coverage and to resolve the strongly forward boosted tracks with a comparable precision like highly declined tracks with low momenta. An artist's view of the detector system is shown in Figure 1.12. The beam of antiprotons is guided inside an evacuated beam pipe through the detector and crosses the target at the interaction point. The target may be comprised of a thin stream of frozen hydrogen which is shot through the target spectrometer perpendicular to the beam pipe. Since the $\overline{\mathrm{P}}$ANDA experimental program foresees operation with heavier target nuclei as well, the target system will be replaced eventually by wire targets [48].

### 1.3.1.1. Target Spectrometer

The target spectrometer encloses the IP such that radially escaping charged particles and photons are detected within a solid angle of almost $4\pi$ coverage with polar angles of more than 22° to the beam axis. The tracking of charged particles is facilitated by a $\phi$-symmetric magnetic field generated by a superconducting solenoid magnet (length 2.8 m) with a massive iron return yoke which assures a field homogeneity along the $z$-axis of better than 2 % [73]. From the curvature of charged particle trajectories inside the magnetic field, momentum and the sign of charge can be inferred. Figure 1.16 shows a cross section of the target spectrometer. From the interaction point toward the outer periphery of the solenoid yoke a variety of subdetectors are instrumented described in more detail in the following paragraphs.
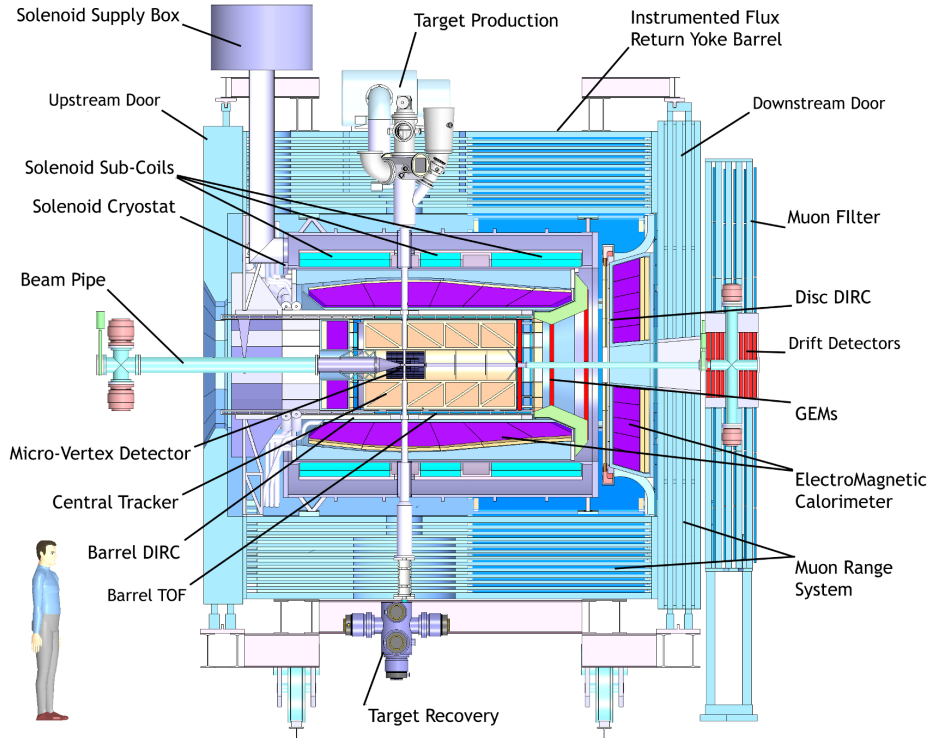
**Figure 1.13.:** Schematic cross section of the $\overline{\text{P}}$ANDA forward spectrometer (TS) [35].

**Micro-Vertex Detector (MVD)**   Close to the interaction point follows the Micro-Vertex Detector (MVD) which shall support the global particle tracking with hit points of high spacial resolution. Those first sampling points are the most critical ones and determine the overall tracking resolution. The particles are subject to minimal scattering inside the beam pipe walls (beryllium with ca. 200 μm thickness) before they traverse the first sensitive layer of the MVD. The geometrical construction, comprised of two layers of silicon pixel detectors (layer 1 and 2 at radial distances of 2.5 cm and 5.0 cm from the IP, respectively) and two layers of silicon strip detectors at radial distances of 9.5 cm and 12.7 cm in the barrel part of the MVD is depicted in Figure 1.14. Furthermore, the forward (downstream) region is instrumented with two silicon pixel discs followed by four hybrid discs with pixel sensors covering the inner disc area and strip sensors equipped at the outside [35]. The MVD is optimized for minimum radiation load yielding high spacial resolution at the same time. The detection of delayed secondary decay vertices characteristic to hadronic open-charm channels with decay lengths of $\mathcal{O}\,(100\,\text{μm})$ (cf. sec. 1.2) shall be possible [74–76]. The data acquisition concept of $\overline{\text{P}}$ANDA foresees a free running un-triggered regime. Each detected hit information (spacial position, time-stamp and energy-loss information) therefore has to be transferred off the detector electronics within finite latency intervals. Consequently, the required data bandwidth of front-end data links will be larger than in experiments exhibiting a central hardware trigger as e.g. LHC experiments with fixed bunch-crossing intervals of 25 ns. Few front-end electronics solutions for un-triggered read-out of silicon pixel- as well as strip sensors exist. Therefore, the development of a new FE ASIC for $\overline{\text{P}}$ANDA was initiated [77–79]. Several options for the FE electronics for the strip detector part are investigated, work on an entirely new chip design was started in 2012 [35,80]. More information and detailed discussions about requirements and design are given later in this work (sec. 4.3).

Max. Length:
~ 40 cm
Max. Radius:
15 cm
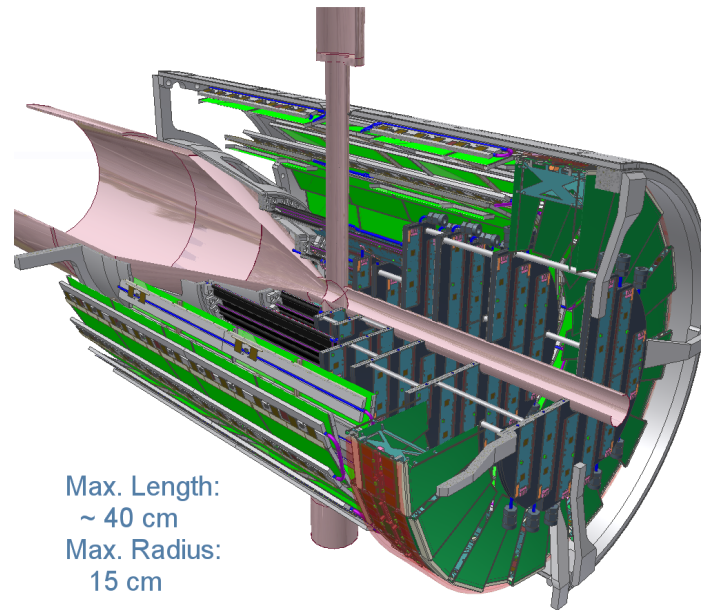
**Figure 1.14.:** The Micro-Vertex Detector [35].

The pixel detector part of the MVD comprises novel epitaxial silicon sensors with very low material occupancy. Sensors based on a standard low resistivity *Czochralski* substrate are deposited with $n^+$ epitaxial layers which form the sensitive volume and segmented into a matrix of $100\,\mu\text{m} \times 100\,\mu\text{m}$ large pixels with this technology. After the wafer processing stage, the substrate is thinned to negligible thicknesses to lower the material budget [81]. Epitaxial thicknesses of $50\,\mu\text{m}$ to $100\,\mu\text{m}$ are evaluated in great detail for feasibility of the application in $\overline{P}$ANDA [35]. The electronic front-end ASIC responsible for the read-out, amplification and preprocessing of charge signals collected by the pixel-cells on the sensor, named "ToPix", is developed by the INFN group in Turin/Italy. Several prototypes have been successfully tested so far. For more details on the FE architecture it is referred to Section 4.3 and Ref. [35]. Latter reference reflects the current R&D status and gives an overview of prototype test results. Connection between sensor and FE ASIC is accomplished by flip-chip mounting both onto each other with proper alignment of the pixel-cells of the sensor and the corresponding, equally sized pixel-cells on the FE chip. A persisting conducting path between pads on both sides will be done by melting small Sn or In–balls placed upon the pads of one side prior to the mounting process thus forming a solder-like bump-bond connection. The assembled entity is finally attached to a multilayer bus structure which contains further passive components and connectors. Signals and power lines are fed from this bus-PCB to the FE-hybrid via wire-bond connections. An artist's view of a completely mounted pixel module is shown in Figure 1.15 together with a cross section of the described bump-bonded assembly of sensor and front-end ASIC.

Requirements, design, construction and prototyping for the MVD strip part is discussed in great detail in Chapter 4. Its description is therefore foregone here.
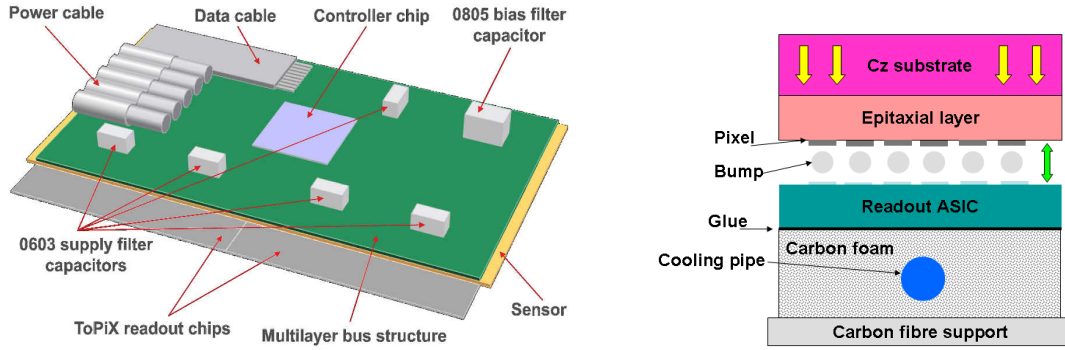
**Figure 1.15.:** Construction of a single hybrid pixel module. Figures adapted from [35].

**Central Tracker**   (STT[10]) The central tracking system following in radial direction after the MVD provides dense track-points within a cylindrical volume with a length of 1.5 m, an inner radius of 15 cm and an outer radius of 50 cm. It will be densely packed with straw-tubes. These consist of long cylinders of Mylar-foil and are filled with gas of slight overpressure wrt. the environmental air pressure such that a self-supporting pipe with a diameter of 1 cm emerges. A thin wire is embedded as central electrode. A charged particle traversing the tube causes ionization of the gas along its track and the liberated charge carriers drift toward the central wire due to the externally applied high voltage. The small drift volume constitutes a fast charge collection. The central tracker volume will be filled with 24 layers of straw tubes running parallel to the $z$ direction. Eight central layers, however, will be mounted with a small skew angle of 3° to provide geometrical reconstruction of the tracks' longitudinal coordinates as well [82].

**Čerenkov Detector System**   (DIRC[11]) Beside the tracking of particles which provides a momentum measurement due to the curvature of the trajectories inside the solenoid field, a full characterization of single particles (particle ID – PID) requires an additional independent determination of its mass or velocity. Latter can be measured for fast particles using the *Čerenkov* effect: when a charged particle enters a medium with a velocity higher than the velocity of light inside the medium, photons are emitted at an characteristic polar angle $\Theta_C$ with respect to the particle's trajectory. Between the opening angle of the ensuing light-cone and the particle velocity exists following relation:

$$\cos\Theta_C = \frac{1}{n\beta} \tag{1.1}$$

where $\beta = v/c$ is the particle velocity in units of the light-speed in vacuum and $n$ the refractive index of the medium. In $\overline{\text{P}}$ANDA, slabs of fused silica radiators are instrumented in the barrel outside the central tracker and in forward direction. This material allows operation down to particle momenta of approx. 800 MeV/$c$. Thin slabs with high surface quality cover the entire acceptance range except the backward region (since particles encountered in this region exhibit usually low $\beta$ values). The light signals are internally reflected toward the back-end side where a focusing optics projects it onto Multi-Channel Plate Photomultipliers (MCP-PMTs) for read-out [83, 84].

---

[10] Straw-Tube Tracker.
[11] Detection of Internally Reflected Cherenkov Light.

**Time-of-Flight Detector TOF**   Since the DIRC system fails to provide useful information for the particle ID at momenta smaller than $\approx 800\,\mathrm{MeV}/c$, the particle velocity is inferred from an additional TOF system in the barrel region (the forward region usually comprises faster particles due to the forward boost) consisting of thin polymeric scintillator slabs. The timing resolution of the system (scintillator response time and electronic processing jitter) has to be better than $\mathcal{O}\,(100\,\mathrm{ps})$ since no start detector can be used inside the critical volumes of MVD and STT. Furthermore, the precise timing should facilitate the read-out of the barrel DIRC system [48,83].

**Electromagnetic Calorimeter EMC**   In radial outbound direction to the DIRC and TOF systems follows the EMC to provide for a superior acceptance of a wide range of photon energies with a high resolution. It consists of roughly 11,000 scintillating lead-tungstate (PWO[12]) crystals whose geometry is chosen such that the particle shower ensuing after the capture of a high-energetic $\gamma$ is contained within one or several crystals without significant leakage. Detection of photons is crucial to the identification of many decay channels of hadronic states. The superior light yield of PWO crystals compared to other scintillator materials, however, requires cooling of the whole EMC array to an operating temperature of -25 °C. The read-out of the barrel EMC crystals will be realized by large area avalanche photodiodes (LAAPDs). Such devices yield a high intrinsic gain which critically depends on proper bias voltage and temperature stabilization. This mode imposes a further constraint on the cooling system which has to correct for temperature variations as small as $\mathcal{O}\,(0.1\,\mathrm{K})$. The crystals in the forward end cap (3,600 crystals) are subject to significantly higher radiation fluxes. APDs would suffer of severe degradation of gain and signal-to-noise ratio and are therefore replaced by vacuum photo-triodes (VPT) for this part. Beside higher radiation tolerances these devices can handle the higher event rates evident in the forward region [85]. The backward region of the target spectrometer is covered with 600 further crystals to provide sufficient acceptance in this region as well.

**Muon Detectors**   The flux-return yoke of the solenoid magnet will be segmented to provide space for muon detectors in a sandwiched pattern between the yoke segments. Since muons are more penetrating than other charged particles, the magnet's iron yoke acts as filter for all particles except muons. A detection of these particles is demanded for the proper separation between pionic decay muons and muons originating from semileptonic or leptonic decays of hadronic states. The detectors are Monitored Drift Tubes (MDTs) for the barrel part and muon drift tubes in the forward region of the TS. Moreover, the sandwich-like pattern of iron and detector allows for a range tracking of muons and other penetrating particles. Additional high-$Z$ stopping materials will be introduced in the forward region between the TS and the FS to compensate for the higher momenta encountered in the forward direction.

**Forward Tracking System**   In forward direction an improved tracking is required since the longitudinal momenta of the particles are very high and lie outside the acceptance of the central tracker. Instrumentation of additional GEMs[13] and Mini Drift Chambers (MDCs) in

---

[12] Convenient short form for $PbWO_4$.

[13] Gas Electron Multiplier: An insulating foil with a large number of microscopic holes and metalizations on both sides is placed inside a gas volume between two electrodes. The electric field geometry with an applied high voltage between the two electrodes in the vicinity of the microscopic holes facilitates a cascade amplification of an incident electronic charge.

the very forward region of the target spectrometer, inside the gap between TS and FS and again behind the TS magnet provide a superior momentum resolution of $\Delta p/p = 0.2\,\%$ for particles with $p = 3\,\mathrm{GeV}/c$ and trajectories with polar angles between 5° and 22° [36].

### 1.3.1.2. Forward Spectrometer

The forward directed part of the particles emerging from the $\bar{p}p$ collisions in the IP can not be tracked with sufficient precision by the detectors in the target spectrometers. Particles with polar angles to the beam axis of less than 10° in horizontal and less than 5° in vertical direction are therefore measured in the domain of the forward spectrometer which contains tracking, particle ID and colorimetric detectors optimized for strongly forward boosted tracks with low and very low transverse momenta. A dipole magnet bends the particle trajectories
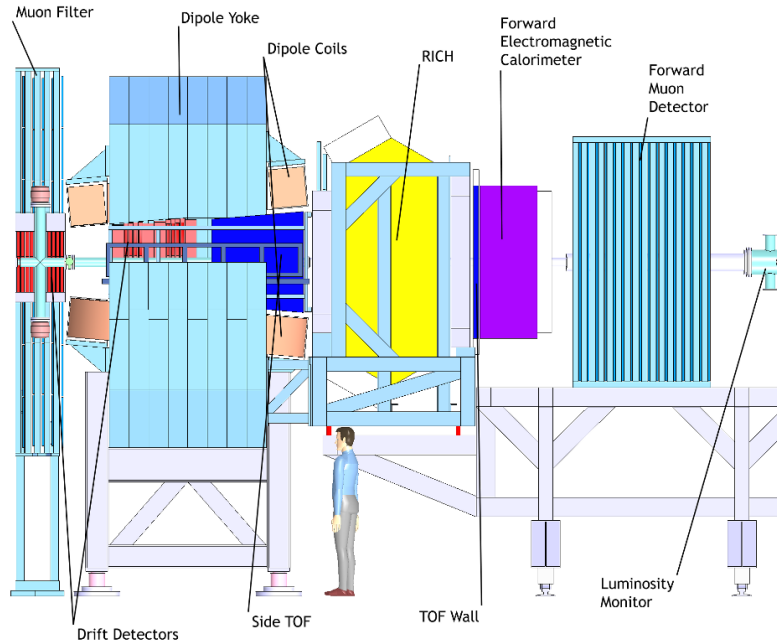


**Figure 1.16.:** Schematic cross section of the $\overline{\mathrm{P}}$ANDA target spectrometer (TS) [35].

in circular curves with radii depending on the momentum [73]. The forward tracking in the FS is realized with 3 stations of MDCs before, inside and behind the dipole magnet and two additional stations before and after the RICH[14]. The latter is a Čerenkov detector with a radiator of silica aerogel and freon gas ($C_4F_{16}$). An array of mirrors behind the radiator focuses the light out of the detector volume perpendicular to the beam axis onto PMTs[15]. This detector contributes to the particle identification for charged particles in the momentum range of $2\dots15\,\mathrm{GeV}/c$. Slower particle momenta are, similar to the redundant PID concept of the target spectrometer, covered by the forward TOF system. Behind the RICH detector an electromagnetic calorimeter is found which exhibits a different design than the EMC counterpart of the target spectrometer. Since the expected momenta are much higher in forward direction, significantly more material is needed to contain the emerging showers

---

[14] Ring-Image Cherenkov detector.
[15] Photomultiplier Tubes.

without leakage. To meet this demand, a shashlik-type calorimeter will be utilized here. This kind of calorimeter consists of modular rods which are composed of absorber (usually lead) and scintillator tiles in alternating order. The scintillating tiles are read out by wave-length shifting optical fibers plunging through holes which run through the entire length of the stack. At the ends of those fibers, PMTs or other sensitive photon detectors convert the light to electronic signals. A high containment of showers at a good energy resolution can be achieved by optimization of the materials, order and thicknesses of the tiles. The $\overline{\mathsf{P}}$ANDA forward EMC will be equipped with an array of $26\times54$ such modules, each having a quadratic face area with a side length of 55 mm, to cover the entire acceptance range [48]. Finally, a muon range system equivalent to the one in the forward part of the target spectrometer is located behind the forward EMC to distinguish between muons and pions for high beam momenta and, additionally, to detect neutrons and antineutrons [36].

In the most downstream position at ca. 10 m behind the interaction point the luminosity monitor (LuMo) is placed which can determine the absolute luminosity with a precision of up to 3 %. This accuracy is required for the envisaged precision of mass and mass-width measurements. The luminosity monitor currently foresees a design with four planes of double-sided silicon strip detectors placed inside a vacuum chamber to minimize parasitic scattering. Very small scattering angles in a range of $\Theta = 3\ldots8$ mrad will be reconstructable with this setup [86].

### 1.3.2. Requirements to the Detector System

The briefly discussed physics objectives to be addressed by means of the $\overline{\mathsf{P}}$ANDA detector require a challenging superior performance of the apparatus with respect to spacial (tracking) resolution, timing resolution, particle identification and disentanglement of mixed-event hits, dead-time free operation, bandwidth as well as event filter latencies. Each of those points significantly directs the development especially of the read-out electronics, digitization concepts, data transfer techniques and preprocessing hard-, soft- and middleware[16] [36, 48, 87].

The data acquisition concept chosen for the $\overline{\mathsf{P}}$ANDA experiment foresees a continuous un-triggered operation of all main detector components [33, 48]. This determination implies a self-triggered, asynchronous read-out scheme for all FE electronics components in contrast to the majority of synchronously working detectors like LHC-based experiments with a fixed bunch-crossing interval of 25 ns. Hence each detector channel, upon registration of a relevant signal, will tag the specific event with a time-stamp which should be sufficiently resolved to prevent mixing of events in the same time bin. As will be shown later in section 4.3 the precise knowledge of the time structure of the expected event rate is imperative for a reasonable layout of the timing accuracy and maximum latencies involved in the data transfer and processing chain. For a constant (time-averaged) event rate, a *Poisson* - distributed number of $n$ particles per time interval $\Delta t$ can be expected with the probability

$$P(n) = \frac{(r\Delta t)^n \exp\left(-r\Delta t\right)}{n!}. \tag{1.2}$$

Task of the front-end electronics designers is to constrain the mean dead-time of a single read-out channel to a value where $P(2)$ (denoting the probability, that after a registered hit

---

[16] The term "middleware" here is used (contrary to the commonly used meaning) for the layer between hard- and software, denoting in particular logic configurations which are software-based at design-time but implemented as gate-circuits in FPGAs or ASICs.

a second one is observed within the dead-time window) from eqn. (1.2) stays below a defined limiting value, e.g. 1 %.
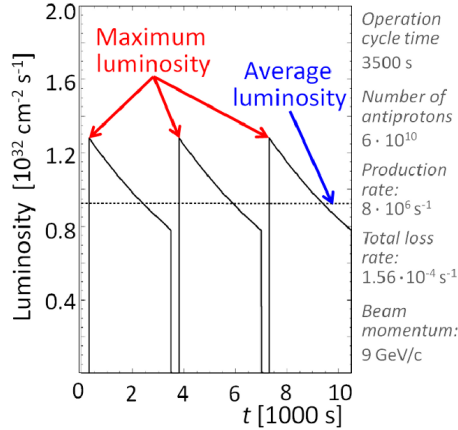


**Figure 1.17.:** Time dependent profile of the luminosity for a beam momentum of $9\,\mathrm{GeV}/c$ [88].

The modulation of the momentary event rate is closely coupled to the luminosity $L$ of the beam-target interaction and in general not constant. Figure 1.17 illustrates the time dependence with an example luminosity profile calculated by [88]. The discussion of the consequences emerging for the design of the front-end electronics for the MVD silicon strip system is rendered in section 4.3.

The spacial resolution of the tracker system is a crucial cornerstone in the physics program of $\overline{\mathrm{P}}$ANDA. Particularly the open-charm channels with delayed decaying $D$ mesons are required to be reconstructed with high efficiencies. Thus, a clear identification of such decay signatures has to be achieved. Table 1.2 lists several hadronic channels which exhibit secondary decay vertices reporting life-times and mean decay lengths of the given channels. The typical decay lengths of hadrons containing charm quarks is well below 1 mm. Those particles decay still inside the beam pipe. The resulting secondary products then are acquired with the tracking system. Thus, a very precise measurement of the movement of those particles upon leaving the beam pipe is mandatory to allow a back-trace to the mutual crossing point. The analysis will then observe whether this point is shifted wrt. the interaction point and ascertain the decay distance to the latter, if applicable. Extensive simulations have been conducted considering the full set of physics processes and an appropriate representation of the detector behavior by *Jäkel* (for $D$ and $D^*$ mesons) and others for a variety of benchmark channels [36,89]. As a result, appropriate segmentation sizes for the pixel and strip detectors of the MVD have been identified. Those feature sizes are considered in the subsequent hardware design process. For the strip detector system, a strip pitch based on these calculations has been chosen which is described in greater detail in section 4.2.

Finally, the impact of the energy released around the IP within all materials must be considered since the envisaged luminosities are very high. Traversing particles interact not necessarily only through ionizing collisions but also infer damage by hard hadronic knock-outs of lattice atoms and a subsequent emerging collision cascade. This phenomenon is very difficult to quantify since the exact composition and interaction cross sections of the target material enter the calculation as well as the spectrum of kinetic energies of impinging particle species. However, a normalization to a comparable quantity, e.g. the non-ionizing energy loss (NIEL) wrt. 1 MeV neutrons or kinetic energy released in matter (KERMA) as introduced in Appendix B is applied to infer the magnitude of radiation damage to several irradiated

components foreseen to be utilized in the construction of a silicon strip barrel detector module for the MVD in Chapter 4. The expected annual 1 MeV neutron equivalent fluences at different locations within the MVD were determined by detailed simulations and reported in [35, 90] are listed in Table 1.1.

| target | $\bar{p}$ momentum | annual fluence ($10^{13} n_{eq} \cdot \mathrm{cm}^{-2} a^{-1}$) | | |
|---|---|---|---|---|
| | | $2\,\mathrm{GeV}/c$ | $9\,\mathrm{GeV}/c$ | $15\,\mathrm{GeV}/c$ |
| $p$ | | 1.3 | 1.4 | 1.9 |
| $^{14}\mathrm{N}$ | | 0.5 | 5.8 | 6.6 |
| $^{132}\mathrm{Xe}$ | | <0.5 | 3.0 | 9.8 |

**Table 1.1.:** Annual fluences of non-ionizing radiation damage (NIEL) at the innermost layers of the MVD normalized to 1 MeV-neutron equivalents taken from [35]. $\bar{p}p$-reaction values were inferred from DPM-Calculations, those for heavy nuclear targets are calculated based on the UrQMD model.

| particle | mean half life $\tau$ | decay length $c\tau$ | prominent decay channels |
|:---:|:---:|:---:|:---|
| $K_S^0$ | 895.3(6) ps | 2.68 cm | $\pi^+\pi^-$ |
| $D^\pm$ | 1.040(7) ps | 311.8 μm | $e^+ x + c.c.$ |
| | | | $K^\mp x + c.c.$ |
| | | | $\overline{K}^0 x + K^0 y$ |
| | | | e.g. $K^-\pi^+\pi^+ + c.c.$ |
| | | | $\overline{K}^0\pi^+\pi^+\pi^- + c.c.$ |
| $D^0$ | 410.3(15) fs | 123.0 μm | $e^+ x + c.c.$ |
| | | | $\mu^+ x + c.c.$ |
| | | | $K^- x + c.c.$ |
| | | | $K^+ x + c.c.$ |
| | | | $\overline{K}^0 x + K^0 y$ |
| | | | e.g. $\overline{K}^0 K^+ K^-$ |
| | | | $K^-\pi^+\pi^+\pi^- + c.c.$ |
| | | | $\overline{K}^0\pi^+\pi^-\pi^0 + c.c.$ |
| $D_S^\pm$ | 490(9) fs | 147.0 μm | $e^+ x + c.c.$ |
| | | | $K^- x + c.c.$ |
| | | | $K^+ x + c.c.$ |
| | | | $\overline{K}^0 x + K^0 y$ |
| | | | e.g. $K^+ K^-\pi^+ + c.c.$ |
| $\Lambda$ | 26.32(20) ps | 7.69 cm | $p\pi^-$ |
| $\Sigma^+$ | 80.18(26) ps | 2.404 cm | $p\pi^0$ |
| | | | $n\pi^0$ |
| $\Sigma^-$ | 147.9(11) ps | 4.434 cm | $n\pi^-$ |
| $\Xi^-$ | 163.9(15) ps | 4.91 cm | $\Lambda\pi^-$ |
| $\Omega^-$ | 82.1(11) ps | 2.461 cm | $\Lambda K^-$ |
| | | | $\Xi^0\pi^-$ |
| | | | $\Xi^-\pi^0$ |
| $\Lambda_c^+$ | 200(6) fs | 59.9 μm | $p\overline{K}^0$ |
| | | | $pK^-\pi^0$ |
| | | | $\Lambda\pi^+\pi^+\pi^-$ |
| | | | $\Sigma^0 + \pi^+\pi^-$ |
| $\Xi_c^0$ | 112(13) fs | 33.6 μm | $\Xi^-\pi^+$(unknown) |

**Table 1.2.:** Strange and charmed hadrons which can be identified by their decay length [35]. ($c.c.$ – charged currents)

# Chapter 2.

# Particle Detection with Semiconductor Devices

Solid state devices for the detection of charged particles have been successfully utilized since several decades with increasing frequency [91–93]. Beside beneficial properties over gaseous or scintillation detectors, the widespread distribution of technologies and materials make the application of semiconductors, and particularly silicon attractive in this field. The key properties of this material, its feasibility for charged particle detection and developments leading to sophisticated modern highly granular particle detectors will be briefly discussed within this chapter.

## 2.1. Semiconductors as Detector Material

In order to access the energy released by traversing particles through ionization inside a material, a depletion from thermally generated charge carriers is necessary, while the signal charges should be extractable by drift in an externally applied electric field. This condition is met in semiconductor materials. Semiconductors are characterized by the absence of intrinsic self-conduction (high resistance) but the ability to conduct charges exceeding a certain energy threshold $E_g$ denoted as energy gap, e.g. by thermally excited electrons. For the basic understanding of this property refer to Figure 2.1. Isolated atoms exhibit a set of discrete energetically allowed eigenstates. A large ensemble of atoms, on the other hand, brought in closer mutual distances, eventually shows an overlap of the atomic wave functions. As
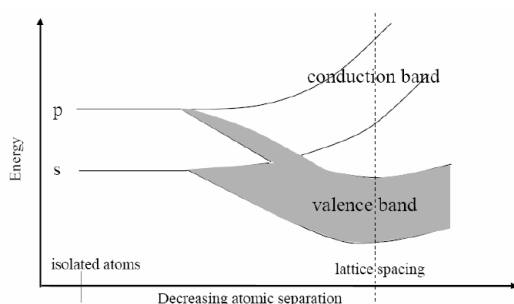


**Figure 2.1.:** Degeneration of atomic levels into energy bands at the transition from isolated atoms to a collective macroscopic state with wave-function overlap in a lattice.

a consequence, the initially discrete energy levels of the collective eigenstates degenerate to several energy bands with non-zero probability distributions for electrons and energetically forbidden areas in-between. The lowest lying band filled with electrons is usually referred to as "valence band" while the next one with higher energy is designated "conduction band".

Schemes of the encountered band structures in GaAs[1] and Si are shown in Figure 2.2. The energetic levels are presented in dependence of the inverse position inside the *Brillouin*-zone, denoted as wave vector $k$. For an introduction to solid state physics and the nomenclature used therein it is referred to Ref. [94]. The gap between the topmost energetic level of the valence band and the lowest-lying allowed level of the conduction band is the material specific energy gap $E_g > 0$ for all semiconductors. While the energy gap for GaAs in Figure 2.2(a)



(a)                                                            (b)
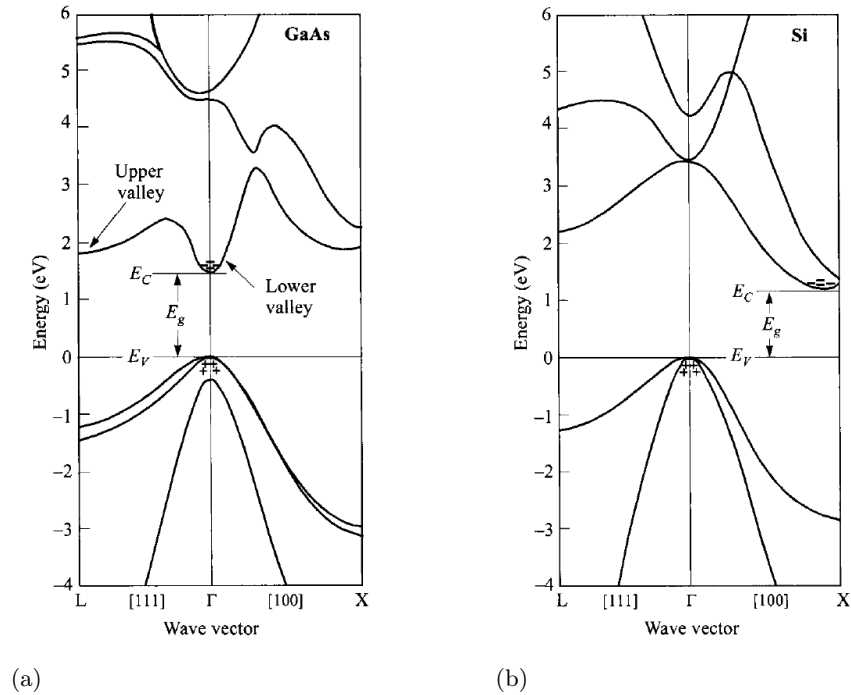
**Figure 2.2.:**  Band structure along wave-vector $\vec{k}$ inside the principal *Brillouin* zone for gallium-arsenide and silicon representing semiconductors with (a) direct energy gap between valence and conduction band bridged by a pure optical transition and (b) indirect bandgap which requires both optical and phononic excitations to overcome the forbidden region, from *Sze* [95].

can be bridged by a direct (optical) transition to excite an electron into the conduction band a further lateral excitation is required in silicon (Figure 2.2(b)) in order to reach the allowed zone of the conduction band. This transition in $k$–space corresponds to a momentum transfer to the crystal lattice (phononic excitation). Semiconductors exhibiting such a combined optical and phononic transition are therefore called indirect semiconductors, while materials where the transition endpoints are located at the same wave vector as shown in the case of GaAs are referred to as direct semiconductors.

### 2.1.1.  Signal Generation

A key parameter characterizing the usability of solid state materials as particle detectors is the number of separated electron-hole charge carrier pairs per incident energy. This quantity is obtained through tedious calculations considering a variety of lattice degrees of freedom, such

---

[1] GaAs is a composite semiconductor from elements located in the 3$^{rd}$ and 5$^{th}$ group of the periodic system and therefore designated a III–V-semiconductor.

as different phononic and photonic excitations demonstrated e.g. for silicon in Ref. [96]. The electron-hole pair creation energy, beside other parameters for different materials is reported in Table 2.1.

|  | Si | Ge | GaAs | C (Diamond) |
|---|---|---|---|---|
| atomic number $Z$ | 14 | 32 | 31+33 | 6 |
| mass number $(u)$ | 28.086 | 72.61 | 69.72+74.92 | 12.01 |
| lattice constant $a$ (Å) | 5.431 | 5.646 | 5.653 | 3.567 |
| mass density $(\mathrm{g \cdot cm^{-3}})$ | 2.33 | 5.33 | 5.32 | 3.52 |
| energy gap $E_g$ ( eV) @ 300 K | 1.11 | 0.66 | 1.42 | 5.6 |
| rel. permittivity $\epsilon/\epsilon_0$ | 11.8 | 16.0 | 12.8 | 5.7 |
| melting point (℃) | 1415 | 938 | 1237 | 3527 |
| intrinsic charge carrier density ( cm$^{-3}$) @ 300 K | $1.01 \cdot 10^{10}$ | $2.4 \cdot 10^{13}$ | $2 \cdot 10^6$ | $\approx 10^{-27}$ |
| electron mobility $\mu_e$ ( cm$^2$/Vs) @ 300 K | 1500 | 3900 | 8500 | 1800 |
| hole mobility $\mu_h$ ( cm$^2$/Vs) @ 300 K | 450 | 1900 | 400 | 1200 |
| electric breakdown field (V/cm) | $3 \cdot 10^5$ | $\approx 10^5$ | $4 \cdot 10^5$ | $3 \cdot 10^7$ |
| mean electron-hole pair creation energy $\varepsilon$ (eV) | $3.67 \pm 0.02$ | 2.9 | 4.2 | 13.25 |

**Table 2.1.:** Properties of some selected semiconductor materials. Values are taken from [23, 92, 95–98].

Analysis of measured electron-hole creation energies $\varepsilon$ of a large variety of semiconductors revealed a strictly linear dependence on the energy gap [99] as reviewed in Figure 2.3. Following
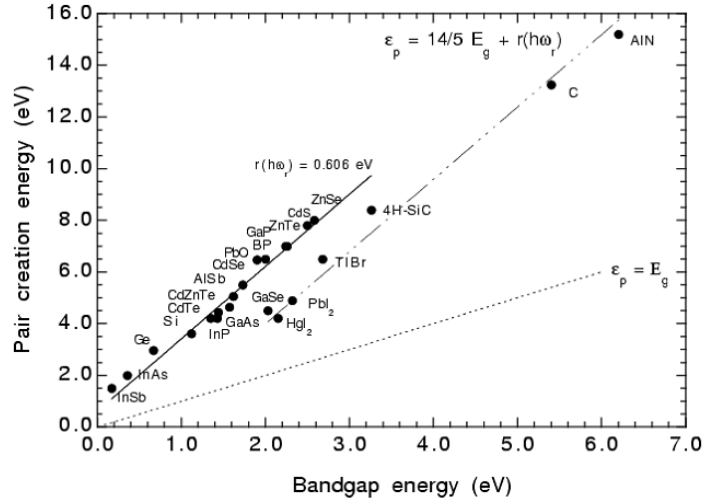


**Figure 2.3.:** Dependence between ionization energy and bandgap measured for the majority of known semiconductor materials, adapted from *Owens et al.* (2004) [100].

relation between energy-hole creation energy and the semiconductor's energy gap is empirically determined from the main branch of those measured values [100]:

$$\varepsilon = 2.8E_g + 0.6 \,\mathrm{eV}, \tag{2.1}$$

Which is valid for most compound semiconductors. Note, that few, mostly asymmetric e.g. III–VI semiconductors like GaSe but also the intrinsic semiconductor diamond populate a secondary branch with similar slope but different intercept. Specific semiconductors may exhibit slightly differing values. In the case of silicon, the bandgap as well as $\varepsilon$ has been measured with high precision (cf. Table 2.1). A good overview of notable measurements is given in Ref. [96]. Since in the further context of this work the focus will remain exclusively on silicon semiconductors, the accurately determined values from Ref. [97] are regarded as reference values, yielding

$$\varepsilon_{\beta^-} = (3.67 \pm 0.02)\,\text{eV}$$

for electrons and

$$\varepsilon_\alpha = (3.62 \pm 0.02)\,\text{eV}$$

for alpha particles. First value is evenly valid for high-energetic photons and may reflect the value for minimum ionizing particles somewhat better than the second one obtained for $\alpha$ particles. Therefore, the former statement is used in the further considerations as reference.

### 2.1.2.  Intrinsic Energy Resolution

Independent of the actual mechanism creating a number of $N_q$ free charge carriers through ionization inside semiconductors, a statistical fluctuation according to *Poisson*'s distribution of $\sigma_q = \sqrt{N_q}$ is expected. In fact, a much smaller spread in the number of electron-hole pairs can be observed upon release of a defined amount of energy in semiconductors. *Fano* (1947) attributed this reduced statistical fluctuation to the limited degrees of freedom due to coupled excitations of phononic and photonic states in solid state devices and derived the correct statistics which yields [101]

$$\sigma_q = \sqrt{F N_q} \tag{2.2}$$

with the *Fano*-factor $F = 0.1$ for Si and Ge. Transposing the fluctuation $\sigma_q$ in the number of electron-hole pairs to the standard deviation referred to the incident energy $E$ reads

$$\sigma_E = \sqrt{F E \varepsilon}. \tag{2.3}$$

This intrinsic energy fluctuation is often referred to as "*Fano*-noise" in literature. For a typical mean energy loss of $120\,\text{keV}$ [2] for minimum ionizing particles in $300\,\mu\text{m}$ silicon a fluctuation of $\sigma_E = 210\,\text{eV}$ can be identified. The total noise figure encountered in a silicon detector system is usually dominated by the noise of the attached preamplifier and the leakage current shot noise of the sensor which are much larger noise sources than the *Fano*-noise.

### 2.1.3.  The $p-n$ Junction

A problem occurring with the use of pure (intrinsic) semiconductors are thermally generated electron-hole pairs bridging the energy gap and causing a measurable current flow upon application of an external potential. The free charge carrier concentration in silicon for a temperature of $300\,\text{K}$ is reported with $n_i = 1.01 \cdot 10^{10}\,\text{cm}^{-3}$ [102]. The specific resistance given for the intrinsic material is determined by those free charge carriers. A minimum ionizing particle, on the other hand liberates free charges inside the sensitive volume of $\mathcal{O}\,(110\,\text{e-h pairs}/\,\mu\text{m})$

---

[2] For the calculation of mean and most probable energy loss see sec. 2.3.

corresponding to the mean energy loss (for detailed description refer to sec. 2.3). Such a signal drowns inside the sea of thermally aroused charge carriers. A possible countermeasure would be constituted by cooling the detector volume to a temperature where the signal charges dominate the thermally generated ones. A different approach, which allows operation of semiconductor detectors above cryogenic temperatures, would be to deplete the detector volume from all free charge carriers. This is accomplished through a semiconductor junction, i.e. the combination of semiconductors with differing *Fermi*-energies. The *Fermi*-level in semiconductors is defined such that it assumes the average energy between the highest occupied state for electrons and the lowest occupiable state for holes. In intrinsic (pure) semiconductors those levels correspond to the upper bound of the valence band and the lower bound of the conduction band, respectively. The *Fermi*-level in the latter case thus would be located in the center of the forbidden energy gap between valence and conduction band.

### 2.1.3.1. Doping

The shift of the local *Fermi*-level required to create a semiconductor junction can be inferred by deliberately placing additional energy levels inside the forbidden energy gap. Physically, this is achieved by introduction of controlled impurities into the bulk lattice with concentrations typically between $10^{11}\,\mathrm{cm^{-3}}$ and $10^{18}\,\mathrm{cm^{-3}}$ (purities between $10^{-13}$ and $10^{-6}$). For tetra-valent semiconductors (semiconductors with four valence electrons contributing to the covalent lattice bindings such as Si or Ge), tri-valent and penta-valent elements as electron-acceptors and donators, respectively are practical dopants [95]. Penta-valent donor dopants lend their additional valence electron to the free electron cloud. Tri-valent acceptors lack one valence electron (compared to Si or Ge) and therefore include a free electron from the bulk lattice into their covalent binding. Acceptor ions thus introduce quasi-discrete energy levels within the energy gap very close to the valence band. Typically, the energy gap between those newly created states and the valence band amounts to $10\ldots50\,\mathrm{meV}$ due to the loose binding of the electron to the impurity-ion. Thus, the effective energy gap reduced to a few meV and all electrons bridging this gap by ionization become free carrier electrons. The location of the introduced doping levels within the bulk band structure is illustrated in Figure 2.4. Depending
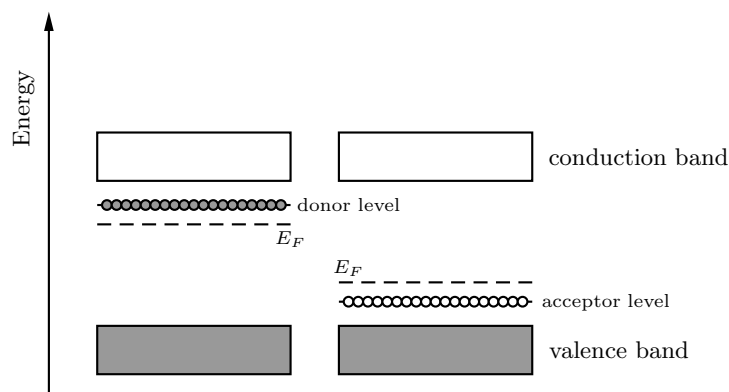


**Figure 2.4.:** Introduction of impurities into the semiconductor crystal lattice creates new allowed quasi-discrete states within the forbidden energy gap. Doping with donor ions establishes a valence-like level close to the conduction band (*n*-type doping, left) while doping with acceptor ions introduces a free-electron state close to the valence band (*p*-type doping, right). In both cases the effective gap reduces for a number of charge carriers corresponding to the number of dopants.

on the actual impurity concentration, the *Fermi*-level shifts toward the valence band. In the limit of large doping concentrations, it relocates very close to the conduction band and the semiconductor indeed tends to behave like a conductor. The situation renders very similar in the case of donor dopants. Penta-valent impurities introduce a weak binding of holes to the ion-body thus creating a valence-type discrete state just underneath the conduction band. The *Fermi*-level consequently shifts toward the conduction band with increasing concentration of donor impurities. Such doped semiconductors are called "*n*-type" semiconductors, while acceptor-doped materials are referred to as "*p*-type" semiconductors. Possible dopant ions for tetra-valent semiconductors and their properties are listed in Table 2.2. The ionization energy is reported indicating the distance of the donor (acceptor) levels from the conduction (valence) bands.

| ion | dopant type | ionization energy |
|-----|-------------|-------------------|
| P   | donor       | 45 meV            |
| As  | donor       | 54 meV            |
| Sb  | donor       | 39 meV            |
| B   | acceptor    | 45 meV            |

**Table 2.2.:** Ionization energies of some doping ions available for group-IV semiconductors such as Si and Ge [95, 98].

### 2.1.3.2. Diode Junction

The combination of two differently doped semiconductors causes a shift of the energy bands on both sides of the junction since the *Fermi*-levels on either side are required to remain on the same potential referenced to an absolute earth potential as illustrated in Figure 2.5. Both
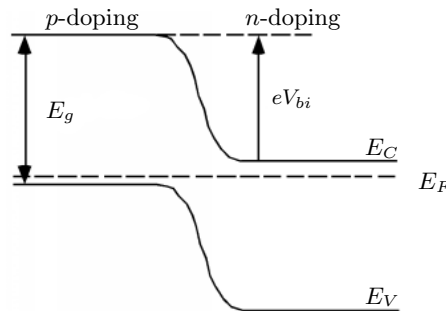


**Figure 2.5.:** Energy bands in the vicinity of a *p-n*-junction.

conduction and valence bands are distorted in the vicinity of the junction contact and connect to each side to preserve the uniform *Fermi*-level in thermal equilibrium. A potential difference between the *n*-side and the *p*-side of the compound emerges, referred to as "built-in" potential $V_{bi}$. Electrons diffuse from the *n*-region (which has an electron excess due to the doping with electron donors) into the *p*-region, while the inverse process moves holes into the *n*-bulk. The volume cleared of mobile charges exhibits the residual charge of the ion bodies of the doping atoms resulting in a local electric field around the junction contact. This electric field counteracts further diffusion and keeps the included volume of the semiconductor depleted of

free charge carriers. The formation of this depletion zone is a fundamental requirement for the utilization of silicon as particle detector raised at the beginning of this section. Trends of the local carrier concentrations, electric field and the potential along the cross-section of a *p-n*-contact is reviewed in Figure 2.6.
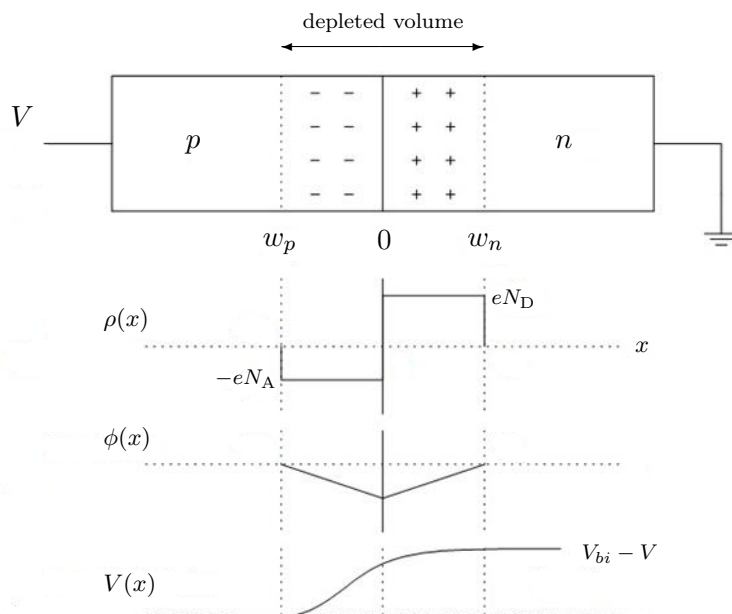


**Figure 2.6.:** The semiconductor diode *p-n*-junction and local charge-carrier density $\rho(x)$, electric field $\phi(x)$ and electric potential $V(x)$ in the proximity of the junction contact.

The built-in voltage $V_{bi}$ may be inferred from the $n$ and $p$-side doping concentrations by [92]

$$V_{bi} = \frac{kT}{e} \ln \left( \frac{N_A N_D}{n_i^2} \right) \tag{2.4}$$

with $n_i$ being the number of intrinsic charge carriers which can be retrieved for $300\,\text{K}$ from Table 2.1 and $N_A$ and $N_D$ the doping concentrations of acceptors and donators, respectively. The depletion zone extends into the $p$ and $n$-doped regions yielding widths depending on the doping concentrations [92]:

$$w_n = \sqrt{\frac{2\epsilon_r\epsilon_0}{e} \frac{N_A}{N_D(N_A + N_D)} V_{bi}} \tag{2.5}$$

for the width of the $n$-side of the depletion zone and

$$w_p = \sqrt{\frac{2\epsilon_r\epsilon_0}{e} \frac{N_D}{N_A(N_A + N_D)} V_{bi}} \tag{2.6}$$

for its $p$-side extension.

Applying an external voltage $V$ to the *p-n*-junction offsets the equilibrium *Fermi*-levels and consequently shifts the bands on either side wrt. each other. A forward biasing voltage

(with the positive potential applied to the $p$-side) counteracts the built-in potential and shifts the $n$-side energy bands upwards (compared to the $p$-side energy levels) until they line up with the $p$-side bands. The junction then becomes highly conductive and the electrons move freely within the external electric field.

### 2.1.3.3. Reverse-Biased Diode Junction

More relevant to the application of the diode junction to particle detection is the reverse-biased regime. It is defined by a negative external voltage applied over the $p$-$n$-contact. The potential barrier characterized by the built-in voltage is elevated by this external bias. Consequently, the width of the depletion zone increases and can be inferred using eqns. (2.5) and (2.6):

$$w = \sqrt{\frac{2\epsilon_r\epsilon_0}{e}\frac{(N_A + N_D)}{N_A N_D}(V_{bi} - V)} \tag{2.7}$$

For typical particle detectors the base material is chosen to be weakly doped $n$ or $p$ material as the sensitive bulk of the sensor. A shallow, heavily doped layer implemented near the surface forms the asymmetric junction structure. According to eqns. (2.5) and (2.6) the depletion width is severely dependent on the doping concentrations. Typically, strongly differing concentrations with $N_A \gg N_D$ are technically realized. The resulting depletion zone extends throughout the whole $n$-type bulk at a well defined voltage (the full depletion voltage $V_{dep}$) while it may range inside the $p$-type layer for a few micrometers only. Therefore one can simplify above expressions for the depletion width to

$$w = \sqrt{\frac{2\epsilon_r\epsilon_0}{eN_D}(V_{bi} - V)} \tag{2.8}$$

and assuming that the $n$-side doping concentration determines exclusively the conduction of charge carriers, the specific resistivity $\rho$ is introduced with $\rho = 1/\sigma \approx 1/eN_D\mu$ leading to

$$w = \sqrt{2\epsilon_r\epsilon_0\rho_n|\mu_n|(V_{bi} - V)}. \tag{2.9}$$

where $\rho_n$ is the resistivity of the bulk material and $\mu_n$ the mobility of electrons (cf. Table 2.1). Latter expression is most useful for verification of the base material's resistivity indicated by the manufacturer.

The reverse-biased $p$-$n$-junction acts as a DC-blocking contact, i.e. the potential barrier suppresses the charge flow within the external electric field. However, since statistical thermal fluctuations can lift electrons over the large energy gap into the conduction band occasionally, a inevitably small but significant current flows in the reverse-biased regime, called "leakage-current". The amplitude of this current, or more general, the current density (unit $\left[\frac{A}{\text{cm}^3}\right]$) is given by the *Shockley*-equation:

$$J = J_S\left(e^{\frac{eV}{kT}} - 1\right) \tag{2.10}$$

with the reverse saturation current

$$J_S = en_i^2\left(\frac{D_n}{N_A L_n} + \frac{D_p}{N_D L_p}\right), \tag{2.11}$$

where $D_n, D_p$ and $L_n, L_p$ denote diffusion constants and free path lengths for electrons and holes, respectively. Evaluation of eqn. (2.10) yields a vanishing exponential term at sufficiently

large reverse bias. The reverse leakage current should therefore be constant up to the reverse breakdown voltage. However, the leakage shows a strong dependence on the temperature. Evaluation of eqn. (2.11) wrt. the junction temperature $T$ yields [93]

$$J_S \propto T^2 \mathrm{e}^{-\frac{E_g}{2kT}}. \tag{2.12}$$

This relation implies a doubling of the leakage current connected with a positive temperature swing of $8\,\mathrm{K}$.

The process of depletion is sketched in Figure 2.7. The highly doped $p^+$-layer in proximity to the surface forms the semiconductor junction together with the surrounding $n$-type bulk volume. Highly doped silicon actually behaves like a metal. Therefore this doping mode is chosen for contacts to metals since the formation of a parasitic junction is avoided in this way. The thin $p^+$-implant thus serves as junction contact exhibiting a very low depletion depth and transition to the overlay aluminum contact at the same time. Without externally applied voltage a thin depletion layer persists underneath the $p^+$-implant which extends into the $n$-bulk volume with increasing bias. Once the full sensitive volume is depleted of free charge
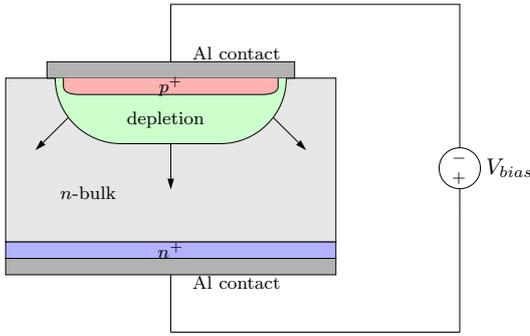


**Figure 2.7.:** Scheme of the depletion process in a reverse-biased semiconductor junction.

carriers the confining negative and positive electrodes (the $p^+$-contact and the backside highly doped $n^+$-contact) form a parallel-plate capacitor. Its capacitance is given by the mutual projected cross section $A$ of the electrodes and the detector thickness $d$ by

$$C = \epsilon_r \epsilon_0 \frac{A}{d} \tag{2.13}$$

with the relative permittivity $\epsilon_r = 11.8$ in case of silicon. Considering the relation between depletion depth and bias voltage from Equation (2.8) the capacitance can be rewritten as

$$C = A\sqrt{\frac{\epsilon_r \epsilon_0 e N_{\mathrm{D}}}{2(V_{bi} + V_{dep})}}. \tag{2.14}$$

The voltage $V_{dep}$ exactly depleting the whole sensor volume has (opposing to above definition) positive sign since the bias voltage of particle sensors which are always operated in reverse-bias regime is positive by convention.

A charged particle, upon passage through the depleted bulk volume, ionizes the lattice atoms and consequently liberates a number of free electrons which depends on the energy loss $\Delta E$ the particle has experienced and the mean energy quantum $\varepsilon$ required to create a free electron-hole pair. Thus

$$Q = \frac{\Delta E}{\varepsilon} \tag{2.15}$$

yields the charge drifting within the externally applied electric field toward the electrodes. The drifting charges induce a charge themselves into the front- and backside strip electrodes. Latter are separated from the bias potential by high resistive networks. Therefore the induced signal can be read out as current pulse by a low-impedance preamplifier. A detailed explanation of the charge collection and signal forming processes in semiconductor detectors can be found in [93] and in [103] with emphasis on silicon strip detectors.

## 2.2. Segmented Silicon Particle Detectors

The basic principle of a depleted semiconductor (mostly silicon) volume driven by a diode junction for the detection of charged particles as described above is utilized in a wide variety of scientific as well as commercial applications. A decent overview of current technologies is given by [104] or more recently by [93]. Particularly the development of the simple single-junction sensor toward highly-granulated topographies is notable which is based on the idea of the integration of several junction structures into a wafer-bulk. The segmentation is realized by a set or an array of mutually isolated $p^+$-implants into a common $n^+$-body (fewer applications use the doping-inverted scheme with highly doped $n^+$-implants in a weakly impurified $p$-bulk). Charges created by ionization inside the depleted bulk then induce a current due to the drifting charges inside those electrodes which include projections of the ionized track. Two common geometries of detector segmentations are shown in Figure 2.8. Pixel-geometries as



(a)                                                                                    (b)
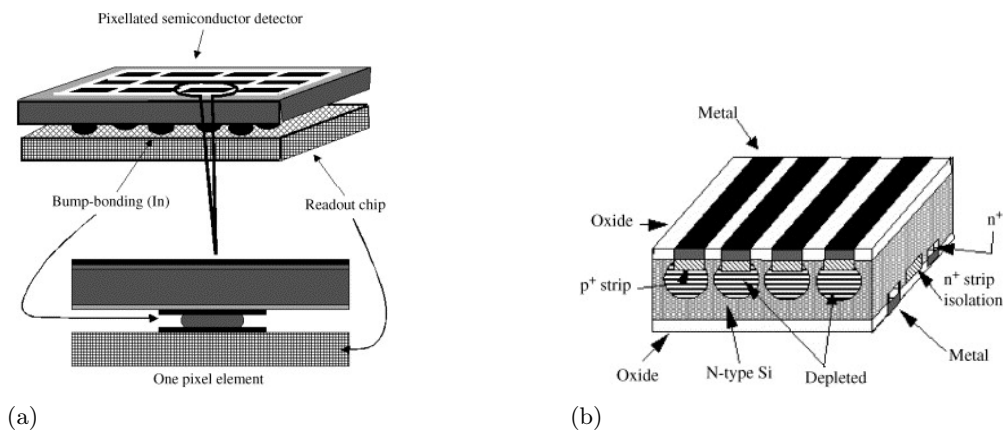
**Figure 2.8.:** Construction of segmented semiconductor detectors. left: Pixel-sensor with each pixel-cell connected via bump-bonds to the front-end ASIC and right: double-sided silicon strip detector (DSSD) showing the doping domains and depletion emanating from the biased $p$-side strips, from [105].

shown in Figure 2.8(a) benefit from the simple $p^+$-in-$n$ structuring and consequently from less complicated production processes but suffer of accessibility of the large set of pixel electrodes. A possible connection scheme is indicated in the same picture: by flip-chip mounting of the front-end electronics chip onto the sensor with small indium-balls as solder-contacts each pixel can actually be fed into an individual front-end read-out channel provided a matching pad grid at the FE ASIC side.

A linear strip geometry exhibiting a large set of long and narrow $p^+$-implants in a common $n$-type bulk is shown in Figure 2.8(b). Such a segmentation, provided its implementation utilizing the single-layer structuring of junction contacts (similar to Figure 2.7) lacks the

full two-dimensional spacial resolution of a pixel array but delivers a one-dimensional hit-coordinate only. A second, by an arbitrary angle rotated strip-sensor would be required to yield the full spacial information. Alternatively, additional structuring of the back-side and forming segmented ohmic electrodes recovers the missing coordinate as illustrated in Figure 2.8(b) in the design of double-sided strip detectors (DSSD). A traversing particle can thus be located via its $x$ and $y$ hit-coordinates[3] coming from the position of the strip electrodes that registered a charge signal. This topology imposes the appearance of ambiguities when several particles create multiple hits on the top and back side of the sensor. This situation will be discussed in more detail on the basis of reconstructed hit patterns originating from actual measurements later in this work.

The biasing of strip electrodes to the required drift potential may be accomplished through a variety of technologies. Silicon wafer processing permits formation of silicon resistors which connect the strip electrodes to a common bias line with the demanded high impedance. Those poly-silicon biasing structures are purchased with additional processing steps during the fabrication process[4]. Another very commonly applied technique is the punch-through biasing scheme (cf. Figure 2.9). The $p^+$-strip electrodes are mutually insulated from the surrounding common bias-ring line (a $p^+$-type implant as well) in the first place. Upon application of a
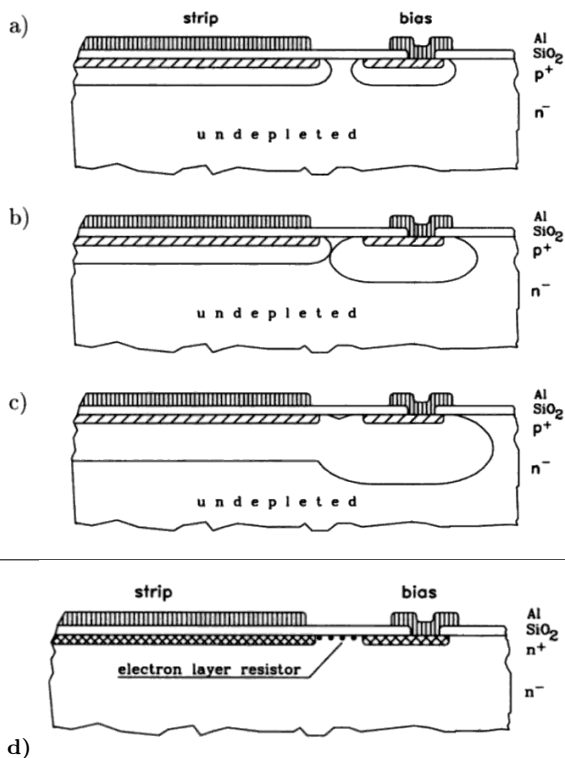


**Figure 2.9.:** Development of depletion of the sensitive $n$-type bulk volume starting from the $p^+$ (junction) side with increasing bias voltage in punch-through biased sensors (a) to (c). Illustration of the $n^+$-strip biasing on the ohmic side through surface layer-resistor at the MOS-interface of Si and SiO$_2$ (d), from [92].

positive voltage wrt. bulk potential a depletion zone emerges at the bias line and starts expansion into the body. Eventually, this depletion zone merges with the yet thin depletion layers of the unbiased strip-junctions. The potential barrier between strip-implants and bias line is overcome and the strip-implants settle on the same potential as the bias-ring. From this point

---

[3] A hit shall be defined as charge appearing at the strip electrodes exceeding a well defined threshold.

[4] Fabrication of silicon sensors out of plain wafers require several processing steps which include: a) diffusion of ions into the bulk or directed diffusion into parts of the wafer (implants) b) deposition with photo-resist and lithographic exposure c) wet-etching and chemical deposition d) plasma deposition of e.g. metalizations.

on the depletion zone extends over the whole active area of the sensor and begins to subduct toward the back side with increasing bias potential. The principle of punch-through biasing has been shown to be very usefully applied to modern particle physics detectors [92, 106]. An extension with an additional gate electrode controlling the potential barrier between bias ring and strips known as FOXFET-biasing is also used occasionally.

Biasing of the $n^+$-strips on the back side works in a different way (Figure 2.9(d)). All structures on the $n$-side are galvanically connected through a thin electron surface accumulation layer inherent to MOS[5]-structure topologies. The isolation between neighboring strips is accomplished by additional $p^+$-implants surrounding the strip electrodes. At the ends of the strip $n^+$-implants, openings in the blocking $p^+$-implants allow a high-ohmic connection of the strips to the bias-ring through the surface layer resistance.

## 2.3. Passage of Charged Particles through Matter

### 2.3.1. Mean Energy Loss and the Formulation of Bethe and Bloch

Charged particles experience a number of various possible interactions when they enter into a volume of material, such as scattering with atomic shells through excitation and ionization, more seldom elastic scattering at atomic nuclei and transition effects at highly relativistic energies like *Čerenkov* radiation. In any case the particle loses a part or its entire kinetic energy and gets eventually stopped inside the material. *Bohr* gave a first classical description of the energy-loss mechanism in 1913 and showed that ionization is the dominating braking effect for sufficiently high-energetic particles [107]. *Bethe* later indicated a more precise quantum-mechanical solution which was subsequently reevaluated by *Bloch* and corrected for large momentum transfers [108, 109]. Later modifications of this *Bethe-Bloch*-formalism included relativistic reformulation, corrections for density and shell effects and others, particularly driven by *Fano* [110, 111]. The currently wide-spread and most accepted description of the mean energy loss of a charged particle in matter per path-length element is [112]

$$-\frac{\mathrm{d}E}{\mathrm{d}x} = 2\pi N_A r_e^2 m_e \rho \frac{Z}{A}\frac{z^2}{\beta^2}\Big[ ln\Big(\frac{2m_e\gamma^2 v^2 W_{max}}{I^2}\Big) - 2\beta^2 - \delta - 2\frac{C}{Z}\Big]. \tag{2.16}$$

The meaning of the parameters is:

| | | |
|---|---|---|
| $r_e$ | : | classical radius of the electron $= 2.817 \cdot 10^{-15}\,\mathrm{m}$ |
| $m_e$ | : | electron mass |
| $N_A$ | : | *Avogadro*'s constant |
| $I$ | : | mean excitation potential |
| $Z$ | : | average atomic charge number of absorber material |
| $A$ | : | average atomic mass of absorber material |
| $\rho$ | : | mean density of absorber material |
| $z$ | : | charge of incident particle |
| $\beta$ | : | $\frac{v}{c}$ of incident particle |
| $\gamma$ | : | $\frac{1}{\sqrt{1-\beta^2}}$ of incident particle |
| $\delta$ | : | density correction |
| $C$ | : | shell correction |
| $W_{max}$ | : | maximum energy transfer of interaction |

---

[5] Metal-oxide to semiconductor junction.

This quantity is also referred to as stopping power $S$, or more precisely:

$$S = \frac{1}{N} \left( \frac{\mathrm{d}E}{\mathrm{d}x} \right) \tag{2.17}$$

with the atomic density $N$.

Above relation (2.16), despite its universality, is valid only for cases where the velocity of the projectile is large compared to *Bohr*'s velocity, i.e. $v \gg v_0 = \frac{e^2}{\hbar}$. Furthermore, a partial or complete neutralization of incident positive charges due to electron capture is not considered. Both cases are discussed in more detail in Appendix B. However, the energy domain relevant for the application of thin semiconductor particle detectors ranges beyond those imposed low-energy limits and is well covered by the *Bethe-Bloch*-equation (2.16).

The stopping power of charged particles ($z = \pm 1$) in several absorber materials is shown in Figure 2.10 in dependence of the particle's momentum expressed in multiples of its mass equivalents $\beta\gamma$. Irrespective of the absorber material (and the particle's mass $m$ which does not explicitly appear in eqn. (2.16)) charged particles exhibit a minimum of ionization at relative momenta of $(\beta\gamma)_{MIP} \approx 3$ and are therefore called "minimum ionizing particles" (MIP). A strong rise of the energy loss toward lower momenta causes rather rapid stopping of slow particles once their kinetic energy falls below the MIP point. On the other hand, a moderate increase of the stopping power toward ultra-relativistic energies is observed.
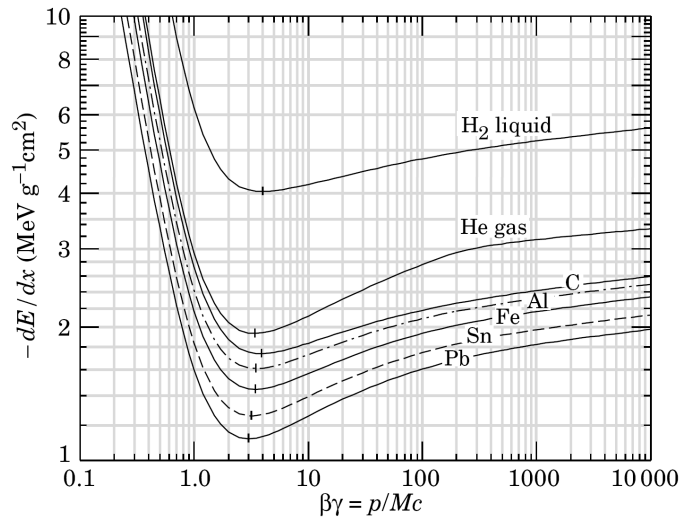


**Figure 2.10.:** Mean energy loss of charged particles ($z = \pm 1$) in different materials [23].

## 2.3.2. Energy Loss Straggling

The energy deposited inside thin detectors by the passage of sufficiently fast particles[6] is well described by the *Bethe-Bloch* formalism (see Section 2.3). However, the obtained stopping

---

[6] As already shown in the treatment of the energy-loss formalism, particles exhibiting very low velocities experience excessively high energy losses and will eventually be stopped inside the detector. The following argumentation excludes such cases since those events barely provide useful information beside the fact that the particles are stuck in passive material before even reaching the sensitive detector volume.

power merely corresponds to the mean energy loss and is subject to larger statistical fluctuations which are asymmetric and therefore tend to skew the distribution. The energy-deposit of one particle event consists of a sub-summation of the energy transferred to the atoms of the target material in single collisions. In each of those collisions, energies ranging from a minimal value given by quantized excitations up to almost the total kinetic energy may be transferred known as energy-loss straggling. The actual energy lost by an individual particle thus turns out to be a highly stochastic and in-deterministic process. However, the distribution of energy losses for an ensemble of events may be described by probability density distributions.

*Landau* derived a first complete analytical solution for the energy loss distribution in thin absorbers, i.e. for small energy transfers to the medium [113]. *Vavilov* later improved the result by considering kinematic constraints on the energy transfer. He indicated a more general family of distributions with a shape parameter $\kappa$ [114]. For very small values $\kappa \ll 1$ the distribution approaches the *Landau* distribution and for large values $\kappa \gg 1$ it becomes *Gaussian*. The *Vavilov* distributions have been shown to describe the energy loss straggling more accurately for thicker absorbers. Later publications incorporated density corrections not considered in the original works of *Landau* and *Vavilov* which become significant at higher kinetic energies of the projectile particles [115]. For very thin absorbers ($t \lesssim 1\,\mu\mathrm{m}$) on the other hand all aforementioned approaches to describe the energy loss distributions break down in the limit of single collisions. *Bichsel* indicated a thorough calculation of straggling functions in this domain with full consideration of the interaction with K, L, and M-shell electrons (in silicon) and the fact that the typical energy loss is not large compared to the binding energy of electron shells (which is a basic assumption in the *Landau-Vavilov* theory) [116, 117]. For larger absorber thicknesses, *Bichsel* suggests an iterative folding procedure using the calculated initial spectrum as convolution kernel. Such obtained straggling probability functions match experimental data (e.g. [118, 119]) to a high degree. An extensive comparison to a large set of measurements is given by *Bichsel* himself in [117].

Beside those straggling functions which are motivated by an analytical description of the underlying physics, a variety of Monte-Carlo approaches exist that deliver energy loss distributions for large statistics of simulated collisions. For appropriate literature be exemplarily referred to [120].

A third approach for the description of the energy loss straggling are more practically oriented empirical or semi-empirical functions that resemble measured energy loss distributions in a limited energy range. A very commonly used parametrization for usual silicon detector thicknesses valid at relativistic energies is the convolution of a *Landau* distribution with a *Gaussian*:

$$f(x, \Delta) = \frac{1}{\sqrt{2\pi x \delta_2}} \int\limits_{-\infty}^{\infty} f_L(\Delta - y) \, \mathrm{e}^{-\frac{y^2}{2x\delta_2}} \, \mathrm{d}y \tag{2.18}$$

yields the probability density for energy loss $\Delta$ and the thickness $x$ of the material. The width of the *Gaussian* distribution is defined by $\sqrt{x\delta_2}$ with the broadening parameter $\delta_2$. Relation (2.18) is equivalent to the precise distribution given by *Bichsel* provided that *Landau* and *Vavilov* distributions show only small differences, i.e. $\kappa \ll 1$ [121].

## 2.4. Radiation Damage

While the ionizing energy loss as discussed above is beneficially utilized for the particle detection, it is accompanied by a variety of detrimental effects to the integrity and the function of the detector material. Such effects, apart from charged particles as well encountered for $\gamma$-radiation and neutrals, are evaluated depending on the function, structure or topology of the exposed material in different radiation damage categories, namely ionizing radiation effects and non-ionizing effects. Both characterizations are merely non-orthogonal projections of the impact of irradiation with a specific particle species and normalize this impact to a comparable scale. An excellent overview on radiation effects in silicon and electronics is presented in [122].

The non-ionizing energy loss (NIEL) description summarizes the part of the introduced energy loss going into displacements of atoms (including phononic excitations at lower energies) or displacement cascades that ensue when primary knock-on atoms (PKAs) pick up sufficient kinetic energy for secondary displacement reactions. The energy transfers accounted for are both, *Coulomb* and nuclear elastic reactions as well as nuclear inelastic processes. A detailed discussion of the involved mechanisms and treatment of collision cascades as well as a guideline for the calculation of PKA spectra is given in Appendix B.

The impact of NIEL on the crystal-lattice of semiconductor materials such as silicon detectors is presumably more severe than on amorphous materials. Some different types of lattice defects considered to unfavorably influence the operational behavior of silicon semiconductor devices are illustrated in Figure 2.11. Crystal defects like vacancies or interstitials alter the
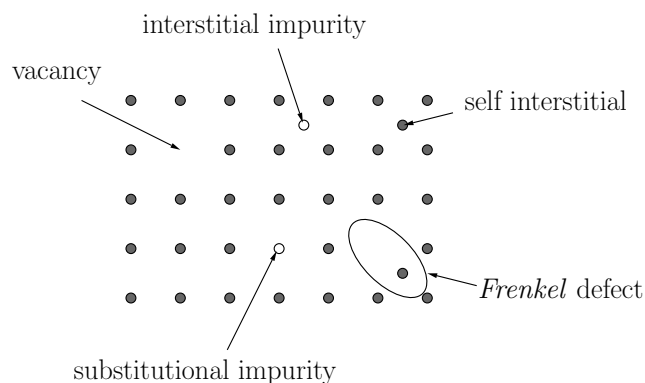


**Figure 2.11.:** Types of crystal lattice damage.

band-structure of the semiconductor bulk by introduction of excess inter-bandgap levels. Consequently, the leakage current increases with the accumulated dose up to a situation where either the associated shot noise or the power dissipation inside the sensor volume become unacceptable. Furthermore, the free charge carriers generated as a result of ionization by traversing particles get trapped in such lattice defects which diminishes the signal yield.

One reference scale for the non-ionizing energy loss was defined such that the damage effects of incident particles of any species with any kinetic energies are scaled to the impact of monochromatic neutrons with 1 MeV. The displacement energy cross section for neutrons, protons, electrons and pions is shown in Figure 2.12. By convention, the displacement damage is often referred to the absolute displacement cross section of neutrons in silicon at 1 MeV kinetic energy yielding an average value of 95 MeVmb and is in this case referred to as "hardness factor" [124, 125]. Several other equivalent representations of displacement effects exist, such

Displacement damage in Silicon
for neutrons, protons, pions and electrons
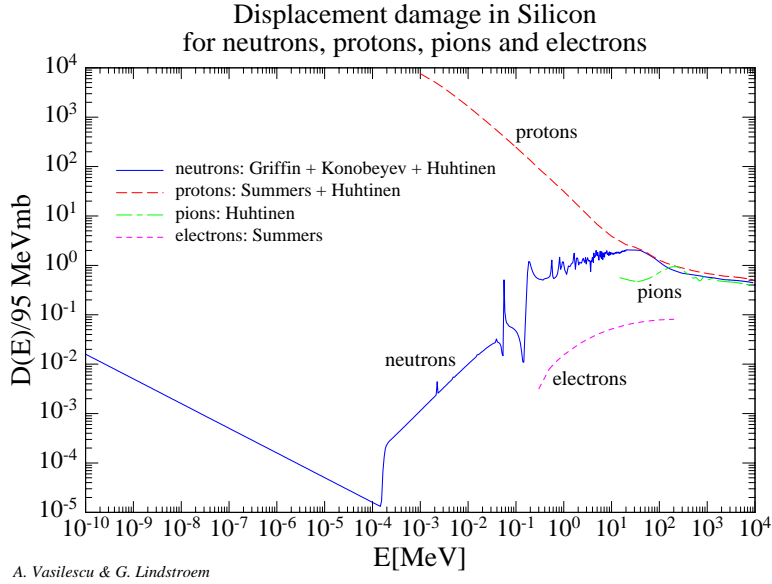


**Figure 2.12.:** Hardness factor of different particles relative to $95\,\mathrm{MeV\,mb}$, i.e. the damage energy cross section for neutrons of $1\,\mathrm{MeV}$ kinetic energy in silicon [123].

as KERMA (kinetic energy released in matter) indicating the energy loss per mass density (comparable to the definition of the stopping power) and DPA (Displacements per Atom). A good general overview on displacement damage effects in Si is provided by [126].

The influence of non-ionizing energy loss on the function of silicon sensors has been studied by the *CERN*-collaboration *RD48* for a large set of sensor materials, incident particles and energies and earlier works in this field were thoroughly comprehended [123, 127, 128]. The leakage current of silicon sensors was found to show an increase after application of defined irradiation doses which follows a reproducible pattern (see Figure 2.13(a)). The observed damage induced leakage current change between pre- and post-irradiation can be parametrized to [129]

$$I_l = \alpha \Phi_{eq} V \tag{2.19}$$

where $\Phi_{eq}$ is the non-ionizing equivalent fluence in $1\,\mathrm{MeV}$ neutron equivalents per square centimeter and $V$ the active sensor volume. The slope $\alpha$ is found empirically from the measured dependence between the volume leakage and $\Phi_{eq}$ to

$$\alpha_{80/60} = (3.99 \pm 0.03) \cdot 10^{-17}\,\mathrm{A\,cm}^{-1}$$

where each sample was subject to a standardized annealing interval post irradiation at a temperature of $80\,°\mathrm{C}$ since the parameter $\alpha$ depends on the annealing time, i.e. the time between the end of irradiation and the actual measurement (Figure 2.13(b)). This behavior can be attributed to the thermally driven reorganization of the crystal lattice into the energetically favorable initial configuration. Vacancies and *Frenkel*-defects dissolve rather quickly and are therefore considered reversible defects. Others, like interstitials or transmuted lattice atoms are more persistent point-defects. However, the most serious damage to the lattice is represented by cluster defects, where larger regions within the material have become disordered or amorphous (irreversible defects) [130, 131].

(a)                                                    (b)
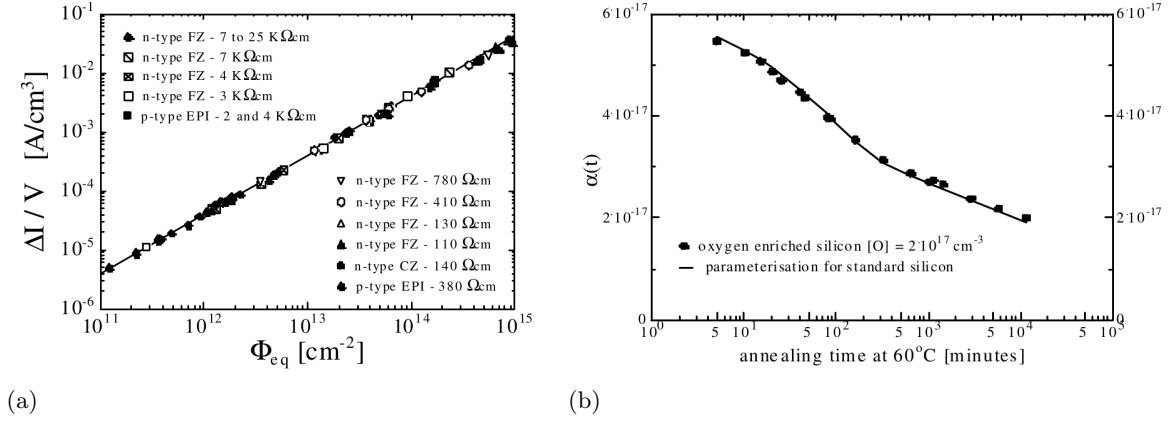
**Figure 2.13.:** Volume leakage current in silicon vs. 1 MeV equivalent neutron fluence (left) and dependence of slope $\alpha$ on annealing time (right) [127].

An accumulation of non-ionizing radiation is accompanied by a change in the effective doping concentration in silicon [127, 128] as shown in Figure 2.14 for untreated and oxygen-enriched $n$-type base material upon exposure to different particles. The reproducible decrease of the concentration up to NIEL dose levels of $\Phi_{eq} \approx 3 \cdot 10^{13}\,\mathrm{cm}^{-2}$ 1 MeV neutron equivalents (after long term annealing) corresponds to a removal of effective donors. Beyond this point the bulk material shows an increasing excess of acceptor levels and changes its characteristics to a typical $p$-type semiconductor [128–130]. This type-inversion appears for irradiation with different particle species approximately at the same fluence. The rise of effective doping concentration at higher fluences on the other hand depends on the concentration of implanted oxygen ions during the production process with one notable exception: irradiation with neutrons accumulates the doping concentration irrespective of an oxygenation of the sensors with a constant rate. The effective doping concentration and the depletion voltage of the sensor
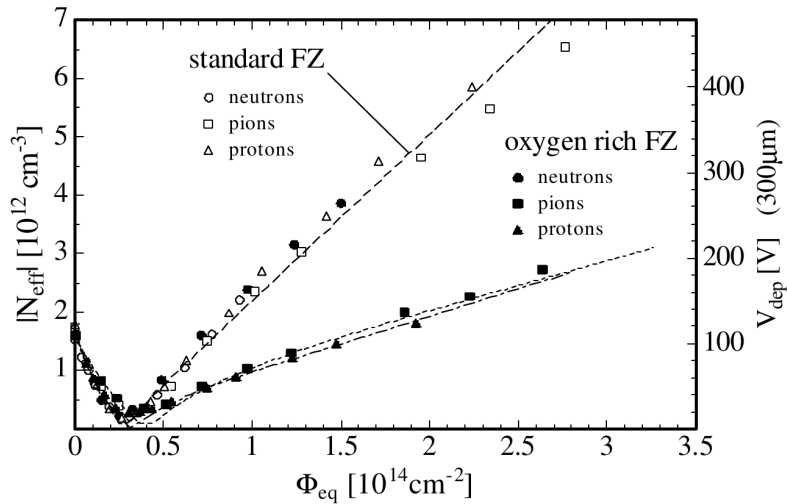


**Figure 2.14.:** Effective bulk doping concentration and required depletion voltage vs. 1 MeV equivalent neutron fluence for standard floating zone and oxygen enriched silicon sensors [127].

are related through Equation (2.8) which yields in rewritten form an explicit expression for

the full-depletion voltage:

$$V_{dep} = \frac{d^2 e N_{\mathrm{D}}}{2 \epsilon_r \epsilon_0} \tag{2.20}$$

with the thickness of the sensor $d$ and the doping concentration $N_{\mathrm{D}}$ of the bulk material.

# Chapter 3.

# Detection of Charged Particles – Experimental Procedures

## 3.1. Overview

Practical aspects in the detection of charged particles and tracking of their trajectories by means of silicon strip detectors has been studied for several years by the group at HISKP in Bonn. Hardware setup, measurement concepts and results of measurements will be presented throughout the next sections. Gained experience and lessons learned as discussed in this chapter are finally beneficially incorporated into the conceptual design for a strip tracking system for the $\overline{P}$ANDA Micro-Vertex Detector introduced in the next chapter.

## 3.2. Setup for Single DSSD Measurements

### 3.2.1. Hardware Configuration

First functional prototypes of DSSD systems were hybridized and studied utilizing $2\times2\,\mathrm{cm}^2$ large sensors produced by ITC/Irst in Trento (Italy) referred to as ITC01 sensors in the further course. Figure 3.1 shows microphotographs of either side of those sensors. Further parameters
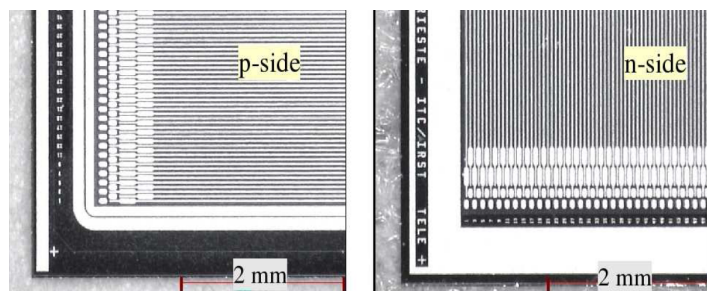


**Figure 3.1.:** Microphotograph of an ITC01 prototype sensor.

are summarized in Table 3.1. A first carrier-PCB was developed intended to serve as mounting frame for sensor and front-end electronics. Its "L"-shape allows both connection to front and back sides of the sensor. Fan-out routing of the sensor channels with a pitch of $50\,\mu\mathrm{m}$ to input pitch of the front-end ($44\,\mu\mathrm{m}$) is accomplished by a micro-structured pitch-adaptor with thin gold traces laid out on ceramic substrate (see Figure 3.2(a)). Electrical connections between the different building blocks are realized by wire-bonding, a technology welding thin aluminum

| active area | $1.92 \times 1.92 \, \mathrm{cm}^2$ |
|---|---|
| thickness | $300 \, \mu\mathrm{m}$ |
| pitch | $50 \, \mu\mathrm{m}$ |
| strips ($p$-side) | 385 |
| strips ($n$-side) | 385 |
| $n$-strip insulation | $p$-stop |
| single metal layer | |
| punch-through biased | |

**Table 3.1.:** Properties of ITC01 prototype sensors.

or gold wires ($25 \, \mu\mathrm{m}$ Au in the current case) by ultrasonic-forced friction onto the landing pad. A more detailed zoom-in of the bond-wire connections between sensor and pitch-adaptor in a two-column pattern is seen in Figure 3.2(b). The assembled module comprises three APV25 front-end chips for the read-out of each set of 384 channels per side, one pitch-adaptor per side and a few passive components as well as connectors for I/O signals and supply voltages (Figure 3.2(c)). Assembly and handling of this first prototype were primary points of interests, initially. However, since no major problems in the assembly procedure could be identified a larger number of modules was produced with one attached PCB for single sided read-out as well as several modules capable of double sided operation.

The utilized APV25-S1 front-end ASICs contain 128 charge sensitive preamplifiers and shapers followed by an analog multiplexer. More detailed information about properties and operation of this front-end chip may be found in [93, 132, 133]. The output signals of the APV25 are time-discrete, but amplitude-analog multiplexed samples of the charge registered at the moment when a trigger signal is asserted (see Figure 3.3).

A measurement setup intended for the operation of this first module prototype is seen in Figure 3.4. All signal lines and supply voltages are routed via fine-pitch flat-band cable to an intermediate transition board which buffers all in-/outgoing signals and generates the required operation voltages. A plastic scintillator underneath the sensor detects particles traversing the sensor completely. The subsequently released photons inside the scintillator material are then detected by a photomultiplier tube (PMT) whose output signal, amplified and discriminated wrt. a certain voltage threshold level, serves as trigger for the simultaneous read-out of all front-end signals. For a more detailed description of the setup it is referred to the $\overline{\mathrm{P}}$ANDA-MVD Technical Note Nr. 5 [134]. The analog multiplexed FE outputs are subsequently sampled and converted into a digital information synchronous to the system clock.

### 3.2.2. Data Acquisition

The sampling and flow of further processing of data is illustrated in Figure 3.5. Following a trigger event (asserted by an event registered in the scintillator or a manual trigger), the quasi-analog samples of 128 FE channels (which are aligned to the system clock and organized in frames belonging to subsequent triggers) are converted to a digitized data stream by means of an analog-to-digital converter (ADC). Next to this stage the frames are separated by front-end-IDs and trigger-IDs and decomposed such that each digitized value is assigned to its

(a)



(b)



(c)
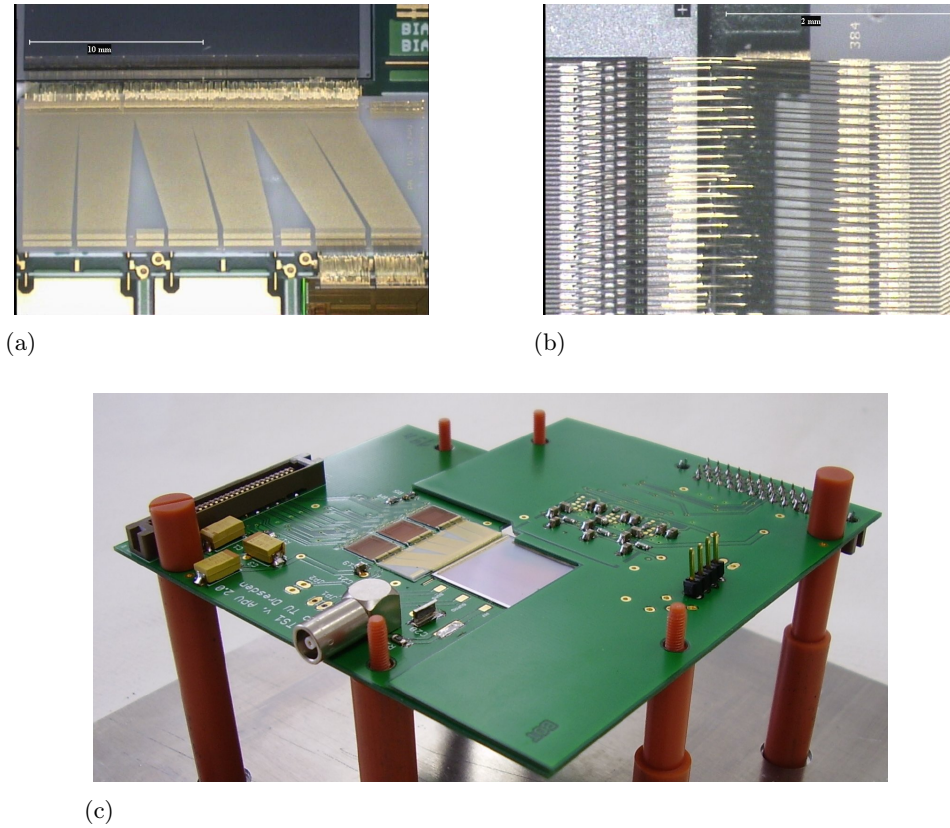
**Figure 3.2.:** Construction and assembly details of the first sensor module prototype with L-shaped read-out electronics carrier boards. (a) Pitch adaptor for fan-out routing from sensor pad-pattern with pitch of 50 µm (top) to three front-ends with input pad pitch of 44 µm (bottom). (b) Zoom detail of wire-bond connection in a bi-stage bridging scheme from a double column of AC-pads of the sensor (left) to a mirrored pad configuration on the pitch-adaptor (right). (c) Assembled module equipped for double-sided read-out with two independent L-shaped PCBs sandwiching the sensor and carrying pitch-adaptor, front-ends and passive components.

appropriate front-end and channel identifier and stored in a ring-buffer. Subsequent values with identical channel and FE-IDs are stored in the same ring-buffer thread. With each newly arriving sample the arithmetic mean is computed over the entire buffer segment yielding one average channel value[1]. This value is referred to as the channel's pedestal. The pedestal value in turn is subtracted from each new digitized raw value belonging to this channel. As a result, a distribution of channel values is obtained whose time average is free of offsets. Fluctuations of channel values wrt. this mean value is equivalent to the channel noise. It is simply calculated as the standard deviation of the channel array. Finally, the entire array of pedestal corrected channel values is scanned for amplitudes exceeding an applied threshold. Matching channels are tagged as "hits" and are further processed. This includes storage of single hit events together with FE-ID, channel-ID, timestamp and auxiliary information as event-word to disk as well as a further cluster-finder stage which identifies sets of adjacent channels (clusters).

---

[1] Assuming that the channel is subject to noise fluctuations around the mean value only and no signal hit occurred during the full buffer interval. If the current sample is supposed to carry charge of a signal hit the storage of this sample to the ring-buffer has to be inhibited.
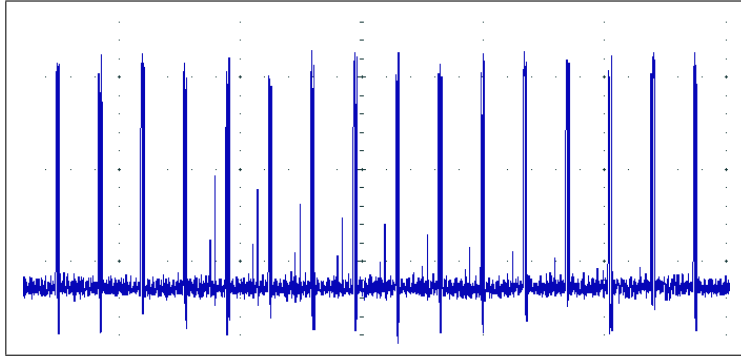
**Figure 3.3.:** Raw output pattern of an APV25 front-end chip. The analog charge distribution of the entire 128-channel array belonging to one trigger is shifted out serially in frames delimited by a digital header. Subsequent frames represent snapshots of all preamplifier outputs progressing in time. A particle hit with charge distributed among two physically adjacent channels (channel indices are re-ordered by the output multiplexer) and the characteristic preamplifier pulse-shape is seen in the center. The single frames are separated by 140 clock cycles, i.e. 3.5 µs at a system clock frequency of 40 MHz.

## 3.3. Measurements

The setup described above allows the acquisition of data in a variety of configurations. This incorporates measurements with charge injections, externally triggered measurements with radioactive sources or cosmic particles or acquisitions with uncorrelated triggering for e.g. noise measurements.

### 3.3.1. Amplitude Measurement

The capacitive load presented to the front-end input due to the connection to the sensor establishes the operating point of the sensor-preamplifier system determining the signal shape and the signal-to-noise ratio (SNR). Former is characterized by the rise- and fall time of the signal. A full record of the preamplifier output over time may be consulted to measure both of those parameters. Figure 3.6 shows such a pulse-shape reconstructed from the acquired amplitude response of one FE channel after repeated injection of a defined amount of charge at the input node. The amplitude at discrete times, separated by one clock period, is recorded after the assertion of a charge injection accompanied by a read-out trigger. This procedure alone allows retrieval of amplitudes with a timing-resolution determined by the clock frequency of 40 MHz. A tapped delay line with a single-stage delay of 3.125 ns implemented into the FE facilitates a fine-tuned scan of sample times resulting in the densely covered pulse shape shown in Fig. 3.6. The spread of samples along the recorded pulse is due to the influence of the noise smearing impressed on the output signal of the preamplifier. The fine-grained measurement of the signal amplitude in time finally permits the precise reconstruction of the time response on a charge pulse of the analog front-end stage. The most interesting magnitude to be extracted from this plot is the rise time of the rising edge between the 10 % and 90 % levels wrt. the maximum.
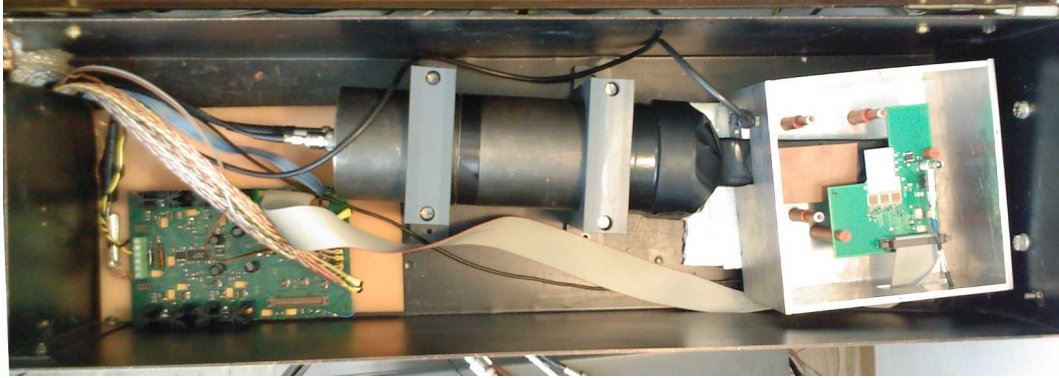
**Figure 3.4.:** Photograph of a single sensor measurement setup. A single-sided sensor module mounted inside a shielding box (right) and connected via flat-band cable with the buffer and supply board (left) can be seen. A plastic scintillator underneath the sensor read out by a PMT (center) serves for the generation of read-out trigger signals once a particle passed the sensor. The entire setup is housed in a light-proof copper box to prevent EMI pick-up.

### 3.3.2. Particle Hits

Next to the response to externally injected charge pulses, the actual charge collected at the read-out contact of the sensor following the passage of ionizing particles is of interest. For this purpose a $^{90}$Sr source emitting $\beta$-particles is placed above the sensor. The sensor itself is assured to be fully depleted due to an applied voltage beyond the full depletion. A histogram of encountered pulse amplitudes for events, where the entire charge was deposited exclusively in a single sensor strip is shown in Figure 3.7. Beside the, physically plausible and expected, typical *Landau*-shaped energy loss distribution, a high frequency of events is registered at very low amplitudes. As was shown in Figure 3.6, each obtained measurement at the output of the analog stage is superimposed with an inevitable noise fluctuation. This leads to the observed noise peak in the vicinity of zero amplitude with its width determined by the noise amplitude, or, more precisely the standard deviation $\sigma_n$ assuming *Gaussian*-distributed noise amplitudes. Below the energy-loss peak a sparsely populated amplitude range is noteworthy in Figure 3.6. A charge discriminating threshold indicated by the dashed vertical line placed in this region obviously would effectively inhibit registration of noise hits while only an insignificant fraction of real hits is lost. Depending on the SNR, both the falsely registered noise hits and suppressed signal hits may become significant. The setting of the charge threshold therefore is a compromise regarding hit rate and detection efficiency.

### 3.3.3. Energy Calibration

The measured digitized pulse height information can be further processed as is as long it is assured that the response to a defined charge deposition is equal for all channels and front-ends. Eventually, the transition to an inter-comparable measure for the amplitude is unavoidable to overcome front-end or sensor-specific gain factors. Particularly the application of algorithms that operate on cluster charge information coming from the two sides of the same sensor as described in Section 4.4 require a precise calibration of the front-end channel gains. This calibration may incorporate just the unification of gains by relative dimensionless factors or
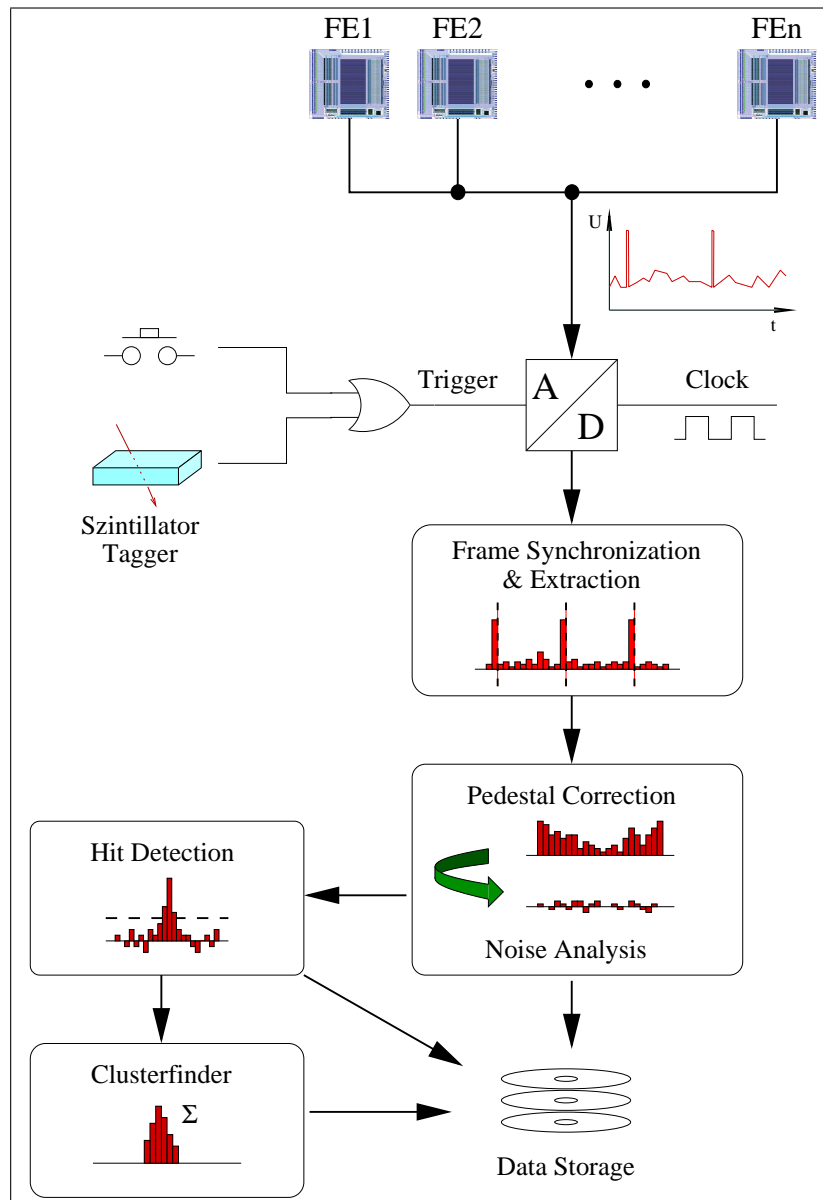
**Figure 3.5.:** Data flow and feature extraction scheme of the single sensor test station.

an absolute translation into e.g. charge equivalents or energy deposit. Following methods of gain calibration are applicable:

- Injection of defined charges by on-chip or external pulse generators

- Injection of defined charges into a separate test channel by external pulse generator

- Calibration using known $\gamma$-emissions of radioactive decays

- One-point calibration using the most probable energy loss of swift minimum ionizing particles (MIPs)

The first method is usually deployed most practically for relative gain calibration. An example of this procedure is given in Figures 3.8(a) to (e). A well known charge is injected into the input node of each channel of an entire front-end. A read-out trigger with appropriate
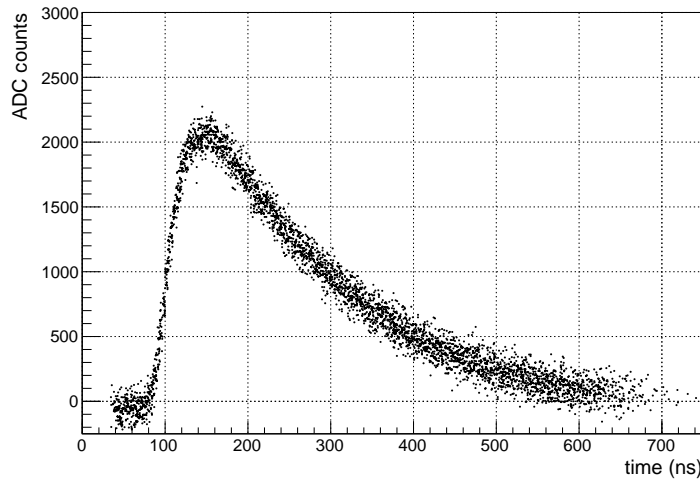
**Figure 3.6.:** Pulse-shape of a 2 fC charge pulse injected into the input of the preamplifier of an APV25 front-end with connected CIS01 sensor (2 cm strip length). The waveform was obtained by repeated sampling of injected charges in 25 ns spaced frames invoking delays in multiples of 3.125 ns by scanning the CSEL-register of the APV25. The amplitude spread of the data points is due to the intrinsic system noise of the specific detector-preamplifier combination. The peaking time $\tau$ in this case was determined to $(38 \pm 2 \, \text{ns})$.

timing is asserted in order to acquire the emerging pulse in the vicinity of the maximum (cf. Figure 3.6) at the preamplifier outputs. The amount of the charge can be chosen by setting the `ICAL`-register of the APV25 front-ends in increments of 625 electrons [132]. The pulse-height of the sample showing the largest magnitude is memorized and correlated to the initially injected charge for the entire set of channels in a single front-end in Figure 3.8(a). A fairly linear dependence between charge and pulse amplitude can be noticed up to charges of $\approx 30 \, \text{k}e$. For higher amounts the response characteristic flattens. The calibration responses of all 128 channels are found to be uniform with closely matching slopes. The linear range is most effectively described by a simple offset-less straight line. Its slope $p_0$ is the scale factor for the transformation between the digitized quantity (i.e. ADC counts) and the physical quantity "charge" with

$$q = p_0 \cdot \text{ADC}. \tag{3.1}$$

The quality of the parametrization can be judged with the fit applied to the acquired calibration responses for an arbitrary chosen single channel in Figure 3.8(b). The difference of the parametrized line and the actually acquired data points, or differential nonlinearity, is shown in Figure 3.8(c) together with a superimposed scale of the DAC register value that sets the amplitude of the injected charge pulse. A summary of all extracted calibration coefficients from all six front-ends which are attached to the prototype sensor (3 FEs for the read-out of the $p$-side strips and 3 for the $n$-side, respectively) appears in Figure 3.8(d). Measured pulse-heights, corrected by the channel-wise individual calibration factors, are histogramed separated by $p$-side and $n$-side in Figure 3.8(e). The parametrization used to fit the measured distributions is composed of a *Landau*-distribution convolved with a *Gaussian*. The treatment of energy-loss distributions is subject matter of more detailed considerations later in this section.
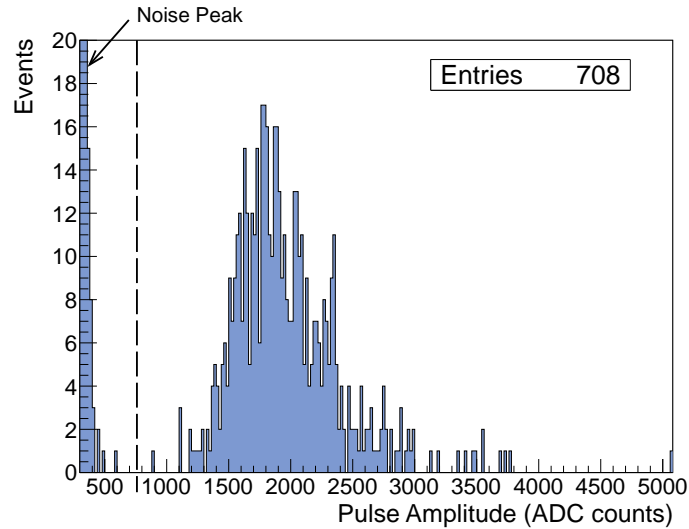
**Figure 3.7.:** Pulse-height distribution of single-strip hit events for near minimum-ionizing particles originating from a $^{90}$Sr source. The high amount of registered events at low amplitudes is due to noise fluctuations of the baseline. A charge threshold effectively avoids acquisition of those noise hits while keeping the majority of signal hits preserved.

A different approach of gain calibration consists in the scaling of measured pulse-heights of physically evident hits to the the known deposited charge or energy loss (provided that it is really known from independent sources). Assuming an ensemble of charged particles with kinetic energies higher than $\beta\gamma \simeq 3$ crossing the sensor orthogonally to its surface, the energy deposited inside the depleted volume of the sensor follows a *Landau* distribution with a well defined Most Probable Value (MPV). The energy loss MPV equals the energy loss value as obtained from calculations of the *Bethe-Bloch* theory. A variety of surveys support the universal validity of the predicted value, e.g. the one undertaken by *Hancock et al.* [119] or a summary of a large set of surveys given by *Bichsel* [117].

Figures 3.9(a) and (b) show energy-loss distributions of one sensor module (with six front-ends for the read-out of both sides as shown above) from a sample taken with $\beta$-particles of a $^{90}$Sr source placed above the sensor. Firstly, a non-uniformity in gain can be noticed among different front-ends while the gain distribution of all channels belonging to the same front-end appears more or less homogeneous. Each channel's energy-loss histogram is subject to a fit of a parameterization as discussed in section 3.3.7 by means of an automatic batch-procedure. The distribution's mean value and the obtained MPV are summarized in Figure 3.9(c) and the inverse of the MPV as calibration coefficients in Figure 3.9(d).

### 3.3.4.  Noise

The limiting magnitude in the performance of a system is the inherent statistical fluctuations, or noise, of the measured quantities. This quantity can be minimized, which is an imperative procedure in systems that shall detect small quantities such as the charge signal introduced by the energy loss of an ionizing particle passing through thin semiconductor sensors, and, moreover, it can be measured. First investigations about the statistical fluctuations in electronic systems, particularly thermal noise, were conducted by *Johnson* and *Nyquist* [135, 136]. Beside
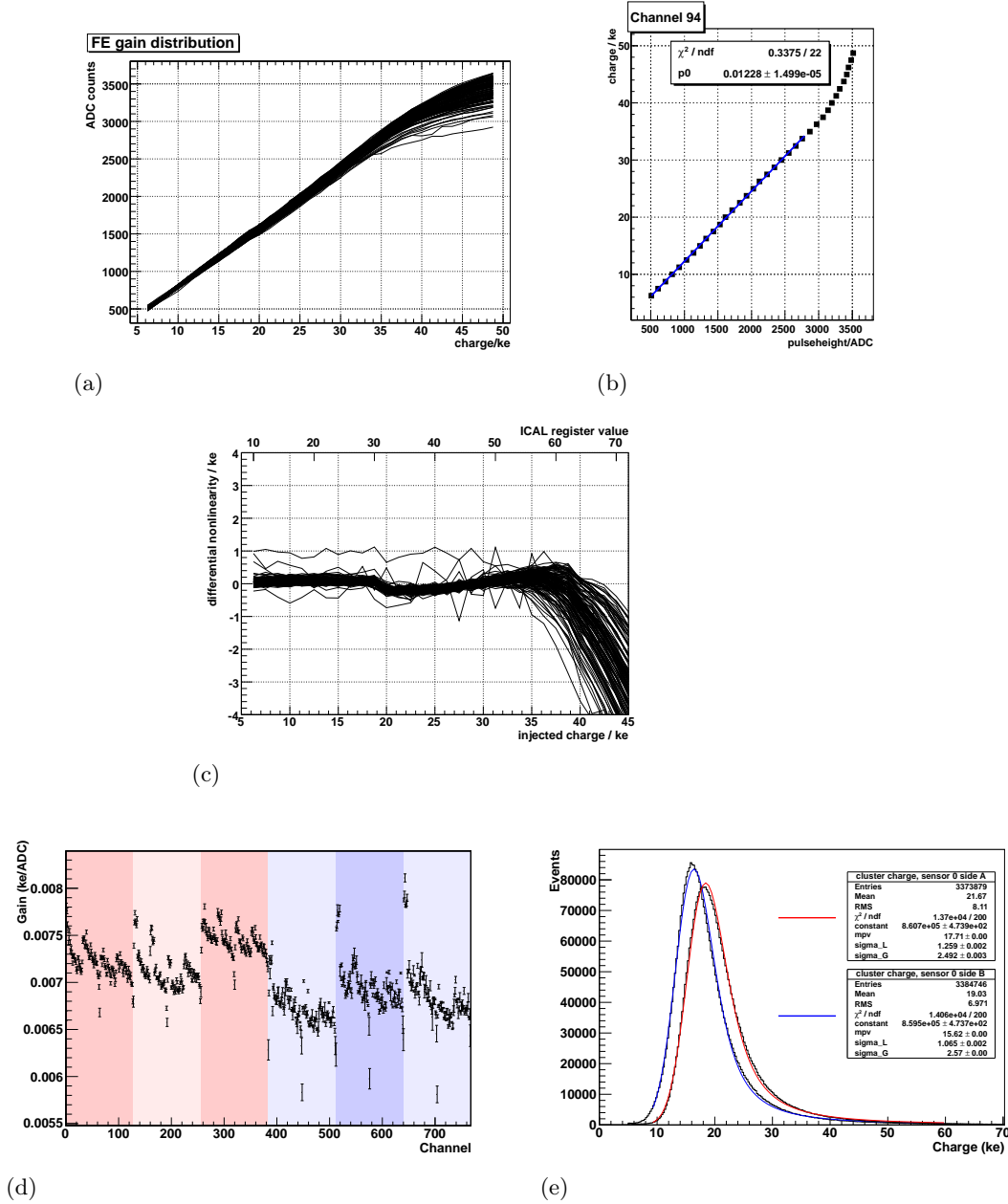
**Figure 3.8.:** Energy calibration of all 128 channels using the internal charge injection circuitry of one APV25 front-end chip (a). The gain is parameterized by fitting the recorded response with a linear, offset-less function as exemplified for a single channel in (b). The quality of this parameterization may be judged in terms of the deviation of the measured response points from the straight line as differential nonlinearity in (c). The ICAL-register value for the equivalent injected charge is overlaid as top scale, which allows to identify discontinuities of injected charge entities originating from an imbalance in the ICAL-DAC as seen in this plot where a jump occurs when the 6th bit of the DAC engages at ICAL≥32. A channel-wise display of the retrieved calibration slopes for a double sided sensor module with three connected front-ends per side is shown in (d). The colorized bars with same hue (same color species) discriminate between different front-ends while different read-out planes (sides) are encoded by different hues with red corresponding to the $p$-side and blue to the $n$-side. Energy loss distributions obtained from the cluster contents after charge calibration with fitted parametrizations for $p$-side (red) and $n$-side (blue) (e). The parameterizations of the energy loss distributions are explained later in the text.
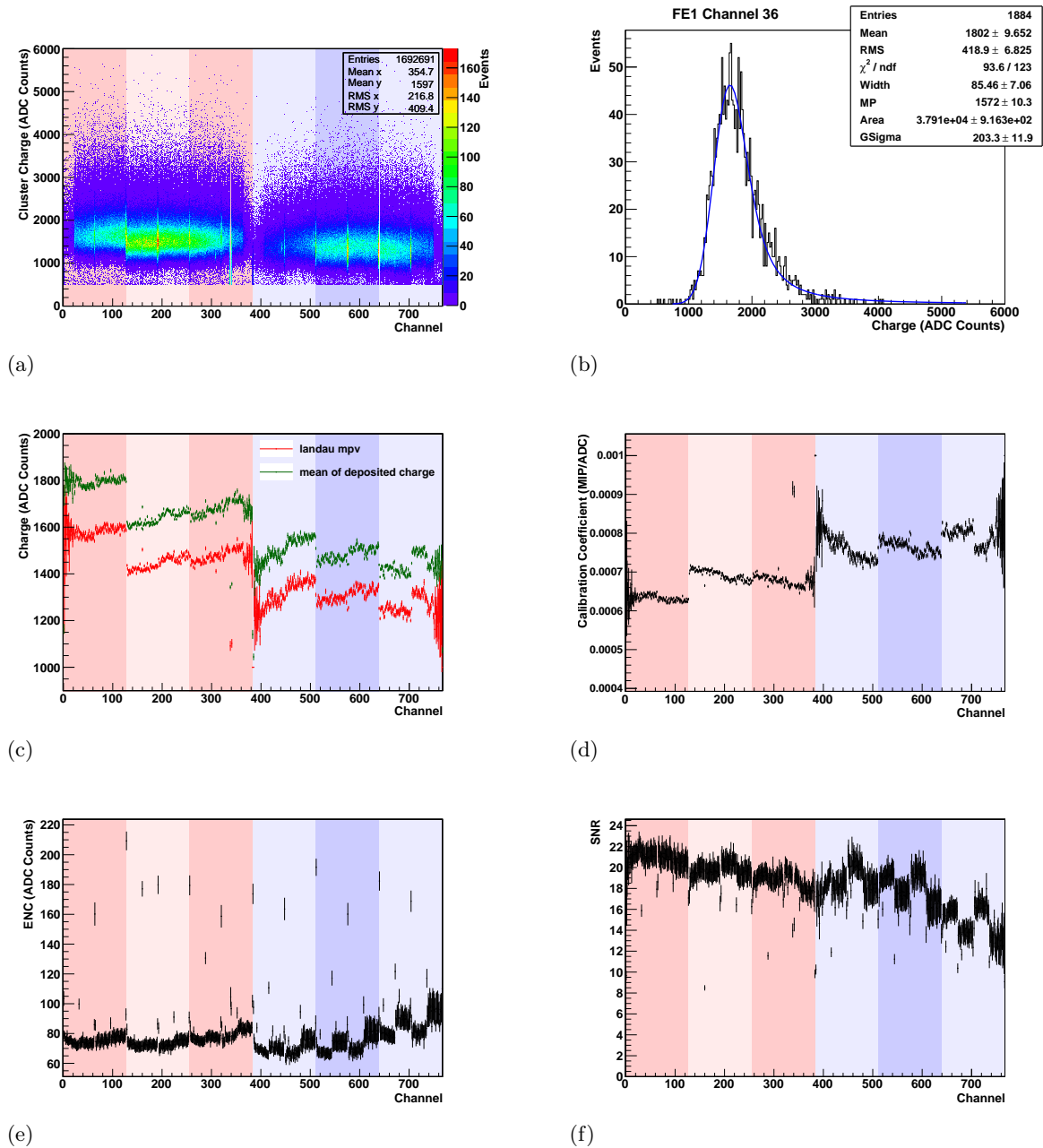
**Figure 3.9.:** Calibration of front-end response by means of detection of the most probable energy loss for each channel of one double-sided sensor module (6 FEs) (a) Energy loss statistics of all 768 FE channels (b) Energy loss histogram of a single channel with fitted parametrization (c) Extracted fit parameters of most probable value (MPV) and mean value of all channels (d) Gain coefficients calculated from the MPV fit parameters (e) Noise and (f) Signal-to-noise ratio (SNR).

the thermally agitated noise, other physical origins for those statistical electronic fluctuations could be identified in the subsequent years.

The signals generated in silicon detectors as a consequence of the passage of charged particles consist typically of a few tens of thousand electron-hole pairs (see section 2.3). The charge at the input nodes of the preamplifiers amounts to merely several fC. Such small quantities are always accompanied by noise fluctuations which are usually not insignificant or even in the order of the signal. A precise knowledge of all relevant noise sources and a subsequent noise analysis of a system's design and validation by means of measurements of real system parameters is imperative for minimization of noise. As will be shown throughout the course of the next paragraphs, the optimization of signal-to-noise ratio is the primary directive in the design of high energy particle detectors.

The relevant noise contributions encountered in a system comprised of DSSD sensor and charge sensitive preamplifier are explained in the following. An equivalent circuit of a single channel of such a system is illustrated in Figure 3.10(a). The detector capacitance $C_d$ is formed by the capacitance of the connected strip electrode to the back side of the sensor and the coupling to all neighboring strips. The biasing circuitry with the intrinsic bias resistance $R_b$ shunted to signal ground by $C_{bias}$ is a parallel resistance to $C_d$ as illustrated in the small-signal equivalent circuit in Figure 3.10(b). The leakage current $I_l$ of the strip implant to the back-side contact is considered in the equivalent circuit for noise analyses as well as cumulative series resistances between the strip electrode and the amplifier input summarized as equivalent resistance $R_s$. The sensor read-out pad is galvanically insulated from the strip implant by a thin oxide layer thus acting as coupling capacitance $C_c$.



(a)                              (b)
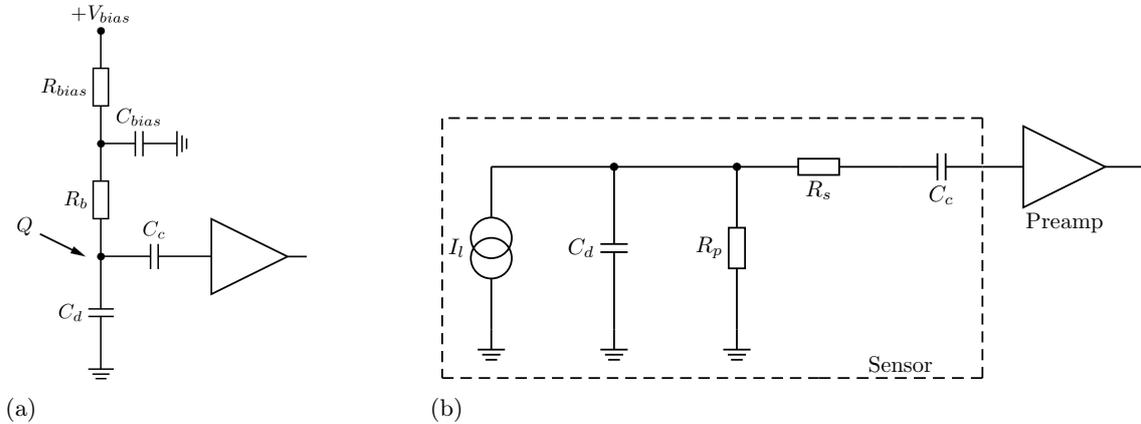
**Figure 3.10.:** (a) Strip detector equivalent circuit of a single channel showing the biasing network of external components $R_{bias}/C_{bias}$ and the internal bias resistance $R_b$. The charge $Q$ is collected at the strip implant and transferred through coupling capacitance $C_c$ between implant and metal strip to the front-end input. (b) Equivalent circuit for noise analysis of the sensor. The amplifier is assumed to be noiseless.

**Parallel Resistance Noise**   This noise source is often erroneously attributed to noise originating from the detector's capacitance. In fact, a pure reactance can hardly arouse noise, but any shunt resistance $R_p$ to this capacitance does if it is a physically ohmic resistance. This phenomenon is caused by thermal excitation of the electron gas within any conductor

irrespective of the applied voltage but it is proportional to the ohmic resistance. It is often referred to as thermal or *Johnson* noise. In the case of DSSDs the intrinsic bias resistor is such a shunt resistance. The spectral voltage density generated by this parallel circuit of the detector's capacitance and the parallel resistance is [93]

$$|e_{np}|^2 = \frac{4kTR_p}{1 + (\omega R_p C_d)^2} \tag{3.2}$$

Integration of this figure yields the noise voltage

$$v_{np}^2 = \int_0^\infty e_{np}^2 \mathrm{d}\omega = \frac{kT}{C_d} \tag{3.3}$$

and the equivalent noise charge

$$q_{np}^2 = v_{np}^2 C_d^2 = kTC_d \tag{3.4}$$

Note: latter result is obtained by integrating over all frequencies and thus becomes independent of $R_p$. Yet, any realistic transfer function imposes a high frequency cut which yields a different result after the frequency integration, where $R_p$ still contributes significantly.

**Series Resistance Noise**   This noise contribution originates, similar to the parallel noise, from the inevitable thermal *Johnson* noise generated by any real resistance

$$e_{ns}^2 = 4kTR_s. \tag{3.5}$$

Its equivalent noise charge is

$$q_{ns}^2 = kTR_s C_d^2 \Delta f \tag{3.6}$$

with the bandwidth $\Delta f$ in which the signal is integrated. Examples for this kind of noise source would be superficial traces on the sensor and PCB as well as bond wires.

**Detector Leakage Current Noise**   The leakage current caused at the junction of the reverse-biased detector bulk and the strip implants generates a broadband, frequency-constant (white) shot noise which creates a voltage drop at the detector capacitance

$$e_{nl}^2 = \frac{2eI_l}{(\omega C_d)^2} \tag{3.7}$$

the equivalent noise charge is

$$q_{nl}^2 = 2eI_l \left( \frac{1}{\omega_h} - \frac{1}{\omega_l} \right) \tag{3.8}$$

with $\omega_l$ and $\omega_h$ the low and high frequency corners of the amplifiers transfer function.

**Punch Through Noise**   The leakage current generates not only noise at the bulk-strip interface but also, in the case of punch-through biased sensors, an additional passage of charge carriers through the potential barrier between strip to bias ring occurs, which adds up a shot noise term in quadrature to the total noise with the same magnitude as the leakage current noise. The latter thus becomes

$$e_{nl}^2 = \frac{4eI_l}{(\omega C_d)^2}. \tag{3.9}$$

In further noise analyses we assume a fully depleted sensor, thus the bias voltage is assumed to be far beyond the punch-through voltage. Otherwise the punch-through induced noise term shapes more complex and eventually dominates the overall noise figure [137].

**Bias Supply Noise** This contribution is considered to be an external noise passed into the sensitive read-out node along the bias resistor $R_b$ and attenuated by the voltage divider formed by $R_b$ and the detector capacitance $C_d$. The resulting noise voltage density at this node is

$$|e_{nb}|^2 = \frac{e_{nB}^2}{1 + (\omega R_b C_d)^2} \tag{3.10}$$

with the external noise voltage density of the bias power supply $e_{nB}$. Partial integration over $\omega$ yields

$$e_{nb}^2 = \frac{e_{nB}^2}{4 R_b C_d} \tag{3.11}$$

and transformation to equivalent charge

$$q_{nb}^2 = \frac{\langle e_{nB} \rangle^2 \Delta f C_d}{4 R_b} \tag{3.12}$$

assuming a white noise distribution from $e_{nB}$ within frequency window $\Delta f$. The both latter equations show that

1. the bias power supply noise is injected through the voltage divider combination $R_b$, $C_d$ into the sensitive node

2. a large value of the biasing resistor is preferable to suppress this noise

**Amplifier Noise** Any amplifier exhibits intrinsic noise originating from current (parallel) noise as well as voltage (series) noise. This noise usually predominantly originates from the first preamplifier transistor; any following stage contributes noise to a fraction diminished by the gain of the previous stage to the total noise factor according to the famous noise propagation formula for cascaded amplifier systems[2] [138]:

$$F_{tot} = F_1 + \sum_{i=2}^{N} \frac{F_i - 1}{\prod_{j=1}^{i-1} G_j} \tag{3.13}$$

or, in the further context in its expanded form:

$$F_{tot} = F_1 + \frac{F_2 - 1}{G_1} + \frac{F_3 - 1}{G_1 G_2} + \cdots \tag{3.14}$$

with index $i = 1 \ldots N$ denoting the amplifier stage. The noise factor $F_i$ is defined as the ratio of the the output to the input SNR of the respective amplifier with closed loop gain $G_i$. An ideal amplifier would exhibit $F = 1$ while a higher value than 1 implies that the amplifier adds its own finite intrinsic noise to the total noise factor. Using the definition of the noise factor $F$, for which eqn. (3.13) was originally specified, one may derive its relation to the input equivalent noise charge $q_{n,i}$ by some reconfiguration and by utilizing $q_o = G q_i$:

$$F = \frac{SNR_{in}}{SNR_{out}} = \frac{q_{x,i}/q_{n,i}}{q_{x,o}/q_{n,o}} = q_{n,i} q_{n,o} \frac{q_{x,i}}{q_{x,o}} = q_{n,i} G q_{n,i} \frac{q_{x,i}}{G q_{x,i}}$$
$$= q_{n,i}^2 \tag{3.15}$$

---

[2] Sometimes also referred to as *Friis' formula*.

Evaluating Equation (3.14) for the total input referred noise, i.e. the virtual noise that would be generated at the input of the chain from the point of each stage yields

$$q_{n,tot}^2 = q_{n,1}^2 + \frac{q_{n,2}^2}{G_1} + \frac{q_{n,3}^2}{G_1 G_2} + \cdots \tag{3.16}$$

Equations (3.13) through (3.16) demonstrate the importance of a low noise first amplifier stage irrespective of the noise contribution of the following stages. The second amplifier along the chain already exhibits a noise factor diminished by the gain of the first stage. Therefore a low noise, high gain preamplifier is desirable in low noise applications.

This principle is most useful in other areas as well, like radio astronomy and telecommunication, where preamplifier designs benefit from the usage of high electron mobility transistors (e.g. GaAs-FETs) in the first stage which pin down the preamplifier's overall noise figure to equivalent noise temperatures[3] of a few dozens of Kelvin [138].

The amplifier input bias current, in analogy to the detector's leakage current, creates a noise voltage drop over the sensor capacitance's reactance

$$e_{nap}^2 = \frac{2eI_{ba}}{(\omega C_d)^2} = \frac{i_{na}^2}{(\omega C_d)^2}, \tag{3.17}$$

where $I_{ba}$ is the amplifier's input bias current and $i_{na}$ the input noise current. The specification of noise current or noise voltage is merely arbitrary and can be interchanged equivalently depending on which of either invoked magnitude eases the calculation effort. However, the origin of the noise can be either current or voltage generated, thus the subscript 'p' in the voltage density $e_{nap}$ is a reminder to the parallel origin of this noise source.

The series or voltage noise density of the amplifier on the other hand breaks up into a part displaying a uniform white contribution as well as a $^1/_f$ - component (often referred to as flicker noise):

$$e_{nas}^2 = e_{na}^2 + \frac{A_f}{f}. \tag{3.18}$$

The white noise term $e_{na}$ is usually given as the amplifier's voltage noise floor and can be estimated by

$$e_{na}^2 \simeq \frac{8}{3} kT \frac{1}{g_m} \tag{3.19}$$

when the transconductance $g_m$ of the input transistor is known. The additional parameter $A_f$ defines the $^1/_f$ - part. Alternatively, the noise corner frequency $f_{nc} = \frac{A_f}{e_{na}^2}$, which specifies the transition from flicker noise to the constant white noise floor can be used:

$$e_{nas}^2 = e_{na}^2 \left( 1 + \frac{f_{nc}}{f} \right) \tag{3.20}$$

Either parameter, $A_f$ or $f_{nc}$ must be stated in order to invoke a complete noise analysis.

For preamplifier systems utilizing a bipolar transistor, the bias current noise limits the noise performance at shaping times larger than $\approx 50\,\text{ns}$ significantly. FET transistors on the other hand show much lower input currents $\mathcal{O}\,(1..100\,\text{pA})$ due to gate leakage which results in

---

[3] The temperature that would generate thermal noise equal to the observed noise in a pure ohmic resistor. Often this reference resistor is chosen to match the system's impedance, e.g. $50\,\Omega$ by convention.

negligible input current noise at the expense of higher voltage noise densities at identical footprints. Modern VLSI-ASICs therefore (beside other advantages like unipolar supply) utilize *p*- or *n*-Channel MOSFETs with large area gate electrodes or JFETs as preamplifier transistors with optimum peaking times in the order of several dozens to hundreds of nanoseconds.

**Total Input Noise**  The total input referred noise voltage density then is the summation of all discussed noise contributions in quadrature:

$$
\begin{aligned}
e_{n,Det}^2 &= e_{np}^2 + e_{ns}^2 + e_{nl}^2 + e_{nb}^2 + e_{nap}^2 + e_{nas}^2 \\
&= \frac{4kTR_b}{1 + (\omega R_b C_d)^2} + 4kTR_s + \frac{4eI_l}{(\omega C_d)^2} + \frac{e_{nB}^2}{4R_b C_d} \\
&\quad + \frac{i_{na}^2}{(\omega C_d)^2} + e_{na}^2 + \frac{2\pi A_f}{\omega}
\end{aligned}
\tag{3.21}
$$

The equivalent noise charge at the input of the amplifier is obtained by integrating the product of the noise voltage density at the input and the complex amplifier's transfer function $A$ with gain $G = 1$ over all frequencies and multiplication with the detector capacitance $(Q = C \cdot U)$:

$$
q_n^2 = c_{norm} C_d^2 \int_0^\infty e_{n,i}^2 \, |A|^2 \, \mathrm{d}\omega
\tag{3.22}
$$

assuming a simple $CR\text{-}RC-$shaper's transfer function

$$
A = \frac{1}{1 + \frac{1}{j\omega\tau_d}} \cdot \frac{1}{1 + j\omega\tau_i}.
\tag{3.23}
$$

Integration and coefficient comparison with an evaluated time domain expression for the signal gain of the shaper and setting the differentiator and integrator time constants equal ($\tau_d = \tau_i \equiv \tau$) yields [93]

$$
q_n^2 = \left(\frac{\mathrm{e}^2}{8}\right) \left[ \left( 4eI_d + \frac{4kT}{R_p} + i_{na}^2 + \frac{e_{nB}^2 C_d}{4R_b} \right) \tau + \left( 4kTR_s + e_{na}^2 \right) \frac{C_d^2}{\tau} + 4A_f C_d^2 \right]
\tag{3.24}
$$

The first term equals the parallel component and is mostly independent of capacitance and is increasing with shaping time. The second term comprehends all series noise sources and is linearly dependent on $C_d$ but it decreases with increasing shaping time. The last term describes the flicker noise which is independent of shaping.

It must be pointed out that the derived formalism (3.24) delivers correct results only under the assumption that a linear, passive and single stage $CR\text{-}RC-$shaper is employed. Particularly the utilization of signal deconvolution or equivalent DSP-techniques apply transfer functions of higher orders into the signal path which must be known in order to calculate the equivalent noise charge and the time domain response.

In Figure 3.11 all discussed noise contributions for an example system with the given properties are shown together with the resulting noise figure. Due to the nature of parallel and series noise sources the overall noise function exhibits a minimum at an optimum shaping time constant. In practical applications often a shaping time different than this optimal setting
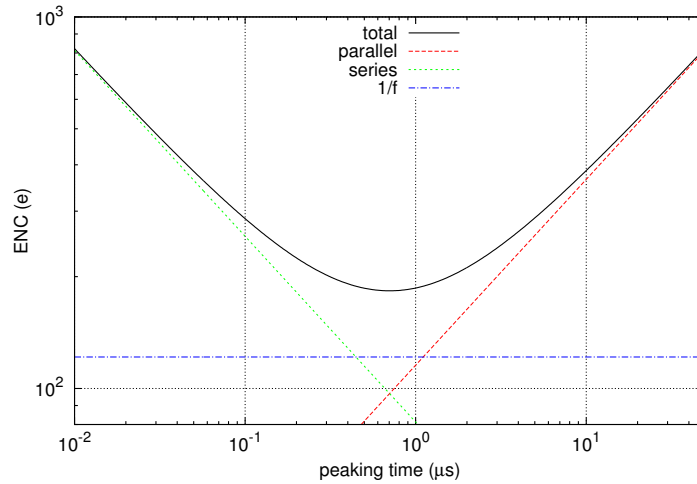
**Figure 3.11.:** Noise contributions for a CSA with single $CR$-$RC$–shaper. $C_d = 10\,\mathrm{pF}$, $I_l = 1\,\mathrm{nA}$, $g_m = 13\,\mathrm{mS}$, $A_f = 10^{-12}\,\mathrm{V}^2$, $R_s = 50\,\Omega$.

is used. The reason for this 'noise mismatch' arises either from constraints in the utilized setup or simply by a lack of knowledge of the system's noise performance.

During a beamtime measurement the system's noise performance was extracted as reported in Table 3.2 together with calculated values according to the discussed model. Those are calculated separately for a single sided connection of the front-end chip as well as $p$- and $n$-side noise values for double sided connection. The difference between the measured $p$- and $n$-side noise values can be explained with a higher capacitance of the n-side strips due to a surface layer of free ion charges around the $p$-strip isolations as well as a smaller parallel resistance value [139]. Likewise the lower noise of the single sided readout compared to the double sided $p$-side read-out connection can be attributed to the unconnected $n$-side strips in the single sided case, which are thus floating from the system's ground potential and do not contribute to the total strip capacitance. Furthermore a larger leakage current (at the same bias voltage) was observed for all detector modules equipped with double sided readout electronics. The reason for this behavior still needs to be investigated.

The basic parameters which found input into the noise calculations were determined either through measurements ($I_l, R_p, C_d$ (from $C_{is}$-measurements)), taken or derived from documentations ($i_{nA}, e_{nA}$ or $g_m$, $A_f$ or $f_{nc}$, cf. e.g. [137]) or estimated from the given configuration, are reported in Figure 3.12 for the single sided case. The other noise figures are calculated with the same set of parameters except those explicitly stated in the caption of Table 3.2. Obviously, the calculated noise matches the measured values within roughly 100 electrons for single sided readout and double sided $p$-side read-out, but fails to describe the higher values obtained for the $n$-side noise. Since the initial parameters above were not determined empirically but preset by typical values, this mismatch might be explained with exceedingly high input bias currents on the $n$-side when the thin oxide insulation layer between strip implants and metal-lines is broken. This argument is actually supported by the increased leakage current at double-sided read-out configurations, implying a partial current drain through the preamplifier input stages. Another possibility is a probably even lower ohmic insulation between the $n$-side strips than the assumed $0.5\,\mathrm{M}\Omega$, which would increase the parallel noise contribution.

| Sensor | Doping Type | ENC ($e$) | Readout Connection |
|--------|-------------|-----------|--------------------|
| 1a | p | 501 | |
| 1b | p | 533 | single sided |
| 2a | p | 520 | |
| 2b | p | 536 | |
| 0 | p | 594 | double sided |
| 0 | n | 823 | |
| 3 | p | 640 | double sided |
| 3 | n | 855 | |

| Noise Contribution | ENC (e) single | $p$ | $n$ |
|--------------------|----------------|-----|-----|
| $n(I_l)$ | 28 | 89 | 89 |
| $n(R_p)$ | 147 | 147 | 208 |
| $n(R_s)$ | 182 | 214 | 247 |
| $n(Amp,s)$ | 331 | 392 | 452 |
| $n(1/f)$ | 85 | 101 | 116 |
| total | 415 | 489 | 574 |

**Table 3.2.:** Measured ENC noise values for 6 sensors during a beamtime campaign (left) and calculated ENC contributions for $\tau = 34\,$ns. Input values for single side read-out: $C_d$=5.0 pF, $R_p$=1.0 MΩ, $I_l$=2 nA; $p$-side values: $C_d$=5.8 pF, $R_p$=1.0 MΩ, $I_l$=20 nA; $n$-side values: $C_d$=6.8 pF, $R_p$=0.5 MΩ, $I_l$=20 nA

The equivalent noise charge calculated above may be approximated by a simple parametrization for a reasonable laid-out system:

$$q_n = q_0 + a \cdot C_d \tag{3.25}$$

where $q_0$ and $a$ are the constant preamplifier and the capacitive noise parameters, respectively and $C_d$ the effective capacitance seen by the preamplifier, i.e. the strip capacitance in series with the coupling capacitance.
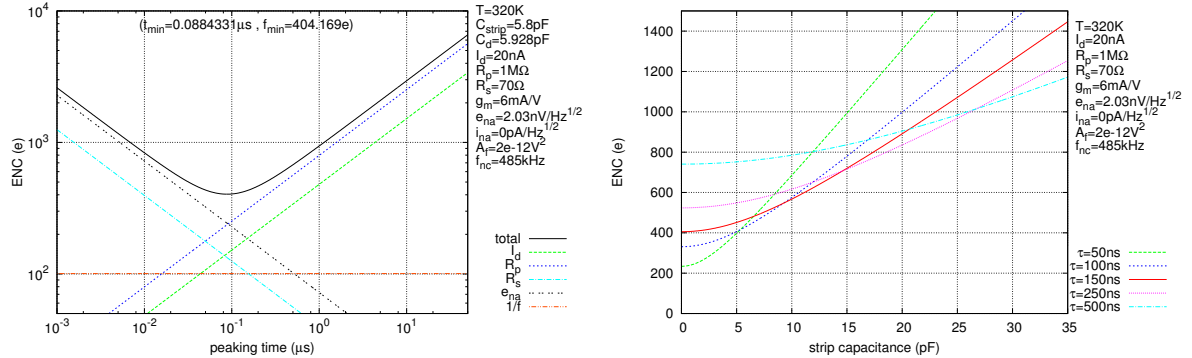


**Figure 3.12.:** Input referred noise of APV25-S1 front-end connected to a short strip of ITC01 prototype sensor (left) and calculated noise in dependence of the effective input capacitance of the same front-end chip.

**Common Mode Noise Correction:** The influence of a shift in the baseline level of all or a group of channels in a frame due to low frequency fluctuations of the front-end ground reference can, under certain circumstances, be remedied. The APV25 front-end multiplexes the entire set of 128 channels for each trigger to the output irrespective if a channel is hit or not. This allows the storage of each channel in a buffer as pedestals. The mean value of this buffer is treated as mean pedestal which is subtracted from each new incoming channel

value, while its standard deviation is identified with the pedestal noise. The registered noise can then be corrected for temporal shifts of the baseline for a subset of channels (since the simultaneous baseline shift for all channels was already corrected for prior to storage of the values into the pedestal buffers) by:

$$N_{corr,j} = \sqrt{\frac{1}{m} \sum_i^m \left[ P_j(i) - \overline{P_j} - \frac{1}{n} \sum_j^n \left( P_j(i) - \overline{P_j} \right) \right]^2} \qquad (3.26)$$

where $N_{corr,j}$ is the common mode corrected noise of channel $j$, $m$ the number of frames contained in the sample, $n$ the number of channels, that belong to the same common mode potential, i.e. the same readout plane, $P_j(i)$ the pedestal of channel $j$ in frame $i$ and $\overline{P_j}$ the mean pedestal of channel $j$. The effect of the common mode noise correction is illustrated in Figure 3.13 (left) showing the noise floor of three front-ends connected to one sensor side without and with applied correction.

**Transmission Noise Correction:**   An additional source of noise is introduced after amplification at the transmission of the sampled analog signals along the path until the ADC-input. This noise again adds up in quadrature to the noise of the analog stage and can be corrected for through the following procedure:

1. switch off the analog front-end-stages

2. measure the (common mode corrected) pedestal noise floor of all front-ends, this will be referred to as transmission noise

3. during normal measurements (with activated analog stages): measure common mode corrected total pedestal noise

4. subtract the transmission noise from total noise in quadrature:

$$N_{corrected}^2 = N_{total}^2 - N_{transmission}^2 \qquad (3.27)$$

An example of the reconstructed noise from the measured total and digital transmission noise is shown in Figure 3.13 (right). The noise contribution of the ADC is included in the transmission noise. Hence, the resulting noise content can be considered to originate from the analog front-end alone. It must be noted, that this procedure is necessary only for front-ends that transmit the analog sampled signals and do not digitize them on-chip.

### 3.3.5. Signal-to-Noise Ratio

The signal amplitude for a detected amount of charge is reasonably assessed in the presence of the noise the same channel is exposed to. This allows first to define a threshold that has to be exceeded in order to assert a hit signal and second to estimate the rate of expected hits that occur when statistical charge fluctuations exceed this threshold. The ratio of the expected signal amplitude to the noise furthermore affects position resolution and detection efficiency, as will be shown later.
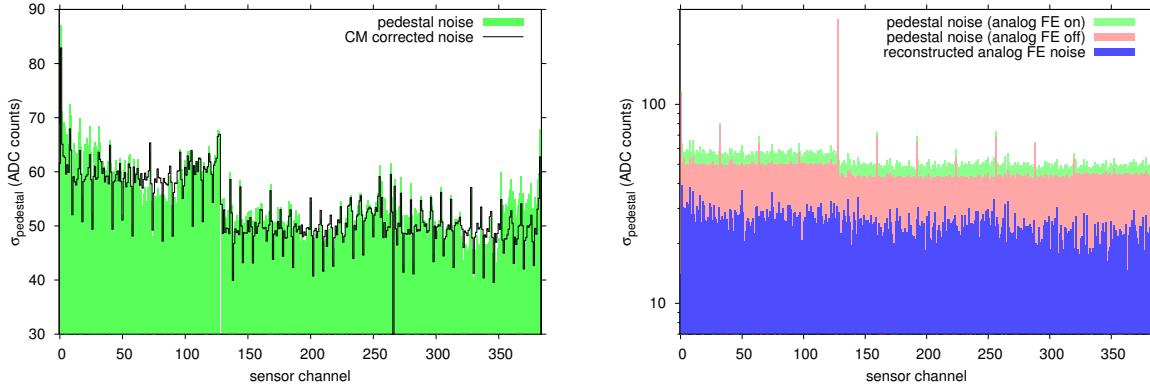
**Figure 3.13.:** Noise contributions measured with the APV25 front-end. Left: Common Mode Noise Correction, Right: Correction of measured noise (green) by subtracting the measured transmission noise (red, with the analog stages of the front-end shut down) in quadrature. The resulting noise distribution should be the one exclusively generated by the preamplifier stage (blue).

**Single-Hit–SNR:** The single-hit signal-to-noise ratio can be defined as the ratio of a known charge $Q_{sig}$ detected and the amount of smearing it is exposed to, due to individual noise with equivalent noise charge $q_{n,i}$ of the $i$-th channel:

$$\left(\frac{S}{N}\right)_i = \frac{Q_{sig}}{q_{n,i}} = \frac{ADC_i\big|_{Q_{sig}}}{ADC_{n,i}} \tag{3.28}$$

with $ADC_i\big|_{Q_{sig}}$ the digitized quantity of a signal charge $Q_{sig}$ and $ADC_{n,i}$ the measured noise of channel $i$ in digitized counts. The equality of the left hand side to both right hand sides of eqn. (3.28) is true only if the channel's transfer characteristics is highly linear, i.e. provided that $ADC_i = c_i \cdot Q$ results in a constant calibration coefficient $c_i$ for any incident charge $Q$.

An example of reconstructed noise and SNR values for a sample obtained for a tracking configuration of four sensors read out by 6 front-ends per sensor obtained during a beam-time campaign at the electron accelerator facility *DESY* in Hamburg is shown in Figure 3.15. The SNR is referenced to the most probable energy loss of the ultra-relativistic electrons inside the sensors equivalent to a charge of 22.5 k$e$. The same charge served as reference for the absolute front-end gain calibration using the MPV of the measured distributions in each channel as demonstrated earlier in this section. The calibration allows the conversion of the measured standard deviation of the pedestal buffer values into the physically meaningful equivalent noise charge ENC. With the given reference charge belonging to the energy loss MPV the signal-to-noise ratio emerges seamlessly.

**Dependence of ENC and SNR on Shaping Time** In Figure 3.16 a scan over the pulse shaping registers `ISHA` and `VFS` of the APV25 front-end with connected short strip sensor is shown. For each setting of (`ISHA`/`VFS`)-tuples noise and gain measurements by injection of a number of 2 fC charge pulses were taken. The noise was corrected for common mode and transmission noise (a) and calibrated through multiplication with the gain conversion factor depicted in (b) to yield the true equivalent noise charge as seen in (c) and (d). Going along the valley of minimum ENC in this plot from left to right equals a successive increase in the peaking time. The ENC values marked by this virtual axis are then compared to the predicted values as
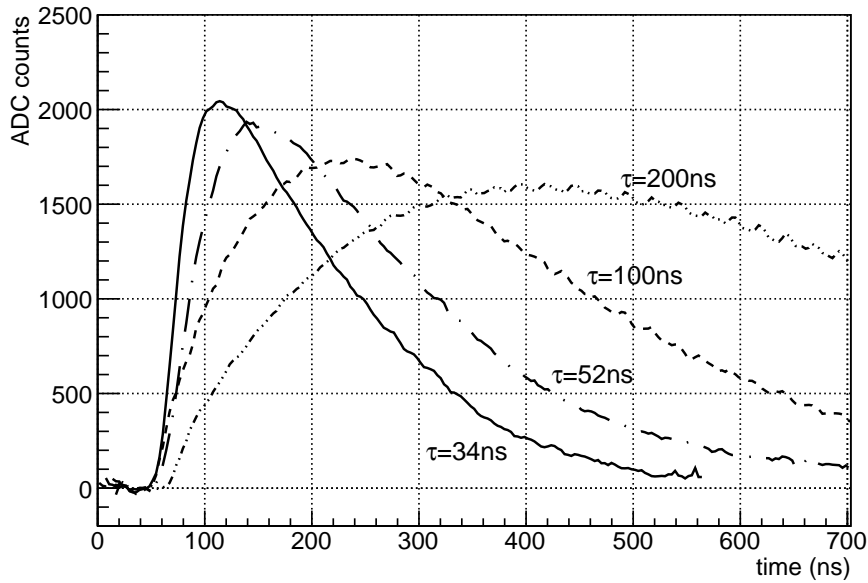
**Figure 3.14.:** Waveform of a 2 fC charge pulse reconstructed with the injection-scan method at different shaping times of the preamplifier.

illustrated in Figure 3.17. The comparison between those theoretical with the measured values at several peaking times are reported in Table 3.3 for two surveys undertaken for the same hardware configuration. The values match well within the error margins although it must be emphasized that the ENC predictions are obtained from a simplified phenomenological model which does not replace a detailed electronic simulation. On the other hand, the good agreement shows that the dominating noise contributions are conclusively described by this approach.

Finally, the maximization of the SNR for the utilized setup is of paramount importance for a clean separation between signal and noise hits. Figure 3.16(e) and (f) visualize the SNR for a signal of 1 fC over the total noise evident at the ADC input. Surprisingly, the peaking
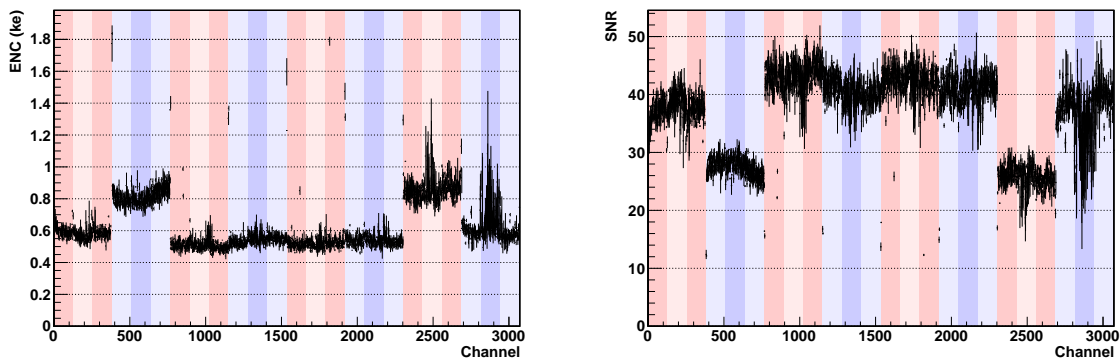


**Figure 3.15.:** System noise and signal-to-noise ratio of the complete readout chain of the tracking setup used during beamtime at *DESY* in channel-wise order.
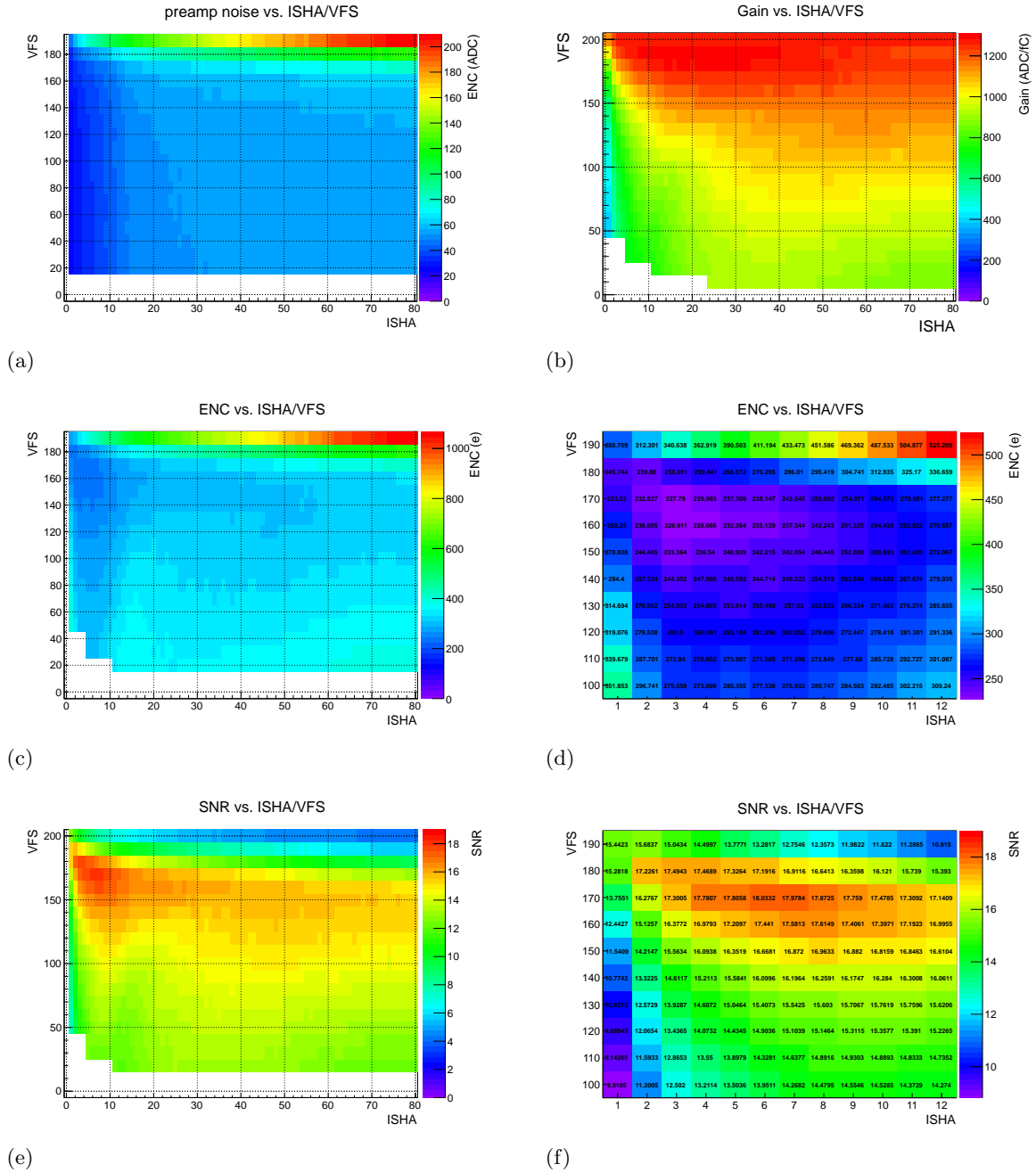
**Figure 3.16.:** VFS-ISHA register scan. (a) transmission noise corrected preamplifier noise, (b) conversion gain for a measured signal of 1 fC, (c) equivalent noise charge at the preamplifier input, (d) zoom into the region of minimal ENC, (e) signal-to-noise ratio for a measured signal with the charge of 1 fC, (f) zoom into the region of register settings with peaking SNR. Note that the global minimum of the preamplifier referred ENC does not necessarily coincide with the maximum of the SNR measured at the input of the ADC as can be seen from the comparison of (d) and (f).
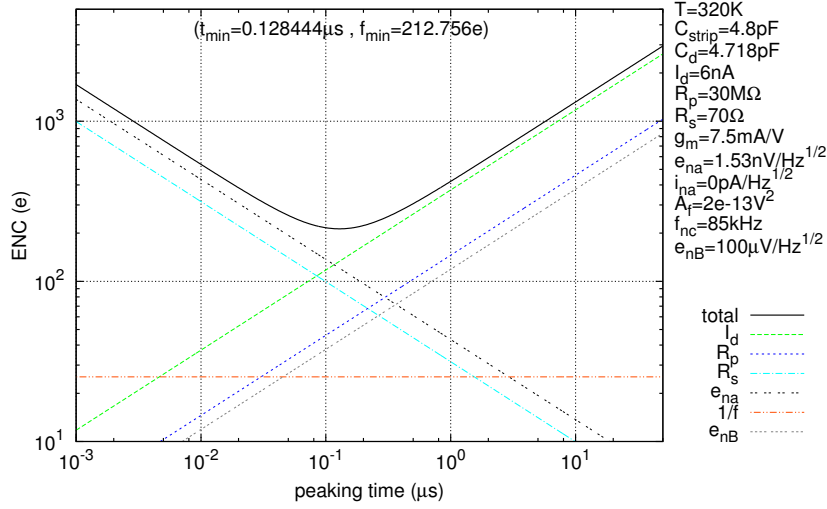
**Figure 3.17.:** Noise figure of APV25 front-end connected to CIS01-S3 sensor for the same configuration as described above.

time setting for the maximum of this quantity does not necessarily coincide with the peaking time for best (lowest) ENC. This fact can be explained with the presence of noise sources that contribute noise other than the one originating from the first preamplifier stage's transistor such as the transmission noise, which would add up in quadrature to the true ENC. Thus, the noise may be dominated by this "external" noise component for shaping times when the analog ("intrinsic") noise is at minimum. Choosing a slightly higher gain would then result in a higher SNR since the intrinsic noise is still dominantly superimposed by the unaltered external component. As a result, the best point of operation can be spotted at a different shaper setting as would be required for the lowest ENC. This observation also applies to front-end systems that digitize the charge immediately on-chip due to susceptibility of the front-end electronics to external noise, e.g. digital switching noise pickup, or, particularly, common mode noise.

**Cluster–SNR:** The SNR for single strips is considered a useful quantity only when the entire charge is contained in this single strip (since the SNR is always referred to a specific charge). As soon as the charge gets distributed over several channels inside a cluster, each strip carries an arbitrary fraction of the total charge, thus obliterating the relevance of the obtained SNR. Instead, the observed cluster charge has to be set in relation to the ENC contributions of the involved strips. Thus, one defines a cluster signal-to-noise ratio with

$$\left(\frac{S}{N}\right)_{cl} = \frac{\sum\limits_{i}^{N} q_i}{\sqrt{\frac{1}{N}\sum\limits_{i}^{N} q_{n,i}^2}} = \frac{\sqrt{N} \cdot Q_{Cl}}{\sqrt{\sum\limits_{i}^{N} q_{n,i}^2}} \tag{3.29}$$

which in case of identical single strip noise charges $q_n$ simply becomes $\frac{Q_{Cl}}{q_n}$, where $Q_{Cl}$ designates the cluster's charge content.

| shaping time | ENC ($e$) | | |
|:---:|:---:|:---:|:---:|
| $\tau$ (ns) | calculated | measured | |
| | | survey #1 | survey #2 |
| 34 | 301 | 318±38 | - |
| 38 | 288 | 310±36 | - |
| 52 | 255 | 305±36 | - |
| 100 | 216 | 241±31 | 216±36 |
| 120 | 213 | 238±30 | 226±34 |
| 170 | 217 | 227±31 | 204±35 |
| 200 | 223 | 236±32 | 204±42 |
| 320 | 255 | 254±37 | 212±42 |
| 530 | 313 | 350±67 | 319±64 |

**Table 3.3.:** Measured and calculated noise values for DTS-CIS01-S3 setup.

**Noise and SNR in Dependence of Bias Voltage:** The ENC and subsequently also the SNR are strongly dependent on the actual operating point of the sensor-preamplifier combination constituted mainly by the input load capacitance and the shaping time. A slight detuning of either of those parameters displaces the operating point resulting in different values for gain and ENC. This interdependence has been demonstrated already for the shaping time earlier in this section. Equation (3.24) suggests a linear relation between the series- and $1/f$-parts of the ENC and the detector capacitance. Latter appears to be well defined for a bias voltage applied to the sensor beyond full depletion. At lower bias voltages, however, a strong change of ENC and signal gain can be observed (Figure 3.18) which is a direct consequence of the rapidly changing capacitance due to the depletion zone detaching from the $p$-side strip implants beyond the punch-through threshold voltage. A more detailed account of the depletion process and its impact on capacitance is given in Section 4.2.4.2. Particularly, the voltage dependent noise characteristics of Figure 3.18(a) compares directly to the actually measured interstrip capacitance of this sensor reported in Figure 4.16.

Recalling the equation for the depletion depth of a reverse-biased $p$-$n$-junction from Section 2.1.3 yields for the extension of the depletion zone

$$d = \sqrt{\frac{2\epsilon}{eN_D}(V_{bi} - V)}. \tag{3.30}$$

On the other hand, the capacitance of the junction was found to be

$$C = \frac{\epsilon A}{d} \tag{3.31}$$

and Equation (3.24) stated for the relation between noise and the capacitance:

$$ENC \propto C. \tag{3.32}$$

Combining the dependencies from eqns. (3.30) to (3.32), one finds

$$d^2 \propto \frac{1}{ENC^2} \propto V. \tag{3.33}$$

(a)



(b)



(c)



(d)
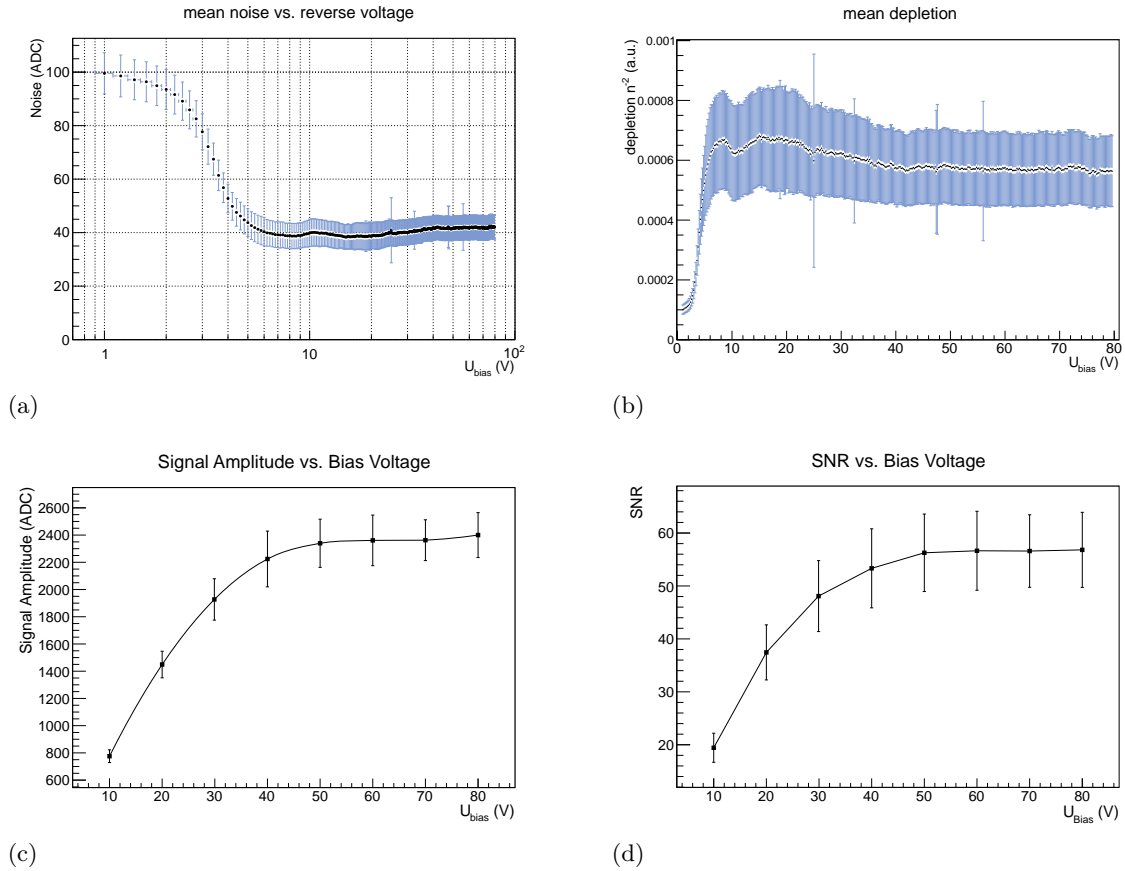
**Figure 3.18.:** Measured noise (a) and depletion (b) in dependence of applied reverse voltage of CIS01-S3 sensor. The error bars do not reflect the measurement error, but indicate the spread of the measured noise values of all channels of one entire sensor side including a $\approx 20\,\%$ fluctuation in gain and noise between the front-end chips. The signal amplitude of the MPV extracted from energy loss distributions of $^{90}$Sr electrons and the corresponding signal-to-noise ratio in dependence of sensor bias voltage are shown in (c) and (d), respectively.

Therefore, plotting the inverse of the noise in dependence of the bias voltage indeed yields a figure of depletion. Figure 3.18(b) shows this representation for the same data set as presented in (a).

The preamplifier gain was measured for a signal equivalent to the MPV of the energy loss distribution of $\beta$-particles originating from a $^{90}$Sr source as shown in Figure 3.18(c). In contrast to the noise, an increase of the signal amplitude up to the full depletion voltage of ca. $50\,\mathrm{V}$ is observed. This can be explained with the circumstance that the volume in which electron-hole pairs are created effectively increases thus yielding an increased signal charge seen by the strip electrodes. At full depletion, finally the entire track of the particle, along which the ionization occurs, runs through the maximally depleted sensor thickness. The ratio of signal and noise (Figure 3.18(d)) is dominated by the signal gain since the noise changes insignificantly above the punch-through voltage.

### 3.3.6. Charge Collection

The electron-hole pairs generated by an ionization process inside the active volume of the sensor are separated due to the externally applied electric field of the bias voltage and attracted toward opposite sides of the sensor surface. An extended charge cloud emerges. At the surface interface layer, the segmentation of the read-out electrodes forces the cloud to break up into fragments defined by the projected area of the strip implants [140]. The total charge thus is shared among the electrodes that are hit by a fraction of the drifting charge cloud. The extent of this cloud and the number of strips which pick up its charge content is determined by a) the charge carrier mobilities b) device geometry (strip width and sensor thickness) c) capacitive coupling between the strips and to the back side d) capacitive coupling to the preamplifier and e) electric field along the drift direction. The first factor is dictated by choice of material and doping concentrations, the second through fourth by the sensor design. The last point is fully mutable through the choice of the bias voltage. The observed sharing of the total charge can be explained as a superposition of the extent of the charge cloud wrt. to the strip pitch and capacitive coupling between adjacent strips. Influence of the capacitive coupling and the bias voltage on the sensor's charge collection efficiency and resolution is analyzed in the following paragraphs.

**Capacitive Charge Collection**   Once completely collected at the strip implant electrodes, the static charge is disintegrated through the biasing resistance $R_b$ into the bias supply potential with a time constant of

$$\tau_b \approx R_b C_d$$

(with the effective strip capacitance $C_d$). This process counteracts the built-up of charge already during the drift-time of the carriers. The time constant $\tau_b$ should therefore be large compared to the average drift time through the whole sensor thickness of typically $10 \ldots 30\,\mathrm{ns}$ to prevent significant loss in charge collection efficiency. The process of charge transfer off the strip implant is assumed in the following considerations to take place within much shorter time intervals than the bias discharge time $\tau_b$.
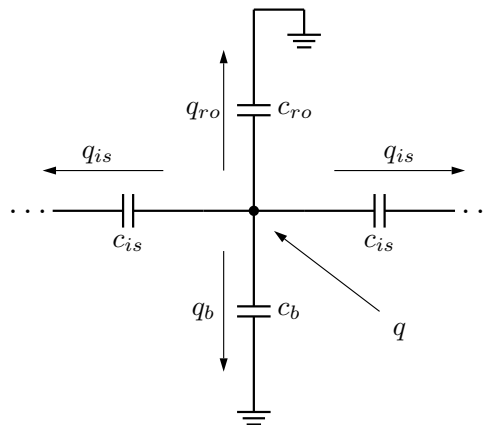


**Figure 3.19.:** Equivalent circuit schematic of a single DSSD channel with read-out of every strip. The effective read-out capacitance $c_{ro}$ is the series circuit of the sensor's coupling capacitance and the preamplifier input capacitance. Paths of the charge fractions coupled off from the central node with accumulated charge $q$ are indicated.

Consider now charge $q$ collected exclusively onto one single strip electrode. Possible discharge paths arise from coupling via capacitance $c_b$ to the back side of the sensor, couplings via $c_{is}$ to the left and right hand neighboring strips and the read-out path to the preamplifier into the effective series circuit of the sensor coupling capacitance $c_c$ and the amplifier's input capacitance $c_{in}$. Figure 3.19 illustrates the configuration. The charge $q$ therefore splits up into three fractions proportional to the coupling capacitances:

$$q = q \Big( \underbrace{\frac{c_{ro}}{c_{ro} + c_b + 2c_{is}}}_{f_{ro}} + \underbrace{\frac{c_b}{c_{ro} + c_b + 2c_{is}}}_{f_b} + \underbrace{\frac{2c_{is}}{c_{ro} + c_b + 2c_{is}}}_{2f_{is}} \Big), \qquad (3.34)$$

with the effective read-out capacitance $c_{ro} = \frac{c_{in}c_c}{c_{in}+c_c}$. The fraction of the charge finally read out by the connected amplifier is:

$$\begin{aligned} q_{ro} &= q f_{ro} \\ &= q \frac{c_{ro}}{(c_{ro} + c_b + 2c_{is})} \end{aligned} \qquad (3.35)$$

The charge drained into the backside capacitance is inevitably lost:

$$\begin{aligned} q_b &= q f_b \\ &= q \frac{c_b}{(c_{ro} + c_b + 2c_{is})}. \end{aligned} \qquad (3.36)$$

The remaining part of the charge is actually not read out by the preamplifier under focus but capacitively coupled to the neighboring strips

$$\begin{aligned} q_{is} &= 2q f_{is} \\ &= 2q \frac{c_{is}}{(c_{ro} + c_b + 2c_{is})}, \end{aligned} \qquad (3.37)$$

where it is subject to a split-up into one fraction lost to the back-side, one actually read out by the corresponding amplifier and one shared again with the next neighbor strip as described above.

**Charge Collection in Dependence of Bias Voltage**   The multiplicity of adjacent channels carrying a considerable fraction of the charge introduced by a single ionizing particle hit (referred to as a cluster) shows a strong dependence in the sub-depletion regime of the bias voltage. A collection of different representations of the cluster size is shown in Figure 3.20. The average cluster extent (Figure 3.20(a)) under normal operating conditions with a bias voltage well above full depletion is generated by histograming the single strip charges with the strip showing the highest contribution defining the center. The resulting distribution, normalized to the number of registered events, is a coarsely binned reflection of the average charge pattern as registered at the front-end inputs. A *Gaussian* fitted to the distribution estimates the width corresponding to $26\,\mu m$. For the same data set, the absolute number of participating strips per cluster is shown in Figure 3.20(b). An exponential decrease of events yielding higher multiplicities can be noticed.

The cluster extent distributions are compared for different bias voltages in Figure 3.20(c) showing an increasing occupancy of peripheral channels as the voltage increases. More specifically, the increase is linearly multiplicative (equivalent to a vertical shift in the logarithmic histogram) and not altering the charge distribution pattern.

(a)

(b)

(c)

(d)

(e)
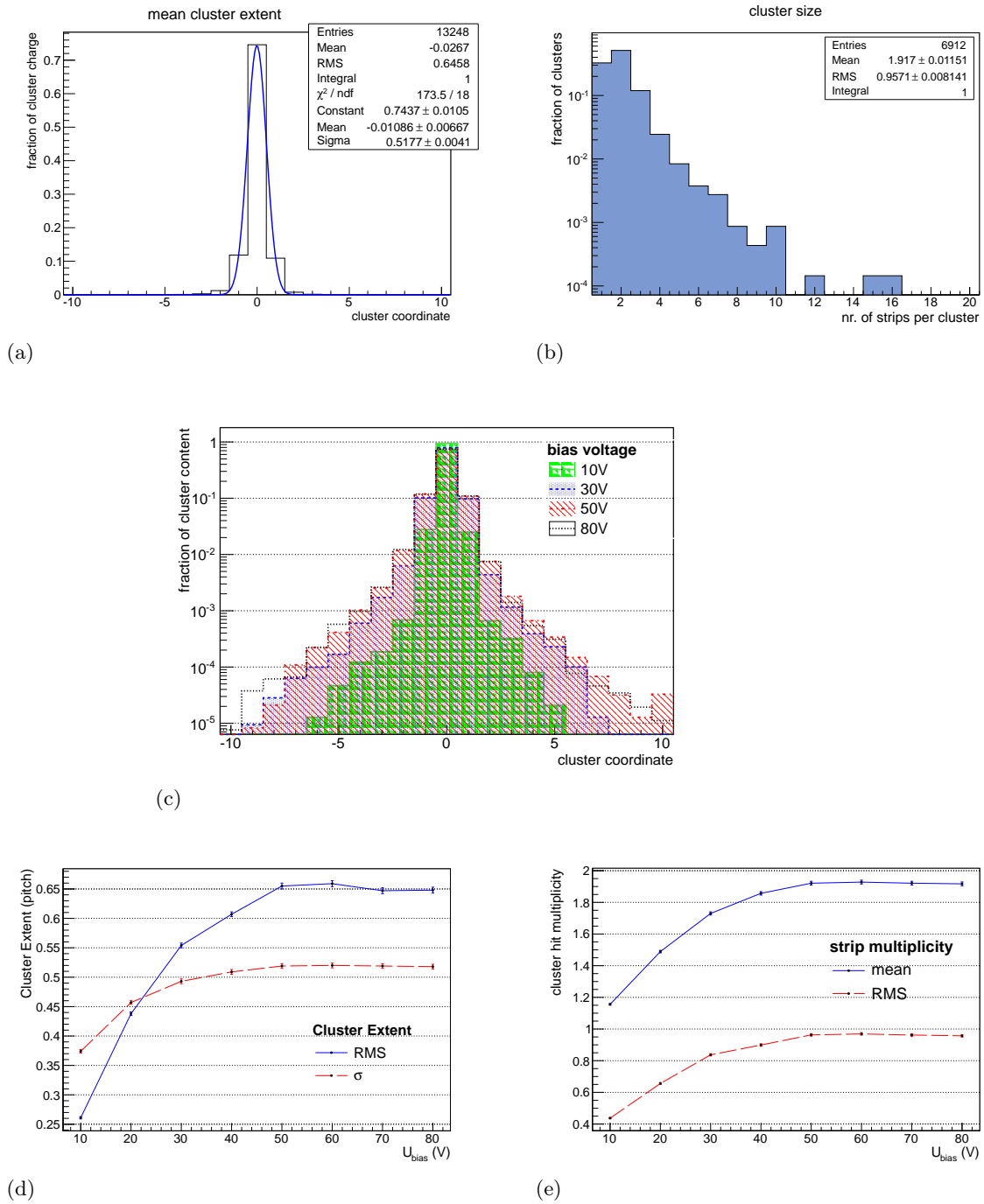
**Figure 3.20.:** (a) Cluster extent defined as the fraction of strip charges in a cluster relative to the central strip (the strip containing the highest charge) with *Gaussian* fit to determine the cluster smearing parameter. (b) Multiplicities of hit strips belonging to the same cluster for every found cluster of one data acquisition run. The binned entries have been normalized by the total number of clusters in that sample. (c) Cluster extent distributions for different bias voltages applied to the sensor. (d) RMS- and $\sigma$ (from *Gaussian* fit) values extracted from those distributions vs. sensor bias voltage. (e) For comparison the same dependence for mean- and RMS-values of cluster strip-multiplicity distributions (as shown in (b)).

Evolutions of RMS and width of the cluster extent distributions as well as the mean and RMS values of the strip multiplicities with the bias voltage is reported in Figure 3.20(d) and (e), respectively. All curves show a clear increase up to the point of full depletion and no further significant change in the over-depletion region. A slight over-swing is notable in the range between $50\,\mathrm{V}$ and approx. $65\,\mathrm{V}$ which can not be explained but might be attributed to the more complicated behavior of the ion surface charge layer on the $n$-side of the sensor becoming noticeable when the full active volume is just depleted.

**Spacial Resolution**   The review of the involved charge sharing mechanisms in strip sensors discussed above identified two major sources responsible for the distribution of charges across several channels. This "deliberate blurring" actually facilitates the reconstruction of the hit centroid with a higher precision than the strip pitch by evaluating a weighted sum of the single strip charges:

$$x_{reco} = \frac{\sum_i q_i x_i}{\sum_i q_i} \tag{3.38}$$

with $x_{reco}$ and $x_i$ the reconstructed and the single strip geometrical coordinates, respectively. Alternatively, this Center-of-Gravity (COG) is calculated in units of the strip index:

$$s_{reco} = s_0 + \frac{\sum_i q_i \cdot i}{\sum_i q_i}, \tag{3.39}$$

where $s_0$ denotes the integral part (offset) of the cluster and the second term of above equation delivers the fractional part provided that the summation is executed over the strips of the cluster starting with the leftmost strip with $i = 0$.

The most inaccurate case conceivable for a detector hit yields clusters with only a single strip carrying the charge information. For a single event the positional accuracy obviously is identical to the strip pitch $p$. The spacial resolution for a statistical ensemble of many hits can then be calculated from the second central moment of the uniform hit distribution within a cell of size $p$ with

$$\sigma_x^2 = \frac{1}{p} \int\limits_{-p/2}^{+p/2} x^2 \mathrm{d}x = \frac{1}{p}\left(\frac{p^3}{24} + \frac{p^3}{24}\right) = \frac{p^2}{12}. \tag{3.40}$$

The best achievable RMS resolution of $p/\sqrt{12}$ for the given case of only one strip hit compares to better resolutions in case of clusters with multiple strips. The gain in resolution is entirely determined by the charge sharing characteristic between two adjacent strip electrodes discussed in the next paragraphs.

**Charge Sharing Characteristic**   The way how the charge is distributed among two adjacent strip electrodes determines the absolute value for the Center-of-Gravity (CoG) and its precision. A measure of this characteristic is often described by the $\eta$-coordinate which may be defined as

$$\eta = \frac{Q_r}{Q_l + Q_r}, \quad \eta \in [0\dots 1] \tag{3.41}$$

where $\eta$ would be interpreted as the linear coordinate between two adjacent strips with 0 being the center of the left-hand strip and 1 the center of the right-hand one. An alternative, but completely equivalent definition of $\eta$ is frequently encountered in literature with

$$\eta = \frac{Q_r - Q_l}{Q_l + Q_r}, \quad \eta \in [-1 \ldots 1] \tag{3.42}$$

where a value of $\eta = -1$ would designate the left strip and $\eta = 1$ the right strip. A value of zero corresponds to the center between the two strips. With either one of those definitions for $\eta$ the distribution of measured events in this coordinate, i.e. the differential $\eta$-distribution, reveals details about the charge collection with respect to neighboring strip electrodes as shown in Figure 3.21(a). The accumulation of entries near the readout strips implies a highly inclined collection of charges in the vicinity of those electrodes while a charge incident in the intermediate region apparently gets forced close to the electrodes as well. An explanation for this pattern can be found in the highly nonlinear charge sharing between two strips. The association of any (measured) $\eta$-value to the corresponding impact point on the geometric linear coordinate $x_0$ can be reconstructed[4] [141], once the $\eta$-distribution is known with the following relation:

$$x_0 = \frac{p}{N_0} \int_0^{\eta} \frac{\mathrm{d}N}{\mathrm{d}\eta} \mathrm{d}\eta, \tag{3.43}$$

assuming a homogeneous distribution of $N_0$ events in the interval between two strips with readout pitch $p$. The particles are furthermore assumed to traverse the sensor perpendicular to the surface. Figure 3.21(b) shows the mapping between $\eta$ and the hit coordinate reconstructed from the $\frac{\mathrm{d}N}{\mathrm{d}\eta}$ distribution in the adjacent Figure 3.21(a).



(a)                                                        (b)
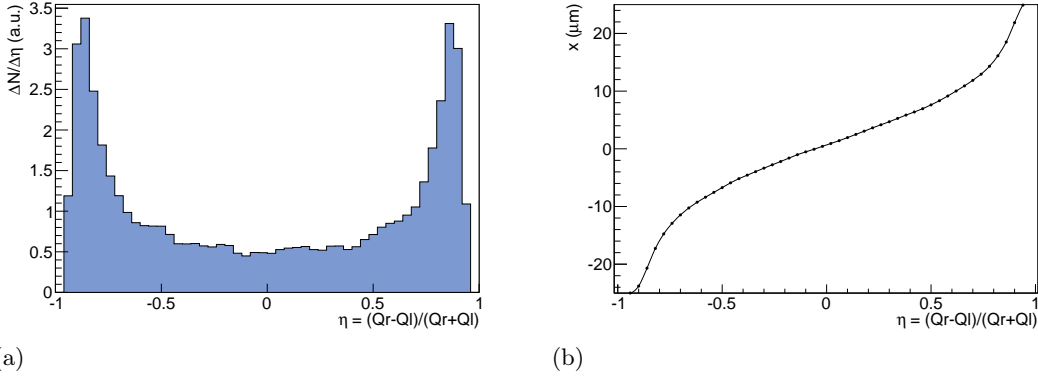
**Figure 3.21.:** Charge collection characteristics between adjacent strip electrodes. (a) Frequency of encountered events with $\eta$-ratio distributed within the principal $\eta$-cell. (b) Reconstructed relation between $\eta$ and the true impact point $x$.

**Reconstruction of the Charge Cloud Distribution**   With the $\eta$-distribution and relation (3.43) now the density of charge carriers around the impact point $f(x)$ can be estimated using a reconstruction method given by *Belau et al.* [141]:

$$\frac{\mathrm{d}N}{\mathrm{d}\eta} = \frac{N_0}{p} \frac{1}{f(-x_0)}. \tag{3.44}$$

---

[4] The coordinate $x_0$ is defined such that its origin is situated at the center between two adjacent strips.

This distribution represents the mean extent of the charge cloud in the vicinity of the impact point. It tends to be error prone at the edges of the $\eta$-interval, where no statistics can be accumulated due to the limitation inflicted by the threshold. This leads to a lack of $\eta$-values showing a large difference between the left and right part of the charge ($\frac{Q_{r/l}}{Q_{l/r}} \gtrsim 20$) which appears as gap at the very edges in Figure 3.21(a). An example of such a reconstructed charge cloud distribution is given in Figure 3.22. The origin of the abscissa is chosen as the mean
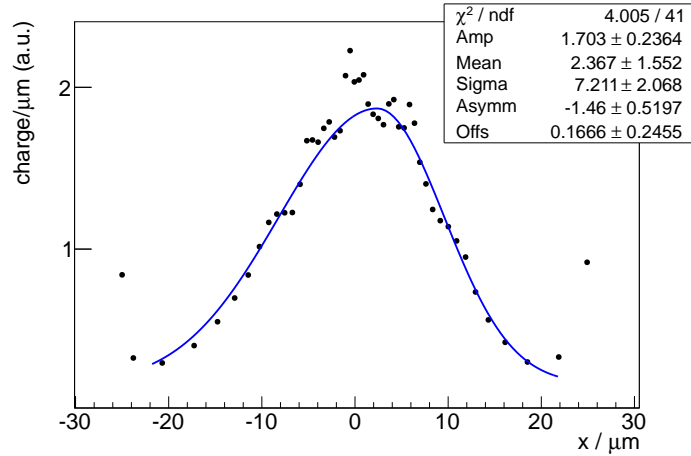


**Figure 3.22.:** Charge cloud distribution around the impact point reconstructed from measured $\frac{dN}{d\eta}$ distribution. The asymmetry of the charge cloud is due to a slight tilt of the sensor w.r.t. the beam axis. The extent of the distribution is determined from a bilateral *Gaussian* fit to $\sigma = (7.2 \pm 2.1)\,\mu\mathrm{m}$. Data points at the edge of the interval are systematically erroneous due to the acceptance gap at the edges of the $\frac{dN}{d\eta}$ distribution.

hit impact center in this representation. An asymmetric bilateral *Gaussian* has been fitted to the distribution yielding width and asymmetry as parameters characterizing the charge cloud. The observed asymmetry in this case can be explained with a slight tilt of the sensor with respect to the trajectories of the impinging particles. In general, asymmetries of the collected charge clouds arise in the presence of strong magnetic fields by the appearing *Lorentz* force accompanied by a shift in the center of gravity (COG). Quantitative parametrizations and measurement results to the dependence of the charge collection on magnetic and electric fields can be found in [91, 141].

**Retrieval of the $\eta$- Function from Incomplete $\eta$- Distributions**    The $\eta$- distributions providing the base for the reconstruction of the charge-sharing characteristics are ideally considered complete which means that the statistics is not biased by an applied charge threshold leading to a loss of events at the boundary of the $\eta$ principal cell. However, in the commonly utilized read-out concepts using a charge discriminator this limitation persists. Calculated $\eta$- function and charge-cloud distribution $f(\eta)$ corresponding to Equations (3.43) and (3.44) do not yield correct results in this case. Figure 3.23 illustrates the situation by means of a double differential distribution in $\eta$ and the total cluster charge measured for a typical energy loss statistics. The acceptance range for measured $\eta$- values entering the distribution is determined by the charge cut largely restricting contributions from lower charges. The integrated event count for each energy bin at the left hand side of the distribution 3.23 shows that the
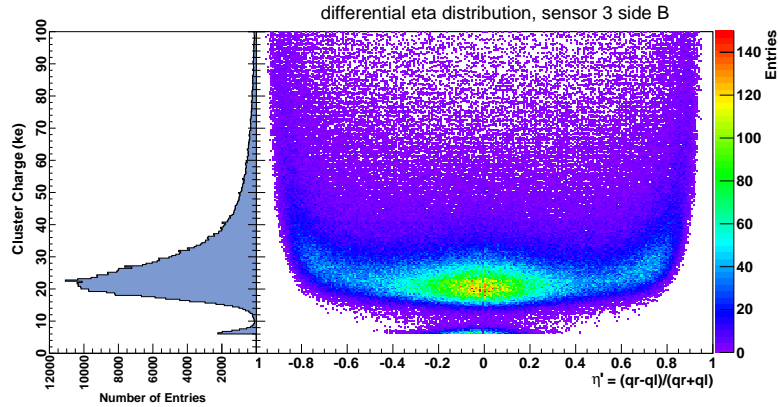
**Figure 3.23.:** Double differential distribution $\frac{\mathrm{d}^2 N}{\mathrm{d}\eta \cdot \mathrm{d}Q}$ obtained for $^{90}$Sr $\beta$ particles. On the left hand side the integrated occupancy over $\eta$ shows the energy loss straggling distribution indicating the most probable values to be found at the lower edge of the acceptance limited by the charge threshold cut.

major statistics is encountered over a region with detrimental acceptance in a relatively wide range near the principal-cell boundaries. This acceptance-incomplete distribution is compared to the full statistics without a limiting charge threshold condition in Figure 3.24(a). Values for $\eta$ from multi-strip clusters (blue area) populate the central region of the $\eta$-space within $\eta \approx 0.2 \ldots 0.8$. Single strip clusters, on the other hand, which correspond to defined values of $\eta = \{0, 1\}$ were counted separately within the measurement sample and prepended into the $\eta$-histogram equally distributed at bins corresponding to values of 0 and 1 (red area). The applied charge threshold prevented the acquisition of the very small, but non-zero charge leaking from the central strip. Those events would show $\eta$-values very close to 0 or 1, but are actually identified as $\eta = \{0, 1\}$-events, instead. As the result of a Monte-Carlo simulation, the full $\eta$-distribution without limiting threshold (green shaded area) and with the same threshold that was applied to the measurement (dotted curve) are shown for comparison in Figure 3.24(a). Although the true position of enqueued events in the acceptance-blind areas can not be corrected, the overall event count integrated over the entire $\eta$-range is kept preserved.

In fact, the preservation of accounted numbers for single-strip and multiple-strip clusters is a crucial prerequisite for a trustworthy reconstruction of the $\eta$- and charge-cloud distributions. This circumstance is directly evident from the integration in (3.43), that calculates binned values for $x$ which depend on the value of all preceding bins in the d$N$/d$\eta$-distribution. Biased or lacking statistics in the measured $\eta$-distributions lead to entirely wrong $x$-$\eta$ relations.

An example for a $x$-$\eta$-distribution reconstructed from the incomplete d$N$/d$\eta$-distribution using eqn. (3.43) is shown in Figure 3.24(b). Reasonable values can be obtained in the central region only containing hits with $\eta$-values not compromised by a charge threshold. The shown $\eta(x)$-relation reflects the ratio of charge shared with the neighbor strip to the right. A step function with the transition in the center between adjacent strips would imply no charge sharing at all. A smoothened step transition means that a charge exchange occurs proportional to the degree of smoothening. In the limiting case of a linear dependence of $\eta(x)$ from $x$ also a linear charge transfer from the left to the right strip can be expected as the impact point moves from the left toward the right boundary of the principal cell. For a configuration with every strip read out by attached amplifiers the general shape of the charge-sharing function

is[5]

$$\eta(x) = \text{erf}\left(\frac{x - x_c}{\sqrt{2}\sigma_x}\right), \quad \text{with } x_c = 0.5 \tag{3.45}$$

Several $\eta$-functions for different smearing parameters $\sigma_x$ are superimposed to the reconstructed $\eta(x)$ data points in Figure 3.24(b) for comparison. Equation (3.45) assumes a symmetric charge sharing and perpendicular trajectories of the percolating particles. Deviations from this prerequisite impose deformations on the actual $\eta(x)$-characteristic and may lead to a mismatch in above parameters $x_c$ and $\sigma_x$.



(a)

(b)

(c)

(d)
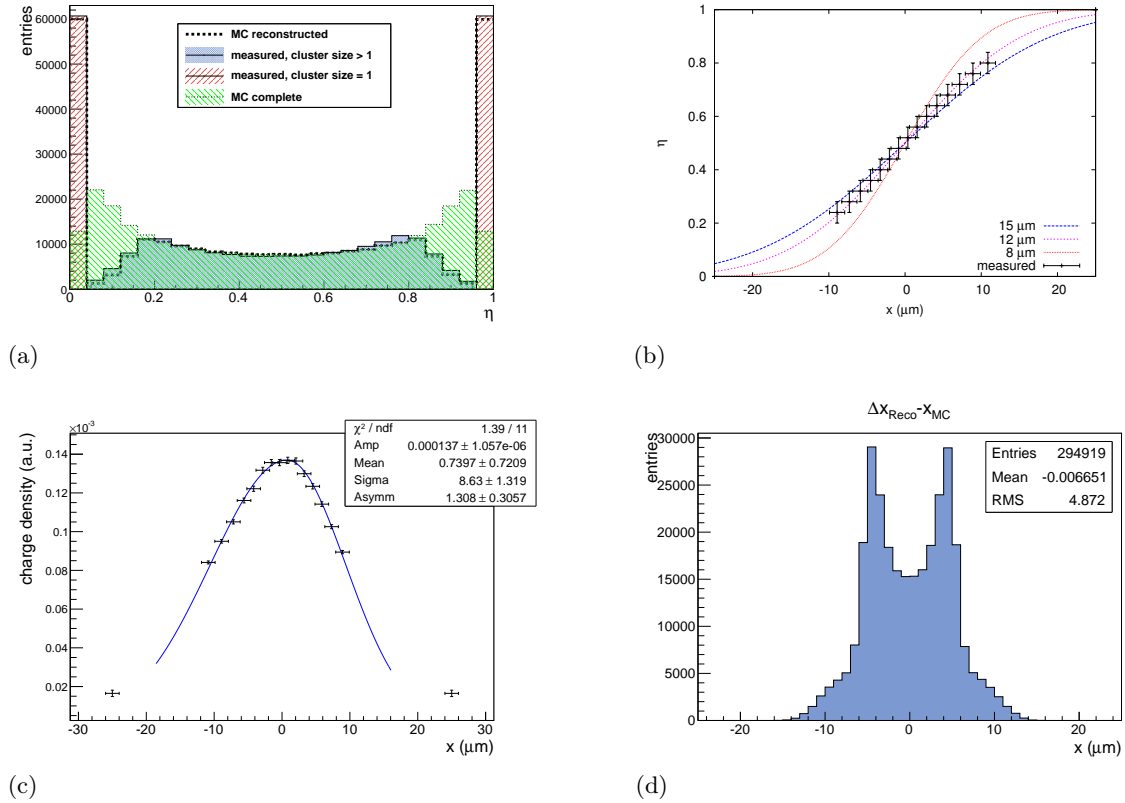
**Figure 3.24.:** Reconstruction of charge sharing characteristic from incomplete $\eta$-distribution and obtainable spacial resolution for a strip pitch of 50 μm and read-out of every channel. (a) Comparison of measured $\eta$-distributions for multi-strip clusters (blue area), separately counted single-strip hits (red areas) and according distributions reconstructed from MC simulations with the same threshold as imposed to the measurements (dotted trace) and without applied charge threshold (green area). (b) Reconstructed relation between measured $\eta$-values and the geometric hit position $x$ centered between two adjacent strips. Calculated $\eta(x)$-functions for different smearing parameters $\sigma_x$ parameterized according to eqn. (3.45) are superimposed for comparison. (c) Shape of the charge distribution at the read-out plane reconstructed from (b). (d) Difference between true and reconstructed hit coordinates $x$ for a sample of MC generated hits. The charge-sharing function was parameterized with the best match for the charge smearing parameter $\sigma_x = 9$ μm obtained from Fig. (c) assuming an SNR of 30.

Figure 3.24(c) depicts the charge-cloud distribution reconstructed according to eqn. (3.44)

---

[5] This is merely a simple model parameterization. It does not take into account local biases and anomalies originating from the complex depletion geometry within the principal cell.

for the same data sample. A slight asymmetry can be noticed again due to a marginal tilt of the sensor wrt. the particle trajectories. The *Gaussian* fitted to the retrieved data points is considered a decent approximation to the charge-cloud distribution evident at the read-out plane. Its width is estimated for the given configuration to $\sigma_x \approx 9\,\mu\text{m}$.

In order to project the influence of the charge-sharing mechanism on the spacial resolution detailed Monte-Carlo simulations were undertaken. In this process a large number of events was generated with a uniform coverage of the linear coordinate $x$ and a *Landau*-distributed energy loss charge-value $q$. Based on the $x$-coordinate, the corresponding $\eta$ - value is calculated from Equation (3.44) with the charge-cloud width supplied as parameter $\sigma_x$. Distribution of the total charge among two adjacent channels, $q_l$ for the left hand strip and $q_r$ for the right hand one is achieved through

$$\begin{aligned} q_l &= q(1 - \eta) \\ q_r &= q\eta \end{aligned} \tag{3.46}$$

(provided that $\eta$ is defined such that $\eta = [0 \dots 1[$). Both strip charges are then superimposed with *Gaussian* distributed noise (parameter $\sigma_n$). Finally, a charge threshold is applied to the resulting charge-amounts. For this last free parameter rather the signal-to-noise ratio wrt. the most probable signal value of the charge distribution (given by the *Landau*-parameters) than the ENC is chosen. All mutable parameters of the MC-simulation are reviewed in Table 3.4.

| MC-parameter | Meaning | Default Value |
|:---:|:---:|:---:|
| $\sigma_x$ | width of charge distribution at the RO plane | $9\,\mu\text{m}$ |
| MPV | most probable value of *Landau* charge distribution | $24\,\text{k}e$ |
| $w_L$ | width of *Landau* charge distribution | $12\,\text{k}e$ |
| SNR | signal-to-noise ratio wrt. MPV | 30 |
| $q_{thr}$ | charge threshold | $1\,\text{k}e$ |

**Table 3.4.:** Parameters entering the MC-simulation for charge distribution.

The Center-of-Gravity calculated with eqn. (3.38) from the simulated strip distribution is compared to the true hit position within the principal $x$-cell resulting in the true RMS resolution for a statistical sample as seen in Figure 3.24(c). The impact of the Signal-to-Noise Ratio on the resolution can be assessed from the series depicted in Figure 3.25. The worst-case resolution, i.e. the RMS-resolution arising from a uniform single-strip statistics for the given configuration and pitch $p = 50\,\mu\text{m}$ is

$$\Delta x = \frac{p}{\sqrt{12}} = 14.4\,\mu\text{m}.$$

As can be seen, the resolution improves with increasing SNR from $\Delta x = 11.8\,\mu\text{m}$ at SNR=10 down to $\Delta x = 4.5\,\mu\text{m}$ at SNR=40. The distributions are, opposing to the single-strip case, not uniform in $x$. A double-peak structure can be noticed for SNR-values of 20 and above in the central region between the electrodes which reflects the slope of the $\eta(x)$-function.

**Readout with Floating Intermediate Strips** It has been shown, that the position sensitivity of strip sensors benefits from an additional floating (passive) strip between the active strips
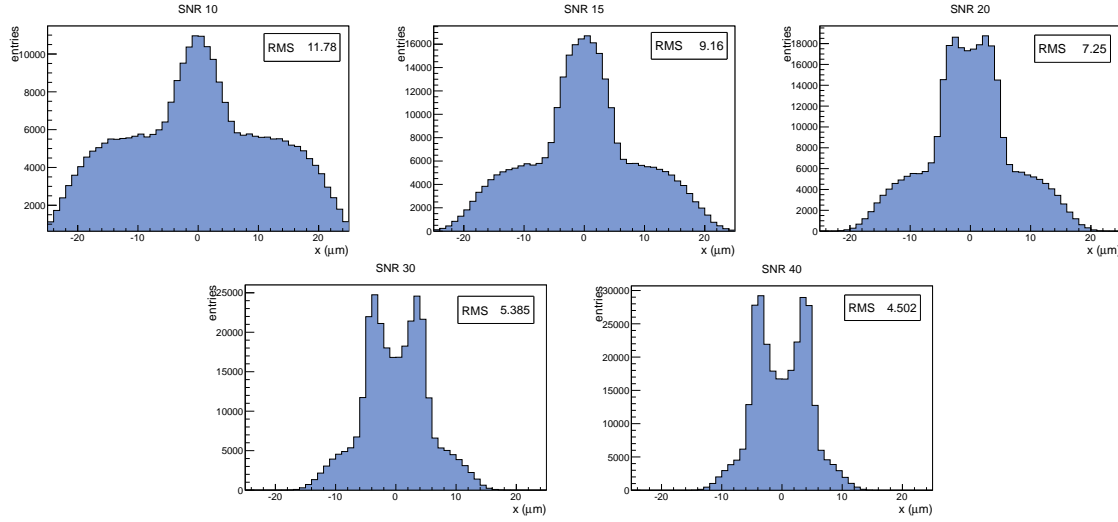
**Figure 3.25.:** Impact of SNR on position resolution.

that are connected to the read-out electronics [140, 142, 143]. The reason for this effect can be seen from the comparison of the $\eta$-functions for a sensor with identical read-out pitch but with a variable number of intermediate strips as illustrated in Figure 3.26. In the case of missing
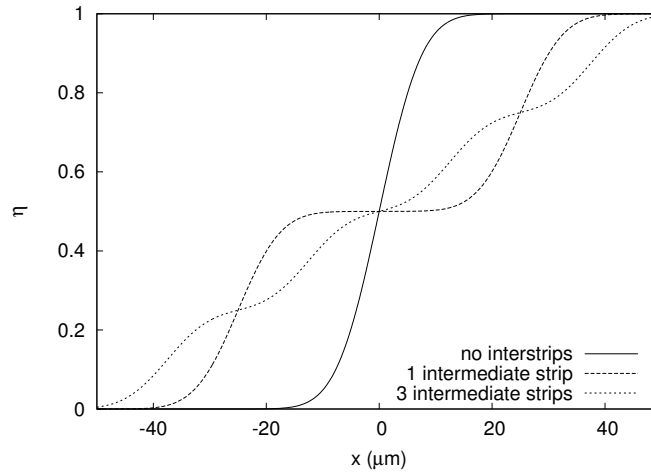


**Figure 3.26.:** Calculated $\eta$-function for a readout pitch of $100\,\mu m$ for zero, one and three intermediate strips. The width of the charge cloud is assumed to be $\sigma_{ch} = 10\,\mu m$ for all functions.

intermediate strips the mapping between the $\eta$-value as retrieved from a measured cluster and the corresponding geometrical impact point can be accomplished uniquely only in the central region exhibiting neither a plateau nor an excessively abrupt transition within the usable $\eta$ range. Near the strip electrode positions at $\eta = 0, 1$ flat mapping between both parameters can be observed in approximately 60 % of the whole range within the principal cell. This "blind" region leads to no significant charge transfer to the neighbor strip with the result that only this single strip contributes a hit information with the maximum position uncertainty of ca. $0.6 \cdot p$ [6]. With the inclusion of additional strips the mapping characteristics gets beneficial

---

[6] Depending on the SNR of the detector.

in the regions toward the readout electrodes. Already with three floating intermediate strips the translation from $\eta$ to $x$ is almost linear thus giving the best possible precision in the determination of the hit coordinate yet merely limited by the noise inherent to the charge measurement.

In Figure 3.27 the reconstructed charge-sharing characteristics are reported for an ITC01-sensor with every connected strip and every other connected strip configurations. The evaluation of the measurements conducted with this sensor revealed the existence of an additional passive intermediate strip on the $p$-side without read-out pads which is not documented by the manufacturer [144, 145]. The extracted widths of fitted charge distributions are comprehended in Table 3.5 for the different read-out configurations.

| readout configuration | nr. of intermediate strips | width of charge distribution $\sigma_G$ ( µm) |
|---|---|---|
| $p$-side, 50 µm r/o pitch | 1 | 6.4±0.3 |
| $n$-side, 50 µm r/o pitch | 0 | 8.6±1.3 |
| $p$-side, 100 µm r/o pitch | 3 | 5.9±1.4 |
| $n$-side, 100 µm r/o pitch | 1 | 10.0±0.9 |

**Table 3.5.:** Widths of charge distributions measured with different readout configurations for ITC01 sensor.

**Charge Sharing with Floating Intermediate Strips** Consider a charge $q$ collected exclusively by an intermediate strip as illustrated in Figure 3.28. Due to the capacitive coupling $c_b$ to the back side and $c_{is}$ to the left and right hand neighboring strips the charge splits into three fractions proportional to the coupling capacitances:

$$q = q \Big( \underbrace{\frac{c_b}{c_b + 2c_{is}}}_{f_{b,is}} + \underbrace{\frac{c_{is}}{c_b + 2c_{is}}}_{f_l} + \underbrace{\frac{c_{is}}{c_b + 2c_{is}}}_{f_r} \Big) \qquad (3.47)$$

$f_{b,is}$ designates the fraction of the charge which is not read out to the neighbors but is drained to the backside and thus effectively gets lost. The fractions $f_l$ and $f_r$ of the original charge couple via $c_{is}$ into the left and right neighboring read-out strips. There, the remaining charge, designated $q_l$ and $q_r$, is again split into fractions drained to the backside ($f_{b,ro}$), into the other channel neighbor ($f_{is}$) and toward the read out electronics ($f_{ro}$):

$$q_{l/r} = q_{l/r} \Big( \underbrace{\frac{c_b}{c_{ro} + c_b + \frac{1}{2}c_{is}}}_{f_{b,ro}} + \underbrace{\frac{c_{ro}}{c_{ro} + c_b + \frac{1}{2}c_{is}}}_{f_{ro}} + \underbrace{\frac{1}{2}\frac{c_{is}}{c_{ro} + c_b + \frac{1}{2}c_{is}}}_{f_{is}} \Big), \qquad (3.48)$$

where $c_{ro}$ denotes the effective read-out capacitance, formed by series connection of the sensor's coupling capacitance and the amplifier input capacitance $c_{ro} = \frac{c_{in}c_c}{c_{in}+c_c}$. The last term in eqn. (3.48) describes the leakage to the side beyond the read-out channel either to the far left or the far right side.

**no intermediate strips**



**one intermediate strip**
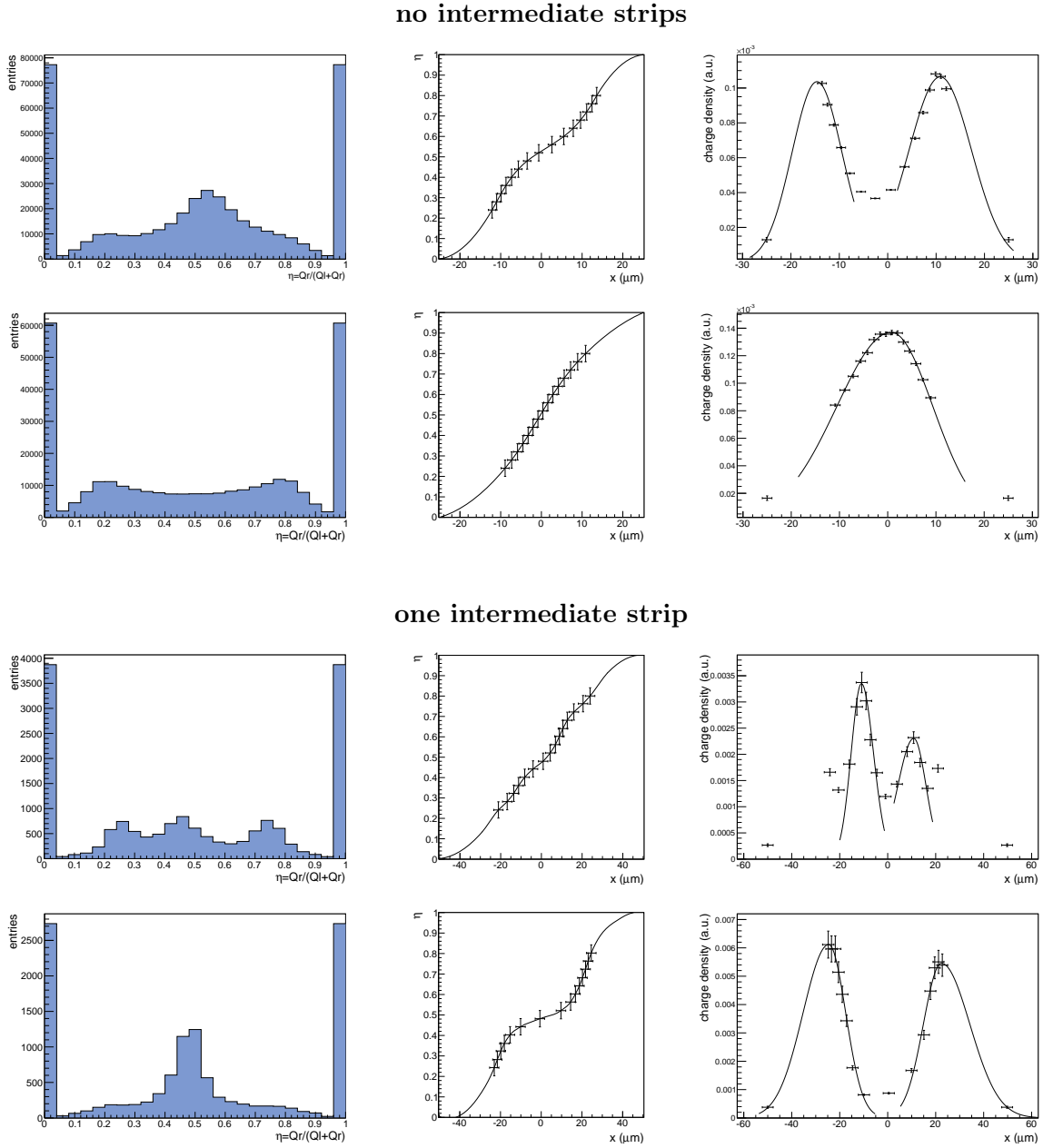


**Figure 3.27.:** $\eta$-distributions, $\eta(x)$-functions and reconstructed charge distributions measured with an ITC01-sensor. The first two rows represent the charge sharing characteristics for a read-out pitch of 50 µm without intermediate strips for the sensor $p$-side (first row) and $n$-side (second row). The two lower rows show the results for a configuration with a read-out pitch of 100 µm at the same strip pitch as above, i.e. with one unconnected strip between the read-out channels (third row: $p$-side; last row: $n$-side). The data points reconstructed for the charge-distributions are overlaid with approximate bi-*Gaussian* functions to guide the eye. From the shape of the $p$-side charge-sharing patterns the existence of an additional passive intermediate strip within the 50 µm interval reported as strip pitch by the manufacturer [144] can be suspected.
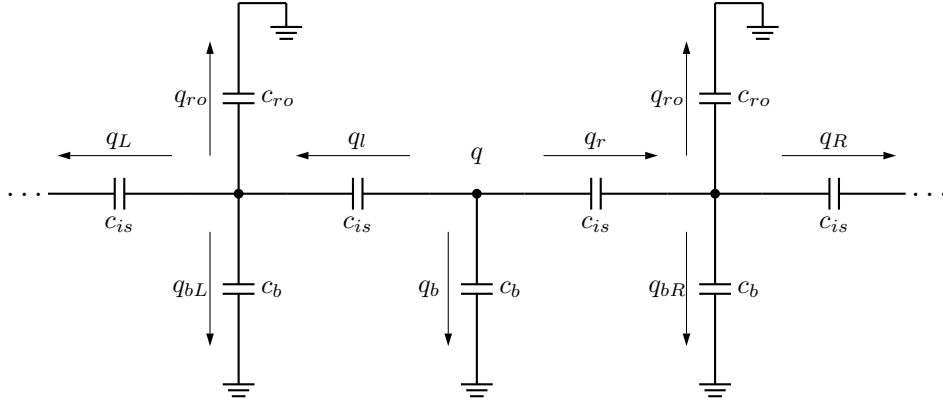
**Figure 3.28.:** Equivalent circuit schematic of a strip sensor read-out with one intermediate floating strip.

The fraction of the charge actually read out by the next pair of connected amplifiers is:

$$
\begin{aligned}
q_{ro} &= 2q f_{is} f_{ro} \\
&= q \frac{2c_{is}}{(c_b + 2c_{is})} \frac{c_{ro}}{\left(c_{ro} + c_b + \frac{1}{2}c_{is}\right)}
\end{aligned}
\tag{3.49}
$$

The charge obstructed to the readout by draining it into the backside capacitance is inevitably lost. It can be quantified with:

$$
\begin{aligned}
q_{lost} &= q \left(2 f_{is} f_{b,ro} + f_{b,is}\right) \\
&= q \left( \frac{2c_{is}}{(c_b + 2c_{is})} \frac{c_b}{\left(c_{ro} + c_b + \frac{1}{2}c_{is}\right)} + \frac{c_b}{(c_b + 2c_{is})} \right)
\end{aligned}
\tag{3.50}
$$

The remaining fraction of the collected charge is transferred to the next neighboring channels where it is subsequently split into a part read out by the corresponding amplifiers and one getting lost into $c_b$, as described above.

As can be seen from Equations (3.49) and (3.50), the efficiency of the charge collection is maximized, if following relations hold:

- $c_b \ll c_{is}$, this is true for the usual geometries considered here

- $c_{ro} \gg c_{is}$, the higher the effective read out capacitance (formed by $c_{in}$ of the amplifier and the coupling capacitance $c_c$) compared to the interstrip capacitance, the lower the charge leakage to neighboring channels. This implies also, that

- $c_{in} \gg c_c$, i.e. that the readout capacitance is approximately equal to the coupling capacitance: $c_{ro} \approx c_c$

For those favorable cases the collected charge $q_{ro}$ in (3.49) converges the incident charge $q$, while the lost and leaking charges tend to vanish.

### 3.3.7. Energy Loss Measurement

The broadening of the energy loss around the most probable value $\Delta_p$ due to statistical fluctuations was already briefly discussed in Section 2.3.2. There, a semi-empirical relation (Equation (2.18)) for the expected distribution is given as convolution of *Landau* and *Gaussian* distributions:

$$f(x, \Delta) = A \cdot f_L(x, \Delta) \circledast \mathrm{e}^{-\frac{\Delta^2}{2\sigma_G^2}} \qquad (3.51)$$

yields the probability density for a specific energy loss $\Delta$ and thickness $x$ of the material. The parameter $A$ is a normalization constant and $f_L(x, \Delta)$ is the *Landau* distribution for energy loss $\Delta$ and thickness $x$. As already pointed out, the validity of this parametrization is limited to the *Landau-Vavilov* regime, i.e. when those respective distributions exhibit no significant difference for the same parameters. This prerequisite is fulfilled for absorber thicknesses up to several hundred micrometers and for relativistic kinetic particle energies of $\beta\gamma > 1$ [121].

The width of the *Gaussian* distribution was defined in Section 2.3.2 to $\sqrt{x\delta_2}$ with the broadening parameter $\delta_2$. This approach did not take the effect of electronic noise into account, neither does (2.18). A further convolution step with a *Gaussian* having a width equivalent to the ENC of the detector system is necessary to include the noise contribution. In fact, eqn. (3.51) yields an overall width $\sigma_G$ which includes either contribution, the *Landau*-broadening and the noise which are related by

$$\sigma_G^2 = \sigma_{\mathrm{ENC}}^2 + x\delta_2 \qquad (3.52)$$

Figure 3.29 shows an energy loss distribution measured in $300\,\mu\mathrm{m}$ thick sensors of type ITC01. The most probable energy loss was first calculated for a mean energy loss obtained from the *Bethe-Bloch* relation. Afterwards, measured energy loss distributions of each individual channel was scaled such that the MPVs of all channel distributions coincide. This
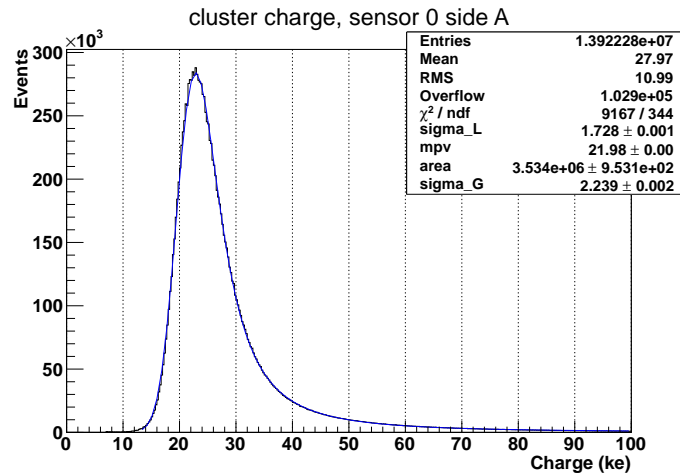


**Figure 3.29.:** Measured energy loss distribution of electrons ($\beta\gamma \approx 7{,}800$) in $300\,\mu\mathrm{m}$ silicon strip detectors (type ITC01) and best fit of semi-empirical parametrization of the straggling probability density distribution as described in the text.

absolute calibration of front-end gains is explained in more detail in Section 3.3.3. For the presented measurement, the total charge was obtained by summation over calibrated charge contributions of all strips in a cluster for each event where no discrimination regarding the

number of clusters in one event was made. The energy loss parametrization of eqn. (3.51) was fitted to the data with best-fit parameters as shown in the figure. The obtained width of the *Gaussian* distribution and electronic noise values calculated according to eqn. (3.52) for several choices of the broadening parameter $\delta_2$ are reported in Table 3.6 for 8 sensor read-out planes.

The precise choice of $\delta_2$ is controversially discussed (see e.g. [117]) and depends on the detector thickness and $\beta\gamma$ of the projectile. *Hancock et al.* gave a value of $\delta_2 = 1105 \frac{keV^2}{cm}$ for a variety of measured energy straggling functions for 300 µm thick Si detectors and a broad range of $\beta\gamma$ [119]. However, as *Bichsel* pointed out, those values were systematically too low (possibly due to an underestimation of detector noise). Instead, he gave a better estimation of $\delta_2$ based on comparisons of the energy loss functions described by *Bichsel*-functions with *Shulek*-functions of equivalent widths [117]. Since $\delta_2$, still, is hard to fix on a reliable quantity, different values for this parameter found in literature have been selected and the resulting values for $\sigma_{\mathrm{ENC}}$ were calculated in Table 3.6. Furthermore, the ENC-values for $\delta_2 = 1900 \frac{keV^2}{cm}$ were calculated which match best the ENC-values obtained independently from pedestal FIFO fluctuations as shown in Figure 3.15. This value is in close accordance to a suggested value of $\delta_2 = 1930 \frac{keV^2}{cm}$ matching several sets of empirically obtained straggling distributions (see also [117] for a discussion of a large set of collected data). The error of these reconstructed ENC-values, however, is rather large because the K-shell excitation represented by $\delta_2$ (the vectorial's triangle long cathete) dominates the overall width of the measured ionization distribution (which is the quadrature sum of the two other contributions) and thus the much smaller noise leg becomes very sensitive to small fluctuations. The difficulty inherent

| Sensor | $\sigma_G$ (keV) | $\sigma_{\mathrm{ENC}_{Sh}}$ [keV (ke)] | | |
|---|---|---|---|---|
| | | $\delta_2 = 1105\frac{keV^2}{cm}$ | $\delta_2 = 1794\frac{keV^2}{cm}$ | $\delta_2 = 1900\frac{keV^2}{cm}$ |
| 0 | 8.240(7) | 5.9 (1.6) | 3.8 (1.0) | 3.3 (0.90) |
| | 8.589(7) | 6.4 (1.7) | 4.5 (1.2) | 4.0 (1.1) |
| 1a | 7.526(7) | 4.8 (1.3) | 1.7 (0.46) | - |
| 1b | 7.975(7) | 5.5 (1.5) | 3.1 (0.85) | 2.6 (0.70) |
| 2a | 7.676(7) | 5.1 (1.4) | 2.3 (0.61) | 1.4 (0.38) |
| 2b | 7.864(7) | 5.4 (1.5) | 2.8 (0.77) | 2.2 (0.60) |
| 3 | 12.037(7) | 10.6 (2.9) | 9.5 (2.6) | 9.4 (2.5) |
| | 11.007(18) | 9.4 (3.0) | 8.2 (2.2) | 8.0 (2.2) |

**Table 3.6.:** ENC values calculated from measured fit parameters $\sigma_G$ for different values of *Shulek*-parameter $\delta_2$. A value of $\delta_2 = 1105 \frac{keV^2}{cm}$ (third column) is used by [119], whereas a more appropriate estimate of $\delta_2 = 1794\frac{keV^2}{cm}$ is given in [117] (fourth column). A choice of $\delta_2 = 1900 \frac{keV^2}{cm}$ describes best the electron data discussed in this work (last column). For ease of comparison with directly obtained ENC-values, the corresponding equivalent noise charges are stated in parentheses.

to the noise reconstruction procedure out of measured energy straggling distributions even at high statistics shows the importance of independent monitoring of the system ENC, as it was conducted utilizing the described hardware setup.

## 3.4. Two-Dimensional Pattern Reconstruction (2d Clustering)

### 3.4.1. Formulation of Algorithm

After the one dimensional clustering stage, the need for an appropriate operation rises, that assigns the obtained sets of clusters on top and bottom sides of the sensor. In general, one finds $m$ clusters on the top and $n$ clusters on the bottom after the clustering stage and cleaning up for cluster charges below a preset cluster charge threshold $Q_{thr,cl}$. The multiplicities $m$ and $n$ are not necessarily equal. Thus, one can most generally indicate two vectors of cluster charges:

$$\mathbf{t} = \begin{pmatrix} t_1 \\ t_2 \\ \vdots \\ t_{m-1} \\ t_m \end{pmatrix} , \mathbf{b} = \begin{pmatrix} b_1 \\ b_2 \\ \vdots \\ b_{n-1} \\ b_n \end{pmatrix} \tag{3.53}$$

with lengths of m and n, respectively. Each element represents the collected charges $t_i$ on the top side and $b_j$ on the bottom side (the designations $t_i$ and $b_j$ for the cluster charges have been chosen for convenience over $q_{t_i}$ and $q_{b_j}$) for the recorded clusters. The remaining cluster parameters, like position or size are not stored within the vector but are explicitly associated with the clusters' index numbers for look up after the 2d-clustering procedure. In general, one associated pair of 1d clusters can be represented in the following way:

$$(k, l) : Q = (t_k, b_l) \tag{3.54}$$

where the expression on the left hand side specifies a pair of top and bottom side clusters with indices $k$ and $l$ while $Q$ is the tuple of the combined charges of those clusters. Similarly, a series of identified cluster pairs

$$[(k_1, l_1), (k_2, l_2) \ldots (k_m, l_n)] : Q = [(t_{k_1}, b_{l_1}), (t_{k_2}, b_{l_2}) \ldots (t_{k_m}, b_{l_n})] \tag{3.55}$$

will be designated a *combination*. As will be shown later, in general a larger number of such combinations exists for a given set of top and bottom side clusters.
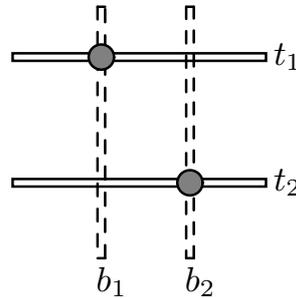


**Figure 3.30.:** Designation scheme for cluster hits in a DSSD. The top side clusters carry charges defined by $t_1$, $t_2$ up to $t_m$. Similarly, bottom side charges are labeled $b_1, b_2 \ldots b_n$. The filled circles indicate the passage of particles through the sensor.

We can now define a matrix $\mathbf{A}$, with

$$\mathbf{A} = \mathbf{t} \mathbf{1}_n^T - \mathbf{1}_m \mathbf{b}^T \tag{3.56}$$

where $\mathbf{1}_i$ is the unit vector with i elements. Each element of $\mathbf{A}$ is therefore

$$a_{i,j} = t_i - b_j. \tag{3.57}$$

Starting from the general hypothesis that the charge quantities generated by a single particle hit in a double sided sensor are correlated, this matrix represents the matching of the charges for each intersection of obtained clusters on front and back side of the sensor for one event:

$$\mathbf{A} = \begin{pmatrix} a_{1,1} & a_{2,1} & \cdots & a_{m,1} \\ a_{1,2} & a_{2,2} & \cdots & a_{m,2} \\ \vdots & & \ddots & \\ a_{1,n} & a_{2,n} & \cdots & a_{m,n} \end{pmatrix} = \begin{pmatrix} t_1 - b_1 & t_2 - b_1 & \cdots & t_m - b_1 \\ t_1 - b_2 & t_2 - b_2 & \cdots & t_m - b_2 \\ \vdots & & \ddots & \\ t_1 - b_n & t_2 - b_n & \cdots & t_m - b_n \end{pmatrix} \tag{3.58}$$

Each element represents the difference of charges from top/bottom side and is already a rough estimate, which combinations are more likely (i.e. low absolute value) and which are not. Hence a more straightforward criterion, like e.g. an a-posteriori probability for the hit combination under focus is favorable. One approach to define such a probability would be to normalize the single-hit charge difference to the total amount of charge differences contained in the entire hit pattern:

$$p_{ij} = 1 - \frac{|t_i - b_j|}{\sum\limits_{k=1}^{m} \sum\limits_{l=1}^{n} |t_k - b_l|} \tag{3.59}$$

This definition has the disadvantage that an absolute measure for the charge mismatch is not achieved. Combinations in different hit patterns may have different probabilities although the charge difference is identical. A better approach would be the calculation of the probability not in relation to the sum of charge differences in a single hit pattern, but to some absolute value to which all charge differences (of all hit patterns) are referenced. This value is practically chosen to be the noise generated fluctuation of the charges in multiples of $\sigma_{\mathrm{ENC}}$, so that for each intersection point of strips a deviation from zero in multiples of this quantile can be indicated. Then one can state a certain probability for this ratio to originate from the involved intersection points within a certain confidence level:

$$p_{ij} = 1 - \mathrm{erf}\left(\frac{|t_i - b_j|}{\sqrt{2}\Delta q}\right) = \mathrm{erfc}\left(\frac{|a_{ij}|}{\sqrt{2}\Delta q}\right) \tag{3.60}$$

The function erf in (3.60) is the error function which is closely related to the characteristic function of the *Gaussian* distribution:

$$\mathrm{erf}(x) = \frac{2}{\sqrt{\pi}} \int\limits_0^x e^{-t^2} \mathrm{d}t \tag{3.61}$$

and erfc its complementary function

$$\mathrm{erfc}(x) = 1 - \mathrm{erf}(x). \tag{3.62}$$

The argument of the error function in eqn. (3.60) is the charge difference in units of the typical charge fluctuation within the two clusters under consideration:

$$\Delta q = \sqrt{(\Delta q_t)^2 + (\Delta q_b)^2} \tag{3.63}$$

with the single cluster charge fluctuation

$$\Delta q_i = \sqrt{n_i \cdot \sigma_{\text{ENC}}^2 + 2q_{thr}^2} \tag{3.64}$$

where $q_{thr} = n_\sigma \cdot \sigma_{\text{ENC}}$ is the single strip discriminating threshold level of the front-end electronics or a hit-finding algorithm (e.g. $3\sigma_{\text{ENC}}$) and $n_i$ the strip multiplicities of cluster $i = t, b$. The rationale for the composition of eqn. (3.64) is derived by following argumentation: 1) each strip in the clusters is subject to noise fluctuation with amplitude $\sigma_{\text{ENC}}$ and 2) an additional charge amount of up to $q_{thr}$ might be cut away from both edges of each cluster, when the corresponding strips carry a fraction of the cluster charge below the discriminating threshold $q_{thr}$. All of the above mentioned errors then are propagated by summing up their square magnitudes.

Following these arguments, the total fluctuation of eqn. (3.63) of the selected cluster combination then is

$$\Delta q = \sqrt{n_t + n_b + 4n_\sigma^2} \cdot \sigma_{\text{ENC}}. \tag{3.65}$$

As becomes obvious from this expression the cluster strip multiplicities $n_t$ and $n_b$ are negligible providing that the threshold $q_{thr}$ is always chosen to exceed $2 \ldots 3\sigma_{\text{ENC}}$. As a result, the expression for the total fluctuation simplifies to

$$\Delta q = 2n_\sigma \cdot \sigma_{\text{ENC}} \tag{3.66}$$

which may be easily computed utilizing simple algorithmic operations opposing to eqn. (3.65).

Focusing again back to Equation (3.60), the square root of 2 in the denominator is derived from the normalization in that way, that the probability at a given charge difference equals the quantiles of the normal distribution. If the charge difference for example amounts to $\Delta q = 6\sigma_{\text{ENC}}$, then the probability is equivalent to the $1\sigma$-confidence level of the normal distribution, or $68.3\,\%$ provided a discriminator threshold of $3\sigma_{\text{ENC}}$. Since we are interested in the probability that yields the area outside of the confidence interval, the complement to 1 is computed which results for the given case above in a probability of $31.7\,\%$ that the hit was reconstructed correctly in this combination.

Finally, the full matrix of probabilities can be built up utilizing the computation of each element in the way shown above:

$$\mathbf{P} = \begin{pmatrix} p_{11} & p_{21} & \cdots & p_{m1} \\ p_{12} & p_{22} & \cdots & p_{m2} \\ \vdots & & \ddots & \\ p_{1n} & p_{2n} & \cdots & p_{mn} \end{pmatrix} \tag{3.67}$$

In order to identify the overall probability $P$ of one set of possible hit combinations, one reduces the hit matrix systematically by developing around one pivot element and multiplying its value with the total probability of one possible branch of its complementary sub-matrix. The expression

$$P = \begin{vmatrix} p_{1,1} & \rule{3cm}{0.4pt} \\[2pt] & \underbrace{\begin{vmatrix} p_{2,2} & \cdots & p_{m,2} \\ \vdots & \ddots & \\ p_{2,n} & \cdots & p_{m,n} \end{vmatrix}}_{\mathbf{P}_{1,1}} \end{vmatrix} = p_{1,1} \, |\mathbf{P}_{1,1}| \tag{3.68}$$

for example equals the probability when clusters (1,1) are chosen to combine while the complementary sub-matrix $\mathbf{P}_{1,1}$ itself decomposes in the same way by developing around one of its elements and multiplying it with the probability of the remaining complementary and so on. The operation $|\ldots|$ in (3.68) indicates the multiplication of the matrix elements along one possible chain of pivot elements. This procedure is continued iteratively until the remaining matrix consists either of a single vector with one row or one column or of a single element. The latter case is evaluated by simply multiplying the single probability with the chain of probabilities collected up to this point for this combination. The first case requires some additional considerations about the evaluation of the probability since obviously either one hit was detected while a corresponding one at the opposite side was not, or one hit was generated erroneously by e.g. noise fluctuations. For either case an appropriate treatment of the hit probabilities needs to be foreseen.
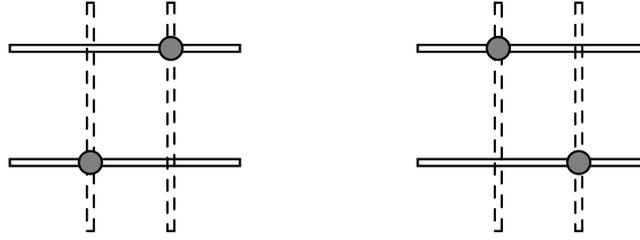


**Figure 3.31.:** Illustration of the associative ambiguities in the presence of multiple cluster hits. The filled circles indicate the passage of real particles through the sensor, while the remaining crossings correspond to virtual detected cluster combinations (fake hits). Both of the shown combinations are exclusive and have to be further judged whether they originate from the real particle crossings by means of charge difference.

The procedure described above identifies exactly **one** chain of combinations with an associated probability. Choosing a different pivot element in any stage of this chain alters the whole combination. Each of those possible alterations results in different exclusive combinations. The number of possible combinations up to the point where the remaining sub-matrix is a single vector or a scalar value is the product of the combinations to choose $n \times m$ sub-matrices of size $(m-1) \times (n-1)$ with the number of combinations to choose in the latter ones (m-1)×(n-1) sub-matrices of size $(m-2) \times (n-2)$ and so on, or more general

$$N^{<m,n>} = \prod_{i=2}^{\min(m,n)} i(i+d) \text{ , with } d = |m-n|. \tag{3.69}$$

Only if $n=m$, i.e. the hit matrix has quadratic shape, the number of possibilities reduces by a factor of two, since in a 2×2 matrix the number of independent combinations is two ([(1,1)(2,2)] or [(1,2)(2,1)]) instead of four (see Figure 3.31).

In case the remainder sub-matrix is a row or column vector (which means unequal hit counts on both sides), two scenarios arise:

1. if $m=1$, i.e. the remaining matrix is a column vector, one strip on the top side was multiply hit (consistently one strip was multiply hit on the back side, if $n=1$ or the sub-matrix is a row vector).

2. one or more strips did not obtain the charge content from a particle hit but generated uncorrelated noise hits.

**1) degenerate strips**    The first case implies that the charges of two or more particles summed up in a single strip on one side while a correlated amount of these charges is contained in separate hits on the opposite sensor side (refer to Figure 3.32).
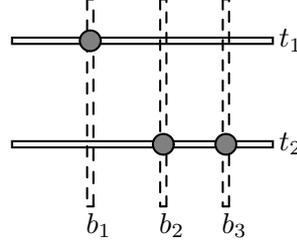


**Figure 3.32.:** Illustrative example for an ambiguous degenerate hit pattern. The in this case degenerate top side cluster $t_2$ either carries the sum of charges $b_2$ and $b_3$, or alternatively, one of the latter bottom side clusters is noise generated. For each hypothesis a cluster combinational probability can be calculated in order to select the best matching case (see text).

Consider e.g. the following simplest case of a hit matrix with unequal hit counts on both sensor sides:

$$\mathbf{A} = \left( \begin{array}{c} a_{11} \\ a_{12} \end{array} \right) = \left( \begin{array}{c} t_1 - b_1 \\ t_1 - b_2 \end{array} \right) \tag{3.70}$$

Here, one hit was registered on the top side and two hits on the bottom side of the sensor. As a first step, it is assumed that a degenerate strip absorbed two hits on the top side, i.e. two physical hits were registered. The matrix $\mathbf{A}$ in (3.70) needs therefore to be transformed into a well shaped quadratic form by reconstructing two separate hit quantities out of the degenerate strip. This is done by replacing the single strip charge $t_1$ by newly defined ones $t'_1$ and $t'_2$ with the following relation:

$$t_1 \rightarrow \left\{ \begin{array}{l} t'_1 = t_1 - b_2 \\ t'_2 = t_1 - b_1 \end{array} \right. \tag{3.71}$$

The new charge quantity $t'_i$ is estimated from the original top charge and the bottom charges since it is assumed that $t_1$ ideally equals the sum of all bottom charges. The bottom side charges are not degenerate, so the transformation behaves neutral:

$$\begin{array}{l} b'_1 = b_1 \\ b'_2 = b_2 \end{array} \tag{3.72}$$

With these transformations the hit matrix may be rewritten into a quadratic form:

$$\mathbf{A} \rightarrow \mathbf{A}' = \left( \begin{array}{cc} a'_{11} & a'_{21} \\ a'_{12} & a'_{22} \end{array} \right) = \left( \begin{array}{cc} t'_1 - b_1 & t'_2 - b_1 \\ t'_1 - b_2 & t'_2 - b_2 \end{array} \right) \tag{3.73}$$

and with (3.71) becomes

$$\mathbf{A}' = \left( \begin{array}{cc} t_1 - b_1 - b_2 & t_1 - 2b_1 \\ t_1 - 2b_2 & t_1 - b_1 - b_2 \end{array} \right). \tag{3.74}$$

Note, that the main diagonal elements are identical. Therefore the leftmost upper matrix element reflects the deviation from the hypothesis, that the degenerate strip $t_1$ absorbed both the charges of the single strips $b_1$ and $b_2$. The lower its absolute value, the better the matching of the single top strip charge and the charge sum of the two back side strips. The matrix elements on the secondary diagonal represent the distribution of the charge on both back side strips and thus are a more appropriate representation of the charge difference considering the double hit hypothesis. The reconstructed combination may then be represented in the following way:

$$[(1,1)(1,2)] : Q = \left[ (t_1', b_1)(t_2', b_2) \right] \tag{3.75}$$

where $Q$ is the vector of associated pairs of cluster charges. The probability for this (1,2)-degenerate hit pattern can be calculated using (3.66):

$$p^{<1,2>} = \mathrm{erfc}\left( \frac{|t_1 - b_1 - b_2|}{\sqrt{8} n_\sigma \sigma_{\mathrm{ENC}}} \right). \tag{3.76}$$

Here, the nominator of the argument of the error function represents the total charge difference of the whole pattern according to (3.60).

**2) noise hits**   The second case assumes an erroneous generation of charge due to noise fluctuations in one ore more strips. Thus, the hit pattern (3.70) has to be treated in a different way and the probability for its occurrence derived by a different approach.

Assume again the simple degenerate (1,2)-hit pattern from (3.70), but this time one of the two bottom side hits was noise generated. Then the hit matrix decomposes in the following way:

$$\mathbf{A} = \begin{pmatrix} a_{11} \\ a_{12} \end{pmatrix} \rightarrow \text{ either } [(1,1)] \text{ or } [(1,2)]. \tag{3.77}$$

Opposing to the degenerate case, where only exactly one combination was found, here a set of two exclusive combinations is provided:

$$\begin{aligned} [(1,1)] : \quad & Q = (t_1, b_1) \\ \text{or} & \\ [(1,2)] : \quad & Q = (t_1, b_2) \end{aligned} \tag{3.78}$$

Either one of the two combinations may be the correct one since one of the two bottom side hits is fake (as is explicitly assumed). The probability for the occurrence of either combination then is simply the probability matrix element $p_{11}$ or $p_{12}$, respectively.

Equations (3.70) through (3.76) cover the case of a (1,2)-hit pattern. To treat the more general class of (1,$n$)-patterns, behold the following hit matrices:

$$\mathbf{A} = \begin{pmatrix} a_{1,1} \\ a_{1,2} \\ \vdots \\ a_{1,n-1} \\ a_{1,n} \end{pmatrix} = \begin{pmatrix} t_1 - b_1 \\ t_1 - b_2 \\ \vdots \\ t_1 - b_{n-1} \\ t_1 - b_n \end{pmatrix} \tag{3.79}$$

The transformation of the top side charges $t_i'$ is performed similar to (3.71):

$$t_1 \rightarrow t_i' = t_1 - \sum_{j=1}^{n} b_j (1 - \delta_{ij}) \tag{3.80}$$

where $\delta_{ij}$ is the *Kronecker* symbol. The representation of the reconstructed combination is

$$[(1,1)(1,2)\cdots(1,n)] : Q = \left[(t'_1,b_1)(t'_2,b_2)\cdots(t'_n,b_n)\right] \tag{3.81}$$

The probability for such a $(1,n)$-degenerate hit pattern can then be calculated in the generalization of (3.76) with

$$p^{<1,n>} = 1 - \mathrm{erf}\left(\frac{\left|t_1 - \sum\limits_{i=1}^{n} b'_i\right|}{\sqrt{8}n_\sigma\sigma_{\mathrm{ENC}}}\right). \tag{3.82}$$

On the other hand, (3.79) may contain a fake entry due to noise or EMI pick-up. Therefore, a new sub vector of the original hit vector might yield a better matching probability, ignoring one entry $j$ at the bottom side that is suspected to be of noisy origin:

$$\mathbf{A} = \begin{pmatrix} a_{1,1} \\ a_{1,2} \\ \vdots \\ a_{1,n-1} \\ a_{1,n} \end{pmatrix} \rightarrow \mathbf{A_j} = \begin{pmatrix} a_{1,1} \\ a_{1,2} \\ \vdots \\ a_{1,j-1} \\ a_{1,j+1} \\ \vdots \\ a_{1,n-1} \\ a_{1,n} \end{pmatrix} \tag{3.83}$$

The new hit vector $\mathbf{A_j}$ is the adjunct to $\mathbf{A}$, i.e. it is created by deletion of the $j$-th element and is again a hit pattern with $n$-1 degenerate entries. Thus the same procedure applies for its analysis as described above for the general case of $(1,n)$-degenerate patterns. The occurrence of the hit vectors $\mathbf{A}$ and $\mathbf{A_j}$ are exclusive and distinct solely by the fact that the $j$-th element is considered to be part of the hit pattern or not. This probability of the occurrence of $\mathbf{A_j}$ may be calculated by (3.82) and can be compared again with the probability obtained by deletion of another of its elements. In the end of this procedure one obtains a table of combinations which includes all combinatorial possibilities starting with the full $(1,n)$-degenerate pattern followed by all $n$-1 combinations obtained by deletion of one single (suspected fake) element descending down to all possible combinations containing $n$-1 fake entries but only one assigned top/bottom hit pair. This is exemplified in Table 3.7 for a $(1,3)$-hit pattern. First the combinatorial probability is calculated that describes the matching of the whole combination as observed. Next step is the decomposition of the initial hit vector by sequential deletion of one of the three elements. The associated probability for all possible three combinations can be calculated according to the formula for $p^{<1,2>}$ (eqn. (3.76)). Finally, all three single elements are assumed to be independent and exclusive hits rejecting the remaining 2 elements as noise entries. The single intersection probabilities specify the appropriate combinatorial probabilities of those combinations directly. For each obtained combination a probability according to (3.76), (3.82) or (3.60) can be calculated that allows the selection of the most probable combination.

The total number of combinations for a given $(1,n)$-hit pattern is the sum of all possible combinations to find subsets of size $1,2\ldots n$ in the original set with size $n$, i.e.

$$N^{<1,n>} = \sum_{i=1}^{n}\binom{n}{i} = 2^n - 1. \tag{3.84}$$

| Nr. | Combination | Probability Computation |
|---|---|---|
| 1 | (1,1)(1,2)(1,3) | (3.82) applied on $\mathbf{A}$ |
| 2 | (1,2)(1,3) | (3.76) applied on $\mathbf{A_1}$ |
| 3 | (1,1)(1,3) | (3.76) applied on $\mathbf{A_2}$ |
| 4 | (1,1)(1,2) | (3.76) applied on $\mathbf{A_3}$ |
| 5 | (1,1) | (3.60) applied on $a_{1,1}$ |
| 6 | (1,2) | (3.60) applied on $a_{1,2}$ |
| 7 | (1,3) | (3.60) applied on $a_{1,3}$ |

**Table 3.7.:** Possible combinations for a (1,3)-degenerate hit pattern with the hit matrix $\mathbf{A} = \begin{pmatrix} a_{0,0} \\ a_{0,1} \\ a_{0,2} \end{pmatrix}$. The applicable rules for the computation of the probability for the occurrence of the corresponding combination are explained in the text.

Taking now into account that in general a hit matrix with arbitrary shape has $\min(m, n)$ independent elements, which are likely to be created by a top/bottom-side hit pair, and $|m-n|$ degenerate elements, which are either caused by charge deposition in same strips or by fake entries, the total number of possible combinations according to (3.69) and (3.84) amounts to:

$$N_{tot}^{<m,n>} = N^{<m,n>} N^{<1,n>} \tag{3.85}$$

Table 3.8 gives an overview of the number of possible combinations for various sizes of hit matrices. This may be consulted as an estimate of the expected computational effort connected herewith as well.

$\max(m,n) \rightarrow$

| $\min(m,n) \downarrow$ | 1 | 2 | 3 | 4 | 5 | 6 | 7 |
|---|---|---|---|---|---|---|---|
| 1 | 1 | 3 | 7 | 15 | 31 | 63 | 127 |
| 2 | | 2 | 18 | 56 | 150 | 372 | 882 |
| 3 | | | 18 | 216 | 840 | 2,700 | 7,812 |
| 4 | | | | 288 | 4,320 | 20,160 | 35,280 |
| 5 | | | | | 7,200 | 129,600 | 705,600 |
| 6 | | | | | | 259,200 | 5,443,200 |
| 7 | | | | | | | 12,700,800 |

**Table 3.8.:** Number of possible combinations for hit patterns of cluster multiplicities $m$ and $n$. Since this matrix is symmetric, the greater of either value selects the column while the other one picks the corresponding row.

## 3.4.2. Application to Measurements

During a general detector test beam run of the *B1*-Experiment at the *ELSA*[7]-Accelerator in Bonn in the year 2010 a set of data was taken with a setup of two DSSDs under test. The configuration of the measurement setup is reviewed in Figure 3.33. A photo of the detectors is shown in Figure 3.34. A small ($\approx 1\,\text{mm}$) lead converter is placed in the high energetic photon beam leading to predominant production of electron-positron pairs with a forward-boosted opening angle $\Theta$ which depends on the energy of the incident photon. The silicon sensors

---

[7] Elektronen-Stretcher Anlage.
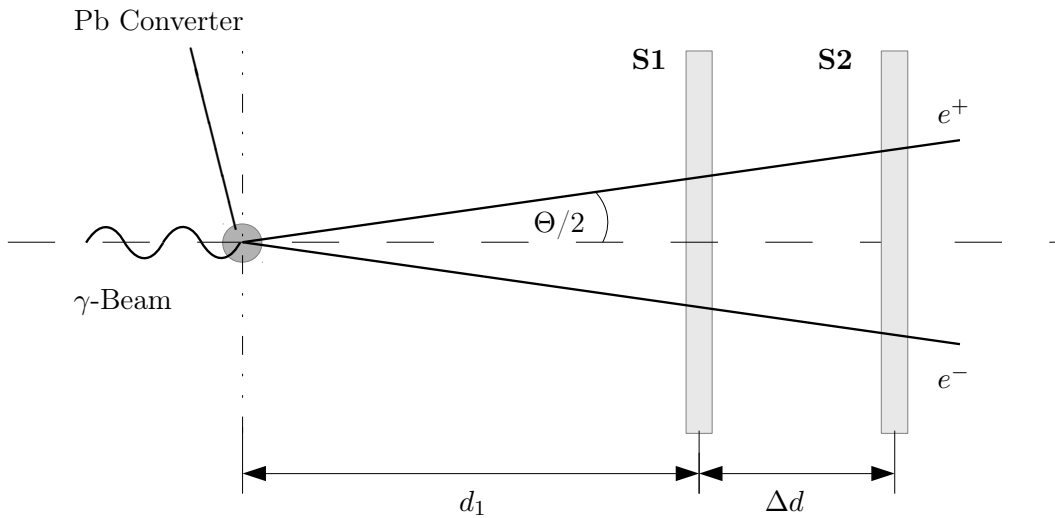
**Figure 3.33.:** *B1* beam test setup.

are located at distances of $d_1$ and $d_1 + \Delta d$ in downstream direction behind the converter. Additionally, the scintillator bars of the photon tagging device were tapped. This facility is positioned behind the primary bremsstrahlung radiator, where the accelerated electrons of defined energy produce the utilized hard bremsstrahlung photons, while the remaining electrons are deflected by a dipole magnet into different angles depending on the electron energy (and thus on the photon energy as well). A comb of scintillating detectors read out by PMTs along the periphery of the magnet (see Figure 3.40) detects those electrons allowing a determination of the gamma energy in binned ranges. The discriminated tagger-bar outputs are persisted together with the data from the DSSD sensor modules event-wise to disk. In this way the center of mass energy of every produced lepton pair can be reconstructed. The
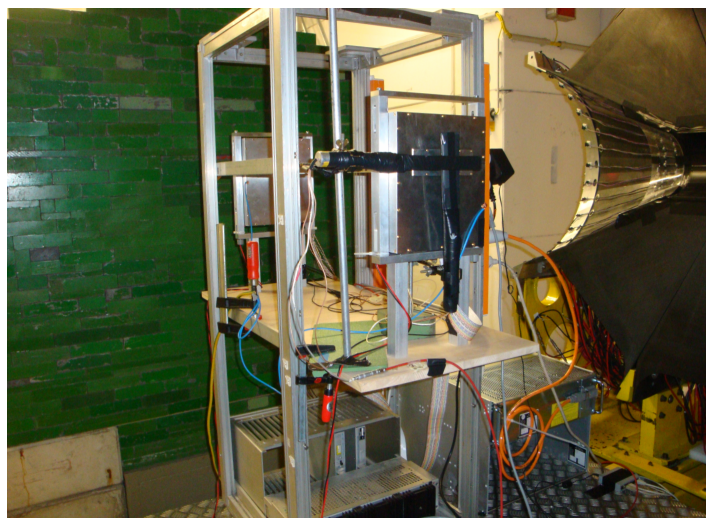


**Figure 3.34.:** Configuration of detectors during the 2010 *B1* test-beam run.

registered hit distribution in the two sensors separated by 80 cm is presented in Figure 3.35(a)

where every registered 1d cluster represents a single entry on a linear scale of successive channels. Each set of 768 of these channels belong to one separate sensor with the first subset of 384 channels connected to the top side and the latter 384 connected to the bottom side. Fluctuations of pedestals are logged during the data acquisition period as noise values represented channel-wise in Figure 3.35(b). A comprehensive statistics of the reconstructed



(a)



(b)



(c)
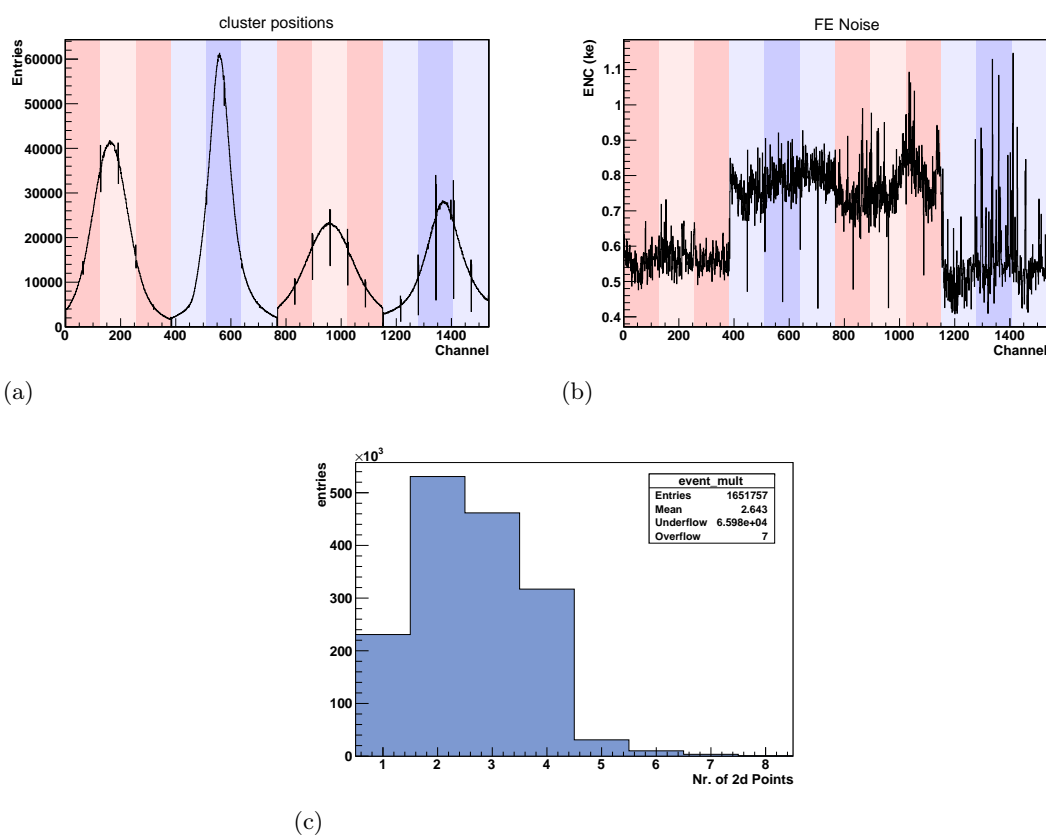
**Figure 3.35.:** (a) Histogram of detected 1d clusters in dependence of position on a linear scale where the first 768 channels are associated with the first sensor and the latter 768 channels with the second sensor. Each subgroup of 384 channels represents one side of a sensor. (b) Distribution of front-end noise derived by tracking the standard deviation of the pedestal values. (c) Multiplicity of reconstructed 2d hit points per event in both sensors.

hits of both sensors and an example of the energy loss distribution as well as a correlation of top and bottom side charge contents of a single sensor is summarized in Figure 3.36.

(a)



(b)



(c)



(d)
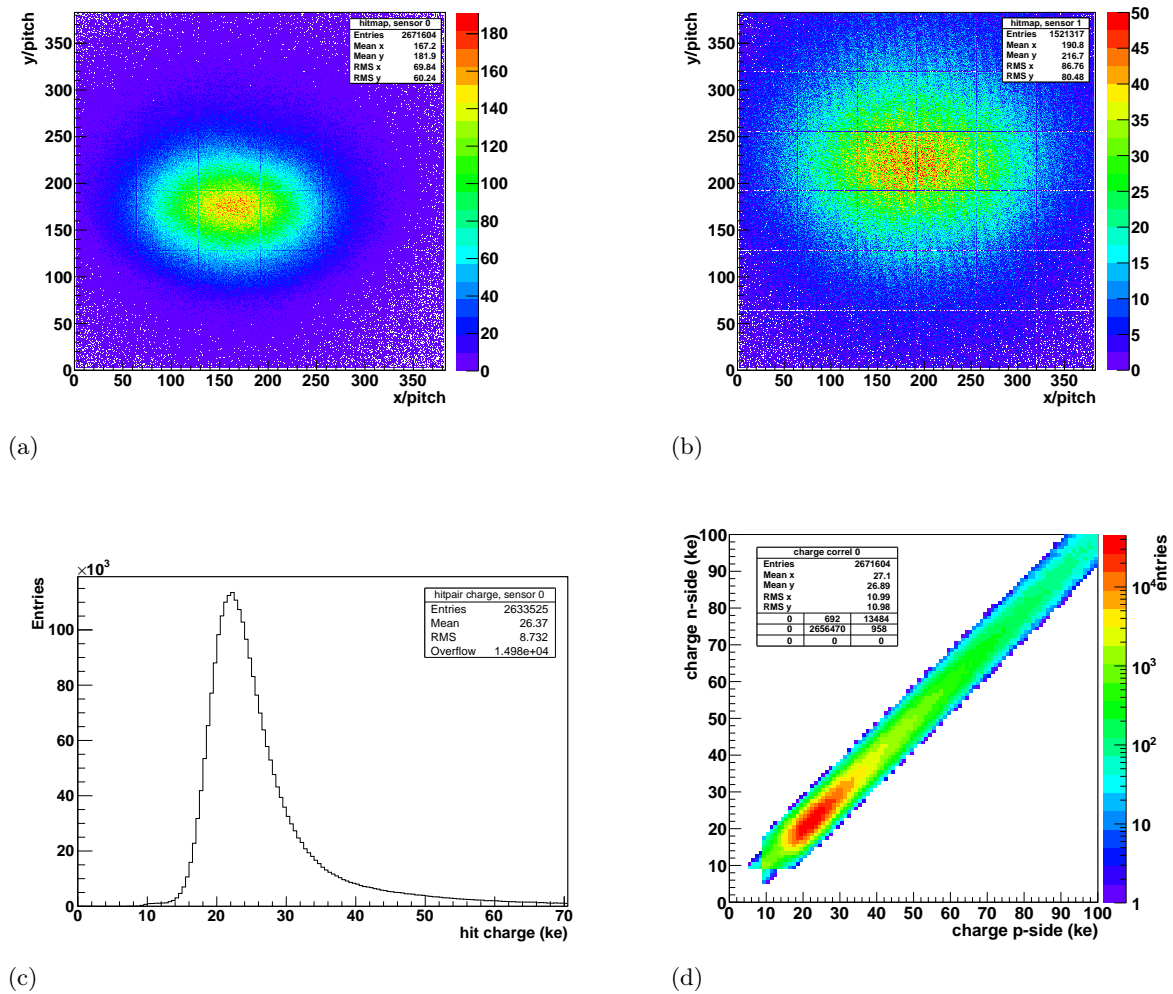
**Figure 3.36.:** Maps of registered hits of two sensors placed at 80 cm distance with respect to each other (a),(b); distribution of the registered charge content following a Landau energy loss straggling distribution (c); correlation of top and bottom side charge contents of a single sensor (d).

The collected data measured with this setup, although initially conceived for the mere purpose of hardware detector verification, was chosen for evaluation of the discussed 2d clustering algorithm due to the distinctive signature of the detected events. For a triggered readout of the silicon sensor system, a typical hit pattern should comprise two hit points per sensor in the majority of events. In practice, the registered hit point multiplicity is well below this expectation as seen in Figure 3.35(c). Reasons for this mismatch are:

- merging of two clusters in the first sensor at very small opening angles $\Theta < \Theta_{min}$
- loss of one or two hit points in the rear sensor due to excessive opening angles $\Theta > \Theta_{max}$
- limited sensor detection efficiency

Each combination is reconstructed following the algorithm given above with the associated hit-pair mapping probability. Distributions of this probability for one analyzed data set for a well calibrated sensor and a sensor with mismatching signal gains of the two sensor sides are shown in Figures 3.37(a) and 3.37(b), respectively. The high peaks at vanishing probabilities are due to mismatching hits on the two sensor sides which are not caused coherently and thus are not assignable at all. The angular correlation (Figure 3.37(c)) shows the dependence of the azimuthal $\phi$-angle of the registered particle pair (with respect to the horizontal) in the first sensor from the $\phi$-angle registered in the second sensor. Assuming, that the four hit points were caused by a lepton pair on divergent trajectories, one expects a constant azimuthal angle independent of $\Theta$ or the position of the sensors. Thus a strong correlation between the azimuthal angles $\phi_1$ and $\phi_2$, measured on both sensors, should exist. This fact is evident as "rising" diagonal (from bottom left to top right) in Figure 3.37(c). However, a secondary, anti-correlated diagonal is visible as well in this plot which accounts for erroneously correlated cluster pairs, i.e. picking the wrong cluster combination as illustrated in Figure 3.31 on one of the sensors. For these combinations, the described algorithm based on the charge correlation of both sensor sides fails because these hit pairs are indistinguishable due to identical charge content or their charge differences are inside the error corridor set by $\Delta q$ as described by eqn. (3.66).

The efficiency of correctly assigned tracks can be further, however yet not significantly, raised by narrowing this corridor through increasing the level of minimum probability demanded for reconstructed combinations. Thus, the ratio of correctly assigned hit-pairs over fake pairs improves slightly (see Figure 3.37(d)) at the downside of reduced overall reconstruction efficiency (which shall be defined as the number of reconstructed hit points at the asserted cut level divided by the number of reconstructed hit points without imposed probability cut, or $\epsilon = \dfrac{N(p_{cut})}{N_0}$) as seen in Figure 3.37(e). The impact of a variation in this parameter can be observed as well in the set of combined cluster charges for a cut-level of $0\,\%$, i.e. the full extent of calculated combinations (Figure 3.38(a)) vs. an imposed cut allowing combinations better than $10\,\%$ to be accepted (Figure 3.38(b)).

The up to this point presented results apply to the evaluation of non-degenerate (2,2)-hit combinations only. The efficiency of the reconstruction algorithm for these cases is naturally limited since the distinction between several combinations depends purely on differing charge contents. To further extend the range of reconstruction, additionally degenerate combinations (primarily (1,2) and (2,1)-shapes) were analyzed. These combinations correspond to hit-pairs found at $\phi$-angles of $0°$ and $90°$ (corresponding to the strip directions) that would be lost in a simple charge correlation algorithm due to the mismatching initial signature of the 1d clusters. Table 3.9 holds the statistics of extracted hits corresponding to the (1,2)-signature. A number

(a)



(b)



(c)



(d)



(e)
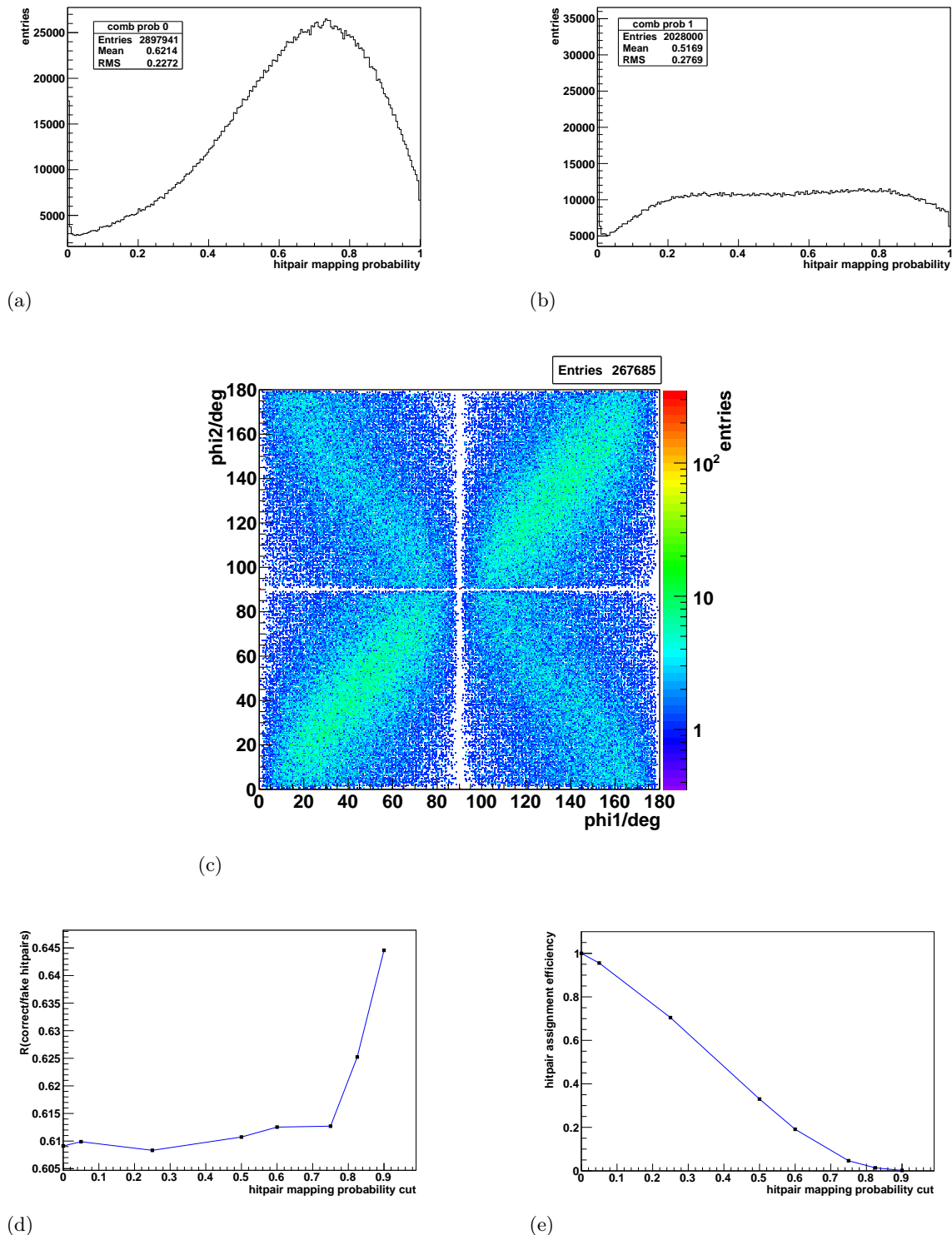
**Figure 3.37.:** Hit-pair mapping probability for all encountered (2,2)-combinations during the 2d clustering analysis of one B1 test data set. The distribution (a) shows a clear peak at higher probabilities for a carefully calibrated sensor with homogeneous gain and offset distributions and (b) a rather broad spread of probabilities for a sensor which yields high noise levels of the hits from one of the two sides. Reconstructed azimuthal $\phi$-angles on both sensors are correlated in (c) in order to visualize the impact of correctly mapped hit-pair combinations (rising diagonal) vs. fake pairs (falling diagonal). By raising the minimum hit mapping probability for reconstructed combinations the distinction between correctly assigned and fake hit-pairs improves somewhat above very strict cut levels of 75 % (d) but at the expense of a poorer overall reconstruction efficiency (e).

(a)                                                                    (b)
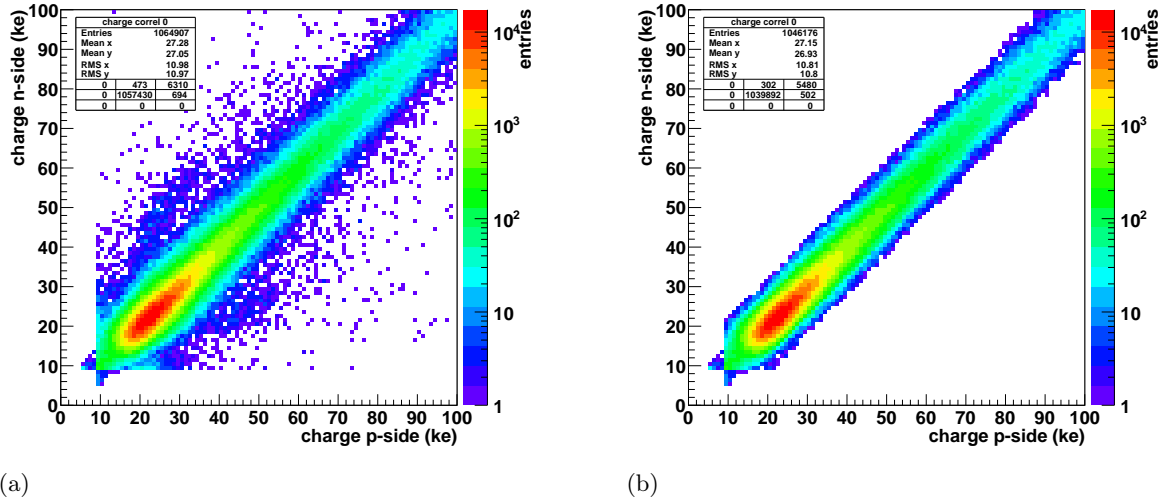
**Figure 3.38.:** Correlation of the top and bottom side charges for each registered event without imposed cut in hit mapping probability (a) and with a cut selecting hit-pairs with 10 % and better mapping probability (b).

| $\phi_1(°)$ | $\phi_2(°)$ | no. of hit-pairs | | fraction | |
|---|---|---|---|---|---|
| 0 | 0 | 3142 | } 6459 | 75.7 % | correctly assigned |
| 90 | 90 | 3317 | | | |
| 90 | 0 | 1129 | } 2070 | 24.3 % | fake hit-pairs |
| 0 | 90 | 941 | | | |

**Table 3.9.:** Statistics of (1,2)-shaped hit combinations for point pairs with horizontal and vertical connection lines between the points on a sensor retrieved from a dataset analyzed for two hit-points per sensor. These hit pairs correspond to $\phi$-angles of 0° and 90°, respectively. The majority of recovered combinations shows identical $\phi$-angles in both sensors and are therefore considered correctly assigned. A total of 260 k hits were processed.

of 8529 combinations additional to the already reconstructed (2,2)-combinations are retrieved out of ca. 260,000 total combinations. This fraction ($\approx 3\%$) plausibly approximately matches the number of missing hits in the acceptance-blind regions along an approximately one degree wide strip around 0° and 90° in Figure 3.37(c). From those additionally reconstructed combinations 76 % proved to be assigned correctly, the remaining 24 % are fake combinations either reconstructed wrongly by initially mismatching charge content or by erroneously assigning noisy clusters to detected (1,1)-combinations.

This set of cleanly identified hit combinations resulting in exactly two hit points per sensor now serves as base for reconstruction of particle tracks. As a first benchmark the opening angles of the suspected tracks of the produced electron-positron pairs are probed by measuring the distances of the hit point pairs found in both sensors. A raw distribution of this angle $\Theta$ is shown in Figure 3.39(a). Due to the limited sensor size of $2\times2\,\mathrm{cm}^2$ and the fact that single clusters should be separated by at least one unaffected strip, the acceptance of the detector system for different $\Theta$-values is not homogeneous and strongly dependent on the position from which the tracks emanated. Therefore, the acceptance in the $\Theta$-domain has been calculated

(a)



(b)



(c)



(d)



(e)



(f)
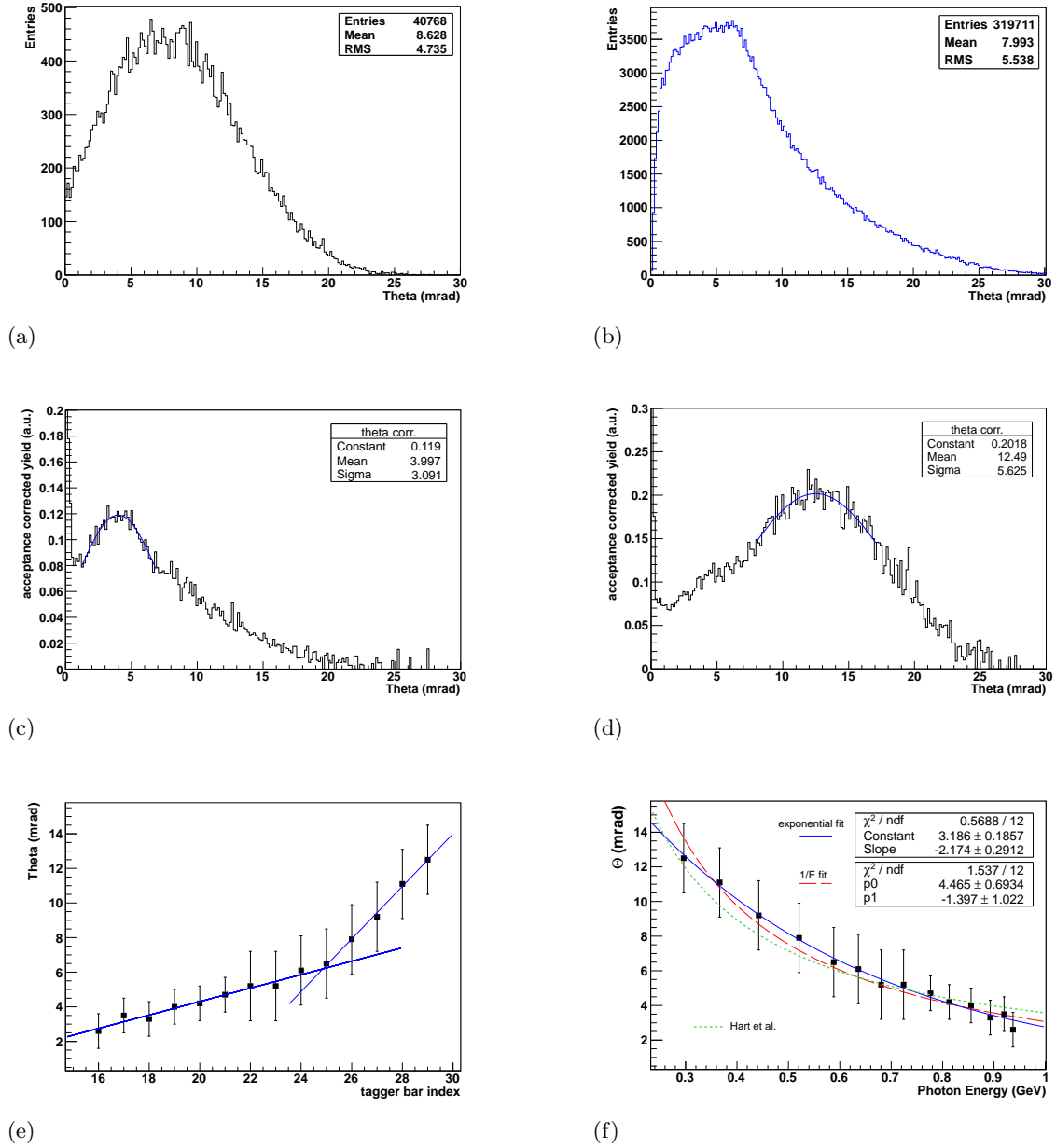
**Figure 3.39.:** Histogram of calculated Θ-angles of registered tracks of paired leptons for the lowest $\gamma$-energy detectable (a), acceptance of the detector system for those tracks obtained from a Monte–Carlo-Simulation with a uniform occupancy of tracks with respect to Θ, $\phi$ and the vertex point $z$ (b). The acceptance corrected distributions of the measured Θ-angles are shown for the highest (c) and the lowest $\gamma$-energies (d) detected (the tagger bars corresponding to the lowest and the highest scattered electron energies, respectively). The measured tracks' Θ-angles corresponding to the electron energies detected by each of the tagger bars are collected in (e). The change of slopes between tagger bar indices № 24 and № 26 can be explained by the geometric configuration of the tagger bar ladder shown in Figure 3.40. Calibration of the tagger bar indices with the corresponding $\gamma$-energies finally renders a more natural representation of the lepton pair opening angle in dependence of the photon energy (f). The applied fits are explained in the text.

by a Monte-Carlo simulation through propagating a number of particle-pairs with a uniform random spread in vertex position $z$, azimuthal angle $\phi$ and the opening angle $\Theta$ itself. Only if the two tracks leave a unique signature of four distinguishable hit points in the sensors, the acceptance histogram gets populated for this very combination of those three parameters. The result of this calculation is presented in Figure 3.39(b). At very small opening angles, the loss in acceptance is due to the already mentioned fact that clusters with small distance to each other tend to be merged by the 1d clustering algorithm thus altering the signature (or multiplicity) of the whole event which leads to a rejection of all hits. On the other hand, the drop of acceptance at increasing $\Theta$-angles can be explained with the limited size of the sensors such that tracks originating from a more distant vertex point (higher $z$) can be detected only at smaller opening angles. The measured $\Theta$-distributions corrected for this acceptance are, exemplified for two different photon energies in Figures 3.39(c) and 3.39(d), consulted to extract the most probable $\Theta$-angle at this energy. Those average opening angles are extracted for all $\gamma$-energies corresponding to each tagger-bar as seen in Figure 3.39(e), where tagger bar index №16 corresponds to the highest, index №29 to the lowest $\gamma$-energy (likewise corresponding to the lowest and the highest energy of the deflected electrons in the tagger, respectively). The uniform decreasing dependence of $\Theta$ with the (to the tagger bars assigned) energy is evident as well as a change of slope between bar indices 24 and 26. This behavior might be attributed to the peculiar tagger comb geometry which is depicted in Figure 3.40. An energy calibration
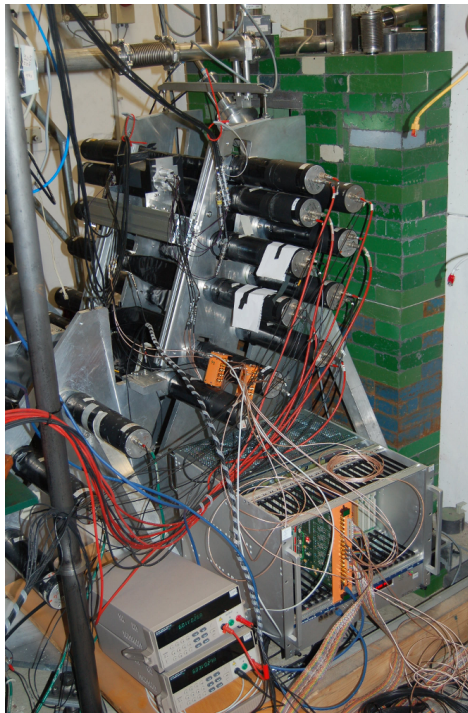


**Figure 3.40.:** Photograph of parts of the *B1* electron tagger (formerly *SAPHIR*) which shows the geometric configuration of the scintillator bars.

therefore was desired in order to linearize the abscissa values. From the predecessor experiment *SAPHIR* which utilized the *B1*-Tagger, an appropriate, yet outdated and thus possibly unreliable calibration could be found on archive (refer to Table 3.10, energy values are given for the center of the respective tagger bar) that allows a more or less precise representation of the measured opening angle in terms of the photon energy as presented in Figure 3.39(f).

However, in this scheme the 'kink' evident in the uncalibrated tagger-bar based representa-

| Tagger Bar Index | $\gamma$-Energy (GeV) |
|:---:|:---:|
| 16 | 0.936886 |
| 17 | 0.919549 |
| 18 | 0.892661 |
| 19 | 0.855332 |
| 20 | 0.812806 |
| 21 | 0.776471 |
| 22 | 0.724054 |
| 23 | 0.680384 |
| 24 | 0.636199 |
| 25 | 0.588263 |
| 26 | 0.520792 |
| 27 | 0.442277 |
| 28 | 0.366379 |
| 29 | 0.296294 |

**Table 3.10.:** *SAPHIR*-Tagger bar calibration values used for energy calibration of measurements in this work.

tion smoothens out. Yet, the acquired data points show a nonlinear decrease over the photon energy. For a conclusive understanding of this phenomenon and the underlying kinematics of the electron-positron pair production process in atomic potentials a good comprehension is given by *Motz, Olsen and Koch* [146]. Another paper by *Hart et al.* [147] states a useful empirical parametrization for the opening angle of the lepton pair

$$\Theta = \frac{4m_e c^2 \phi}{E_\gamma} \tag{3.86}$$

where $m_e$ is the electron mass, $E_\gamma$ the energy of the incident photon and $\phi$ is a parameter obtained by fits to extensive sets of existing data with

$$\begin{aligned} \phi =&\, 1.54 \pm 0.07; \quad 50\,\text{MeV} < E_\gamma < 200\,\text{MeV} \\ &\, 1.67 \pm 0.10; \quad 200\,\text{MeV} < E_\gamma < 1040\,\text{MeV} \\ &\, 1.70 \pm 0.10; \quad 1040\,\text{MeV} < E_\gamma. \end{aligned}$$

This parametrization is indicated by a short-dashed line in Figure 3.39(f) as comparison to the values rendered in this work. Furthermore, a pure empirical exponential function as well as a $^1/_E$-like function which accounts to the nature of the pair creation process according to eqn. (3.86) was fitted to the data points.

# Chapter 4.

# Architecture of a DSSD Module Prototype

## 4.1. Overview

The two outer barrel layers of the MVD will be instrumented with rectangular shaped double sided silicon strip detectors. An optimized constellation of sensors within these barrels with respect to acceptance, coverage and low material occupancy was identified as illustrated in Figure 4.1. A shingled alignment of the modules with tilt angles of $\alpha = -12°$ and $\alpha = 10°$
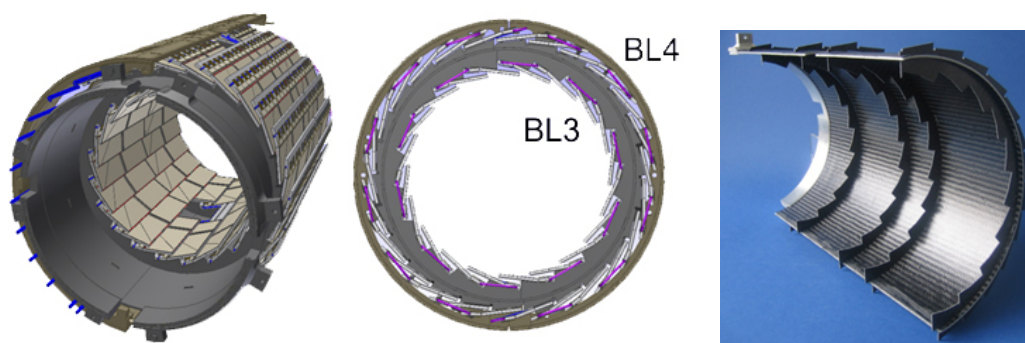


**Figure 4.1.:** CAD model of fully equipped double barrel of the MVD strip tracker (left, middle) and photograph of prototype carbon fiber half-shell support structure (right).

yielding a total number of 20 and 26 elements for layers 3 and 4, respectively has been chosen [35, 88]. A detailed view of the module positions within the outer barrel is given in Figure 4.3. A low mass carbon fiber half-disk holding structure was produced by ZMT Jülich in cooperation with RWTH Aachen (photograph on the right hand side of Figure 4.1).

A detailed sketch of a single DSSD barrel module is shown in Figure 4.2. Upon a rigid frame consisting of a $200\,\mu m$ to $400\,\mu m$ thick carbon-fiber shroud filled with carbon foam or ROHACELL-PMI-E-foam[1] the sensors and hybrid PCB are attached. The latter implements fan-out routing structures, front-end electronics, the module data concentrator chip (MDC) and passive blocking and coupling capacitors as well as connectors. A cooling pipe underneath the front-end chips is foreseen to take away the excess heat produced by the front-ends' power consumption and consequently to keep the sensors at the lowest possible temperature. All of those briefly introduced components are going to be described in greater detail throughout the following sections.

---

[1] ROHACELL is the trade name of a poly-methacrylic-imide hard foam.
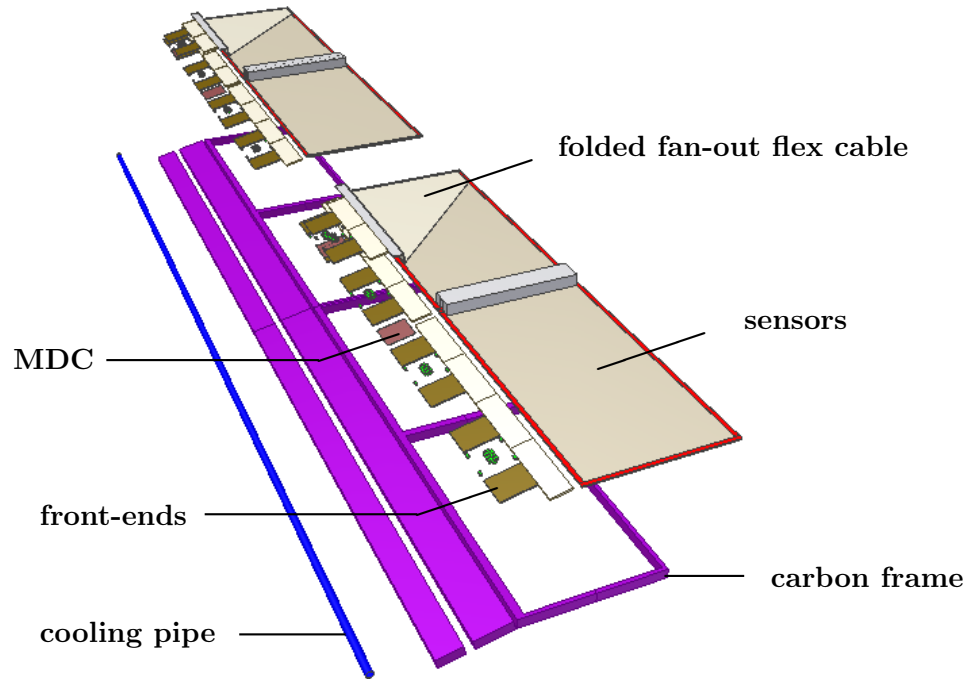
**Figure 4.2.:** Construction schematic of one MVD barrel module [148].

## 4.2. Sensors

### 4.2.1. Overview

The most rigorous limitation of positional resolution for particles escaping from the interaction zone is inflicted by small angle scattering due to intermediate layers of material before they are actually detected by the DSSDs in barrel layers 3 and 4 of the MVD. The expected smearing due to the scattering for different particle species and different traversed material thicknesses is depicted in Figure 4.4. The first two layers of the MVD, i.e. the pixel layers, are arranged around the beam pipe at close distance to the interaction point. The presented scattering angles are calculated based on the assumption that the scattering process takes place in a single thin layer composed of silicon only. Deviations from this condition arising from the actual spacially distributed composition of the pixel barrel layers leads to different, but effectively smaller widening of the trajectory cones. The presented calculations in Figure 4.4 are therefore to be understood as an upper estimation. Active areas of sensor modules in barrel layers 3 and 4 are, as illustrated in Figure 4.3, roughly situated at radial distances of 9 cm and 12.5 cm wrt. the beam axis, respectively. A worsening of the spacial resolution for hits in layers 3 and 4 to RMS-values of 135 μm and 190 μm must be taken into account for 1 GeV/c pions. Lower particle momenta lead to even wider scattering cones and, assuming
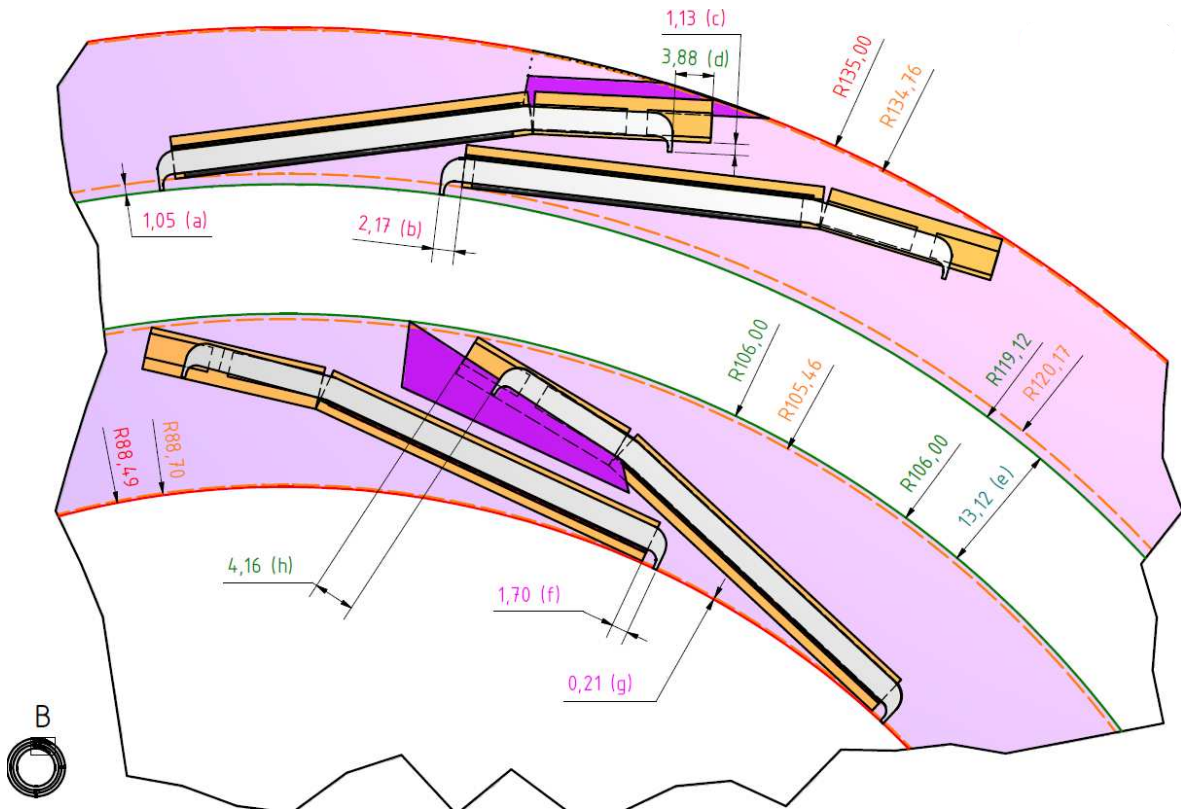
**Figure 4.3.:** Constellation of the strip modules inside the MVD in barrel layers 3 and 4 [148]. Only two of the modules from a total of 20 in layer 3 and 26 in layer 4 are shown.

the highest possible momentum to be identical to the beam momentum of the antiprotons with $p_{max} = 15\,\mathrm{GeV}/c$, at least $\approx 10\,\mu\mathrm{m}$ position uncertainty in layer 3 should be anticipated. Since the overwhelming majority of secondary particles carries only a fraction of the incident beam particle kinetic energy the true scattering deterioration is expected to be greater than this value. Thus, to be thorough, RMS-resolutions achieved within the entire strip tracking system better than $\approx 10 \ldots 20\,\mu\mathrm{m}$ should not yield any gain in tracking performance.

These considerations led to the development of a first prototype sensor intended to investigate the feasibility of the general handling, assembly and double sided read-out of large sensors and to verify the achievable resolution and the radiation hardness of the material. Documentation about first studies conducted to cover those objectives is given within the next sections.

### 4.2.2. Design Choice and Sensor Layout

First $\overline{\mathsf{P}}$ANDA full-size prototype sensors were produced in 2011 by the company CiS in Germany. Its layout utilizes a 10 - Layer process with single metal and passivation layers on 4″ wafers. The raw wafers are $\approx 0.3\,\mathrm{mm}$ thin slices cut off mono-crystalline rods in $\langle 111 \rangle$ orientation. Structures are implemented by means of alternating photolithographic and etching processes applied to the slug. The starting material is grown or deposited ultra-purified silicon molten in a floating-zone (FZ) process to obtain a high purity crystal lattice after re-solidification of the ingot.
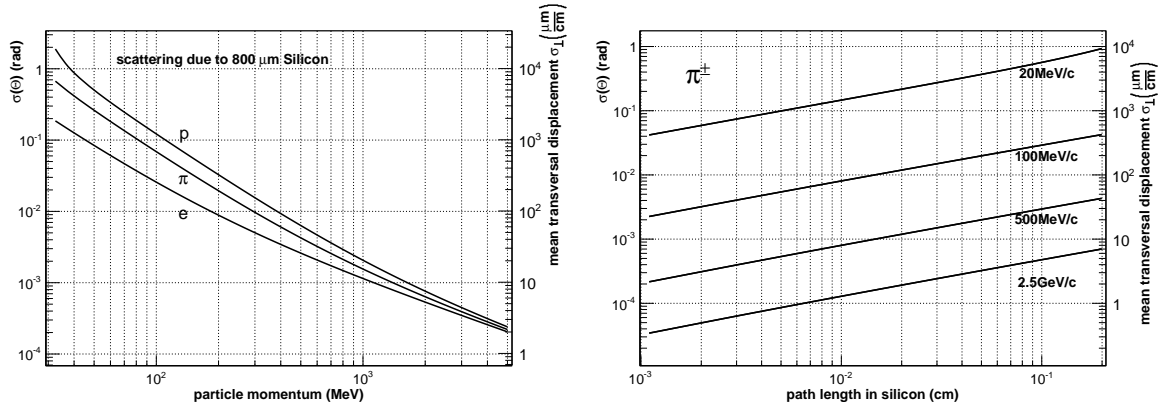
**Figure 4.4.:** Small angle scattering due to the first two layers of the MVD (ca. 800 μm of solid silicon equivalent) for three particle species (left) and impact of traversed path length inside silicon on the opening of the scattering cone (right). The gauge at the plots' right hand side indicates the mean lateral displacement due to the scattering process after free movement in air incident on a plane perpendicular to the trajectory.

A variety of sensors and test structures were placed within the usable wafer area, some of them contain test patterns used during fabrication. A floor plan of the wafer layout and the implemented structures can be seen in Figure 4.5. Table 4.1 gives an overview of the specifications of the sensors. Front side strips are realized as $p^+$ in $n$ doping, whereas the back side contains $n^+$-strips embedded in the $n$-substrate. All sensors are laid out with read-out structures on both front and back side with the strip electrodes oriented orthogonal to each other. The depletion of the active volume is achieved by punch-through biasing (see Section 2.2 for explanation of the method) from the bias ring toward the strips on both front and back side. The charge separation on the $n$-side is realized by $p$-type isolation strip implants ($p$-spray). The active area is protected by eight guard rings on the $p$-side to assure sufficient insulation between the bulk zones under opposite potential and a stable electric field within the active volume. In the following sections, front side is considered the junction or $p$-side, while the ohmic, or $n$-side, is referred to as back side.

Beside the full size $\overline{\text{P}}$ANDA prototype sensors, a smaller, square shaped sensor S3 with 50 μm pitch and an active area of roughly $2\times2$ cm$^2$ found place on the delivered wafer (see Figure 4.5). This sensor was foreseen to be an equally sized replacement for already existing prototype sensors (see section 3.2.1) from earlier prototyping stages in order to benefit from the existing readout infrastructure. Furthermore five "Baby"-Sensors (S4) with only 128 strips on either side were placed on the wafer. Additional test structures are implemented as well, serving mainly as markings during wet-processing stages, bonding calibration tags or similar. Finally, fourteen diodes with different numbers of guard rings are placed around the main elements on the wafer. These diodes may be used to derive the radiation dose during irradiation tests.

Figure 4.6 shows a detail of the corner of the sensors on the $n$-side (left picture) and the $p$-side (right picture) with the first strips and the high potential bias contact ring with the square-shaped openings inside the passivation layer. $n$-side-pads on the strips are connected to the odd-numbered $n^+$- implants, while the even-numbered pads are located at the opposite edge. Those direct access-points to the buried strip-implants are referred to as DC-pads. On the junction- or $p$-side additional guard ring structures for insulation of the high potential
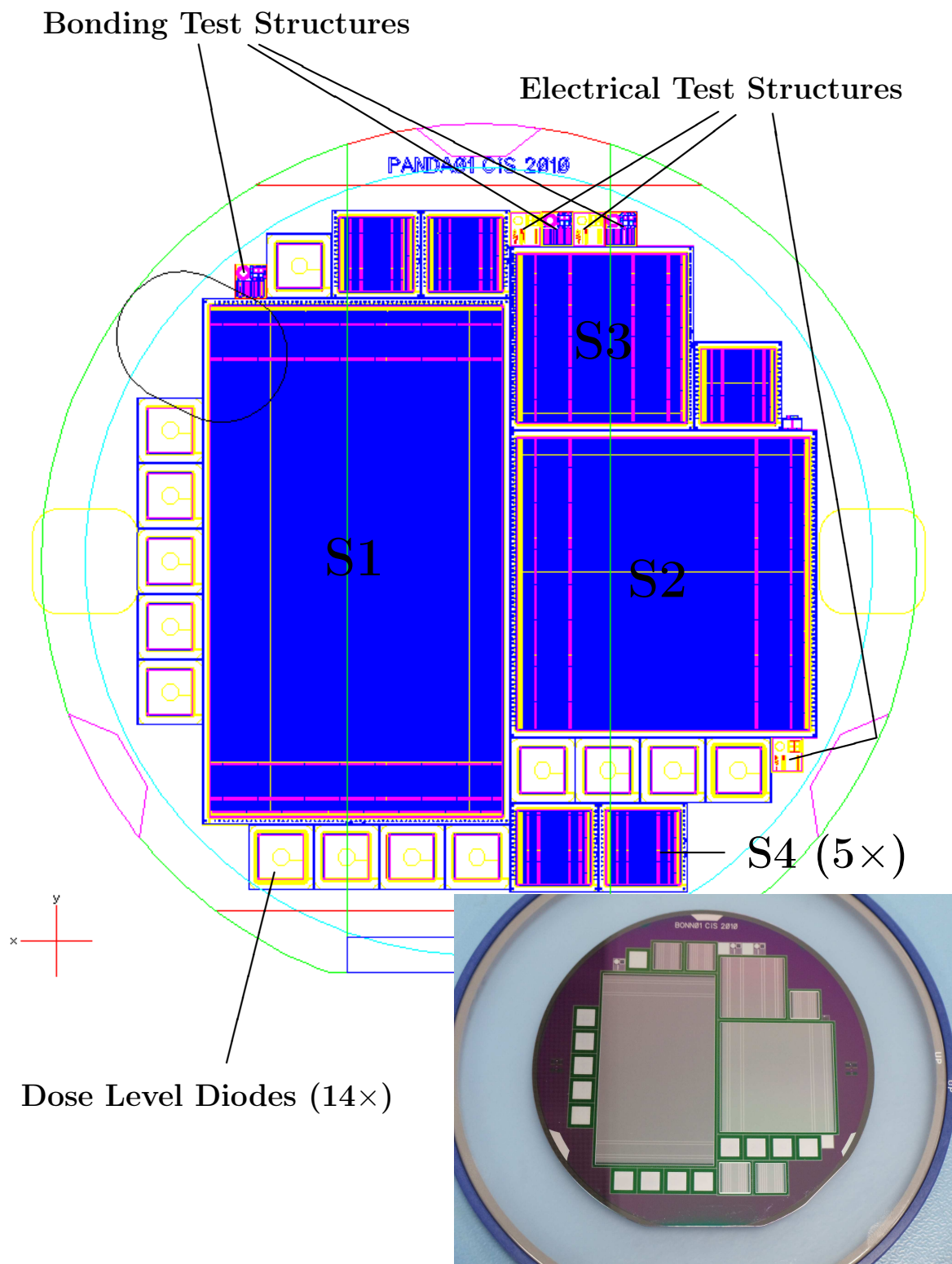
**Figure 4.5.:** Layout of $4''$ - Wafer with DSSD prototype sensors. Beside the main sensors S1 – S4 a variety of additional test structures reside on the silicon wafer with a diameter of $10.1\,\mathrm{cm}$. The small picture shows a photograph of the completed, yet undiced, wafer (courtesy CiS GmbH).

| Property | Value | Unit |
|----------|-------|------|
| **General** | | |
| wafer material | FZ Si, 4″ | |
| thickness | 285±10 | µm |
| resistivity | 2.3...5.0 | k Ωcm |
| $n$-side isolation | $p$-spray | |
| guard rings | 8 | |
| stereo angle | 90 | ° |
| passive rim | 860 | µm |
| **S1** | | |
| $p$-side/$n$-side strips | 896/512 | |
| pitch/width | 65/30 | µm |
| active area | 58.275×33.315 | mm$^2$ |
| **S2** | | |
| $p$-side/$n$-side strips | 512/512 | |
| pitch/width | 65/30 | µm |
| active area | 33.315×33.315 | mm$^2$ |
| **S3** | | |
| $p$-side/$n$-side strips | 384/384 | |
| pitch/width | 50/20 | µm |
| active area | 19.230×19.230 | mm$^2$ |
| **S4** | | |
| $p$-side/$n$-side strips | 128/128 | |
| pitch/width | 65/30 | µm |
| active area | 8.355×8.355 | mm$^2$ |

**Table 4.1.:** Properties of CIS01 prototype sensors.

difference to the bias line are necessary. The contacts along the inner bias line are used for the distribution of the negative bias potential. Additional orientation and position marks etched into the metal layers aid microscope-based operations.

In the microphotography (Figure 4.7) of one CIS01 sensor prototype the AC-pads which are situated on the metal-strip lines toward the center of the sensor are seen. A staggered configuration of odd and even strips can be noticed due to the limited lateral space. This set of AC-pads is implemented with the outer (odd) row at a distance of 2.86 mm from the cut edge (and symmetrically at the opposite edge as well). For reasons of flexibility during the prototyping stage a second identical set at a more internal location was added at a distance from the cut edge of 6.86 mm.

### 4.2.3. Measurement Setups for Sensor Characterization

To evaluate most of the important properties of the sensors, two main connection setups are imaginable:

1. connection to the DUT[2] with removable probe needles in a probe station setup

---

[2] Device under Test.
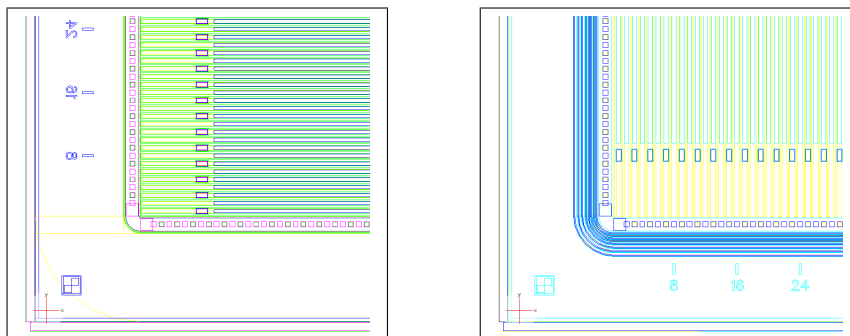
**Figure 4.6.:** Layout detail of double sided strip sensor prototypes CIS01: the *n*-side (left) shown with the first strips and the high potential bias contact ring with square shaped passivation openings. On the *p*-side (right) additional guard ring structures for insulation of the high potential difference from the bias line are necessary. The contacts along the inner bias line are for the supply of the negative bias potential. DC-pads shown here on the strips are direct connections underlying strip implants and therefore yield high potential under operating conditions. For ease of channel identification, additional orientation numbering and position marks are implanted inside the metal layer.
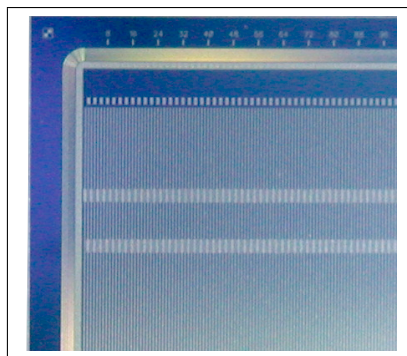


**Figure 4.7.:** Microphotograph of a CIS01 sensor detail showing the *p*-side. The metal strips are clearly visible with implemented AC-pads in staggered rows and DC-pads for connection of even numbered strip implants at the top. The active volume is protected against breakdown to the positive bias supply potential by circumferential guard-ring implants.

2. interconnection with a probe-PCB[3], e.g. by bonding wires

Former method is usually applied when the same sensor undergoes further processing stages (glueing, bonding interconnection etc.) and intermediate parameter monitoring is needed. Assuming a certain homogeneity among sensors from different wafers (but identical lots) often justifies the sacrifice of a single sensor from a lot or a smaller test structure foreseen for exactly this purpose from each wafer for application of the latter case i.e. the mounting onto a stiff PCB structure with fan-out of a part or the entire set of connections (Probe Card). This method is also applicable if the sensor shall be mounted in a condition where the whole unit can be utilized for another purpose than for the pure sensor characterization alone, e.g. the usage in a detector module either in a single sensor or a multi-sensor tracking configuration (see section 3.2.1).

---

[3] Printed Circuit Board.

### 4.2.3.1. Probe-Station

A temporary connection to the sensor contacts can be accomplished by placing electrically connected needles onto the contact pads in a probe station setup. The basic construction of
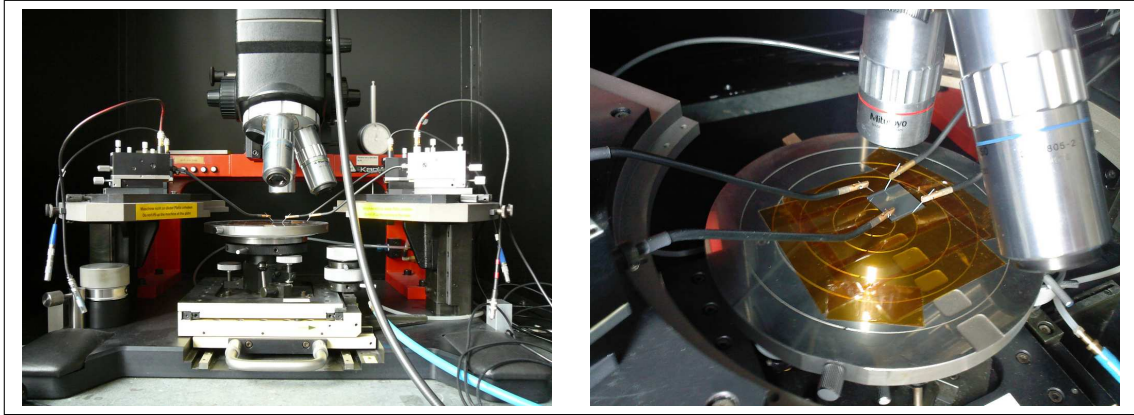


**Figure 4.8.:** Photographs of a Probe-Station setup for the measurement of sensor parameters without permanent connection. The microscope is mounted above the chuck on which the DUT is placed (left). Probe devices with micrometer drives are seen on both sides of the chuck with shielded booms and contact needles set upon a sensor (right).

such a probe station is seen on the photographs in Figure 4.8. Upon the solid, fine-adjustable metal plate (chuck) in the center of the setup a Device under Test (DUT) is placed and held in position by vacuum featured by a number of small holes in the planar surface of the chuck. Needles with manual micrometer drive allow the contact with the DUT under visual supervision by a microscope mounted above the chuck. The chuck itself provides electrical contact to the DUT, if desired. Otherwise the DUT should be placed electrically insulated from the conductive support. The probe-needles provide the signal through coaxial connectors with sufficient shielding. The whole apparatus is enclosed by a metal sheet case to prevent noise pickup and avoid exposure of the DUT to ambient light.

### 4.2.3.2. Probe-Card

The described probe-station setup is sufficient to acquire a subset of important sensor parameters, such as global leakage current or interstrip or coupling capacitances. However, some important key properties are not accessible through this setup, as for example the backside capacitance since for its measurement requires the connection of the entire back side strips to signal ground. A PCB, acting as mounting frame which carries the sensor and allows the connection of both front- and back side pads via wire-bonds to pads onto the frame was developed and utilized instead. Figure 4.9 shows a photograph of such a fixed-contact probe-card[4]. The sensors are glued onto the PCB and all AC-pads are wire-bonded to a common signal line on both sensor sides. Those signals together with the tapped bias rings are routed to connectors for external access. Furthermore, DC and AC-pads of some channels are bonded to separate pads in order to determine coupling capacitance and single strip depletion behavior.

---

[4] In contrast to the probe-card usually denoting a PCB with a set of needles which contact the DUT temporarily similar to the discussed probe-station setup. However, the incomplete term "probe-card" will be used in the further text for convenience.
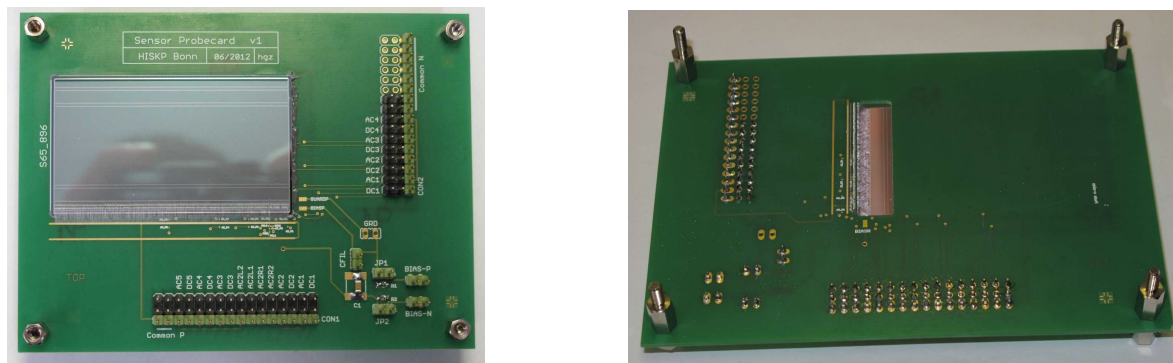
**Figure 4.9.:** Photographs of the sensor probe card assembly. The sensor is attached to the top side of the PCB (left) and the entire set of *p*-side channels wire-bonded to a common line. Through an opening in the PCB all sensor *n*-side channels are connected to a common line on the back side of the assembly (right). Additionally, few strip implants (DC-pads) and metal strips (AC-pads) are connected to separate pads on both sides for individual probing. Those signals together with the bonded bias-supply lines are accessible through pin headers (seen at the right and bottom in the left photograph).

The persistent mounting by glueing the sensor onto the probe-card means that it can not be retrieved eventually for further usage. This setup usually addresses properties which have to be generally identified for whole production lots, not for measurements of marginally fluctuating quantities. Therefore the sacrifice of one sensor out of a production lot[5] is justifiable.

### 4.2.4. Electrical Characterization

In order to conduct precise measurements of the the global sensor leakage current and capacitance, an LCR-Meter[6] (*Sourcetronic* ST2819) was prepared such, that an external variable voltage can be applied 1) without influencing the measured object by the voltage supply's intrinsic impedance and 2) avoiding the external voltage to be applied to the LCR-Meters inputs directly. The first condition is satisfied by a series R-L-network to raise the supply's impedance at signal frequencies while the latter one is realized by series-capacitors at the inputs of the LCR-Meter (see Figure 4.10). In order to keep the introduced errors by the additional capacitances low a value of 100 nF was chosen. Hence the obtained values are unbiased only, when the measured reactance is small compared to the isolation capacitors' reactance, otherwise the measurement accuracy tends to be dominated by the errors in the line impedances (i.e. by the coupling capacitors).

The measurement is done via the compensated four-wire method with the stimulus applied to the outer contacts (H1 and L1 in Figure 4.10) while the inner ones (H2 and L2) sample the voltage with a high impedance at the DUT. This configuration usually guarantees a high precision of the measurement since the stray properties and voltage drops of the four measurement wires are compensated thus resulting in an exclusive measurement of the parameters beyond the joint H1-H2 and L1-L2 contacts, respectively.

---

[5] One lot, i.e. the smallest processed quantity of wafers during a production run is usually 24 or 25 wafers in $4''$ and $6''$ processes. Sometimes half batches of 12 wafers are equally accepted for a run [149].

[6] Device for precise measurements of inductivity, capacitance and resistance at different frequencies.
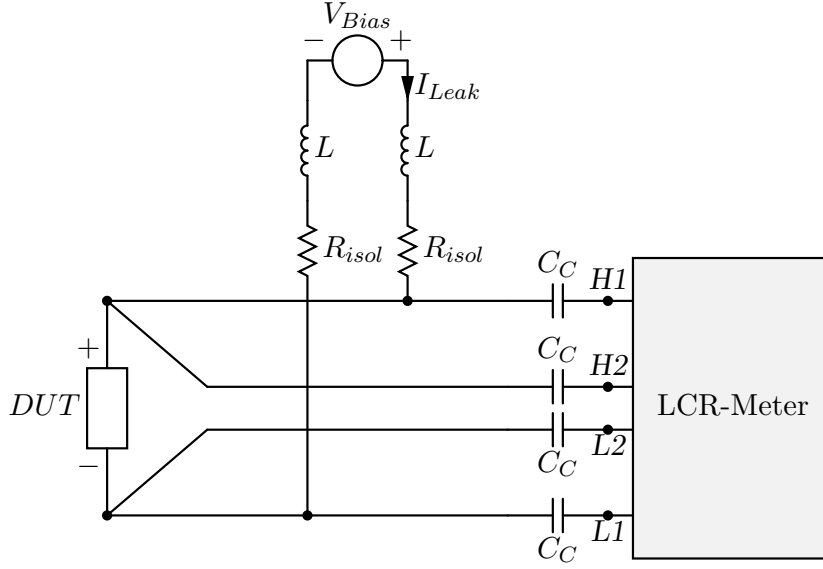
**Figure 4.10.:** Biasing scheme for measurement of global sensor parameters. To protect the LCR-Meter from overvoltage the measurement setup is isolated by series capacitors $C_C$ while the bias voltage source's intrinsic low impedance is isolated from the DUT by series chokes $L$ and resistors $R_{isol}$.

It turned out, that, in order to achieve highest precision at a reproducible level, the matching of the insulation capacitors $C_C$ is critical (see above). For that reason a sample of 52 commercially available metalized polypropylene film capacitors (manufacturer WIMA) with a nominal value of 100 nF and a rated voltage of 400 V were surveyed and 4 capacitors whose actual values are located inside a 0.1 % tolerance band were selected.

Measurement of the two-port model parameters is conducted utilizing the LCR-meter setup described above. Acquisition of parallel capacitance and the dissipation factor $D$ is chosen since diode devices and particularly the encountered impedances of DSSD sensors are best described by the equivalent circuit in Figure 4.11 with negligible series resistance. Exceptions from this model are explicitly treated as such, namely the coupling capacitance as described later in this text.
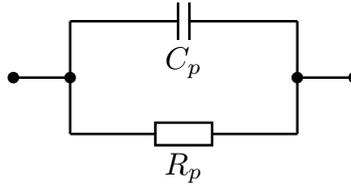


**Figure 4.11.:** Parallel two-port model assumed for LCR-measurements.

The dissipation factor $D$ is defined as

$$D = tan\delta = \frac{\Re(Z)}{\Im(Z)} = \omega C_s R_s = \frac{1}{\omega C_p R_p}. \tag{4.1}$$

The resistance $R_s$ is also referred to as the equivalent series resistance ESR, while $R_p$ is the shunting resistance of the capacitance under investigation. The capacitance measured in series

mode $C_s$ equals the true capacitance $C$ when the parallel resistance $R_p$ is sufficiently high. Likewise, the measured parallel mode capacitance $C_p$ is comparable with $C$ only when the series resistance $R_s$ is negligible. The dissipation factor is a measure for the reliability of the assumption that the reactance caused by the capacitance equals the measured impedance. The higher $D$, the more complex the description of the DUT's equivalent circuit.

### 4.2.4.1. Reference Measurements

A benchmark measurement with a device with known capacitance behavior is shown in Figure 4.12. For an unbiased precision measurement nulling of the LCR-Meter with open contacts prior to the actual measurement is mandatory. The obtained values then are free of stray capacitance and just distributed by the noise as documented by [150].
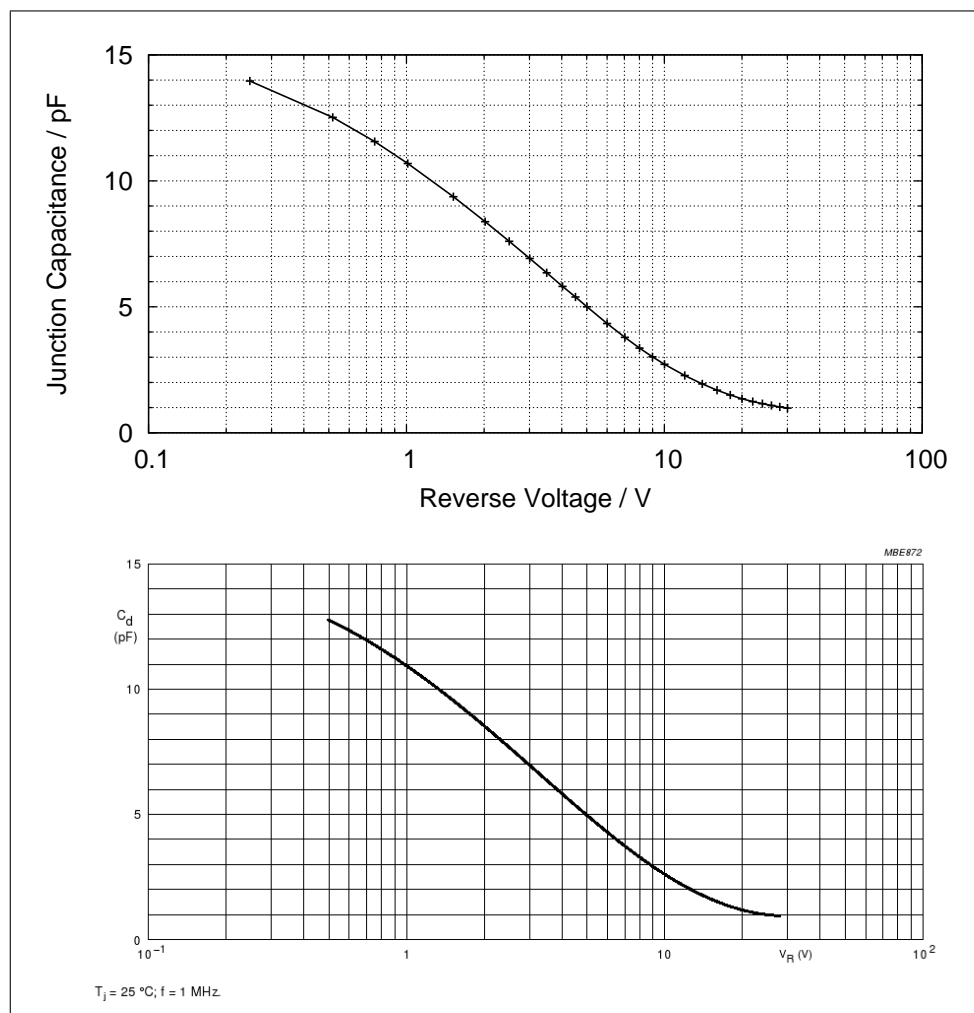


**Figure 4.12.:** Measured (top) and from [151] reported (bottom) *C-V*-Curves of capacitance diode BB131 for comparison. The measurement was done with a *Sourcetronic* LCR-Meter with matched isolation capacitors and external high impedance voltage source. The measurement frequency was 200 kHz and the temperature of the diode junction was settled at 22 °C.

#### 4.2.4.2. Sensor Measurements

The introduced setup for the electrical characterization is capable of acquiring most of the interesting parameters which make up a rather complete characterization of a strip sensor. Some of those parameters can be retrieved exclusively with the full set of sensor connections featured by the probe-card assembly. However, the remaining parameters might prove sufficient for the characterization of basic sensor operational quantities. As a result a simple probe-station survey of sensors could be sufficient to ascertain functionality within desirable limits.

**Leakage Current**   The connection scheme shown in Figure 4.10 was used to determine the dependence of the leakage current at reverse biased junction configuration for several sensors of the CIS01 type wafer. Figure 4.13 gives an impression of a typical $I$-$V$-characteristics of
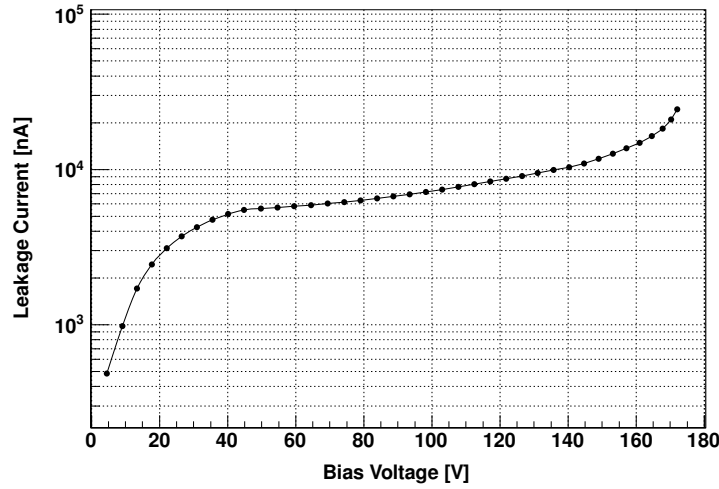


**Figure 4.13.:** Measured leakage current of a CIS01-S1 prototype sensor.

a large S1-type sensor. The increase up to the point of full depletion $U_{dep} \approx 50\,\text{V}$ primarily depends on the expansion of the depleted volume. Beyond full depletion a smooth increase can be noticed which is not explained by the simple diode model but in fact constantly observed. At voltages far beyond the full depletion the current starts to increase exponentially up to the zener breakdown. The relevant fraction of leakage current $I_l$ during operation for a single channel in the total leakage current $I_{l,tot}$ which contributes to the current noise is equivalent to the fraction of the area of a single strip compared to the total active area. This ratio is evenly expressed by the fraction of a single strip in the number of total strips $N$ of one read-out side:

$$I_l = \frac{1}{N}I_{l,tot}. \tag{4.2}$$

for the analyzed large sensor (cf. Figure 4.13) the measured total leakage current of $I_{l,tot} \approx 6\,\mu\text{A}$ at $V_{dep} = 60\,\text{V}$ thus translates into single-channel leakages of

$$I_l(p) = \frac{1}{896}6\,\mu\text{A} = 6.7\,\text{nA}$$

for the $p$-side and

$$I_l(n) = \frac{1}{512}6\,\mu\text{A} = 11.7\,\text{nA}$$

for the $n$-side channels of the sensor.

The reverse breakdown voltage, as can directly be derived from the $I$-$V$-characteristics, represents another selection criterion. Since the operating voltages (in over-depletion regime) will be between $50\,\mathrm{V}$ and $100\,\mathrm{V}$ up to several hundreds of volts at the maximum accumulated non-ionizing dose at the end of the projected $\overline{\mathsf{P}}$ANDA lifetime, care must be taken upon this avalanche breakdown limitation all semiconductors are subject to. The exponential increase of the current at and beyond the breakdown voltage may destroy the device unless the current is limited at a level that the total dissipated power does not exceed the quotient of the maximum allowable avalanche energy[7] and the time the sensor is subject to the breakdown condition. However, since the sensor must be operated at a bias voltage far beyond the full depletion voltage to compensate for the signal-to-noise loss at high accumulated irradiation doses, a certain margin beyond the allowable depletion voltage range to the breakdown voltage is desirable.

**Capacitances**   A simplified equivalent circuit of involved capacitance in a typical micro-strip sensor is depicted in Figure 4.14(a). A charge collected at the strip-implant sees a capacitance $c_b$ to the back side of the sensor (more precisely to the opposite junction interface of the depletion zone, i.e. $n$-side for electrons and $p$-side for holes. However, beyond full depletion the sensor volume becomes "transparent" for electric potentials on the opposite side thus exposing the strip electrodes to the effective capacitance). On the other hand, the charge is drained through the isolated metal strips on top of the implants (which act as series coupling capacitors) into the connected preamplifier. The amplifier's input represents a load with an equivalent capacitance $c_{in}$, that is determined in first approximation by the charge integrating feedback capacitor and the amplifier's voltage gain ($c_{in} = G \cdot c_f$). The effective capacitance of the read-out path $c_{ro}$ presented to the charge thus is the series circuit of the input capacitance and the coupling capacitance:

$$c_{ro} = \frac{c_{in}c_c}{c_{in} + c_c} \tag{4.3}$$

shown in Figure 4.14(b). Since a capacitive coupling to the neighboring strip implants exists via $c_{ii}$ the charge is drained into these channels partly and will be read out by the corresponding preamplifiers. Additionally, the adjacent metal strips are coupled weakly to each other through $c_{im}$. Thus a modified interstrip coupling capacitance $c_{is}$ in Figure 4.14(b) absorbs both the coupling between the strip inter-implant as well as the inter-metal capacitances. This effective interstrip capacitance $c_{is}$ shares charge between adjacent strips and therefore helps to improve position resolution significantly at incident angles close to 90° (see section 4.2.5).

**Back Side Capacitance**   The capacitance to the back side $c_b$ may be determined with the entire back-side strips connected to signal ground. Such a configuration is achieved with the probe-card setup only. Probe-station measurements are not feasible to retrieve this value directly. However, there exist several ways to estimate this parameter, if a direct access through measurements is not available. An estimation of the capacitance can be made on the basis of a simple geometrical plate-capacitor model with edge fringing.

---

[7] The maximum allowable avalanche energy $E_{AS}$ for single pulses depends strongly on the geometry, size, doping concentrations and homogeneity of the depletion zone of the semiconductor device. A very coarse estimate of this parameter for silicon devices is in the order of $1\,\mathrm{mJ}\dots1\,\mathrm{J}$ [152].
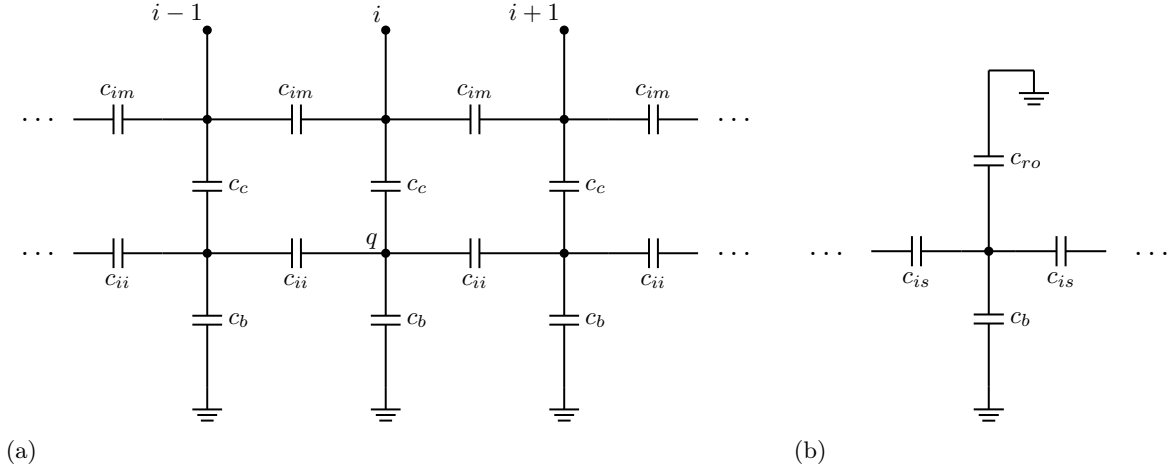
**Figure 4.14.:** Equivalent circuit of a strip sensor (a). The charge $q$ is collected at the strip implant which has a capacitance $c_b$ to the back side (assumed to sit on signal ground) but also a coupling to the neighboring strip implants by $c_{ii}$. Coupling to the top metal strips is symbolized by $c_c$ which have in turn capacitive contact to the neighboring metal strips by $c_{im}$. The read-out of the charge is accomplished by preamplifiers connected to the metal strips (AC-Pads) at the top of the figure. The amplifier's input capacitance in series with the coupling capacitance can be substituted by an equivalent load capacitance $c_{ro}$ that is seen by the hit strip while the inter-implant and inter-metal capacitances may be thought of as a modified total inter-strip capacitance $c_{is}$ (b).

Basically, a single strip electrode forms a simple planar capacitor to the backside which displays the capacitance per unit length

$$c_b = \epsilon \frac{p}{d} \tag{4.4}$$

with the permittivity $\epsilon = 11.8\epsilon_0$ of silicon, $p$ the strip pitch and $d$ the sensor thickness. Since a strip implant usually forms a lengthy rectangle with the length being much larger than its width the stray capacitance at the edges showing non-parallel electric field lines are not negligible. This is particularly true if the implant width is different from the strip pitch. Thus above equation is modified into

$$c_b = \epsilon \frac{p}{d + p \left( f\left(\frac{w_p}{p}\right) + f\left(\frac{w_n}{p}\right) \right)} \tag{4.5}$$

with $w_p, w_n$ the strip widths on $p$-side and $n$-side, respectively and $f(x)$ an empirical function parametrizing the capacitive fringing effect in dependence of the $\frac{w}{p}$ ratio [139]:

$$f(x) = -1.11 \cdot 10^{-3}x^{-2} + 5.86 \cdot 10^{-2}x^{-1} + 0.240 - 0.651x + 0.355x^2$$

A measurement of the body capacitance is conducted with all $p$-side strips connected to one contact of the LCR-measurement system ($\text{H}_{\text{CUR}}/\text{H}_{\text{POT}}$) and all $n$-side strips to the other one ($\text{L}_{\text{CUR}}/\text{L}_{\text{POT}}$). Figure 4.15 reviews the result of such a measurement obtained with the probe card setup. The capacitance decreases with increasing bias voltage in the depletion region beyond the onset of the volume depletion at the punch-through voltage. Latter is characterized by a rapid drop in capacitance because the depleted channel beneath the bias ring expands rapidly across the active area on the $p$-side and isolates the $p$-side-strips from
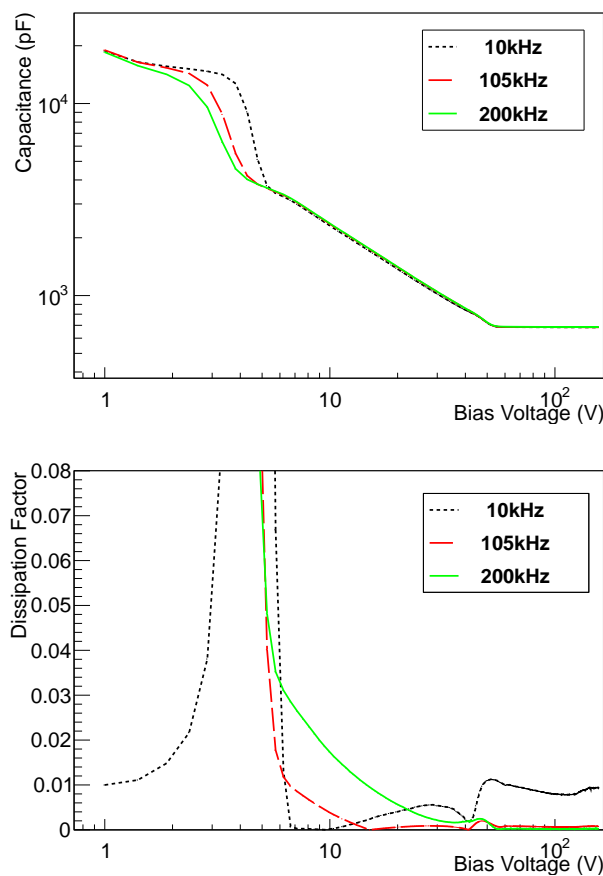
**Figure 4.15.:** Measurement of the body capacitance of a large (CIS01-S1) sensor (top) and dissipation factor (bottom).

the opposite potential. This process is entirely equivalent to the gate voltage dependant formation of the conducting drain-source channel while traversing the pinch-off voltage in MOSFETs. In contrast to those devices the channel pinch-off is referred to as punch-through in case of semiconductor detectors. The punch-through threshold shows a strong frequency dependence. Since the $D$-factor behaves abnormal in this region this observation leads to the conclusion that the actual impedance is too complex to be explained by the two-port model. Hence the measured apparent capacitance at the onset of the depletion is merely a frequency dependant parameter and not identical with the true body capacitance. However, the model is confirmed to accurately resemble the true capacitance beyond the punch-through voltage above approx. 7 V by the low $D$-value and the frequency invariance of the capacitance curve. Above applied bias voltages of ca. 52 V the capacitance remains constant. At this point the depletion zone extends throughout the whole sensor volume and exposes the back-side strip-implants. The body capacitance for the fully depleted sensor in the above example was found to be

$$C_{body} = (683.5 \pm 1.5)\,\mathrm{pF}.$$

The back-side capacitances of a single strip is found from this value by simply dividing it by

the number of strips $N$ on the same side as the strip under focus, i.e.

$$C_b = \frac{1}{N}C_{body}, \tag{4.6}$$

yielding values of $C_b = (0.7628 \pm 0.0017)\,\text{pF}$ and $C_b = (1.3350 \pm 0.0029)\,\text{pF}$ for the $p$-side and $n$-side strips of the sensor, respectively.

**Interstrip Capacitance** $(c_i)$    This magnitude depends on the implant separation, metal separation and other geometric factors. It describes the coupling of one strip (implant and metal) to the next $n$ pairs of neighbors and should not be confused with the capacitance between two adjacent strips $c_{is}$. By convention $c_i$ denotes the coupling to the next neighbors only. In order to distinguish the amount of coupled neighbors the interstrip capacitance shall be additionally denoted with the order $n$ of the coupling $c_{i,n}$. Several models exist that describe the interstrip capacitance in dependence of the geometrical parameters. A good match to within 5 % has been found to measured capacitances for a wide variety of device topologies [153, 154].

A measurement scheme for retrieval of this capacitance takes following steps:

- connect bias voltage to $p$- and $n$-side bias ring contacts; apply voltage sufficient to fully deplete the active volume

- connect $\text{H}_{\text{CUR}}$ and $\text{H}_{\text{POT}}$ contacts to the strip under investigation

- connect $\text{L}_{\text{CUR}}$ and $\text{L}_{\text{POT}}$ contacts to the first $n$ pairs of neighboring strips

The subsequent measurement delivers a value for $c_{i,n}$. For probe-station based measurements the connection of the first pair of neighbors (yielding a value for $c_{i,1}$) is still feasible. A total of five probe-needles is required for this procedure. However, measurement of higher couplings is not practical with this setup. On the other hand, the probe-card setup may be utilized to determine $c_{i,\infty}$ provided that a single channel my be detached from the common signal line on which the entire array of strips is connected to and tapped separately for probing. A measurement following exactly this scheme is depicted in Figure 4.16. Below built-up of the depletion zone underneath the $p$-side strips, the complex impedance is again not described well by a simple capacitive reactance as can be deduced from the erratic $D$-value in this region. Beyond ca. 20 V a reasonable low $D$-factor is observed and the capacitance dropped to an almost constant value. This can be explained with the circumstance that the interaction between neighboring strips should not change substantially once the depletion cleared a thin layer directly underneath the strip-implants from space charges. Further wandering of the depletion-interface through the sensor volume does not affect the field lines between the $p$-side strips any more. For bias voltages beyond full depletion a slight but continuous decrease in capacitance is observed, however. A possible explanation could be found in the tight-bound oxide charges residing on the surface oxide layer which get expunged with increasing electrical field strength as suggested by [137].

**Coupling Capacitance**    The signal charge collected at the strip implant is capacitively coupled onto the overlying aluminum strip. This coupling capacitance $c_c$ depends on the strip geometry and the thickness of the intermediate insulating oxide layer. In order to prevent excessive drainage of the charge into neighboring channels and the back-side capacitance, the magnitude of $c_c$ is intended to be as large as possible. Usual values range at $c_c = 10 \dots 30\,\text{pF}/\,\text{cm}$ for
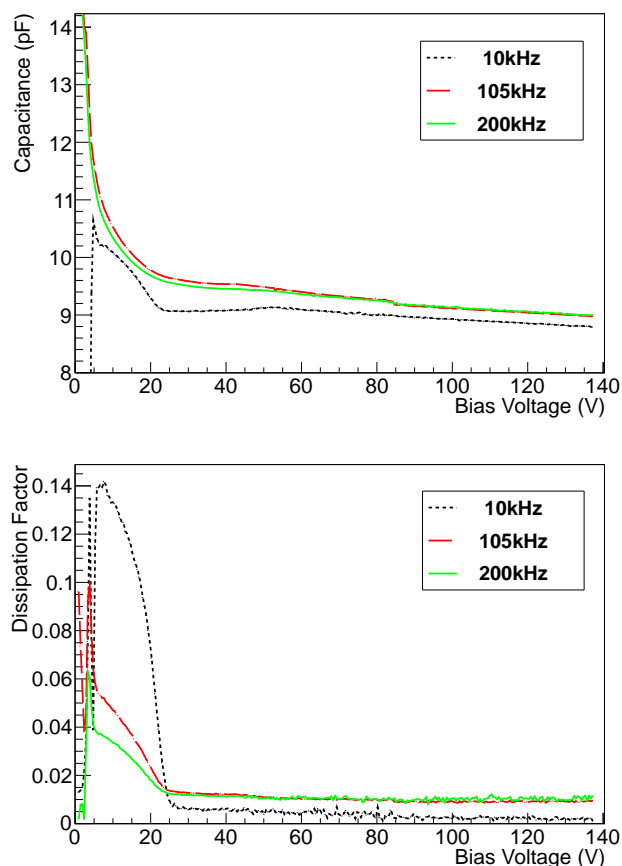
**Figure 4.16.:** Interstrip capacitance $c_{is,\infty}$ between a single $p$-side-strip and all others on the same side (top) and the associated dissipation factor (bottom) of a CIS01-S1 sensor.

30 µm strips [93, 139, 155]. Measurement of the coupling capacitance is accomplished by tapping the DC and AC-pads of one strip with the probe contacts ($H_{CUR}/H_{POT}$ and $L_{CUR}/L_{POT}$) with all other contacts floating. Table 4.2 lists measurements of $c_c$ at different probe frequencies for two CIS01-S1 sensors and one CIS01-S4 sensor for several strips. It can be noticed that the large sized sensors (S1) show a strong dependence from the probe frequency. The complex impedance obviously can not be described with the simple two-component analysis of the LCR-meter at higher frequencies. This observation is supported by the simultaneously acquired parallel resistance which show sufficient high values $\mathcal{O}\,(10\,\mathrm{M\Omega})$ at $10\,\mathrm{kHz}$ but drop at measurement frequencies of $100\,\mathrm{kHz}$ and above to several kiloohms. Thus the dissipation factor is no more dominated by the imaginary reactance but by the resistive part of the impedance which renders the capacitance reading at those frequencies unreliable. However, the low frequency value is considered a fair estimate of the true coupling capacitance as shown by a comparison of the full evaluation of the impedance and *SPICE*-simulations [139, 156]. On the other hand, values presented in Table 4.2 for the higher probe frequencies are the actual effective capacitances encountered for the discharge at the given frequency. A collected charge thus "sees" different coupling strengths toward the read-out node at different signal frequencies. Therefore contributions in the upper part of the frequency domain are attenuated more than the lower parts. This characteristic is similar to the typical frequency response of a low-pass filter. For an explanation of this effect, let the simplest conceivable equivalent

| f (kHz) | coupling capacitance $c_c$ (pF/cm) | | | | | |
|---------|---------|-------|-------|-------|-------|-------|
| wafer | | S1-W2 | S1-W2 | S1-W2 | S1-W4 | S1-W4 | S4-W4 |
| strip-index | | 213 | 495 | 27 | 433 | 275 | 2 |
| 10 | | 43.9 | 43.9 | 44.3 | 36.0 | 35.5 | 51.3 |
| 100 | | 10.7 | 10.7 | 10.8 | 9.2 | 9.1 | 48.6 |
| 200 | | 7.7 | 7.7 | 7.7 | 6.6 | 6.5 | 42.1 |

**Table 4.2.:** Measured coupling capacitances $c_c$ (CIS01-S1 and -S4 sensors) at different frequencies.

circuit of the interaction between the two strip electrodes (implant and metal) be invoked as illustrated in Figure 4.17. The strip implant has non-negligible intrinsic resistivity represented by distributed resistances $r$. Every element along the strip is coupled capacitively through specific capacitance $c$ to the metal strip. The impedance encountered between the two con-
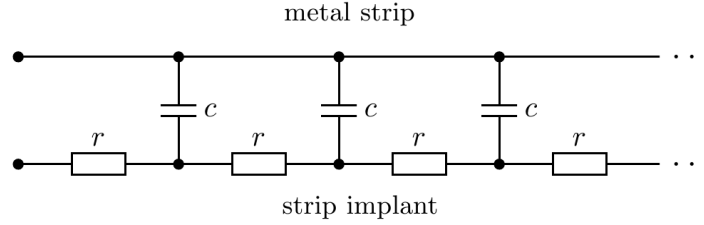


**Figure 4.17.:** Distributed element model of the coupling between strip implant and metal.

tacts is composed by the ohmic series resistance and a capacitive reactance. It is therefore dominated by the capacitive contribution at low frequencies while in the high frequency limit the ohmic part is much larger than the capacitive resistance. A measured value for $C_c$ at high frequencies is therefore expected to substantially deviate from the true capacitance. Furthermore the dissipation factor should be large at higher frequencies since the real (ohmic) part of the impedance dominates over the imaginary (reactive) part.

Figure 4.18 reports frequency dependent measurements of the coupling capacitance between the strip implant and the overlying metal strip of both $p$-side and $n$-side of a large prototype sensor (CIS01-S1). The curves reproducibly reflect the discussed frequency dependence of $c_c$. The drop of capacitance beyond measurement frequencies of a few kilohertz is accompanied by an observed transition of the dissipation factor $D$ from low to large values as expected.

The coupling capacitance is measured in the low frequency limit as the value converges the true capacitance (supported by the low $D$-factor). Consequently, integral capacitance values extracted from Figure 4.18 are

$$C_c = (180 \pm 5)\,\text{pF}$$

for the $p$-side and

$$C_c = (270 \pm 5)\,\text{pF}$$

for the $n$-side. The coupling capacitances are usually indicated as geometry-independent specific capacitances. Above values thus would read as

$$c_c = (54.0 \pm 1.5)\,\text{pF/cm}$$
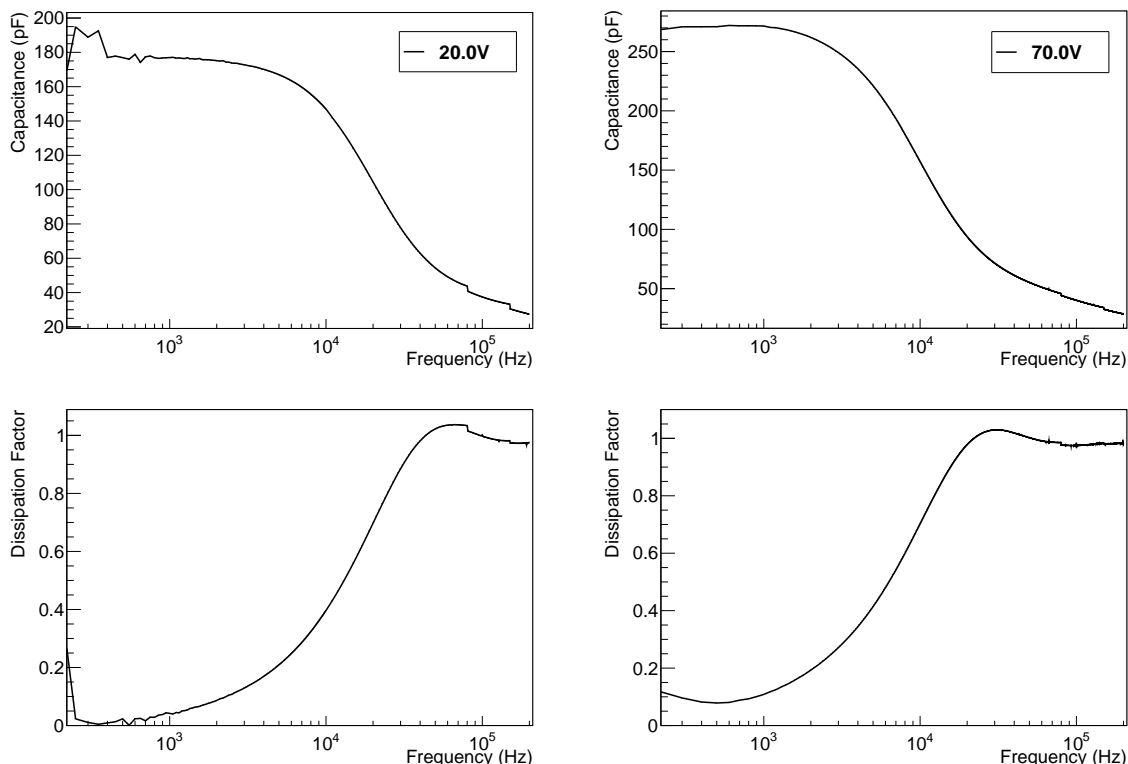
**Figure 4.18.:** Coupling capacitance $C_c$ between a single strip implant and the overlying metal strip of $p$-side (left) and $n$-side (right). The bias voltages for which the measurements were made are chosen such that the strip implants see a sufficiently depleted volume underneath themselves. The associated dissipation factors are reported for the $C$-$f$-measurements as well (bottom).

and

$$c_c = (46.3 \pm 0.9)\,\mathrm{pF/\,cm}$$

for $p$-side and $n$-side strips, respectively.

**Stray Capacitance** The capacitive coupling of a single strip is not completely described by the couplings to back-side and strip neighbors. A residual capacitance is due to the fringing to the bias/guard-rings which reside at signal ground. Therefore an increased stray capacitance is expected at the strips close to the edges of the active area. Larger sensors should display a lower influence on the total strip capacitance. The measurement of the stray capacitance was done by connecting one strip (via the AC-contact pad) to one LCR-contact pair and the bias ring of the same side to the other one. All other contacts are left floating. Figure 4.19 reports the measured dependence of the stray capacitance of single strips and the corresponding capacitance between the bias ring contacts. The decrease of stray capacitance until the onset of full depletion coincides with the back-side capacitance characteristic. It can be explained by the capacitance emanating between the $p$-side strips and the backward interface of the depletion zone traversing the sensor bulk with increasing bias voltage. Beyond the full depletion little decrease in the capacitance is noted. The expulsion of a surface ion charge layer at the back side is suspected to explain this observation [139]. The actual single strip stray capacitance $C_{stray}$ can not be measured directly since a strong coupling to to the bulk via the interstrip
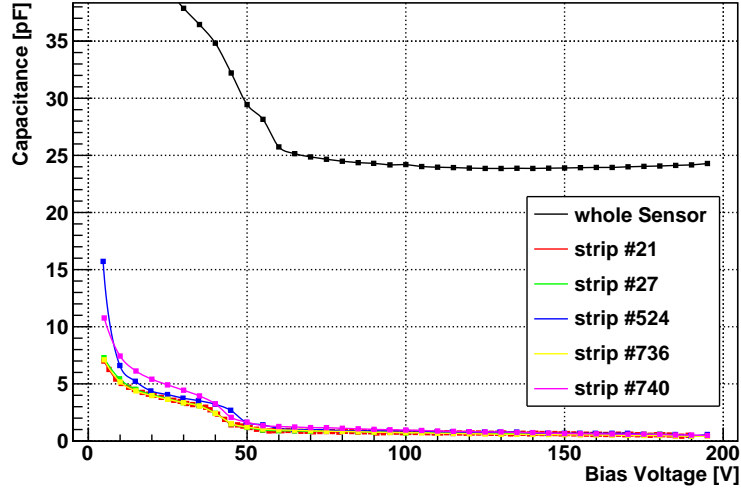
**Figure 4.19.:** Capacitance characteristics of $p$-side strips of one large $(6.0 \times 3.3 \, \text{cm}^2)$ prototype sensor CIS01-S1. At full depletion the stray capacitance of single strips is as low as ca. 0.5 pF. The capacitance between both bias contacts $C_{p-n}$ (black) is shown for comparison.

capacitances to all other strips exists, but it can be reconstructed from the measured values in two ways. First, it may be inferred from the $p$-side bias-line to $n$-side bias-line capacitance $C_{p-n}$ (black trace in Figure 4.19) through division by the number of strips[8] or, secondly, by correction of the measured stray value for the coupling to all neighbors which requires the knowledge of $c_{is}$.

Under operational conditions, i.e. with wires bonded to all AC-pads of front and back side to the front-end electronics as well as properly connected bias contacts a single strip carries a combination of all aforementioned capacitances since the entire back-side contacts and neighbor-strips represent signal ground. With the given values for $c_{is}$ and $c_b$ a first order estimate of the total strip capacitance seen by a connected preamplifier can be met:

$$C_{strip} = c_{i,\infty}l + c_b l + C_{stray}. \tag{4.7}$$

To obtain a full characterization of the sensor, the capacitances shown in Figure 4.14 are determined by the probe-card setup as described above. Following sequence of measurements is proposed:

1. capacitance between strip-implant and bulk (DC-Pad to bulk): $C_{stray}$

2. capacitance between metal-strip and strip-implant (AC-Pad to DC-Pad): $c_c$

3. capacitance between strip (AC-pad) to all other channels of the same side: $c_{i,\infty}$

4. capacitance between all channels of one side to all channels of the opposite side: $c_b$

Values for $c_{is}$, $c_b$, $c_c$ and $C_{stray}$ obtained from measurements and a comparison to model predictions is given in Table 4.3. The predicted values for $c_b$ are calculated according to eqn. (4.5). Representative values for the expected interstrip and coupling capacitances were taken from literature [93, 139, 153–156].

---

[8] Application of this method assumes that the impedance is dominated by the reactance $(j\omega C_{p-n})^{-1}$ which is approximately true at high probing frequencies.

| Property | | Capacitance | | | |
|---|---|---|---|---|---|
| | | predicted | ITC01 | CIS01-S1 | CIS01-S4 |
| $c_{is}$ | (pF/cm) | 2.0 | 2.4(2) | 2.88(15) | — |
| | | | | $2.70(6)^{\dagger}$ | |
| $c_b$ | (pF/cm) | 0.25 | — | $0.2290(4)^{\dagger}$ | — |
| $c_c$ | (pF/cm) | >10 | 11(1) | $p$: 41.6(6) | $p$: $51.3(10)^{\dagger}$ |
| | | | | $p$: $54.0(15)^{\dagger}$ | |
| | | | | $n$: $46.3(9)^{\dagger}$ | |
| $C_{stray}$ | (pF) | — | — | $0.025(2)^{\ddagger}$ | — |
| | | | | $0.026(2)^{\ddagger}$ | — |

**Table 4.3.:** Values for sensor capacitances predicted from geometrical capacitor model with edge fringing ($c_b$) or reported values for similar sensor configurations ($c_{is}$) [139, 153, 154] and measured values for three different sensor types. (†) indicates that the corresponding values were obtained with the probe card setup, the values marked with (‡) were reconstructed based on the measured stray capacitance $C_{p-n}$ between the bias contacts.

The full depletion voltage $V_{dep}$ for each sensor is extracted from the $C$-$V$-characteristics of the stray capacitance as shown in Figure 4.20. The steep decrease of capacitance following a power law below full depletion fades into a, theoretically, constant value. Practically, the capacitance still increases beyond the full depletion with increasing voltage from the reasons unfolded above in the description of the stray capacitance. Linear approximation of the points measured on either side of the slope transition and identification of the mutual crossing point obtains the voltage at which the sensor is just fully depleted.
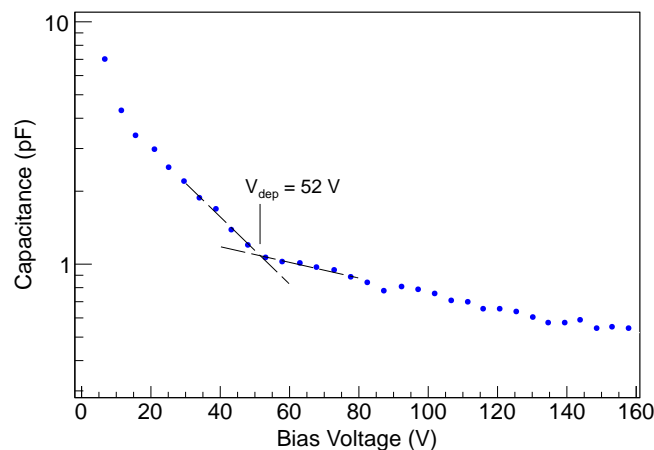


**Figure 4.20.:** Single strip stray capacitance characteristic used to determine the transition between extension of the depletion zone through the sensor volume and full depletion.

### 4.2.4.3. Measurements on Auxiliary Wafer Structures

Together with the double sided strip sensors additional devices are delivered on the produced wafers. A number of 14 diodes with an effective area of $16\,\text{mm}^2$ provides means to determine

quality and depletion behavior of the devices housed on the wafer without actually subjecting the sensors to any tests. Those diodes are used for radiation hardness examinations as well. Furthermore, their leakage current, as is directly related to the accumulated non-ionizing dose may be consulted to determine the radiation level the diode is exposed to. An example measurement of the leakage current in dependence of the reverse bias voltage is shown in Figure 4.21.
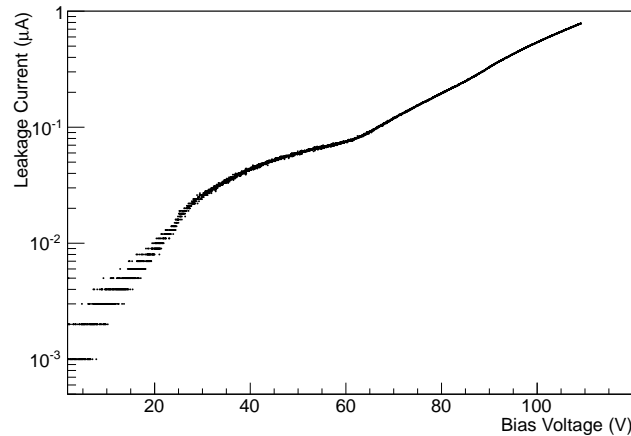


**Figure 4.21.:** Leakage current of one wafer test diode.

In the voltage dependant characteristics of the dissipation factor $D$ on the right hand side of Figure 4.22 a clear peak can be found in the vicinity of the full depletion voltage $V_{dep}$ evident at the two higher probe frequencies (105 kHz and 200 kHz). In the higher resolved scan around this point shown in Figure 4.23 a shift of this peak toward lower voltages with increasing frequency is noteworthy. Since the maximum available probe frequency is limited to 200 kHz by the utilized equipment the behavior at higher frequencies could not be studied. It is therefore strongly desirable to record the dissipation factor in this range in future characterizations as well to assess the depletion voltage reliably. Two other notable features are made visible by the $D$-$V$-Plot in Figure 4.22, namely one less prominent peak evident at all measuring frequencies between 5 V and 10 V which may be attributed to the formation of a depleted zone when the punch-through voltage is exceeded and a much less pronounced bump at $\approx 24$ V visible again only at the higher probe frequencies whose origin can not be explained.

### 4.2.5. Spacial Resolution

In Section 3.3.6 the parameters influencing the spacial resolution of a strip sensor were thoroughly discussed. The introduction of intermediate floating strips between the read-out electrodes was shown to significantly improve the reconstructed position uncertainty. Furthermore, an increased SNR of the pre-amplified charge signal proved to be beneficial for the hit resolution as well, particularly when the positive charge sharing capabilities of intermediate strips are utilized. A set of Monte-Carlo simulations (which was described in somewhat greater detail in Section 3.3.6) was deployed in order to investigate several options for the read-out of the DSSDs of $\overline{\mathsf{P}}$ANDA.
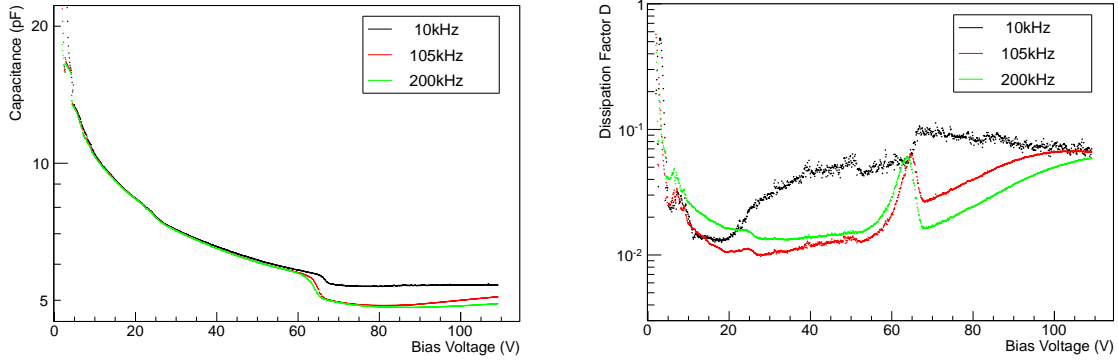
**Figure 4.22.:** Capacitance and dissipation factor of a wafer test diode.
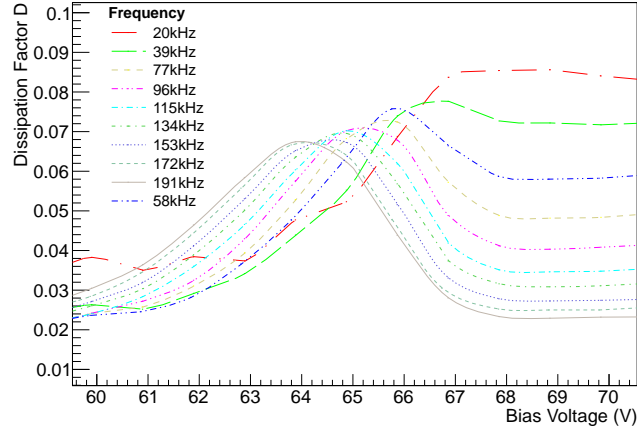


**Figure 4.23.:** Dissipation factor in the vicinity of full depletion voltage.

Charge-sharing characteristics obtained from the MC-simulations are reported in Figure 4.24 for configuration options with varying read-out pitches of 65 µm and 130 µm with and without intermediate strip. It should be noted that the resulting RMS-resolutions are valid for events showing at least two channels above thresholds per cluster. Single-strip hits on the other hand yield the maximal positional uncertainty of $\pm\frac{p}{2}$, or, for a statistical sample, an RMS-resolution of $\frac{p}{\sqrt{12}}$. Therefore the charge-sharing for a specific sensor and read-out configuration should assure a sufficient fraction of leaking charge into neighboring strips and thus to exploit the potential sub-pitch resolution of multi-strip clusters. As discussed above, this spacial smearing of the introduced charge intrinsically originates in the extent of the charge cloud of $\mathcal{O}\left(10\,\mu m\right)$. For strip pitch significantly larger than this extent no notable fraction of the incident charge is shared between adjacent strips. Capacitive coupling between the strip electrodes helps to share the charge among neighboring strips instead.

Achievable RMS-resolutions for different read-out configurations and SNRs calculated by means of the discussed MC-algorithm are reported in Table 4.4 for a sensor pitch of 65 µm.

$p = 65\,\mu\text{m}$, no intermediate strip:
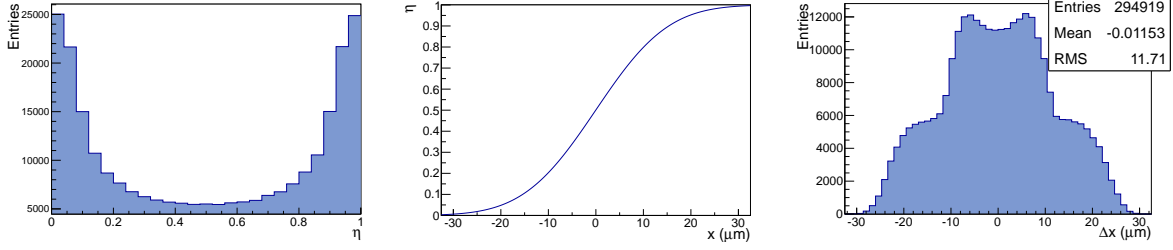


$p = 130\,\mu\text{m}$, one intermediate strip:
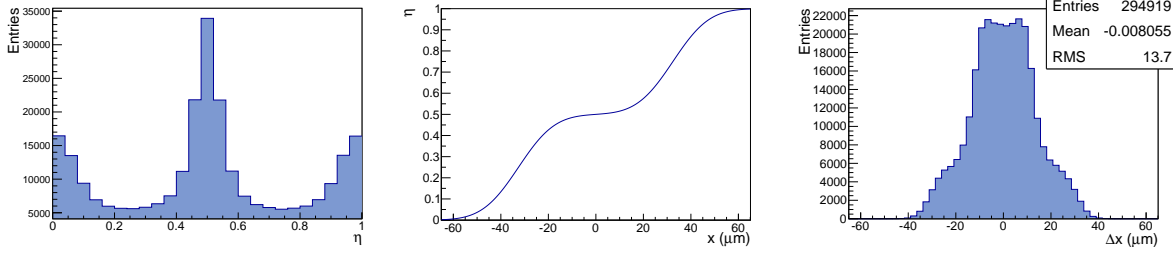


$p = 130\,\mu\text{m}$, no intermediate strip:
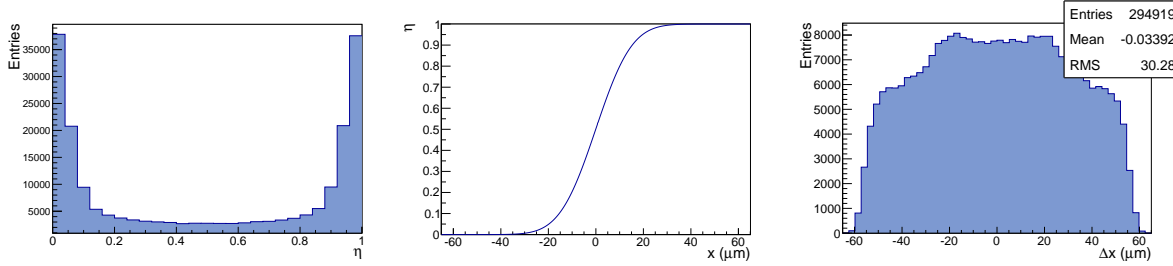


**Figure 4.24.:** $\eta$-distributions, charge-sharing functions and projected spacial resolutions for different read-out pitch and interstrip configurations obtained from Monte-Carlo simulations.

### 4.2.6. Radiation Tolerance

Systematic studies of the behavior of prototype sensors under irradiation have been started. For the qualification of radiation hardness several wafer elements have been irradiated with protons and neutrons of several fluences in order to categorize the obtained sensors with respect to the systematic radiation damage studies undertaken by the RD48 collaboration [127].

Irradiations with slow (14 MeV) protons were carried out at the cyclotron facility in Bonn with a total fluence of up to $2.2{\cdot}10^{13}$ p·cm$^{-2}$. The equivalent fluence referenced to 1 MeV neutrons is obtained by scaling this value with the hardness factor found from the NIEL scaling in Figure 2.14 for a proton kinetic energy of 14 MeV

$$\frac{\Phi_{p,14\,\text{MeV}}}{\Phi_{n,1\,\text{MeV}}} \approx 3.$$

This translates into a 1 MeV neutron equivalent fluence of roughly $6{\cdot}10^{13}$ cm$^{-2}$. *I-V* and *C-V*–characteristics of the irradiated sensors (type CIS01-S4) have been measured in different time intervals after the end of the irradiation (Figures 4.25 and 4.26). The measurements took place between annealing intervals of 20 hours (red curves), 310 hours (green curves) and after

| r/o pitch ( µm) | worst RMS resolution $\frac{p}{\sqrt{12}}$( µm) | nr. of intermediate strips | SNR | spacial resolution RMS ( µm) |
|---|---|---|---|---|
| 65 | 18.8 | 0 | 10 | $16.09 \pm 0.02$ |
|  |  |  | 16 | $13.08 \pm 0.02$ |
|  |  |  | 25 | $10.63 \pm 0.01$ |
| 130 | 37.5 | 0 | 10 | $34.70 \pm 0.05$ |
|  |  |  | 16 | $31.64 \pm 0.04$ |
|  |  |  | 25 | $29.28 \pm 0.04$ |
| 130 | 37.5 | 1 | 10 | $24.92 \pm 0.03$ |
|  |  |  | 16 | $16.13 \pm 0.02$ |
|  |  |  | 25 | $12.11 \pm 0.02$ |
| 195 | 56.3 | 2 | 10 | $44.52 \pm 0.06$ |
|  |  |  | 16 | $26.68 \pm 0.03$ |
|  |  |  | 25 | $13.84 \pm 0.02$ |
| 260 | 75.1 | 3 | 10 | $54.62 \pm 0.07$ |
|  |  |  | 16 | $35.92 \pm 0.05$ |
|  |  |  | 25 | $18.11 \pm 0.02$ |

**Table 4.4.:** Resolution of reconstructed hits for various r/o configurations. The strip pitch in all cases is $p = 65\,\mu m$.

an annealing at a temperature of 60 °C for 24 hours (blue curves). The green curves correspond to the standard annealing interval of 80 min in a 60 °C environment as proposed by [127]. The *I-V*-trends in Figure 4.25 are normalized to the volume leakage current in order to have a proper comparison to measurements available from other groups. The obtained leakage current of $\approx 1\,mA \cdot cm^{-3}$ after irradiation meets well with the value to be expected from field studies [129].

The recorded post-irradiation *C-V*-trends in Figure 4.26 show the annealing yielding a decrease in overall capacitance as well as the change in the full depletion voltage from 60 V to 50 V due to the change in the doping concentration according to Figure 2.14.

Some of the S4-sensors from the CIS01 wafer run were subjected to proton irradiations in a variety of fluences at the cyclotron facility at the HISKP in Bonn. Figure 4.27 shows the irradiation setup with the sensor mounted to kapton tape inside a field cage to prevent static discharge. The suspension is embedded inside a vacuum vessel which is depressurized to fine vacuum during the actual irradiation procedure in order to minimize parasitic scattering of the protons.

Leakage currents and depletion voltages were obtained from each individual sensor after a controlled standard annealing interval of 80 minutes at a temperature of 60 °C. The results are reported in Figure 4.28. Data points at the lowest and the highest equivalent fluences were obtained by irradiation with AmBe source neutrons and fission reactor neutrons, respectively. The fluence values are scaled according to NIEL to 1 MeV neutron equivalents as discussed in Section 2.4 and Appendix B. The leakage current rise follows the parametrization given by the *RD48*-collaboration (see Section 2.4) with slope $\alpha = 4 \cdot 10^{-17}\,A\,cm^{-1}$ up to equivalent fluences of $1 \cdot 10^{14}\,n_{1MeV\,eq}\,cm^{-2}$. Beyond this point a flattening of the current can be noticed
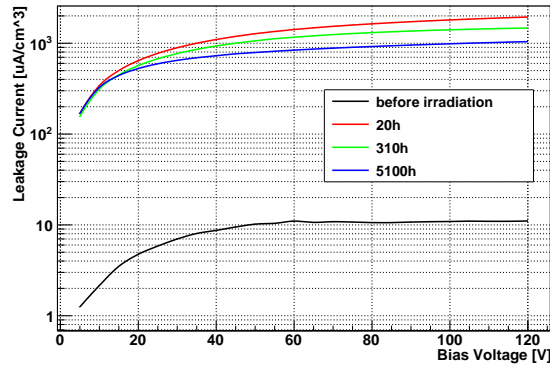
**Figure 4.25.:** Annealing behavior of leakage current characteristics after irradiation of CIS01-S4 sensors with 10 Mrad 14 MeV protons. The $I$-$V$-trends of the sensors were recorded after 20 hours (red), 310 hours (green) and 5100 hours (blue) of annealing time normalized to 25 °C.
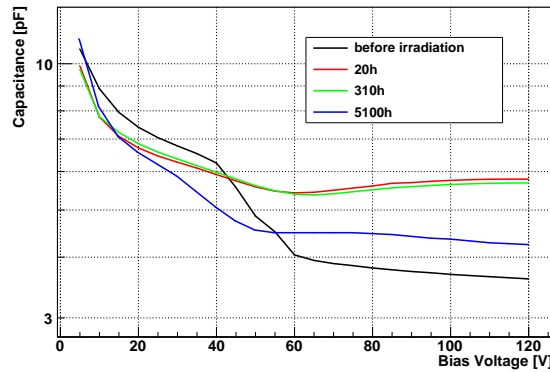


**Figure 4.26.:** Annealing behavior of capacitance characteristics after irradiation of CIS01-S4 sensors with the annealing times given in figure 4.25.

which is probably due to the limiting ohmic bias resistor ($940\,\mathrm{k\Omega}$) within the measurement fixture.

The full-depletion voltages were reconstructed using the $C$-$V$-characteristics of the stray capacitance measurement fixture (see above) at a probe station for all sensors. For the higher fluences a clear change of slopes as in Figure 4.20 which marks the full depletion is missing. The estimated values therefore exhibit systematically larger errors. It must be stated at this point that the $V_{dep}$-values for the largest three fluence values might be entirely wrong since the slight change of slope in the $C$-$V$-curve which was taken as point of depletion could have been misinterpreted while the true depletion voltage was already so high that it was not acquired within the measured voltage range.
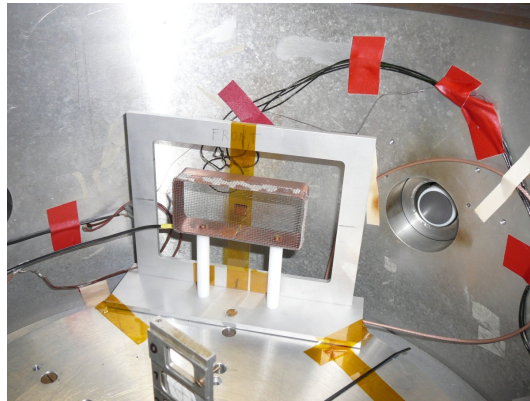
**Figure 4.27.:** Setup used for proton irradiation of sensors. The device under irradiation is attached to the kapton tape in the middle. A field cage in front of the sensor sitting at moderate negative potential avoids static discharge in the proton beam.
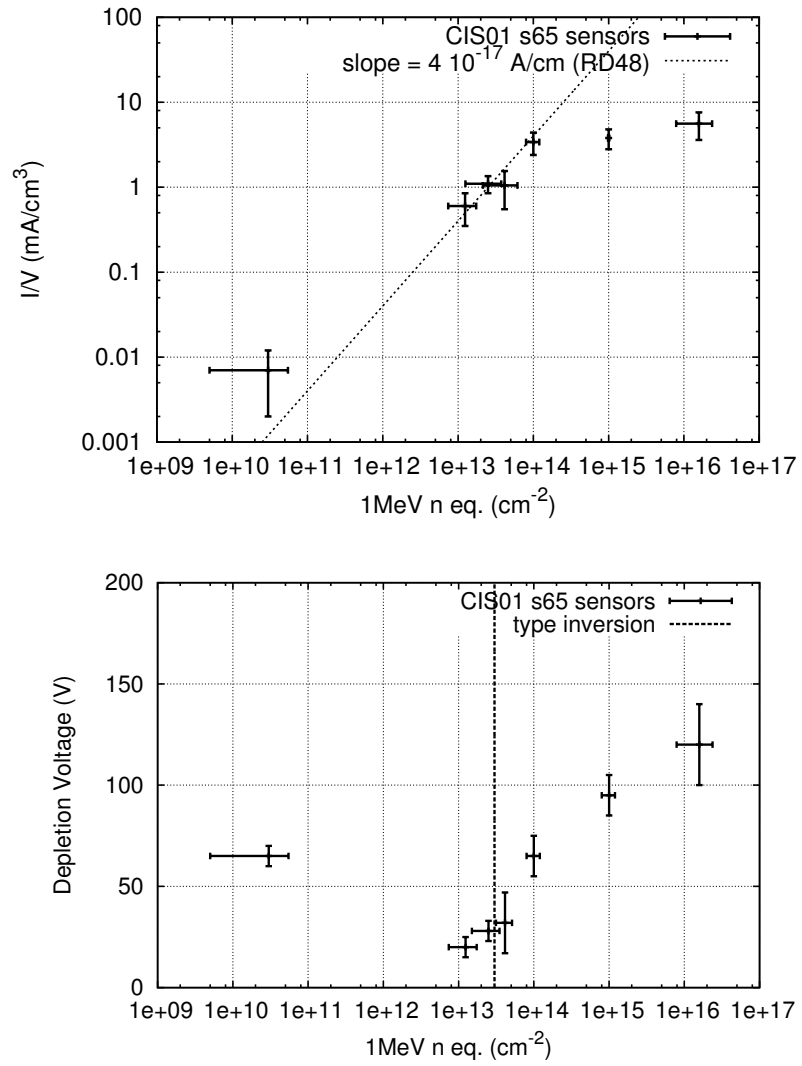
**Figure 4.28.:** Evolution of leakage current (top) and depletion voltage (bottom) with accumulated irradiation fluence.

## 4.3. Front-end Electronics

### 4.3.1. Requirements

Mechanical, electrical and thermal constraints in the construction of the MVD impose a set of limitations to architecture, form factor, power dissipation etc. of the front-end ASICs that will be utilized for the read-out of the silicon strip detectors as well. A part of those constraints have already been discussed in the previous sections, others will be enrolled along with the arising design steps for the strip front-end in the succeeding text. Table 4.5 comprehends a set of more or less specific requirements to the strip readout ASIC to be used as a reference throughout the following sections.

### 4.3.2. Existing Front-ends

Re-utilizing an already existing read-out ASIC is the most obvious and convenient course of action to take when designing a detector system. Presently[9] there are, in fact, a couple of more or less appropriate VLSI-system solutions available. A short overview of a (incomplete, yet best matching wrt. the design requirements for $\overline{\mathsf{P}}$ANDA) subset is given in the next paragraphs accompanied by caveats concerning a possible application for $\overline{\mathsf{P}}$ANDA.

- **FSSR2**
  The Fermilab Silicon Strip Readout ASIC is a spin-off development from the BTEV FPIX2 pixel front-end chip. It has an entirely self-triggered architecture and a 3 bit fast Flash-ADC digitization stage. The preamplifier input stage consists of an $n$-MOSFET with a gate geometry W/L=1500/0.45 μm resulting in an excellent noise figure. The output emits a 24 bit wide data word at a rate of 140 Mbit/s once a channel exceeds the adjustable threshold [157–159].

- **n-XYTER**
  This ASIC was originally designed for a neutron detection experiment and is fully self-triggered due to its split design into two shaper branches, the fast and slow channels, following the preamplifier. The fast channel showing a peaking time of $\approx 20$ ns is fed into a discriminator whose output triggers the emission of a data packet via the mixed $4\times8$ bit serial-parallel interface containing channel number and a 12 bit time-stamp with a resolution of 2 ns at operating clock frequencies of 128 MHz. The output of the slow shaper channel is transmitted as time-discrete sampled analog value. A digitization of the amplitude information is not implemented [160, 161].

- **AToM**
  This ASIC was designed for the *BABAR* Silicon Vertex Tracker (SVT) [162]. It comprises a common source cascode with capacitive feedback at the preamplifier input, a $CR$-$(RC)^2$ shaper with selectable shaping times of 100 ns, 200 ns, 300 ns and 400 ns and a simple comparator. The design is optimized for silicon strip detectors with higher capacitances ($C_d > 20$ pF) but it could be modified for low capacitance detectors by an additional design option as stated by the design engineers [163]. The comparator is laid out with a weak feedback to smoothen the digital transition jitter noise by imprinting a hysteresis onto the transfer characteristic. Its output is sampled with a 15 MHz clock

---

[9] As of first half of 2012.

| Parameter | Value | Remarks |
|---|---|---|
| **Geometry** | | |
| width | $\leq 8\,\mathrm{mm}$ | |
| depth | $\leq 10\,\mathrm{mm}$ | |
| input pad pitch | $\leq 50\,\mu\mathrm{m}$ | |
| FE channels | $2^6 \ldots 2^8$ | default: 128 channels |
| **Input Compliance** | | |
| sensor capacitances | | |
| | $<16$ pF | rect. short strips |
| | $<25$ pF | rect. long strips |
| | $<25$ pF | fw. disc strips |
| charge polarity | either | selectable via slow control |
| input ENC | $< 800\,e^-$ | $C_{Sensor} = 10\,\mathrm{pF}$ |
| | $< 1200\,e^-$ | $C_{Sensor} = 20\,\mathrm{pF}$ |
| **Signal** | | |
| dynamic range | $160\ ke^-$ | |
| min. SNR for MIPs | 10 | 22.5 ke MPV of MIPs in $300\,\mu\mathrm{m}$ silicon, guaranteed within lifetime |
| peaking time | $\approx 50 \ldots 250\,\mathrm{ns}$ | |
| digitization resolution | $\geq 8\,\mathrm{bit}$ | |
| **Power** | | |
| overall power dissipation | $<1W$ | assuming 128 channels/FE |
| **Dynamic** | | |
| trigger | internally generated | when charge pulse exceeds adjustable threshold level |
| time stamp resolution | $<20\,ns$ | |
| dead time / ch | $<6\,\mu\mathrm{s}$ | baseline restored to within $1\,\%$ of equilibrium |
| overshoot recovery time / ch | $<25\,\mu\mathrm{s}$ | |
| average hit rates / ch (poissonian mean) | | simulations @ 15 GeV beam mom. |
| hot spots | $9{,}000\ s^{-1}$ | $\bar{p}p$ |
| | $40{,}000\ s^{-1}$ | $\bar{p}\,Au$ |
| average occupancy | $6{,}000\ s^{-1}$ | $\bar{p}p$ |
| | $30{,}000\ s^{-1}$ | $\bar{p}\,Au$ |
| **Interface** | | |
| slow control | any | DC-balanced |
| data | sparsified serial differential | DC-balanced |

**Table 4.5.:** Requirements to the strip front-end ASIC.

and transmitted zero suppressed to the DAQ when a read-out trigger signal is asserted which selects a certain part of the ring-buffer pipeline in which the comparator output is sampled. The achievable ToT resolution is 67 ns with a range of 4 bits.

Table 4.6 comprehends the key properties of the introduced front-end ASICs. Yet, only

| | AToM | n-XYTER | FSSR2 |
|---|---|---|---|
| input pad pitch | 42 µm | 50.7 µm | 50 µm |
| channels per front-end | 128 | 128 | 128 |
| dynamic range | n/a | 16 fC | 25 fC |
| ENC | $300\,e^-+37\,e^-$/pF | $200\,e^-+27\,e^-$/pF[a] | $220\,e^-+24\,e^-$/pF |
| ENC @ 20 pF | $1040\,e^-$ (200 ns) | $740\,e^-$ [a] | $700\,e^-$ (125 ns) |
| peaking time | 100...400 ns | 18.5 ns [a] | 65...125 ns |
| power consumption | 4.9 mW/ch | 12 mW/ch | 4.0 mW/ch |
| digitization method | ToT | — | Flash-ADC |
| digitization resolution | 4 bit | — | 3 bit |
| time resolution | 67 ns @ 30 MHz | 2 ns @ 128 MHz | 132 ns |
| data interface | diff. serial | 4×8 bit diff. | diff. serial |
| output rate | 30 Mbit/s | 128 Mbit/s | 140 Mbit/s |
| hit word | 48 bit | 32 bit | 24 bit |
| number of data lines | 2 pairs | 1 pair | 1 to 6 pairs |
| control interface | custom differential | I2C | custom LVDS |
| fabrication process | 0.8 µm CMOS | UMC 0.18 µm | TSMC 0.25 µm |
| total ionizing dose (TID) | >2.4 Mrad | 10 Mrad | up to 20 Mrad |

[a] Values for the fast (timing) shaper channel.

**Table 4.6.:** Comparison of properties of different front-ends for strip detector systems which allow un-triggered operation. The AToM front-end requires an additional RO trigger which selects the read-out location in the ToT-buffer pipeline. Values are taken from [157, 160, 162, 163].

two of them, namely the n-XYTER and the FSSR2 are entirely self-trigger capable. The AToM requires additional external hardware effort in order to trigger a read-out cycle when a hit was stored in the ToT-pipeline.

The read-out of the FSSR2-chip is immediate; there are no buffers involved that enqueue a registered hit when the output interface is still transferring the previous hit off chip [159]. This imposes a global chip dead time of 28.6 ns (for 140 Mbit/s interface speed, 24 bit data word size and the maximum possible allocation of 6 output lines). Furthermore assuming an estimated peak hit rate of $\simeq 5.5\,\mu s^{-1}$ per FE during operation of the $\overline{\text{P}}$ANDA detector in high luminosity mode of the HESR as reported by *Würschig* [88, 164] yields a probability of $14.54\,\%$[10] to encounter one ore more hits during this blind interval. This fraction of total hits will be inevitably lost.

The n-XYTER front-end ASIC exhibits a more robust buffering design due to the single channel buffer FIFOs and the token-ring-readout architecture [161]. However, this ASIC possesses no means of internal charge digitization which increases the complexity connected

---

[10] For *Poissonian*-distributed events with the given rate $r$ and observation interval $\Delta t$ the probability for "no event within the dead time window" can be calculated with $P(0) = exp(-r\Delta t)$. The probability for "any event within the dead time window" then simply is the complement to one: $\overline{P(0)} = 1 - P(0)$.

with the construction of a module under the guidelines given above. Moreover, the average power consumption is inadmissibly high (cf. Table 4.6).

### 4.3.3. ToPix for Strip Read-Out

In the last section a set of front-ends were introduced and their suitability for the application in the $\overline{\text{P}}$ANDA strip tracker was discussed. The significant differing read-out philosophy of the $\overline{\text{P}}$ANDA detector inflicts a focus on critical design parameters other than in previous detector systems. Therefore the decision for the development of a dedicated front-end for the read-out of strip detectors on the basis of an already existing development line of a pixel read-out chip for the $\overline{\text{P}}$ANDA-MVD, named ToPix (TOrino PIXel front-end) was met in early 2012. The development of ToPix as well as the branched-off development for the strip read-out front-end is conveyed by the INFN-group in Turin (Italy) [77, 80].

#### 4.3.3.1. Pixel Readout Front-end Chip ToPix

The design of the ToPix front-end chip [35, 77–79] foreseen for the pixel sub-detector of the $\overline{\text{P}}$ANDA-MVD employs the Time-over-Threshold (ToT) technique for amplitude measurement. Thus a good linearity and a high dynamic range are achieved because the charge will still be determined safely even if the preamplifier reaches saturation. The ToT and the event time are both derived from an internal 12 bit time-stamp counter distributed to the entire pixel array. A total of 12,760 pixels organized in 55 double columns á 2×116 pixel cells are foreseen for the final front-end.
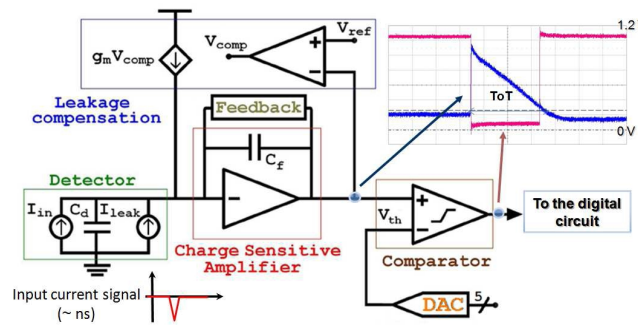


**Figure 4.29.:** Schematic of the ToPix analog cell [35].

The structure of a single pixel cell is reviewed in Figure 4.29. A charge sensitive amplifier at the input of the cell configured as a low-noise direct cascode preamplifier with capacitive feedback and a constant current discharge circuit. Additionally a leakage current compensation provides a stable pre-amp output common mode by a low frequency feedback loop to the input compensating the input bias and providing a stable current return path due to the DC connection to the sensor. A calibration pulse may be fed to the input node through an integrated capacitor (not shown) in order to determine the gain of the analog stage. The preamplifier output is routed to the input of a comparator with a preset reference level (threshold). Once the preamplifier registers a charge, its output exceeds the comparator threshold level switching the output from zero to one. This edge latches the content of the time-stamp counter into the leading-edge register (LE) of the cell. The charge on the integration capacitor

is now constantly depleted through the current feedback network eventually leading to a second crossing of the comparator threshold. The output switches back from one to zero. This transition latches the time-stamp counter value into the trailing edge (TE) register. Both, the
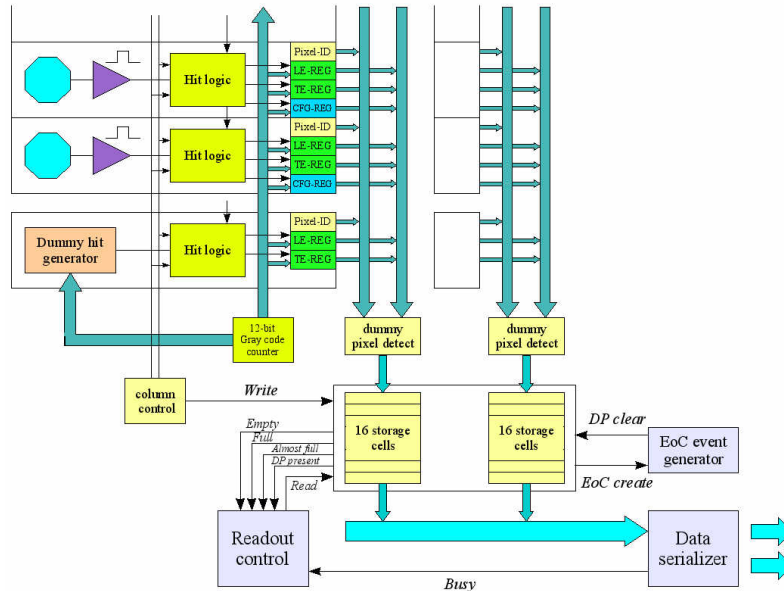


**Figure 4.30.:** Schematic of the ToPix read-out architecture [35].

LE and the TE register together contain the full information about event time as well as the amplitude-proportional Time over Threshold (ToT).

The hit-related values gathered inside the pixel have to be transferred off the cell in order to re-enable it for new hits. For the sake of floor space on the chip the single pixels are not connected individually with a central Readout Controller. Instead, pixels belonging to one double column are connected to the same bus for the LE and TE registers. In Figure 4.30 an overview of the Readout architecture is depicted. Additionally each pixel contains a *busy*-flag which is OR-connected with the *busy*-flag of the preceding cell. The OR-output in turn connects to the succeeding cell thus forming an OR-chain which signalizes the Column Readout Control Unit (CRCU) that at least one cell was hit. A cyclic read-out now starts to connect the first pixel with asserted *busy*-flag to the LE and TE-busses and latches their contents into a 16 cell Column-End FIFO[11] together with a hard-wired address of the pixel. The *busy*-flag of the current pixel cell is cleared and the read-out moves on to the next cell with active *busy*-flag.

**ToPix Prototypes**

**ToPix 1.0** The first prototype contains 32 analog cells, each one with a Charge Sensitive Amplifier (CSA) using a feedback capacitance of 10 fF, a constant current feedback and a baseline restorer and a discriminator followed by a digital buffer. The analog and digital lines are directly accessible on output pads for each cell. No digital read-out logic is included.

---

[11] The size of the Column-End-FIFO is not definitely fixed yet. An extension to 32 cells is possible depending on future test results under high occupancy conditions.
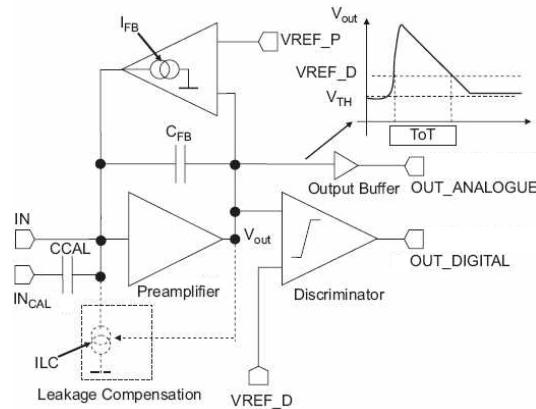
**Figure 4.31.:** Schematic of the ToPix 1.0 pixel cell [35].

**ToPix 2.0**   This chip includes an additional digital read-out circuitry serving a 128-cell and two 32-cell pixel columns working at a reduced clock speed of 50 MHz (cf. Figure 4.32). The analog cells are already developed in the final version. A single event upset (SEU) mitigation technique is applied to the layout of the digital part by designing all latches and registers as fully static and based on the DICE architecture which requires a factor 2 more floor space compared to the space penalty of 3.5 . . . 4 of a triple redundant layout [35].
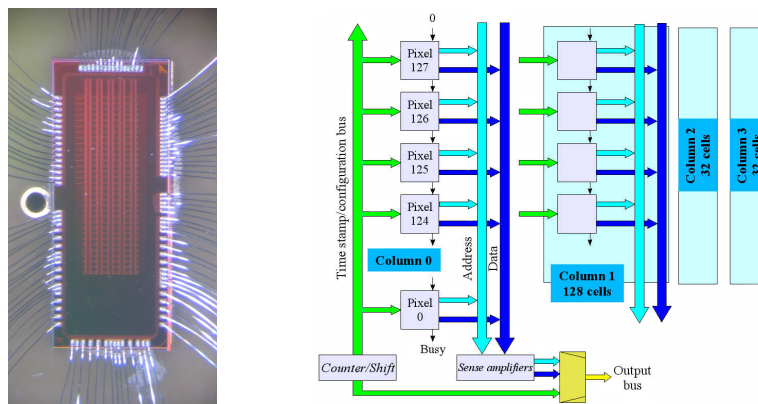


**Figure 4.32.:** Microphotograph of a mounted ToPix 2.0 die (left) and readout architecture (right) [35].

**ToPix 3.0**   In this stage the column readout logic is laid out for operation with the final design clock frequency of 155 MHz. The columns were extended to $2\times128$ and $2\times32$ cell double columns and the column-end-logic blocks with 32 cell FIFOs fully implemented as illustrated in Figure 4.33. The output multiplexer and serializer are still not in the final design shape, simplified logic has been placed instead. The novel output drivers are foreseen to work according to the SLVS-standard [165]. The connections to the sensor are implemented with bump bonding pads in each pixel cell such that a pixel sensor can be flip-chip mounted through small tin or indium bumps onto the front-end.
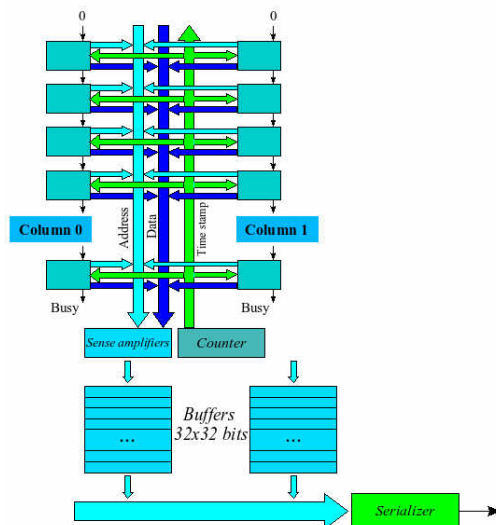
**Figure 4.33.:** Readout architecture of the ToPix 3.0 prototype ASIC [35].

### 4.3.3.2. Overview of the Strip Readout Front-end

An adoption of the recent development branch of the ToPix to an ASIC capable of evaluating signals from silicon strip detectors was initially discussed by *Potenza* [80]. The design of the analog input stage, beside the general requirements from Table 4.5, has to consider following important differences to the pixel design:

- The sensor capacitance (of a connected strip) amounts to typically 4-30 pF and is significantly larger than that of a single pixel ($\approx 200$ fF). The arising implications are manifold. Particularly the shaping time and the minimum achievable noise levels may differ dramatically.

- The effective area of a strip is larger than the sensitive pixel area. The expected hit rates therefore have to be accordingly scaled.

- The number of channels covering the same area is lower than in pixel detectors. While the total number in latter systems scales with the area (n×m) the number of strip electrodes relates linearly to the geometric sensor size (n+m) in DSSD systems.

- The direct match between the front-end single pixel cell to the sensor pixel due to the necessity of a flip-chip assembly process constraints the available floor space of the single channel electronics in the pixel case. This limitation does not exist for strip systems since only a linear set of channels are connected to the front-end, mainly by wire-bonds. The thus gained degree of freedom can be exploited for noise optimization by the layout of large input transistor gate electrodes.

- The power consumption of the analog cell stage in strip systems is usually higher than for the pixel cell. The reason is the higher bias current of the input transistors needed to match the higher input capacitances and in the same time to minimize the noise. However, since a strip detector front-end implements much less channels than a typical pixel front-end the total power consumption per chip can be expected to stay well below that of the pixel ToPix.

Taking these considerations into account a design of a complete single-channel cell was started [80]. The preamplifier and the ToT-stage are going to be described in the following paragraphs. An overview schematic of the modified cell is given in Figure 4.34. The most striking difference to the design of the pixel cell are the multiple ToT-building blocks which will be introduced later in this text.
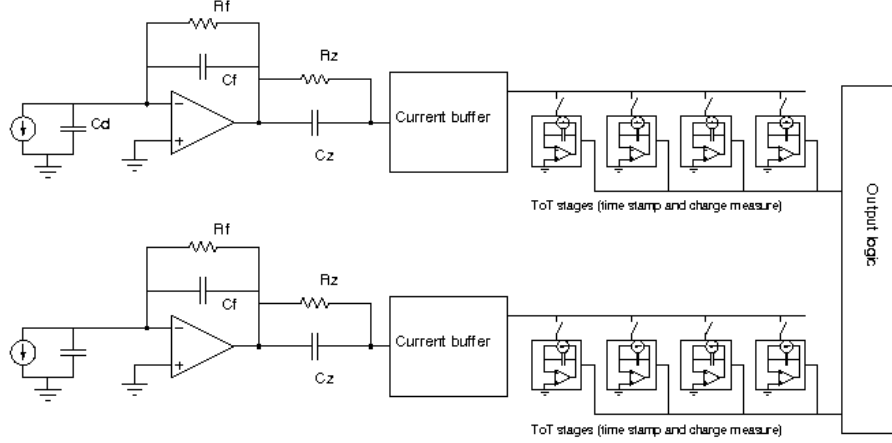


**Figure 4.34.:** Schematic of modified ToPiX ASIC for strip readout [80].

### 4.3.3.3.  Modified Analog Stage

The new preamplifier design comprises a few small differences to the ToPix issue, e.g. the lack of a leakage current compensation since in strip detectors usually the insulated metal strip layer is used as read-out electrode, yet the overall topology follows the standard design comprising a charge integrator, transimpedance buffer and pole-zero cancellation network (cf. Figure 4.35). The first amplifier acts as a charge integrating stage with a feedback capacitance $C_1$. It is the most critical device wrt. noise contribution within the chain. It should be laid out with low noise transistors and a high open loop gain.

A result of the configuration of the input stage as charge integrator utilizing a cascode (a combination of a common source amplifier operating at low gain and a common gate amplifier offering high isolation and high gain) as seen in Figure 4.36 is the potential *Miller*-capacitance introduced by the feedback capacitor which increases the input capacitance by its value multiplied with the voltage gain $A_v$, or more precisely

$$C_{in} = C_d + C_1(A_v + 1). \tag{4.8}$$

This (usually considered detrimental or parasitic) capacitance turns out to have the beneficial effect of imparting a high input capacitance (low input resistance at signal frequencies) to the preamplifier. The charge incident at the strip electrode thus is almost exclusively collected by the preamplifier instead of being spread to neighboring channels or even getting lost to the sensor backside capacitance due to the capacitive divider composed of interstrip or backside capacitances on one side and the series capacitance to ground represented by the preamplifier input capacitance on the other side. An equivalent circuit representation with the involved capacitances and charge-flow paths was discussed more deeply in Section 3.3.6.
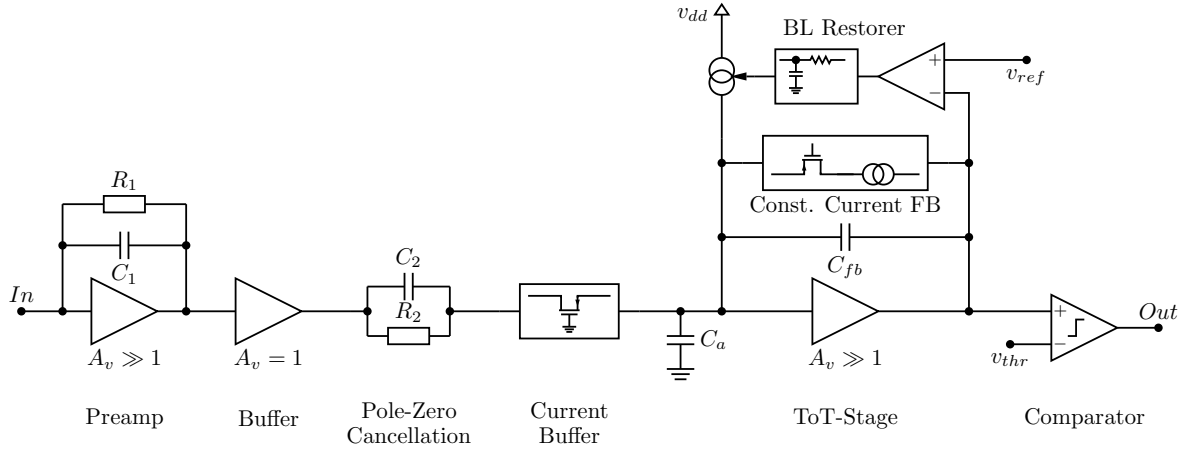
**Figure 4.35.:** Block schematic of preamplifier and ToT stages of one single channel of the new front-end.

The input voltage may be preferably expressed in terms of the input charge, since this is the characteristic magnitude in CSA-systems. Thus

$$v_{out} = A_v v_{in} = A_v \frac{Q_{in}}{C_{in}} \overset{(4.8)}{=} A_v \frac{Q_{in}}{C_d + C_1(A_v + 1)} \tag{4.9}$$

The charge-to-voltage conversion gain $G_q$ of the preamplifier for the desired case of low input resistance, i.e. $A_v \gg 1$ and $C_1(A_v + 1) \gg C_d$ can now be calculated with

$$G_q := \frac{v_{out}}{Q_{in}} \approx A_v \frac{Q_{in}}{Q_{in} A_v C_1} = \frac{1}{C_1}, \tag{4.10}$$

which means that for a sufficiently large voltage gain of the cascode stage the charge-to-voltage conversion ideally becomes independent of fluctuations in gain or input capacitance and is exclusively determined by the feedback loop.

The static charge fully accumulated on the feedback capacitance now faces the input transistor's input resistance as only path to be drained beside the parasitic sensor's parallel resistance. The former is usually in the order of $10^{10} \dots 10^{12}\,\Omega$ for MOSFETs due to the finite resistance of the thin layer of insulating silicon-oxide or silicon-nitride underneath the gate electrode[12]. The charge thus flows through the much smaller parallel detector resistance $(1 \dots 100\,\mathrm{M\Omega}$ for medium and large sized DSSDs) toward signal ground. Yet, either path of drainage results in discharge time constants strongly dependent on parameters which are difficult to reproduce, to control or to keep inside a narrow range for production-related reasons which is not desirable. Therefore a controlled discharge path is created by an additional resistor $R_1$ in Figure 4.35 ($R_{fb}$ in Figure 4.36 respectively) in parallel to the feedback capacitance. This resistor also assures the DC-restoration of the output bias level.

Other components shown in Figure 4.36 are current sources usually formed by current mirror configurations of MOSFETs and can be considered ideal current sources. The preamplifier is followed by a transconductance buffer in order to isolate it from the following stage. It terminates the cascode's high output impedance by a high input impedance and drives the

---

[12] The increase of this resistance by means of processing and material technology is limited by the intervening tunneling effect in thin layers [95].
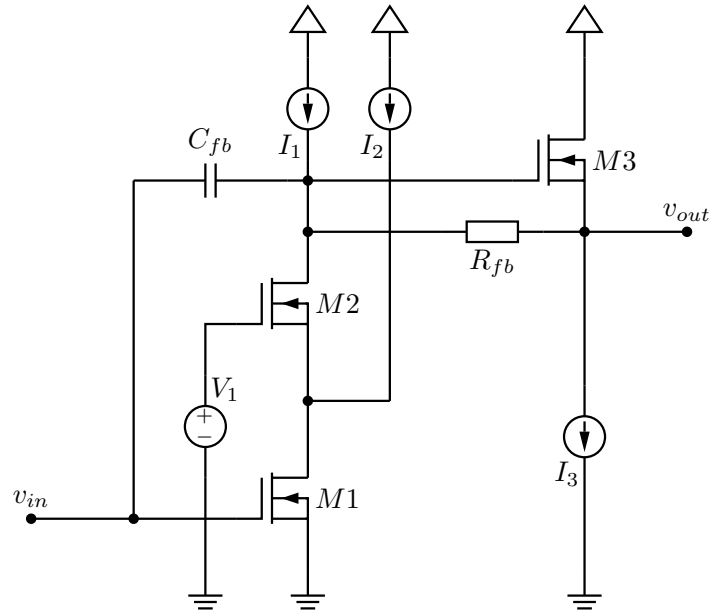
**Figure 4.36.:** Schematic of the preamplifier stage following a standard low noise amplifier design composed of a cascode in the input stage (M1 and M2) and a transconductance buffer (M3). The charge integration and controlled discharge is accomplished by an overall feedback using $C_{fb}$ and $R_{fb}$, respectively. Only components important to the signal path are shown. Voltage and current sources provide adequate biasing of the transistors.

connected load with a low output impedance. The buffer thus effectively avoids feedback from the following stages on sensitive parameters of the preamplifier.

The next stage illustrated in Figure 4.35 following the preamplifier-buffer is the pole-zero cancellation stage (PZC). It consists of a parallel combination of a capacitor and a resistor and differentiates the signal. In fact, a proper choice of the component values compensates a pole in the transfer function introduced by the feedback impedance of the preamplifier accompanied by an increase in bandwidth of the combined stage. In the time domain the pulse-shape shows a prolonged tail after the preamplifier due to the time constant of the discharge network $C_1, R_1$. The differentiation by the PZC shortens the pulse (equivalent to extending the bandwidth) and by this decreasing the probability of pile-up events, i.e. hits that occur on top of the trailing edge of an earlier registered hit.

Between the PZC and the ToT-stage another, additional element can be noticed: the current buffer. It acts as a conversion stage between the PCZ driven by the source follower in the preamplifier buffer exhibiting a low output impedance and the charge sensitive ToT-amplifier. The latter shall provide as only discharge path of the feedback capacitor its own current discharge feedback. Providing the pre-amplified signal therefore requires high impedance drive. This is accomplished by a transistor in common-gate configuration for low input impedance and a cascode buffer with high drive impedance at the output.

The last stage inside the analog chain is the ToT-circuit consisting of a high open-loop gain amplifier. Incoming charge signals are accumulated on capacitance $C_{fb}$ in the feedback network of this amplifier. This charge is disintegrated through the constant current discharge network connected in parallel to the feedback capacitor. It is formed by an adjustable current sink (or better: adjustable conductivity) which allows to set the discharge speed, also referred

to as ToT-gain. The time needed for a complete discharge of the capacitor depends on the collected charge, and thus on the amplitude of the signal registered by the preamplifier.
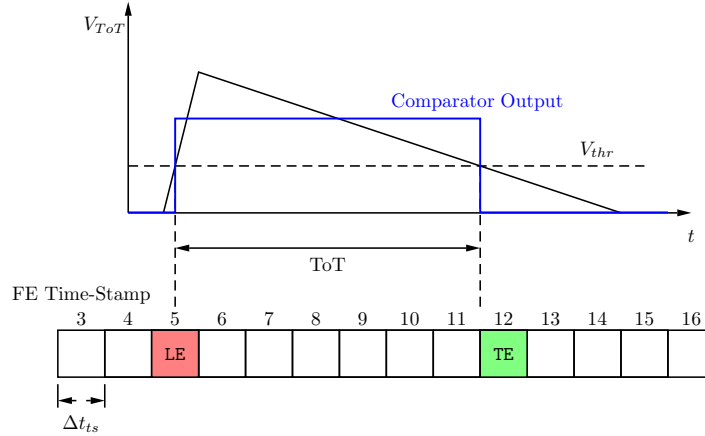


**Figure 4.37.:** Principle of Time-over-Threshold (ToT). The comparator output changes to the "high"-state when the input signal exceeds the preset threshold. The transition latches the current time-stamp counter to the leading-edge (LE) register. When the signal crosses the threshold at the falling edge again, the reverse transition of the comparator output triggers latching of the time-stamp into the trailing-edge (TE) register.

Finally, a baseline restoring circuit (BLR) was added to the feedback loop which assures the clamping of the DC level at the output of the ToT-amplifier to a defined voltage. This is necessary since the discharge process following a deflection of the amplifier by a signal shifts the zero-level in dependence of the signal amplitude. The BLR feeds the difference of the output and a reference voltage back to the input via a voltage controlled current source after limitation of the bandwidth. In this way only the low frequency component is used to inject a compensating charge into the input node which restates the output reference level at a fixed value of $v_{ref}$. The low-pass filter can effectively be designed using exclusively MOSFET structures on the ASIC. The series resistance is realized by the drain-source channel of a FET with its gate shorted to the source. The parallel capacitance is simply formed by the gate-to-channel capacitance of a transistor with appropriate size. The thus achieved cutoff frequencies may be as low as a few Hertz [80].

A comparator following the ToT-stage translates the signals from the analog domain to the digital circuitry of the chip. Its output switches from logical '0' to '1' when the ToT-output exceeds the threshold voltage level $v_{thr}$ provided at the reference input of the comparator. The ToT, which is the time of the signal above the applied threshold level is proportional to the ToT-amplifier input and therefore a direct measure for the charge incident at the preamplifier input. Figure 4.37 illustrates the operation of the ToT-stage and the comparator.

**Noise Analysis** Given the topology of the preamplifier as discussed above and assuming reasonable values for the involved components the noise at the input of the ToT-stage can easily be calculated with the model introduced in Section 3.3.4. Preamplifier, source follower and the pole-zero-cancellation stage form a CSA-Shaper-combination with a fixed shaping time. The integrator time constant $\tau_i$ is set by the preamplifier feedback network $C_1, R_1$, while the differentiator time constant $\tau_d$ is determined by the PZC-network, i.e. $C_2$ and $R_2$. For optimum noise performance both time constants are assumed to coincide ($\tau = \tau_i = \tau_d$).

The voltage noise density depends on the transconductance of the first amplifier transistor. Recall the according relation from Section 3.3.4

$$e_n^2 = 4kT\gamma_n \frac{1}{g_m} + \frac{A_f}{f}, \tag{4.11}$$

with an excess noise coefficient dependent on charge carrier concentration and device geometry empirically determined to be $\gamma_n \gtrsim 0.5$ [93]. The first term corresponds to the equivalent input noise voltage and the second one is due to the $1/f$-noise. The flicker noise contribution coefficient can be expressed in terms of device and technology dependent magnitudes

$$A_f = \frac{K_f}{WLC_g^2}, \tag{4.12}$$

with the width $W$ and length $L$ of the transistor and the capacitance $C_g$ of the gate to the underlying channel which is strongly dependent on thickness and permittivity of the insulation layer. The empirical device constant $K_f$ depends on the transistor type ($n$-or $p$-MOSFET or JFET) and on fabrication technology. Equation (4.12) reveals the various dependencies to which the $1/f$-noise is subject. For the further noise analysis typical values are assumed for $A_f$ obtained from the literature [93, 95, 133]. The input current noise is neglected here since the leakage current of a FET device is usually much smaller than the shot noise caused by the sensor leakage current. The equivalent noise charge at the input of the transistor is

$$q_{na}^2 = 4kT\gamma_n \frac{1}{g_m} \frac{C_d^2}{\tau} + A_f C_d^2 \tag{4.13}$$

depending on the shaping time $\tau$ and the effective sensor input capacitance $C_d$ including all parasitic and stray capacitances and the feedback capacitance if the transistor is configured as CSA-input as discussed above in detail. It is furthermore assumed throughout this document that the input-FETs input capacitance is negligible. For the discussed transistor topology, in fact the input capacitance can be roughly estimated to $C_i \approx 1\,\mathrm{pF}$ assuming typical values for the silicon-to-silicon-oxide interface layer [93, 95] which is indeed much smaller compared to the expected strip capacitances of $C_{strip} \geq 10\,\mathrm{pF}$.

Since the combination of digital and analog circuitry on the same chip substrate is currently only offered in CMOS processes at justifiable costs[13], the following argumentation will exclusively refer to FET devices. Unlike bipolar transistors, the transconductance of FETs is more complicated to describe. In fact, there are three regimes of operation distinguished by the behavior of the normalized transconductance $g_m/I_d$ in dependence of the normalized drain current $I_d/W$ (or current density) as shown in Figure 4.38. This representation of the FET-parameters is chosen for inter-comparability between devices of different geometries [166]. The first region at low current densities showing a constant $g_m/I_d$ is called "weak inversion". The transconductance increases with increasing drain current linearly. At very high currents, the "strong inversion"-region, the normalized transconductance is almost flat as well, but at much lower absolute values. The rapid decrease in the intermediate region is denoted as "moderate inversion". Obviously, $I_d$ increases faster than $g_m$ here.

It can be seen that the preferable mode of operation is in the weak inversion regime since the efficiency, i.e. the transconductance at the cost of the power consumption is at maximum and scales directly with the drain current, i.e. $g_m \propto I_d$ opposed to the strong inversion, where

---

[13] The BiCMOS process technology could be considered as an exception (see [93]).
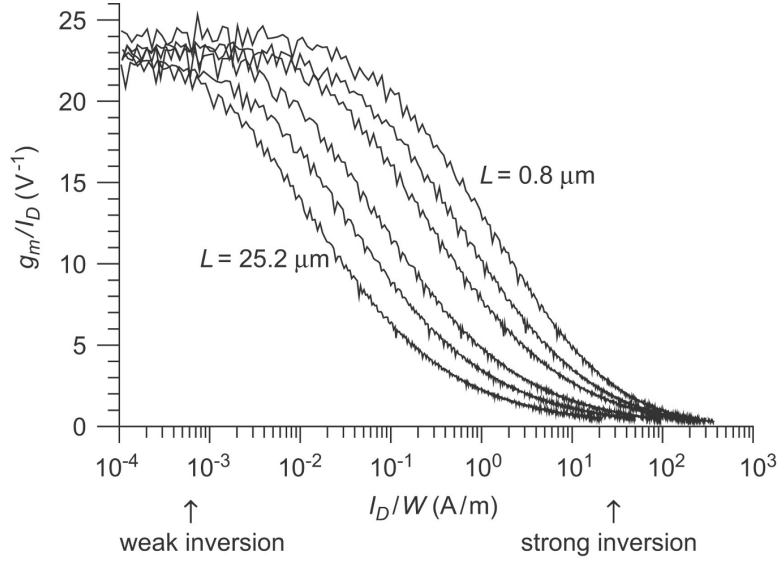
**Figure 4.38.:** Normalized transconductance curves in dependence of the FET-channel current density for different channel lengths [167].

$g_m \propto \sqrt{I_d}$. However, since the minimum achievable noise is the critical design criterion, higher transconductances may become desirable in accordance with eqn. (4.11) which may shift the point of operation into the moderate inversion region.

*Potenza* [80] suggests a design laying out the input MOSFET M1 with a geometrical size of (W/L)=1.5 mm/500 nm and a nominal drain current of 300 µA. This results in a normalized $I_d/W = 0.2\,\text{A m}^{-1}$ and from the normalized transconductance curves in Figure 4.38 extrapolated to a channel length $L = 0.5\,\mu\text{m}$ a value of $g_m/I_d \approx 20\,\text{V}^{-1}$ can be determined. The transistor thus operates in weak inversion. For the transconductance follows a value of $g_m = 6.0\,\text{mS}$ at nominal drain current. All relevant parameters that found input into the noise analysis are comprehended in Table 4.7. The FET is supposed to work in saturation for all considered cases.

| Parameter | Value |
|---|---|
| $(W/L)_{\text{M1}}$ | $1500\,\mu\text{m}/0.5\,\mu\text{m}$ |
| $I_d$ | $300\,\mu\text{A}$ |
| $I_d/W$ | $0.2\,\text{A m}^{-1}$ |
| $g_m/I_d$ | $20\,\text{V}^{-1}$ |
| $g_m$ | $6.0\,\text{mS}$ |
| $\gamma_n$ | $1.0$ |
| $A_f(n/p)$ | $1 \cdot 10^{-12}\,\text{V}^2$ / $2 \cdot 10^{-13}\,\text{V}^2$ |

**Table 4.7.:** Parameters used for noise analysis of the input transistor M1.

For $p$-type MOSFETs the $1/f$–noise is much lower than for $n$-MOSFETs [133]. While for latter transistors associated flicker noise parameter values of $A_f(n) \approx 2\ldots3 \cdot 10^{-12}\,\text{V}^2$ are reported, investigations at $p$-channel FETs with different geometries obtained reproducible values of $A_f(p) \approx 7 \cdot 10^{-14}\,\text{V}^2$ with noise corner frequencies of $f_{nc}(n) \approx 2\,\text{MHz}$

and $f_{nc}(p) \approx 50\,\text{kHz}$, respectively [168]. An increase in noise level of ca. 5% is observed after application of ionizing doses of 50 Mrad and following annealing phase for $p$-MOSFETs. The noise corner frequency increased from 50 kHz to 400 kHz at a total dose of 80 Mrad corresponding to an increase of the flicker noise parameter by one order of magnitude to $A_f(p)_{80\,\text{Mrad}} \approx 6 \cdot 10^{-13}\,\text{V}^2$. The noise increase for $n$-MOSFETS is observed to be significantly larger for the same irradiation dose [168]. A design with $n$-channel MOSFETS in the first noise-critical stage is thus not recommended.

The calculated ENC is reported in Figure 4.39. Single noise contributions are shown for detector capacitances of 10 pF and 20 pF in the upper two figures. The behavior of the ENC in dependence of the connected capacitance is illustrated in Figure 4.39(c) for different choices of the shaping time. Finally, the influence of the drain current of the input transistor M1 on the ENC is shown in Figure 4.39(d). For this last figure the associated transconductance values are obtained in the same way as described above by graphical retrieval of the normalized transconductance $g_m/I_d$ for a given $I_d/W$–value using Figure 4.38.
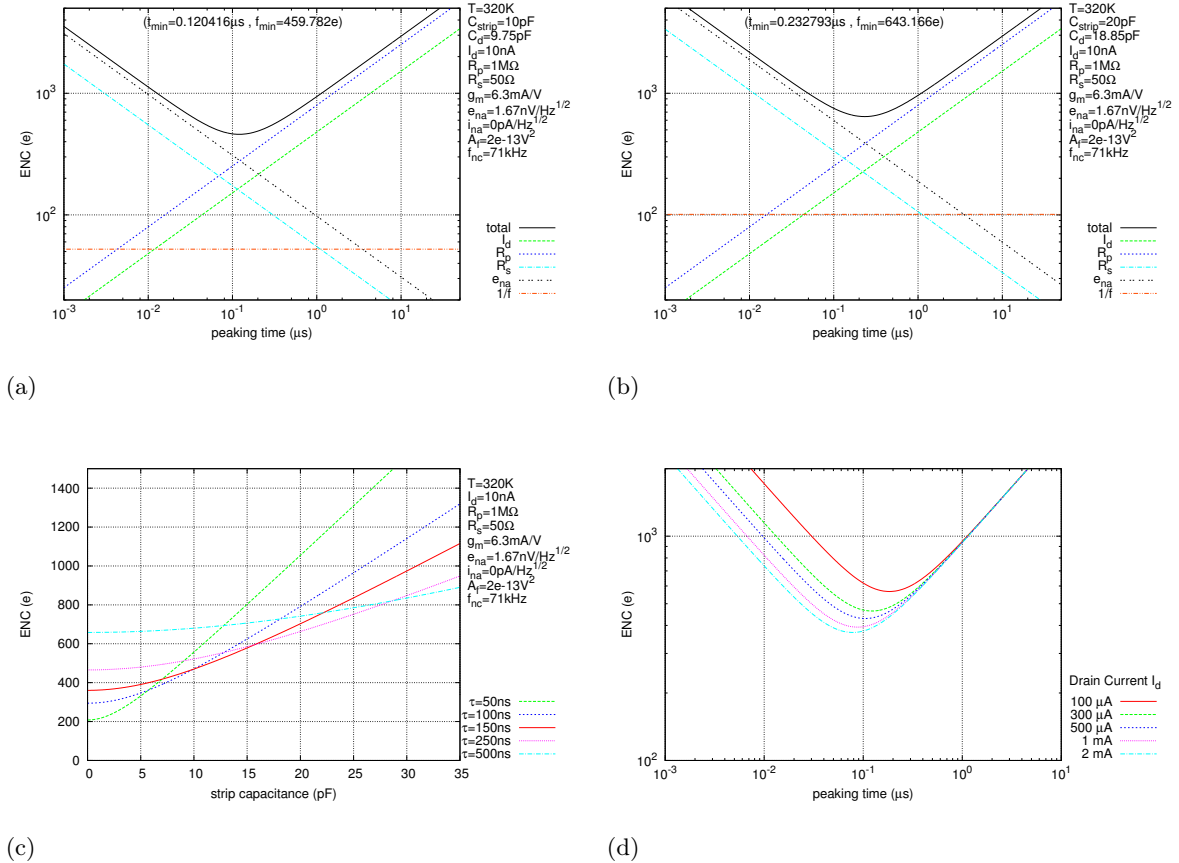


**Figure 4.39.:** Calculated noise of the strip front-end preamplifier taking into account the contribution of the input transistor (M1) only. (a) and (b) Noise in dependence of the shaping time with all fractional contributions for a detector capacitance of 10 pF and 20 pF, respectively. (c) Dependence of the noise on detector load capacitance at different shaping times. (d) Variation of minimum achievable noise and the associated shaping time in dependence of the input transistors drain current ($C_d = 10\,\text{pF}$).

**Caveat to the Noise Analysis**   The calculations presented up to this point assumed the first input transistor M1 as dominant source of the total noise. This is a reasonable hypothesis as long as the closed loop gain of the first stage is sufficiently high to lift the signal out of the noise far enough that the intrinsic noise of all following stages can be neglected with respect to the amplified input noise. Revisiting Equation (3.14) one finds

$$q_{n,tot}^2 = q_{n,1}^2 + \frac{q_{n,2}^2}{G_1} + \frac{q_{n,3}^2}{G_1 G_2} + \frac{q_{n,4}^2}{G_1 G_2 G_3} + \cdots \tag{4.14}$$

The first term describes the noise factor of the first transistor which is immutable. The second term adds the intrinsic noise contribution of the second stage divided by the gain of the first stage. It can thus be neglected if the latter happens to be sufficiently large. In fact, the envisaged design of the preamplifier for the novel DSSD front-end as shown in Figure 4.36 foresees a cascode circuit at the input with a transconductance amplifier M1 with unity gain and a high gain common gate configured FET M2. The argumentation unfurled above concerning noise optimization of M1 should therefore be extended to the following transistor M2 as well[14].

*Potenza* describes a design with a closed loop gain $G_1 = 5$ of the input cascode [80]. Using this value in above Equation (4.14) together with the unity gain $G_2 = 1$ and noise charge $q_{n,2}$ of the source follower stage and the noise contribution of the current buffer $q_{n,3}$ and assuming that the following stages contribute no further noise yields

$$\begin{aligned} q_{n,tot}^2 &= q_{n,1}^2 + \frac{q_{n,2}^2}{5} + \frac{q_{n,3}^2}{5 \cdot 1} \\ &= q_{n,1}^2 + \frac{1}{5} \left( q_{n,2}^2 + q_{n,3}^2 \right). \end{aligned} \tag{4.15}$$

The last equation shows explicitly the high noise contributions of stages two and three, which are the input transistors M11 and M59/M60 (referring to the design of [80]) of the preamplifier buffer and the current buffer[15], respectively which are not negligible. Even if a highly optimized noise contribution of those transistors (similar to the one achieved for M1/M2) is presumed, a fraction of at least 20 % additional noise is added to the total input referred ENC. Raising the gain of the preamplifier could effectively lower this extra noise and relax the layout constraints of the low noise design in the mentioned stages. Alternatively, a second subsequent low noise amplifier stage behind the preamplifier buffer would yield the same result.

However, a further, more detailed analysis considering all noise contributions distinguished by input noise and input referred noise (which was used without differentiation in this analysis) up to the current buffer is strongly encouraged.

**Influence of Radiation on Noise**   The expected radiation field is going to affect all active electronic components inside the MVD in different ways. Naturally, a higher susceptibility to these effects can be found in analog circuitry with high sensitivity or high gain factors. The sensors and the preamplifier stages of the front-ends are such elements. As demonstrated in the previous paragraphs the noise due to the input amplifier strongly depends on characteristic

---

[14] Actually, M1 and M2 form a unified amplifier stage also known as Dual-Gate MOSFET which should be treated appropriately in the noise analysis.

[15] This includes all transistors that contribute to the same drain-current paths as the mentioned ones as well, i.e. current-mirror and buffer transistors.

transistor parameters such as transconductance $g_m$. It has been shown that the transconductance curves of FETs show a strong dependence from ionizing radiation doses particularly in the weak inversion regime [169]. The degradation effects are conveniently comprehended in the excess noise coefficient

$$\gamma_n = \frac{e_n^2 g_m}{4kT} \tag{4.16}$$

rather than considering a device-dependent transconductance. Exemplary studies at PMOS-FETs with large widths and small lengths at $I_d/W$-ratio of $0.2\,\mathrm{A\,m^{-1}}$ showed an increase of $\gamma_n$ from 1.40 to 2.15 after a $^{60}$Co irradiation to 5 Mrad [169, 170]. Since the dependence of the white noise charge is $q_n \propto \sqrt{\gamma_n}$ (cf. Equation (4.13)), this would result in an increase of the ENC by approximately 25 %. The behavior of the $1/f$–noise is more difficult to parameterize since not only $A_f$ increases by a factor of roughly 5 to 10 after a 5 Mrad dose, but also the structure of the low frequency component changes substantially [170].

The calculated ENC for different irradiation scenarios is reported in Figure 4.40. Beside the pre-irradiated state (a), noise figures are computed for the before-mentioned 5 Mrad post-irradiation values for $\gamma_n$ and $A_f$ (b) and additionally for realistically increased sensor leakage currents as a consequence of the irradiation (c) and (d). It can be noticed that the increased shaping time for optimum ENC as a result of the pre-amp irradiation is heavily counteracted by the strongly increased shot noise due to the excessive sensor leakage at high irradiation doses shifting the best-noise shaping times to values as low as 40 ns compared to a pre-irradiation value of $\approx 300$ ns.

Another radiation induced effect observed in MOSFETs changes the free path of holes at their movement from the gate electrode through the $SiO_2$-Si junction. Holes get increasingly trapped with the applied radiation dose while electrons are not. This leads to a build-up of space charge in the oxide layer and, consequently, to a change of the gate voltage belonging to the same drain current, and thus, to a shift in transconductance and gain [169]. This phenomenon can be counterbalanced by adjusting the gate voltages by DACs and setting the operational points by current mirrors wherever possible.

**ToT-Noise**   The signal at the input of the comparator is sampled at equidistant, discretely spaced times dictated by the time-stamp clock (TSC). This imposes a digitization jitter to the acquired leading and trailing edges irrespective to the RMS-noise at the input of the comparator. The sampling of an asynchronous event by means of a synchronous clock with period $\Delta t_{ts}$ causes an uncertainty characterized by the first moment of the timing distribution:

$$\sigma_{t,dig}^2 = \frac{1}{\Delta t_{ts}} \int\limits_{-\frac{\Delta t_{ts}}{2}}^{\frac{\Delta t_{ts}}{2}} t^2 \mathrm{d}t = \frac{\Delta t_{ts}^2}{12} \tag{4.17}$$

This "aperture jitter" applies to both, the leading as well as the trailing edge and has to be summed up in quadrature to account for the digitization noise of the ToT-value.

On the other hand, a fluctuation imposed on the voltage at the input of the comparator generates an uncertainty in the precise time in which the signal crosses the threshold level. It can be easily understood that this time is the better determined the more rapidly the voltage traverses the threshold. Therefore the slope of the discharge of the feedback capacitor
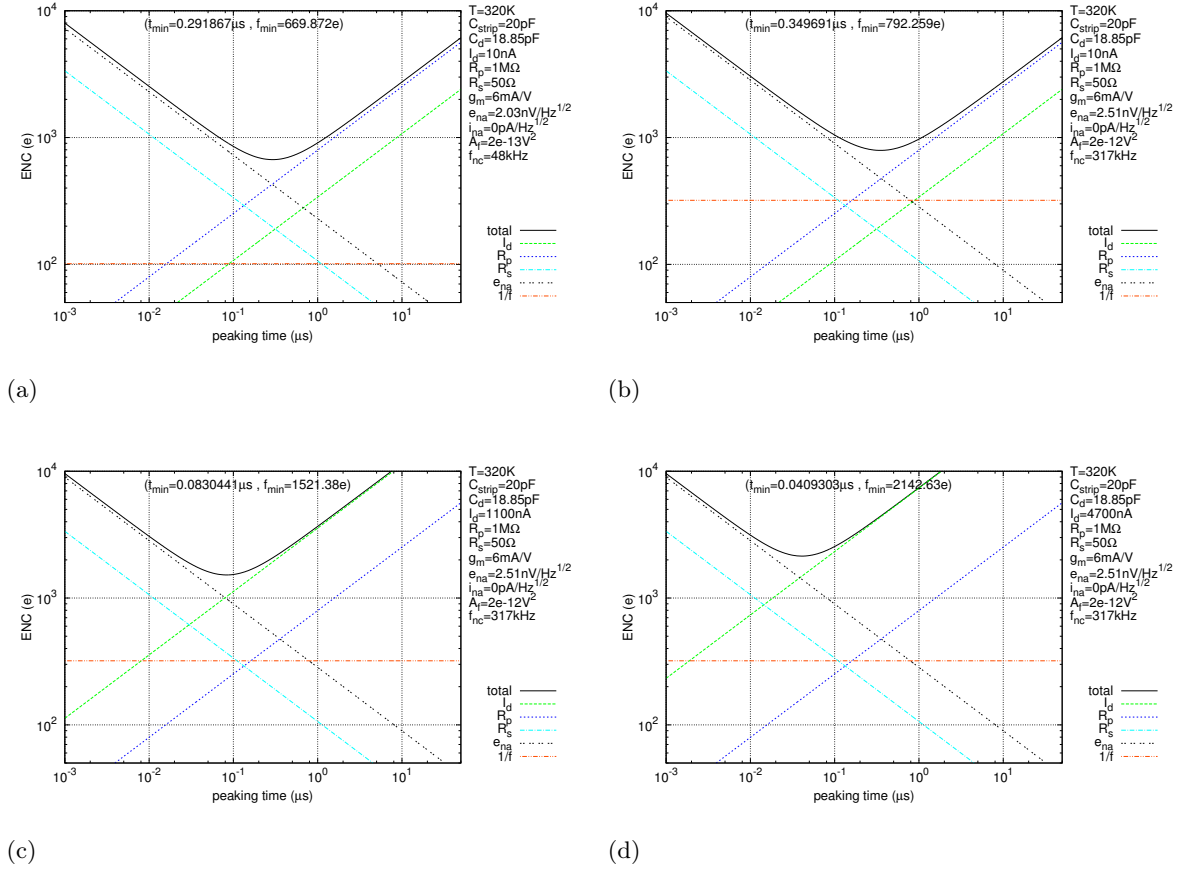
**Figure 4.40.:** Expected ENC under different irradiation scenarios. (a) Noise in dependence of shaping time without assumed infliction of radiation effects (Pre-Rad scenario, $\gamma_n = 1.4$) (b) Noise of the preamplifier only (with connected un-irradiated sensor) after an accumulated ionizing dose of $5\,\mathrm{Mrad}$ ($\gamma_n = 2.15$) (c) as before, but with sensor irradiated to $2.5 \cdot 10^{13}\,\mathrm{n_{1MeV\,eq}\,cm^{-2}}$ and (d) with sensor irradiated to $1 \cdot 10^{14}\,\mathrm{n_{1MeV\,eq}\,cm^{-2}}$. All noise calculations are performed for an assumed detector capacitance $C_d = 20\,\mathrm{pF}$.

$C_{fb}$ inside the ToT-stage determines the amplification of the RMS-noise $\sigma_{v,tot}$ present at the comparator input resulting in a ToT-jitter of

$$\sigma_{t,tot} = \frac{\sigma_{v,tot}}{\frac{\mathrm{d}V_{tot}}{\mathrm{d}t}} = \frac{\sigma_{v,tot}C_{fb}}{I_{fb}}. \tag{4.18}$$

The overall timing jitter of a sampled ToT-value then is the quadratic sum of both contributions

$$\sigma_t^2 = 2\sigma_{t,dig}^2 + \sigma_{t,tot}^2. \tag{4.19}$$

The factor of two in the first term is due to the fact that the ToT-value contains the jitter of the leading-edge *and* and the trailing-edge values and is equal to their difference.

Obviously, a lower jitter can be obtained for high ToT-gains, i.e. high discharge currents. This in turn reduces the effective ToT-resolution having the same charge digitized in less clock cycles and thus deteriorating the ToT-precision by the relatively higher aperture jitter $\sigma_{t,dig}$. An optimization for the most probable encountered ToT-value (corresponding to the MPV of

the particle energy loss) would reasonably minimize the jitter of both contributions by setting them equal ($\sigma_{t,tot} = \sqrt{2} \cdot \sigma_{t,dig}$). With eqn. (4.19) this results in the best achievable timing resolution for the most probable ToT-value

$$\sigma_{t,min} = 2\sigma_{t,dig}. \tag{4.20}$$

Operation of the envisaged front-end with a TS clock frequency of 155 MHz yields a value for the best possible MPV timing resolution of

$$\sigma_{t,min} = 3.72 \, \text{ns}.$$

Finally, the required discharge current, adjustable through a DAC-register in the front-end implementation, obtains ideally

$$I_{fb} = \frac{\sigma_{v,tot} C_{fb}}{\sqrt{2} \cdot \sigma_{t,dig}}. \tag{4.21}$$

It must be emphasized again that this condition paraphrases the theoretical best possible timing resolution for ToT-values in the vicinity of the MPV of the energy loss only. Dynamic range, on the other hand compromises ToT-resolution at low values. An optimization for the actually required configuration with respect to parameters like sensor charge, pre-amp ENC, max. ToT and others through appropriate adjustment of the ToT-gain is advisable.

Figure 4.41 illustrates an example of the encountered noise during a threshold scan with varying externally injected charges measured with an FE-I3 pixel front-end [171]. This ASIC [172] exhibits a ToT-stage similar to the one of the ToPix, and consequently to the one planned for the DSSD strip front-end. The number of registered hits increases rapidly in
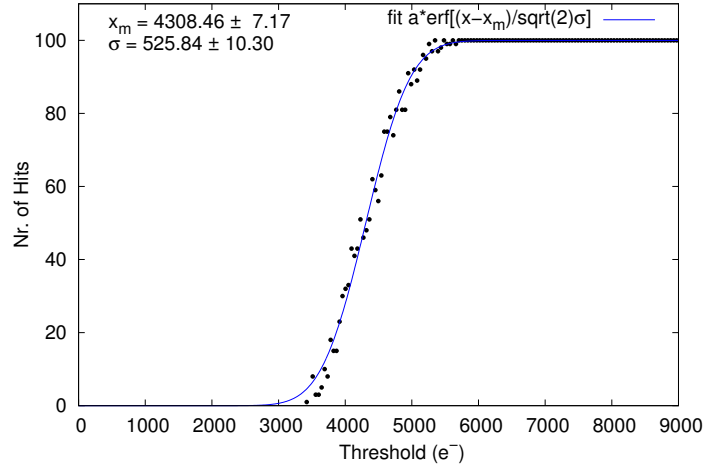


**Figure 4.41.:** Threshold Scan ("S-Curve") for a single cell of the FE-I3 pixel front-end obtained by repeated injection of successively increasing charges. In the vicinity of the comparator threshold level the number of registered hits increases rapidly. The slope of the transition is determined by the total noise superimposed on the signal at the comparator input.

the region of the threshold while gradually raising the calibration amplitude. The inherent noise leads to a smeared-out response function of the discriminator precisely characterized by the convolution of a step function with a *Gaussian* leading to the probability density distribution

$$\phi(q) = \text{erf}\left(\frac{q - q_{thr}}{\sqrt{2}\sigma_n}\right) \tag{4.22}$$

with the width of this commonly called "S-Curve" related to the total noise by $\sigma_n$.

A recorded transfer characteristic of the ToT-stage for the FE-I3 front-end is depicted in Figure 4.42 for different ranges of input charge. While a strongly linear dependence of the ToT-length from small input signals can be noticed in the left figure an increasingly compressed response at higher charge amounts is encountered (right figure).
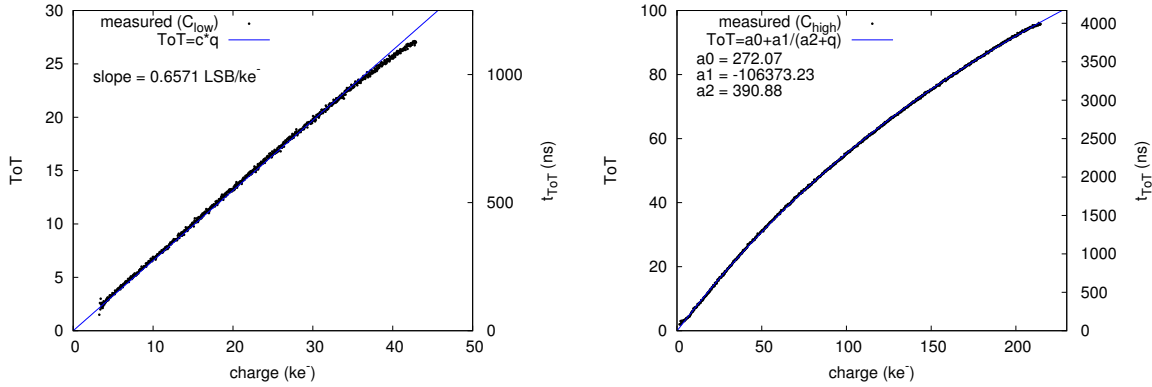


**Figure 4.42.:** ToT-characteristics of the FE-I3 pixel front-end for low feedback capacitance (left) and high capacitance setting (right). In the lower input charge regime ($\lesssim 35\,\text{k}e$) a linear relation to the ToT-value can be noticed. For higher charges the ToT experiences a dynamic compression behavior.

### 4.3.3.4.  Digital Part

The digital read-out scheme introduced for the ToPix pixel read-out chip was already discussed in detail above. The digital architecture is supposed to be adapted without larger complications. Since the number of channels required for read-out in the strip front-end chip is much smaller than in the pixel case, the utilization of only one double column read-out is sufficient. A multiplexer for the End-of-Column logic (cf. Figure 4.30) thus is not needed and the chip read-out logic greatly simplifies. In return, the EoC FIFO-buffer could be extended to 64 cells.

A major difference of the strip front-end chip to the ToPix will be made up by the expected hit rates per channel due to the differing ratio of active channel areas. Arising implications to the digital front-end architecture will be discussed in the next section.

**Output Format**   The read-out of the EoC buffer will be managed by a serializer operated with a clock frequency $f_{ro}$ whose value is still to be specified. The ToPix 3.0 design currently foresees this clock to be identical with the time-stamp clock, i.e. $f_{ro} = f_{ts} = 155\,\text{MHz}$. Future implementations propose the transition to the GBT E-Link [35, 173, 174] with maximum data rates of 320 Mbit/s.

The custom data format currently in use with the ToPix 3.0 prototype serializes the hit data belonging to the same time-stamp cycle into frames with a varying number of hit data words (see Figure 4.43). A frame consists of a header word and a trailer word embracing a number of at least one data word. Each of those word types are 40 bits wide. An event thus contains at least a count of 120 bits. With a readout rate of 155 MHz a limiting rate of
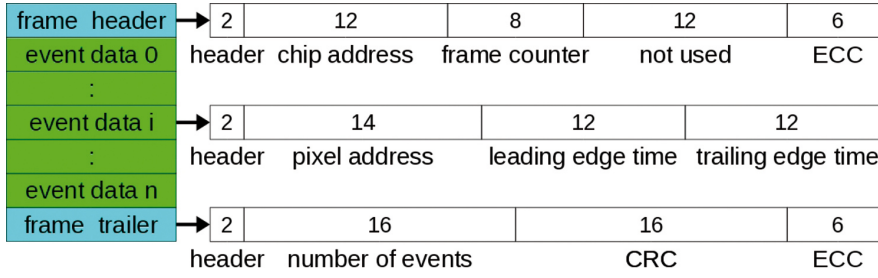
**Figure 4.43.:** ToPix output data frame [35].

$1.3 \cdot 10^6$ hits per second results at maximum throughput. A further increase of the allowable front-end hit rate may be achieved by the utilization of the GBT E-Link as already briefly mentioned. A GBT frame consists of 120 bits, where 80 bits are available for payload data. Using one GBT-frame for one hit-word leaves plenty of space for additional information like FE-ID status bits etc. A frame can be distributed among several physical links with different configuration options [173, 175] as listed in Table 4.8. The highest throughput at lowest line-count is achieved by configuring the transmission speed to 320 Mbit/s using a subgrouping of two links. With this configuration a continuous, lossless transmission of hit data up to a

| Mode | Type | Data Rate (Mb/s) | Notes |
|------|------|------------------|-------|
| OFF | Power off | – | E-link group powered off |
| 2× | serial/parallel | 80 | 8 E-links per group |
| 4× | serial | 160 | 4 E-links per group |
| 8× | serial | 320 | 2 E-links per group |

**Table 4.8.:** Configuration options for a GBT E-link group [175].

rate of $5.3 \cdot 10^6$ hits per second per FE is achieved. The maximum peak rate in the region of highest occupancy within the MVD strip tracker taken from [164] on the other hand accounts to $\lesssim 5.5 \cdot 10^6 \, \mathrm{s}^{-1}$. The chosen link topology should therefore be able to cope even with the highest possible hit rates inside the $\overline{\text{P}}$ANDA-MVD under consideration of following caveats

- The interaction rate peaks at the beginning of the beam cycle due to injection of antiprotons into the HESR as can be retrieved from Figure 1.17 and decays continuously. The absolute maximum hit rate of $\lesssim 5.5 \cdot 10^6 \, \mathrm{s}^{-1}$ given above thus sustains for an infinitesimal short time period only. The extended EoC FIFO assures to buffer short periods of higher hit rates than $5.3 \cdot 10^6$, which is the maximum sustained rate that can be transferred without losses off chip.

- The simulations in [88] assumed longer strip lengths along the $z$-axis (parallel to the beam axis). Therefore the corresponding rates are overestimated.

- From those simulation results only the absolute upper limits for the peak rates are taken. The true peak rates are expected to be lower.

The output interfacing circuitry will be implemented by differential drivers in order to reduce pick-up noise which couples on the common-mode of the transmission line and therefore is suppressed effectively in the receiver during reconstruction through subtraction of voltage

levels on both differential lines. In the latest ToPix prototype, buffers using the SLVS[16]-standard [165] were successfully implemented [35]. SLVS is a preferred choice over e.g. LVDS[17] or LVPECL[18] due to lowered voltage swings and common mode levels which greatly reduces power consumption. Galvanically isolated transmission and encoding of the data stream for DC-level balancing will be described in somewhat greater detail in Section 4.4.6.

### 4.3.3.5. Hit Rates

For the layout of the digital front-end and the hit correlator capabilities implemented in the MDC a proper knowledge of the expected hit rates is of utmost importance. On the other hand, however, the detector system is going to deal with inevitable noise as described in full detail in section 3.3.4. Since the $\overline{\mathsf{P}}$ANDA silicon strip tracking system will utilize a threshold discriminating front-end, special attention must be paid to the tuning of the discriminator regarding signal and noise levels in order to

- maximize the susceptibility to signal hits
- minimize noise hits

Both optimization efforts counteract each other. The optimal operating point therefore represents a compromise between signal sensitivity and noise occupancy providing that either contribution is fully understood.

**Signal Hit Rate**   Due to the almost unmodulated nature of the antiproton beam inside the HESR on small time scales and the quasi-continuous stream of target material through the beam aperture a poissonian distributed pattern of primary events is to be expected. Given an average event rate $r$, the probability for a number $n$ of hits in a determined time interval $\Delta t$ can be calculated with:

$$P(n) = \frac{(r\Delta t)^n \exp{(-r\Delta t)}}{n!}. \tag{4.23}$$

Assuming an estimated peak rate of $\simeq 0.07\,\mu\text{s}^{-1}$ per channel for the parts of the MVD strip tracker with the highest occupancy during operation of the $\overline{\mathsf{P}}$ANDA detector in high luminosity mode of the HESR as reported by *Würschig* [164], the probabilities for at least one, two and three more hits within the maximum ToT-interval leading to a pile-up condition are reported in Table 4.9 for different ToT-ranges from 7 to 10 bits. Those values should be seen as absolute maximum probabilities since the average, or more precise, most probable ToT-length is far below the maximum ToT and is given by the particles energy loss distribution and the available dynamic range. Evaluating the pile-up probability for a ToT-range of 8 bits demanding at least one hit inside the corresponding dead time of 1.65 µs for instance yields a maximum of 10.9 % pile-up at the given rate. One possibility to circumvent this loss of events is the introduction of one additional independent ToT-stage which gets connected to the preamplifier output when the first stage currently discharges an earlier registered charge. Additional switching and busy-flag logic would be required beside the instantiation of the extra ToT-electronics inside the channel cell. The probability for locking up both ToT-stages now requires to accumulate at least two hits inside the dead-time interval of a maximum ToT-deflection and can be obtained

---

[16] Scalable Low-Voltage Signaling.
[17] Low-Voltage Differential Signaling.
[18] Low Voltage Positive Emitter Coupled Logic.

|            |           | pile-up probability | | |
| ToT range | dead time | $P(n > 0)$ | $P(n > 1)$ | $P(n > 2)$ |
| (bits) | ( µs) | | (percent) | |
| 7 | 0.83 | 5.6 | 0.16 | 0.003 |
| 8 | 1.65 | 10.9 | 0.62 | 0.02 |
| 9 | 3.3 | 20.6 | 2.3 | 0.17 |
| 10 | 6.6 | 37.0 | 7.9 | 1.2 |

**Table 4.9.:** Pile-up probabilities calculated for various ToT-ranges and multiplicities ($f_{ToT} = 155\,\mathrm{MHz}$).

from the above table from the $P(n > 1)$-column. For otherwise same conditions as above, the corresponding pile-up probability with two active ToT-stages now yields $0.62\,\%$ compared with over $10\,\%$ comprising just one ToT-stage. A further decrease of the pile-up probability down to $0.2\,‰$ as well as the associated effective dead-time may be achieved with a third ToT-stage. Instantiation of further ToT-blocks should not yield a significant gain any more.

The read-out of additional ToT-blocks per channel cell can easily be coordinated by the EoC-Logic. A cell output buffer merely must coordinate the addressing of the correct ToT-stage e.g. based on a cyclic assignment of ToT-blocks.

**Noise Hit Rate**   Since the noise amplitudes ideally follow a *Gaussian* distribution, a first measure would be to raise the detection threshold to a level which minimizes the frequency of encountered noise hits to a minimum while still being sensitive to a maximum of signal hits. This implies that the noise hit frequency at any threshold level and, thus, also at a threshold of zero is known. It turned out, that this rate can be derived if the frequency response of the entire system up to the discriminator is known. In fact, the systems transfer function is mainly determined by the shaper whose parameters are fortunately well established.

A tedious analysis of the time domain response of an ideal band-pass filter with cutoff frequencies $f_{lp}$ and $f_{hp}$ of the low-pass and the high-pass components, respectively, yields the frequency of zero crossings at the output of the shaper [176, 177]:

$$f_0 = 2\sqrt{\frac{1}{3}\frac{f_{lp}^3 - f_{hp}^3}{f_{lp} - f_{hp}}}. \tag{4.24}$$

This result can be evenly applied to the output of a *CR-RC*-shaper if the cutoff frequencies are replaced by the $3\,\mathrm{dB}$-corner frequencies for the noise voltage. Assuming, that the lower cutoff frequency of the shaper does not significantly contribute to the noise rate[19], Equation (4.24) simplifies to

$$f_0 = \frac{2}{\sqrt{3}}f_{lp}. \tag{4.25}$$

The more conveniently used shaping time constant $\tau$ is related to the noise bandwidth of a low-pass filter through

$$f_{lp} = \frac{1}{4\tau} \tag{4.26}$$

---

[19] This assumption is justified for a single pole *CR-RC*–stage since the noise cutoff frequencies are related by $f_{lp} = 4.5 f_{hp}$ [93].

and the fact that the noise rate is just half the number of zero crossings delivers the wanted dependence of noise rate at zero threshold level $f_{n0}$ and the shaping time:

$$f_{n0} = \frac{1}{4\sqrt{3}\tau}. \tag{4.27}$$

Now the interesting quantity is the expected noise rate in the presence of a threshold. A hit event is registered if the charge at the discriminator input exceeds this threshold. Since the amplitudes of the noise are distributed following the *Gaussian* distribution, one expects an exponential decrease of the noise rate with increasing threshold level. On the other hand, the length of noise pulses follows a *Gaussian* distribution as well which imposes a limit to the actual noise rate. Once the discriminator is triggered by a noise event, a certain time passes after which the voltage level crosses zero toward the positive range again eventually. Thus the combined *Gaussian* probabilities for amplitude *and* time distributions lead to an expression for the noise rate in dependence of the threshold level [178]:

$$f_n = f_{n0} \exp\left(\frac{-Q_t^2}{2Q_n^2}\right) = \frac{1}{4\sqrt{3}\tau} \exp\left(\frac{-Q_t^2}{2Q_n^2}\right), \tag{4.28}$$

where $\frac{Q_t}{Q_n}$ defines the charge ratio of the threshold to noise levels. Alternatively, the corresponding voltage or digit-ratios are used instead, if applicable. A variety of noise rates calculated according to Equations (4.27) and (4.28) at threshold of zero and threshold-to-noise ratios of $3\sigma_n$, $5\sigma_n$ and $7\sigma_n$ are reported in Table 4.10. These rate-estimates do not take into account effects introduced by digital circuitry like discriminator dead time, pipeline read-out cycles or FIFO stalls by overflows etc., which impose serious limitations to the actual rate when the discriminator toggle frequency is situated in the same order of magnitude like the system's read-out frequency.

| peaking time ( ns) | $f_{n0}$ ( $\mu s^{-1}$) | noise rate ( $s^{-1}$) for threshold | | |
|---|---|---|---|---|
| | | $3\sigma_n$ | $5\sigma_n$ | $7\sigma_n$ |
| 50 | 2.89 | 32.1 k | 10.8 | $6.6 \cdot 10^{-5}$ |
| 100 | 1.44 | 16.0 k | 5.4 | $3.3 \cdot 10^{-5}$ |
| 150 | 0.96 | 10.7 k | 3.6 | $2.2 \cdot 10^{-5}$ |
| 200 | 0.72 | 8.0 k | 2.7 | $1.7 \cdot 10^{-5}$ |
| 250 | 0.58 | 6.4 k | 2.2 | $1.3 \cdot 10^{-5}$ |
| 300 | 0.48 | 5.3 k | 1.8 | $1.1 \cdot 10^{-5}$ |
| 500 | 0.29 | 3.2 k | 1.1 | $6.6 \cdot 10^{-6}$ |
| 1000 | 0.14 | 1.6 k | 0.5 | $3.3 \cdot 10^{-6}$ |

**Table 4.10.:** Expected noise rates for various shaping times.

Using eqn. (4.28), a required threshold-to-noise ratio can be computed for any given noise rate:

$$\frac{Q_t}{Q_n} = \sqrt{-2\ln\left(4\sqrt{3}f_n\tau\right)}. \tag{4.29}$$

This expression is useful, when e.g. the noise rate $f_n$ was determined experimentally with a given setup.

## 4.4. Module Data Concentrator ASIC (MDC)

The digitized data streams emerging from each front-end on a single detector module require to be routed out from the MVD volume. This scheme, however, brings up a couple of problems which are efficiently resolved or even avoided by the introduction of an intermediate multiplexing stage on module level. Initial key parameters and first iteration of design and ideas about the implementation are going to be discussed in the next sections.

### 4.4.1. Overview

On each detector module a number of front-end chips with a count of 128 channels per front-end will be utilized for the read-out of $p$- and $n$-sides of the sensor. Assuming a number of $M$ and $N$ front-ends for the read-out of both sides this would result in an amount of $N+M$ differential signal pairs[20] to be routed off the module. Multiplexing those data streams into a single or a small number of links exhibiting a higher bandwidth would mean a significant reduction of physical signals required to route away the complete data. An overview of the proposed layout of the on-module electronics and its interconnection is illustrated in Figure 4.44. The MDC implements the multiplexer of $M$ top side and $N$ back side front-end inputs acting on up to $K$ output links, depending on the expected data rates. As shall be demonstrated later, the bandwidth of the multiplexed links can be smaller than the sum of the single front-end bandwidths. One of the novel design features of the MDC will be the implementation of a 1d-clustering stage and a 2d-cluster correlation processor. This latter feature requires the particular connection scheme of sensor top and backside front-end outputs to separate MDC port groups FEINA(1...M) and FEINB(1...N). The following list summarizes the tasks to be executed by the proposed MDC ASIC:

- reception, decoding and buffering of front-end datagrams

- ordering of hits in event intervals based on the hit timestamps

- one-dimensional cluster finder

- two-dimensional cluster correlation processor

- bidirectional interface(s) to back-end sided electronics

- slow control processor for adjustment of individual front-end specific as well as MDC specific parameters, monitoring and calibration

The last point includes the logic to interface the control entities of each connected front-end via the front-end control ports FECONA and FECONB via multidrop busses as shown in Figure 4.44.

---

[20] For the transmission of signals a physical connection via a differential conductor pair with defined impedance is assumed, as e.g. the LVDS standard complies to.
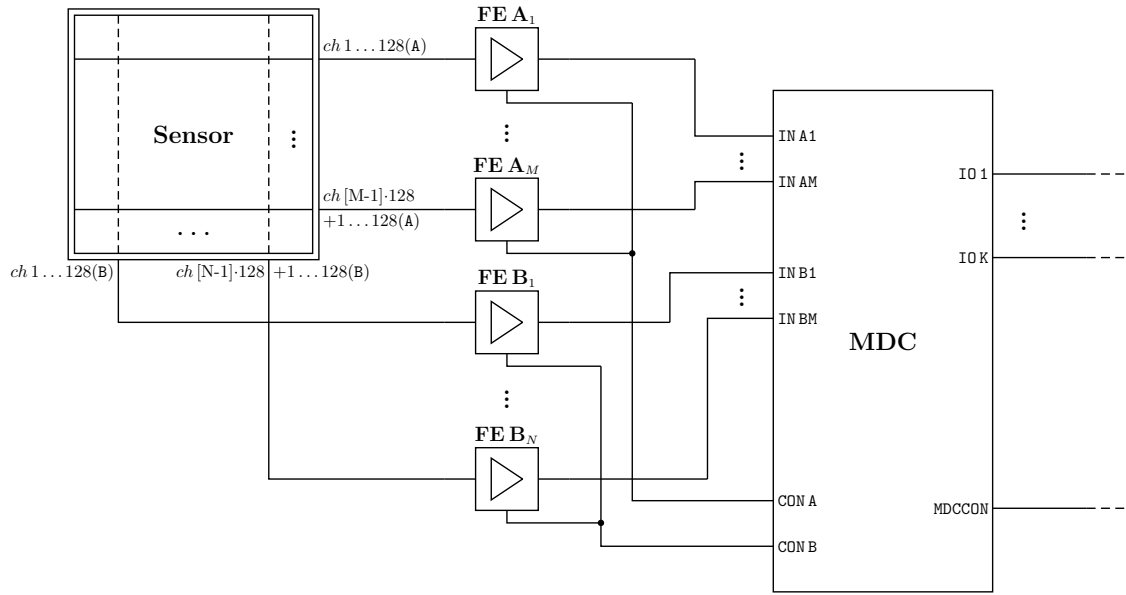
**Figure 4.44.:** Schematic of the connections between front-ends and MDC on a single sensor module. The outputs of $M$ front-end chips of the sensor's $p$-side and $N$ front-ends of the $n$-side are fanned into the MDC to the corresponding inputs INA1...INAM and INB1...INBN, respectively. The front-end slow control ports are served by the front-end control lines CONA and CONB of the MDC. The MDC itself is controlled by the MDCCON port on the DAQ side consisting of clock, reset and other control lines as well as synchronization and slow-control signals. The connection to the DAQ electronics is accomplished by scalable serial links via IO1...IOK.

## 4.4.2. Architecture

As already pointed out, the MDC has to be able to gather the serial data streams on event basis from each connected front-end and translate them to a single multiplexed stream. The incoming datagrams have to be decoded and interpreted by the FE input stages in the following manner (in the given order):

1. Decode level balanced encoded data stream. The algorithm to be applied is most likely the 8b/10b decoding scheme corresponding on the actual encoding impressed onto the data by the front-end.

2. Find Start-of-Event (SOEV) bit pattern marking the head of a valid data word.

3. Extract leading edge (LE) and trailing edge (TE) values from data word and calculate ToT. Correct for time stamp counter wrap-around.

4. Validate data word by check against included CRC-checksum code. Tag event in Error Register if not successful. Otherwise enqueue hit in main hit ring-buffer (HRB) at the position given by the LE-value for time reordering. Transcode and enqueue hit in raw hit output FIFO (L1FIFO) for read-out of unordered hit data if this output mode is selected.

A schematic overview of the internal MDC architecture is given in Figure 4.45.

Furthermore the data contained in the front-end datagrams or the data packets retrieved from any of the higher stages of the MDC's data processing sections will have to be transcoded

into appropriate data packets. They will be referred to as MDC-data packets. An overview of the different MDC-data packet types is given in Figure 4.48.
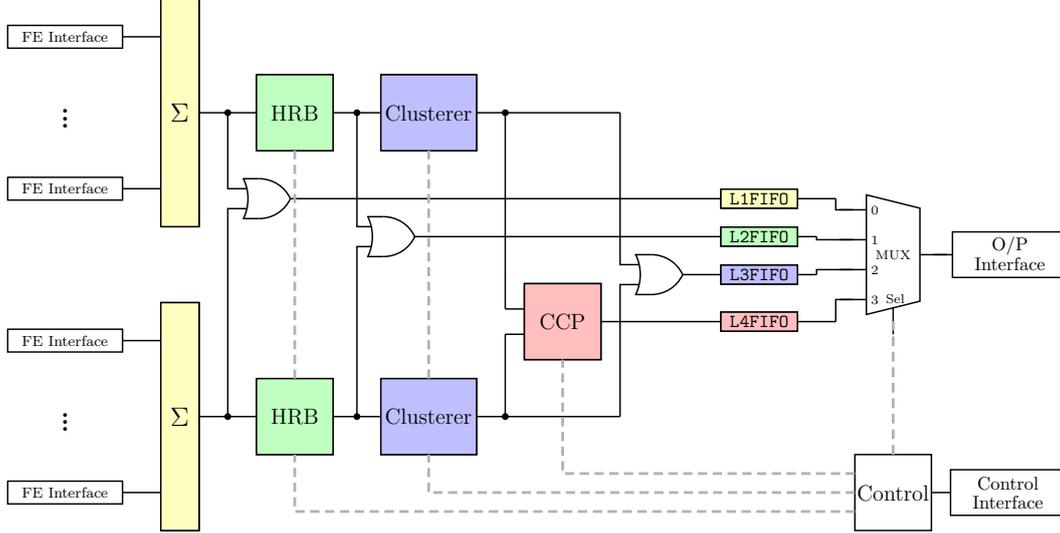


**Figure 4.45.:** Overview of the internal architecture of the proposed MDC. Via the control interface data packets at different stages of the processing chain can be selected for read-out through the output multiplexer: Unordered hit data packets (yellow), time ordered hit packets after the HRB (green), cluster-centroids and -sums after the 1d-clustering stage (blue) as well as 2d-hit points after the CCP (red). The corresponding stage outputs are buffered by the FIFOs L1FIFO...L4FIFO (HRB=Hit Ring-Buffer, CCP=Cluster Correlation Processor).

The input process[21] described above continuously samples all incoming hit words and fills them into the HRB according to the actual event time-stamp given by the LE-value to compensate for the different times of arrival (ToA) of the data packets in dependence of the ToT. A simple scenario illustrating this timing sequence is shown in Figure 4.46. The minimal HRB-length is given by the largest time-stamp period. The reason for this constraint can be found in the fact that the data-packets are emitted at the trailing edge of the event and thus exhibit a latency equal to the time-over-threshold. Time-stamps delivered by arriving packets in this case can be assigned uniquely to the actual epoch only. If the LE-value refers to a preceding epoch, the retrieved time-stamp is ambiguous and thus unusable. Therefore, it must be assured that hits with the maximum possible ToT-value can still be related to the current TS-epoch according to their LE-value. However, additional buffer capacity should be foreseen since the transmission of a hit packet from the front-end may be delayed e.g. when the front-end's output FIFO is well filled due to high hit occupancy. For these cases, a delay of $N_{delay,max}$ packet readout cycles must be anticipated, where $N_{delay,max}$ denotes the maximum number of time intervals which are needed to expose the packet to the read-out stream. An additional read-out cycle should be regarded for the decoding of the data-packet in the MDC input stage. Each interval $\Delta t_{Packet}$ consists of the number of bits inside the data-packet $N_{bits}$ multiplied with the time interval of the read-out clock $\Delta t_{ro}$. The minimum number of total time-stamp cells which have to be provided for the HRB thus can be estimated with

$$N_{\mathrm{HRB}} = 2^{N_{ts}} + \frac{(N_{delay,max} + 1)\, N_{bits}\Delta t_{ro}}{\Delta t_{ts}}, \qquad (4.30)$$

---

[21] To be understood as synchronous process described in HDL.
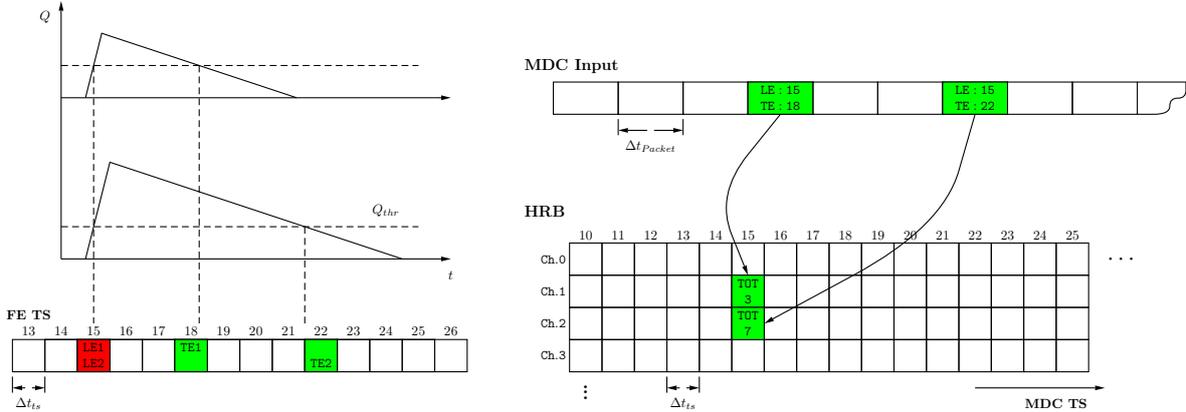
**Figure 4.46.:** Example for the timing sequence of hits in two different channels of one front-end by registration of leading edge (LE) and trailing edge (TE) asserted by the Time-over-Threshold-discriminator in discrete time-bins $\Delta t_{ts}$ of the time-stamping (TS) clock (left). The data packet is queued for read-out in the front-end output FIFO once the trailing edge of the pulse-shape is detected, even if two events exhibit the same event time marked by the LE-value. An example output sequence seen by the MDC input decoder provides the corresponding data packets of the hits at different read-out-times separated by multiples of the read-out-time interval $\Delta t_{Packet}$ (upper right). In the subsequent decoding process the data packets are enqueued according to the LE-time into the Hit Ring Buffer (HRB) array thus compensating for the differing times of arrival (lower right). The HRB, here depicted as two-dimensional array for the sake of illustration, is actually implemented as linear array of FIFOs.

where $N_{ts}$ denotes the bit-length of the TS counter in the front-end data words. Implementing an HRB of this size means that a) events with ToT-values beyond the maximum ToT[22] and/or b) data packets that arrive later than $N_{delay,max}$ packet cycles from the front-ends can not be queued into the HRB anymore. The packet must be considered lost, the event with the according event time stamp considered faulty. An appropriate error count in the Error Register should reflect each event affected by this condition.

A second, concurrent process manages the read-out of the HRB array. It consists of a pointer which is cycling around the ring-buffer with the same frequency that defines the front-end time-stamp clock $f_{ts}$. This pointer will be referred to as Read-Out Pointer (ROP) in the subsequent text. Initially, all time-stamp counters are reset to zero. With evolving time, hit packets arrive eventually filling the HRB from left to right. The ROP moves on to the right synchronous to the front-end time-stamp clock with a fixed offset. This offset is an adjustable parameter and shall be denoted as read-out latency (ROL). If this offset is set to zero, the ROP runs behind the current TS with the maximum distance of the HRB length. It may be desirable to shorten this distance by increasing the ROL in order to adapt to differing ToT-gains and to optimize read-out latency. The column marked by the current ROP is then tagged for read-out. All hit packets inside this column will be transferred to the next stage, a FIFO of ordered hit packets combining the read-out of all HRBs assigned to the connected front-ends. Furthermore, the time-stamp column pointed to by the ROP can be extended to one ore more neighboring columns in succeeding TS direction. The hit packets visible in the resulting aperture of width $w$ are then taken to the HRB output FIFO instead of just a single column. For this case the ROP moves forward by $w$ columns every $w$ TS clock cycles, such that the average ROP movement still remains synchronous to the time-stamp clock. An

---

[22] This case may indeed commence when the TS counter wraps twice before the trailing edge is detected.

illustration of the discussed HRB operation is given in Figure 4.47. Note, that the HRB is
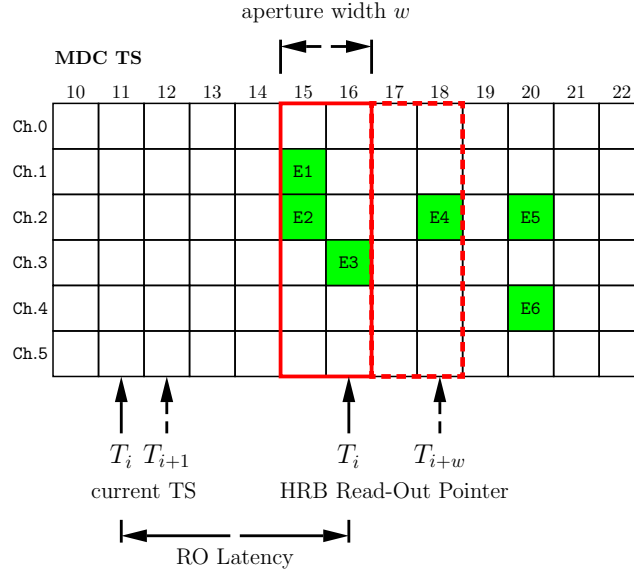


**Figure 4.47.:** Illustration of the HRB readout process. The read-out pointer (ROP) marks the FIFO which holds all hits with the LE equal to the ROP. All hits inside the aperture characterized by width $w$ is transferred to the next stage in the read-out process. The ROP evolves forward by $w$ cells each $w$ TS clock cycles. The current time-stamp, i.e. the LE-time which hits with a ToT of zero and no read-out delay would exhibit, moves synchronous to the ROP with a distance of $N_{\text{HRB}}$-ROL (see text).

actually implemented as linear array of FIFOs with multiplicity $N_{\text{HRB}}$ and shallow depths of $\mathcal{O}(20)$ depending on the available memory space in the final implementation. Thus, events exhibiting higher hit multiplicities than this depth will be truncated. This state should be detected by FIFO-full flags and treated as an error condition appropriately.

The minimum allowable latency (ROL) must always be chosen such that the current time-stamp follows, but never catches up with the ROP. Therefore the ROL should be set to greater than or at least equal to $w$. Possible sizes of the HRB for various configurations differing in the number of front-ends, time-stamp cycles and maximum front-end read-out delays are computed as reported in Table 4.11. Up to now it is assumed that each connected front-end will be assigned to a corresponding individual HRB. In the actual hardware implementation one global HRB collecting the hit packets of all FEs may prove sufficient or even more efficient. In this case the minimum required memory size for the HRB can be obtained from the given values in Table 4.11 through division by the number of front-ends. On the other hand, an increase of the FIFO-depth is advised since the hits of the entire sensor have to be enqueued into the FIFO instead of the hits originating of only a single front-end. The corresponding values then have to be additionally scaled by a factor of $n/20$, with the new FIFO-depth $n$. The calculated HRB-sizes are merely a design help. A reasonable layout of the HRB in an actual implementation would rather foresee a fixed length accounting for all ever conceivable worst cases of FE read-out delays. The MDC read-out delay then can be adapted by means of the ROL-register to a reasonable value accounting for the specific configuration.

| Nr. of Front-ends $p/n$ | TS cycle (bit) | max. FE read-out delay | min. HRB length $((\Delta t_{Packet})^{-1})$ | | total HRB-size (MByte) | |
|---|---|---|---|---|---|---|
| | | | $f_{ts} = f_{ro}$ | $f_{ts} = 2 \cdot f_{ro}$ | $f_{ts} = f_{ro}$ | $f_{ts} = 2 \cdot f_{ro}$ |
| 7/4 | 8 | 2 | 375 | 495 | 3.3 | 4.4 |
| | | 5 | 495 | 735 | 4.4 | 6.5 |
| | | 10 | 695 | 1135 | 6.1 | 10.0 |
| | | 25 | 1295 | 2080 | 11.4 | 18.3 |
| 7/4 | 9 | 2 | 631 | 751 | 5.6 | 6.6 |
| | | 5 | 751 | 991 | 6.6 | 8.7 |
| | | 10 | 951 | 1391 | 8.4 | 12.2 |
| | | 25 | 1551 | 2336 | 13.6 | 20.6 |
| 4/2 | 8 | 2 | 375 | 495 | 1.8 | 2.4 |
| | | 5 | 495 | 735 | 2.4 | 3.5 |
| | | 10 | 695 | 1135 | 3.3 | 5.4 |
| | | 25 | 1295 | 2080 | 6.2 | 10.0 |
| 4/2 | 9 | 2 | 631 | 751 | 3.0 | 3.6 |
| | | 5 | 751 | 991 | 3.6 | 4.8 |
| | | 10 | 951 | 1391 | 4.6 | 6.7 |
| | | 25 | 1551 | 2336 | 7.4 | 11.2 |

**Table 4.11.:** Calculated Hit Ring-Buffer (HRB) sizes for different choices for the number of front-ends, timestamp cycles and front-end packet delays (FIFO-depth: 20; front-end data packet size: 40 bit).

### 4.4.3. Implementation of Feature Extraction Algorithms

Once the hits are reordered in time after the read-out from the HRB each timeslice of width $w$ in time-stamp counts inside the aperture window as illustrated in Figure 4.47 from both port groups is stored in the L2FIFO buffer for immediate read-out (if selected) and additionally passed on to the clustering stage. This unit scans the available hits and considers adjacent channels as originating from the same event. Those channels are grouped together as a "cluster". The amplitude weighted sum of channel positions, i.e. the center of gravity (COG), is calculated as well as the sum of the ToT-values within only a few clock cycles as obtained with an exemplary implementation [179]. The involved latency proved to be constant for all implemented cluster-finders. This observation justifies the perpetuation of the time-stamp information field in the L3 output data word (cf. Figure 4.48). The obtained cluster information (separate for ports A and B) then are made available for immediate read-out by filling them into the L3FIFO. Additionally the clusters found on both sides are further passed over to the Cluster Correlation Processor (CCP) which searches for all possible combinations of the clusters on either side based on the combinatorial probability algorithm described in great detail in Section 3.4. The given instructions for the computation of the cluster assignment probability, however, must be adapted to the considerably different layout of hardware logic devices over software algorithms. An implementation of the error functions appearing in Equations (3.60) through (3.76) therefore should make use of Look-up-Tables (LUT) as well as synchronous fixed latency hardware multipliers. All remaining algorithmic operations are implemented trivially in synchronous pipelined logic. The number of the resulting possible combinations increases rapidly with the number of top- and bottom-side clusters as reported in Table 3.8. A limiting multiplicity of single-side clusters should therefore be foreseen as

adjustable parameter in the configuration section of the MDC together with other important factors like a threshold for minimum allowable multiplicity for the piped-out cluster combinations, a minimum cluster-sum threshold and others.

The resulting list of combinations of cluster-pairs is finally buffered in the output FIFO (L4FIFO) together with the corresponding combinatorial probabilities for read-out.

The involved latencies, i.e. the throughput times between the true event time (marked by the LE time-stamp) and the time at which the data-packets are written to the corresponding output FIFOs, are key parameters for the correct mapping of the event-time in the overall DAQ-chain. Following statements concerning the latencies that occur in the different stages of the MDC can be met:

- L1-data packets exhibit no fixed latency at all since the ToA at the input of the MDC depends on the ToT. However, event-times can be safely reconstructed if the receiving system has a time-stamp counter wrap-around cycle beyond the maximum allowable ToT including a certain margin for allowable transmission delays. This circumstance was already discussed in somewhat greater detail in Section 4.4.2. The properties pointed out there for the HRB are evenly valid for all following stages along the read-out-chain.

- L2-data packets are delayed by the HRB-mechanism according to their ToT-value such that a constant latency regarding the event-time is achieved. An additional Bit in the TS-field assures synchronicity even for larger delays which would arise at high occupancies.

- L3-data packets experience the same delay like L2 packets plus a fixed small number of clock cycles introduced by the clustering pipeline.

- L4-packets are delayed with respect to the event-time due to the extensive calculation of hit-mapping probabilities. A multiplication factor given by Table 3.8 for higher multiplicities of clusters than one on both sensor sides must be anticipated. The maximum allowable multiplicity permitting an unambiguous reconstruction of the event-time within the transmitted epoch of 12 bits is still unclear and should be determined by simulations.

### 4.4.4.  ASIC Implementation

The final implementation of the MDC has to incorporate radiation-hardening techniques to avoid fail-states in the digital logic due to Single Event Upsets (SEUs). Such states can occur when particles introduce a higher amount of energy into the bulk material, particularly in the vicinity of a MOSFET channel which then may lead to triggering of current flow through the channel. Transistors employed in digital circuitry can lock up the state of a logic gate (usually a Flip-Flop) under this circumstance. Detection of such faulty states as well as their correction becomes mandatory in intense radiation environments such as the MVD. One possible countermeasure usually is the layout of critical logic in a three-fold identical instantiation. The outputs of all three logic blocks are supervised by a 2-out-of-3 majority decoder which outputs the state with the highest abundance among the three logic cells. The MDC will have to be designed with this triple redundancy. Furthermore, each data word transmitted within the MDC will utilize an extra data field holding error correction codes. Each stage checks the data words on reception in order to detect and, if necessary, correct bit-flip errors.

Since each sensor module requires only one single MDC, the additional material budget, the power consumption and the thermal load of this overhead component will be negligible

compared to that of the front-end chips. The design of the first stages and the internal data transmission and multiplexing infrastructure is currently in progress [180]. front-end interfaces for n-XYTER (including a separate ADC-read-out) and ToPix data formats are currently available for testing. The design is fully VHDL-based using Xilinx FPGA as technological platform. The modular structure of the design guarantees a minimum effort to incorporate different front-end solutions or additional features in future versions. First tests have been performed using device simulations. A first functional design of the first multiplexer and buffering stage is able to buffer up to 5 simultaneous hits at a front-end read-out clock speed of 128 MHz. Based on a Xilinx Spartan 6-device undertaken timing simulations yielded a latency of approximately 150 ns for the multiplexing of 11 front-end data streams (n-XYTER plus ADC).

### 4.4.5. Data Format

The data interface of the MDC is planned as GBT E-link endpoint (refer to [173, 175]) as described in more detail in section 4.3. This choice allows a bandwidth-flexible, bidirectional interface with the capability of galvanic isolation of signals. A GBT-frame consists of 120 bits where 80 bits are available for payload data. The MDC output data frames will be placed inside this space.

The format of the MDC output data depends strongly on which stage of the data processing chain is selected for output since each stage exhibits its own characteristic set of parameters. Therefore the receiving stage must possess the knowledge of which type of data can be expected for each transmitted packet. This may be accomplished by a limited set of well defined packet types able to self-identify themselves at the receiver site. Figure 4.48 proposes such a set of packet types. After the SOEV-Bit each packet states its type identifier. Once, this field is evaluated, number and meaning of the remaining bits in the data stream are clearly determined. The MDC output control might as well allow the transmission of data packets from all stages simultaneously which is most useful for debugging and testing purposes. The meaning of the introduced data fields in Figure 4.48 is reviewed in Table 4.12. The CRC fields

L1[39:0]: unordered front-end hit data packets

| SOEV | TYP[2:0] | STS[3:0] | PRTID | FEID[2:0] | FECH[6:0] | LE[8:0] |
|------|----------|----------|-------|-----------|-----------|---------|

| TE[8:0] | CRC[2:0] |
|---------|----------|

L2[39:0]: time ordered front-end hit data packets with fixed latency

| SOEV | TYP[2:0] | STS[3:0] | TS[9:0] | PRTID | FEID[2:0] | FECH[6:0] |
|------|----------|----------|---------|-------|-----------|-----------|

| TOT[7:0] | CRC[2:0] |
|----------|----------|

L3[47:0]: cluster parameter data packet

| SOEV | TYP[2:0] | STS[3:0] | TS[9:0] | PRTID | CNTRI[9:0] | CNTRF[3:0] |
|------|----------|----------|---------|-------|------------|------------|

| CLSUM[9:0] | CRC[2:0] | RSRVD[1:0] |
|------------|----------|------------|

L4[71:0]: cluster correlator output data packet

| SOEV | TYP[2:0] | STS[3:0] | TS[11:0] | CNTRXI[9:0] | CNTRXF[3:0] |
|------|----------|----------|----------|-------------|-------------|

| CNTRYI[9:0] | CNTRYF[3:0] | CLSUM[9:0] | CPROB[9:0] | CRC[2:0] |
|-------------|-------------|------------|------------|----------|

| RSRVD |
|-------|

**Figure 4.48.:** Output data format of different MDC processing stages.

may be omitted or used for additional bits of the time-stamps since the GBT-frame already foresees adequate error detection and correction data structures. The LE, TE and TS fields have to be adapted to the actually required extent. The latter has to be studied in a full chain setup with all involved latencies.

| DP Section | Bits | Meaning |
|---|---|---|
| SOEV | 1 | start of event, always '1' |
| TYP | 3 | data packet type identifier |
| STS | 4 | event status |
| LE | 9 | time-stamp of leading edge |
| TE | 9 | time-stamp of trailing edge |
| TS | 10…12 | mean TS of event |
| TOT | 8 | Time-over-Threshold of event in TS cycles |
| FEID | 3 | front-end index |
| FECH | 7 | channel index on front-end |
| PRTID | 1 | input port group identifier |
|  |  | 0: event occurred on input group A |
|  |  | 1: event occurred on input group B |
| CNTRI | 10 | integer part of cluster centroid |
| CNTRF | 4 | fractional part of cluster centroid |
| CLSUM | 10 | cluster sum |
| CNTRXI | 10 | int. part of cluster centroid, x-dimension (group A) |
| CNTRXF | 4 | fract. part of cluster centroid, x-dimension (group A) |
| CNTRYI | 10 | int. part of cluster centroid, y-dimension (group B) |
| CNTRYF | 4 | fract. part of cluster centroid, y-dimension (group B) |
| CPROB | 10 | hit mapping probability of combination[a] |
| CRC | 3 | checksum bits |
| RSRVD | x | reserved/not in use |

[a] Refer to Section 3.4 for the definition of "combination".

**Table 4.12.:** Description of the data fields in the MDC output words.

### 4.4.6. Connection Scheme

A key requirement in the design of the I/O stages arises from the existence of several independent potential domains on the sensor module. The sensor $n$-side read-out electronics is referenced to the positive sensor bias supply potential, while the $p$-side read-out refers to the negative bias supply rail. The ground reference for the MDC should not interfere with either of them. It should thus kept floating wrt. front-end supply references. The same applies for the MDC-supply itself; it may not be referred to the DAQ-sided ground potential galvanically in order to suppress high return currents along ground paths which could considerably bias the reference potentials within the system and thus lead to common-mode oscillations. The

entirely stage-wise insulated powering scheme demands a higher attention to the strict separation of the potential domains. A common security ground rail, existing in all parts of the chain, may be attached to the local grounds only by low ESR capacitors.

A simple illustration of the discussed connection scheme is given in Figure 4.49 showing the domain crossing between the front-ends of both sensor-side readout planes and the MDC referenced to a completely unrelated power domain. Due to the differential transmission of the signals which facilitates reconstruction through the potential difference on both lines a common mode reference may be omitted[23]. However, this requires that the high-pass filter
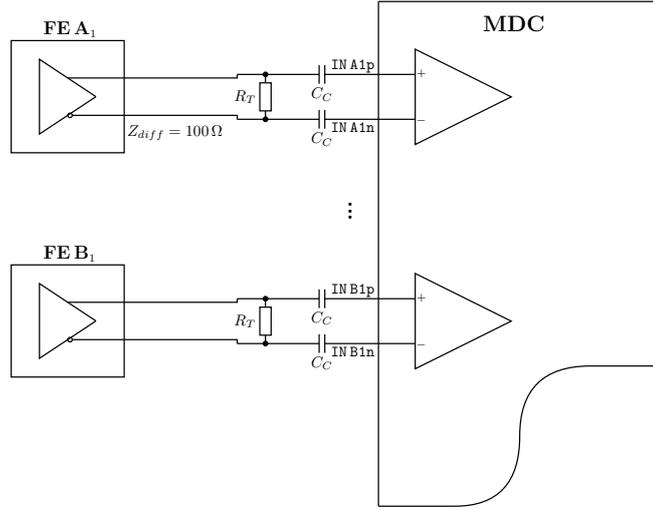


**Figure 4.49.:** Connection Scheme of the MDC inputs.

time constant introduced by the coupling capacitances $C_c$ and the receivers input impedance $Z_i$ is

$$Z_i C_c \gg \Delta t_{max}, \tag{4.31}$$

where $\Delta t_{max}$ denotes the largest observed time interval in which a logical transition (bit toggle) occurs. This time interval depends on the clock frequency of the transmission and on the maximum number of subsequent bits of the same state. The validity of above Equation (4.31) for at least one clock cycle is imperative to the general functionality of the transmission. With an increasing number of clock-cycles in which the bit pattern does not change its state the voltages behind the coupling capacitors drift back to zero level (or input common mode level of the receiver if it features input self-biasing). The differential signal amplitude thus decays exponentially within time intervals that show no change of logic state

$$V_{diff} = V_{diff,DC} \cdot e^{-\frac{t}{Z_i C_c}}, \tag{4.32}$$

with the full deflection $V_{diff,DC}$ and $t = 0$ set with the last transition. Since the white noise superimposed to the signal is coupled into the receiver almost without loss, the SNR worsens proportional to $V_{diff}$. Operation at the maximum SNR is desirable which implies either $C_c$ to be chosen very large or the maximum number of clock cycles without bit flips, also denoted as "run length", is limited to a small amount. Latter method is known as DC-balancing because the common-mode behind an isolation barrier is kept at zero while the signal difference is

---

[23] Capacitive coupling of differential signals obliterates the common mode, anyway.

always near $V_{diff,DC}$. DC-balancing of differential signals is achieved by transcoding the data into a system with a minimum rate of bit-toggles per time interval under the penalty of overhead data bits used for encoding information. The time-intervals between two adjacent bit-toggles are (in contrast to the un-encoded case) predictable. This facilitates the recovery of the clock phase from the data stream at the receiver site by means of a phas-locked loop (PLL). This additional circuitry synchronizes an on-chip oscillator continuously to the link clock frequency through comparison of the phase alignment of the transitions. An additional clock signal line may be omitted in this case.

Different suitable DC-balancing algorithms are listed in Table 4.13 and compared by some key properties as the maximum sequence of identical bits (run length) and the overhead created by the encoding of the raw data[24]. Beside the well established and commonly used 8b/10b-encoding algorithm several other, partly sub-derived encoding schemes exist that offer lower run-length (Manchester[25]), better efficiency (7b/8b and 9b/10b) or special features like lower noise emission (TMDS[26]).

|  | un-encoded | Manchester | 8b/10b | 7b/8b | 9b/10b | TMDS |
|---|---|---|---|---|---|---|
| coding overhead | 0 % | 50 % | 25 % | 14.3 % | 11.1 % | 25 % |
| max. run length (bits) | – | 1 | 5 | 5 | 7 | 8 |
| clock synchronization capable | no | yes | yes | yes | yes | yes |

**Table 4.13.:** Comparison of some selected DC-balancing coding schemes [181–183].

Other ports of the MDC are supposed to be connected following the same scheme as described above. This includes the GBT-uplink from the MDC to the front-ends and the MDC up- and downlinks to the DAQ.

---

[24] The ratio of the additional encoding-related data size to the raw data volume $R = \frac{N_{tot} - N_{raw}}{N_{raw}}$.

[25] A generic classification term for several phase modulated coding schemes.

[26] Transition Minimized Differential Signaling.

## 4.5. Hybrid Carrier PCB

### 4.5.1. Overview

The combination of all discussed components to a sensor module entity, also referred to as hybridization, involves technologies and procedures that are specifically developed within the course of design and layout of the strip tracking hardware. Particularly the demand for non-commercial components and technologies impedes construction of the modules. However, a reasonable hybridization concept has been developed that will be discussed in the continuation of this section.

Figure 4.50 illustrates schematically the basic layout of a stave ladder housing two separate strip super-module entities. Every super-module contains two rectangular sensors, each one connected with either side to a read-out electronics flex PCB. The overall number of readout channels could be further decreased by connecting the long strips of two neighboring sensors. This layout option is denoted as "sensor-ganging" and considered as backup option for the case that space or power density is critical. The more detailed edge-on view of the CAD-model drawing in Figure 4.50 reveals the composition of the proposed barrel strip module. The main carrier structure is composed of carbon fiber plates filled with carbon foam as already described in somewhat more detail above. Sensors and thin electronic carrier PCB (denoted "flex-PCB") are glued onto the carbon fiber frame from both read-out planes of the sensor on the top and bottom of the read-out-panel. The flex-PCB is conceived to be glued onto the sensors with overlap and wire-bonded to connect to them. The PCB hosts sensor fan-out structures as well as front-end electronics, MDC chips, passive components and connectors. Beside electrical traces and vias additionally a large amount of thermal through-hole contacts (thermal vias) are foreseen underneath the FE-chip mounting positions in order to transport the dissipated heat with lowest possible thermal resistance to the back side and consequently into the carbon foam bulk which embeds the cooling pipe.

### 4.5.2. Choice of Material

The material of the front-end electronics carrier structure should satisfy the following requirements:

- **low material occupancy**: achieved by lowest possible thickness at high structural integrity and material content with low nuclear mass numbers (low Z materials)

- **structurability**: ability to introduce electrical structures onto the carrier through commonly available structuring processes. Small feature sizes are demanded by the design requirements for the pitch adaptor structures.

- **frequency stability**: the signal transmission behavior, i.e. impedance, propagation delay and skew at different frequencies is related to the dielectric constant $\epsilon_r$[27]. Its

---

[27] The dielectric material constant referred to in many textbooks is actually the real part of the complex dielectric tensor:

$$\epsilon = \epsilon' + i\,\epsilon'' \tag{4.33}$$

where $\epsilon'$ is the dielectric material constant and the imaginary part $\epsilon''$ is defined as the dielectric loss. It is often more convenient to state the tangent of the phase of the complex dielectric constant instead. In this case the dielectric loss tangent $\tan\delta$ is specified.

**Super Module (front/back side)**



**Edge-on view**



**Edge-on view (zoom)**
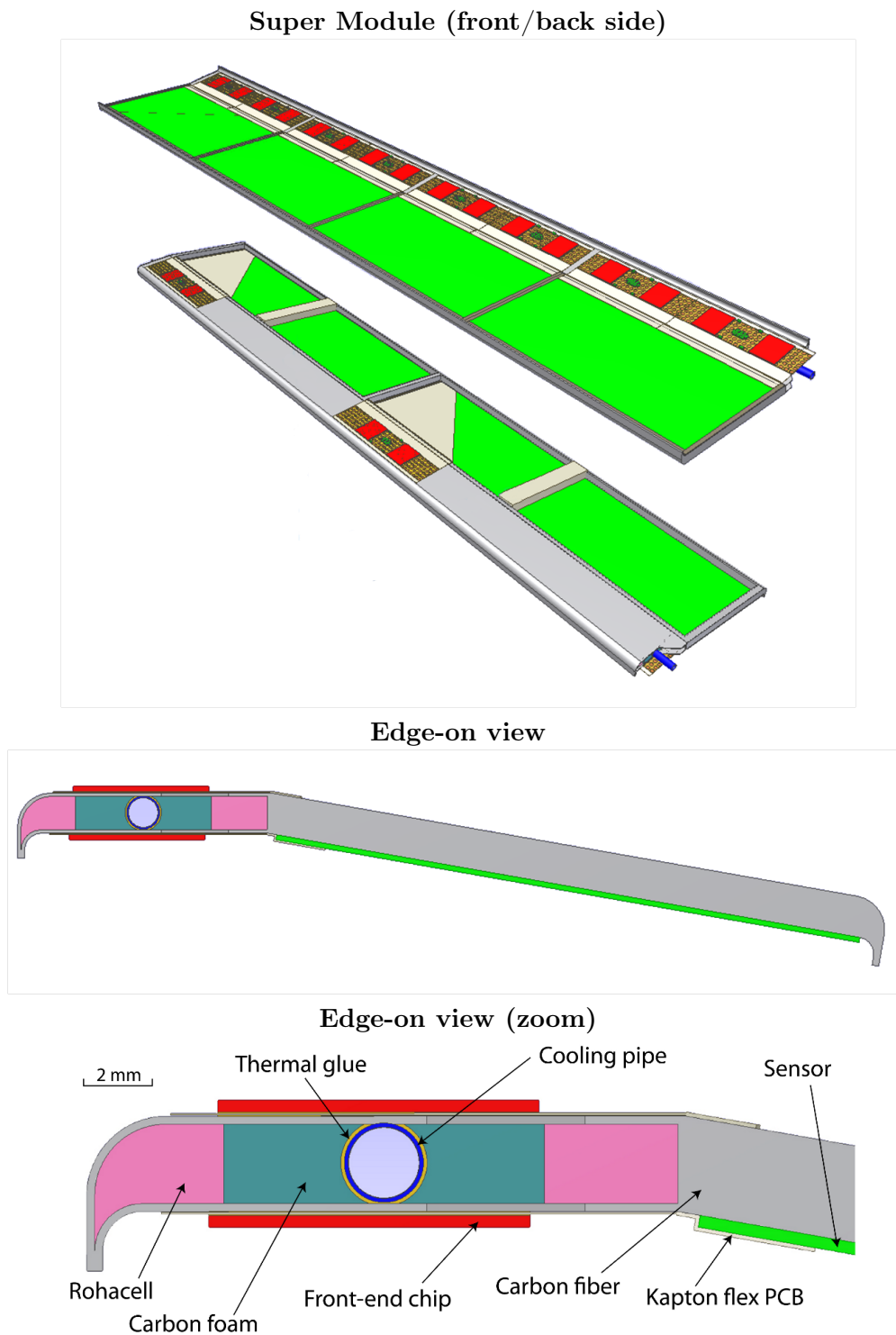


**Figure 4.50.:** View of a fully equipped barrel stave ladder [148] showing the front and back-side routing of the kapton flex cables from sensors to the front-ends (top). Shown here is a setup with ganged adjacent sensors using only two front-ends per super-module for the read-out of the long strips. The default option foresees the read-out of the long strips of each sensor without ganging. An edge-on view (middle) and the zoom-in (bottom) visualizes the different components involved in the construction of the hybrid.

frequency characteristic determines the quality of impedance matching and transmission bandwidth.

- **radiation hardness**: sustaining mechanical and electrical parameters after accumulation of the maximum allowable dose of ionizing as well as non-ionizing radiation is obviously imperative to the function of the exposed systems

- **mechanical stability**: the material shall withstand eventual mechanical stresses, tensions etc. and must not show deformation or degradation of other parameters within the specified temperature range

A set of materials that satisfy all or the majority of these selection criteria was selected and further studied for their application as front-end carrier PCB. A brief overview of those materials is given below.

**FR4** (Flame Retarded Material) Compound of woven fiber glass tissue and phenolic epoxy in alternating multiple layers. This material is extraordinary cheap and has a well defined dielectric constant (material subtype G10). The latter, however, shows a significant dependence on the signal frequency. In addition, above 1 GHz the dielectric losses tend to dominate the figure [184]. This material has shown to be extremely radiation tolerant up to total ionizing doses in excess of $10^7$ Gy [185].

**Polyimide** (specifically Kapton-Polyimide[28]) Chemical composition: poly-(4,4′-oxydiphenylene-pyromellitimide), $(C_{22}H_{10}N_2O_5)_n$. This material sustains structural integrity up to temperatures of $500°C$ and is considered to be radiation tolerant up to a total ionizing dose of 1 MGy (100 Mrad) where mechanical properties start to deteriorate [185, 186]. The dielectric constant of Kapton is very well defined and constant over a broad frequency range. The dielectric losses are low [187, 188].

**RO-4000 Family** This group of ceramic base materials was developed for excellent high frequency behavior (at least up to 11 GHz) with low loss tangents by the Canadian company *Rogers Ltd*. Its application fields are telecommunication and space proved applications, thus a certain radiation tolerance can be expected, although it needs to be further verified. Unfortunately this technology allows relatively thick layer compositions only.

**PTFE** (Polytetrafluorethylene, also known as Teflon) This material is characterized by its very high electrical surface resistivity, a very low dielectric constant and very low loss tangent. However, due to the fragile Fluor bindings it disintegrates even under moderate radiation environments [185]. A somewhat better radiation tolerance may be expected from the similar material ETFE[29] due to its shorter chained molecular structure. No experience exists so far for this material in this specific field of application as PCB base material, though.

**LTCC** (Low Temperature Co-fired Ceramic), the base material is a a flexible compound of microscopic glass or ceramic spherules and a binding agent which may be mechanically formed

---

[28] Developed and patented by *DuPont*.
[29] *DuPont* trade name *Tefzel*.

and structured according to the desired shape. Superficial structuring techniques such as thick-film processes are applicable. Parts of the base material may be replaced by conductive material or material with varying permittivity. Several such customized layers then may be sandwiched before the final fixation process is applied. This is performed by exposing the compound to temperatures of 900 °C causing an effective sintering of the spherules while the binding agent volatilizes which results in a solid composition of 3d-structured mechanical and electrical features. A schematic cross-section through an example LTCC-hybrid is shown in Figure 4.51 demonstrating most of the design features available in this technology. Embedded resistor and capacitor structures as well as cavities (e.g. for RF-oscillators) or cooling paths were successfully implemented. A current lower limit for the achievable electrical feature sizes is 100 µm [189, 190].
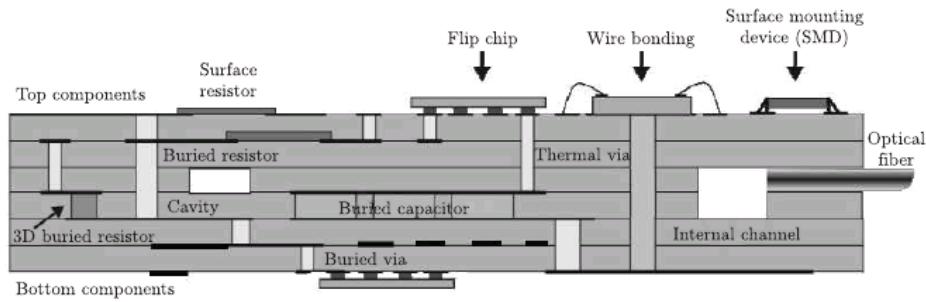


**Figure 4.51.:** Construction of a typical LTCC module [190].

A comparison of key parameters for those substrate materials which match best with the mentioned requirements is listed in Table 4.14. These parameters, when given as thickness dependent magnitudes, are reported for the thinnest available base materials. The coefficient of temperature expansion (CTE) for the materials has to be compared with the CTE of silicon with 3.2 ppm/K. Therefore LTCC base material would cause the lowest amount of thermal stresses within the composite module.

An account for the material occupancy presented to the particles incorporating density and nuclear mass reflects in the relative radiation length usually stated in units of the absolute material radiation length $X_0$. This quantity is equivalent to the mean free pathlength of a charged particle in the specific material characterized by charge and mass numbers $(Z, A)$. An empirical and commonly consulted parameterization yielding the absolute radiation length is [23]:

$$X_0 = \frac{716.4 \cdot A}{Z(Z+1)\ln\left(\frac{287}{Z}\right)} \ \ [\text{g}\cdot\text{cm}^{-2}] \tag{4.34}$$

which agrees to within 2.5 % with measurements for elements heavier than helium. The density attenuation coefficient $X$ on the other hand depends simply on the pathlength $l$ of traversed material with density $\rho$

$$X = \rho l. \tag{4.35}$$

The accumulated relative radiation length in compound materials can then be expressed as

$$X/X_0 = \sum_i \frac{\rho_i l_i}{X_{0,i}}, \tag{4.36}$$

assuming that the material components forming the compound are present in sectional, distinct adjacent layers. Otherwise, if a homogeneous mixture or a molecular composite of the

| Property | FR4[1] | Kapton polyimide[2] | LTCC[3] |
|---|---|---|---|
| Dielectric thickness (µm) | >150 | 25 | min 42[4] |
| Dielectric constant | 4.2...4.8 | 3.4 | 7.85 |
| Dielectric loss tangent | 0.017 | 0.004 | 0.0045 |
| Conductor type | Cu | Cu | Cu,Au,Ag |
| Conductor thickness (µm) | 9 | 18 (9[5]) | $\gtrsim$5 |
| min. line width (µm)[6] | 40 | 40 | 100 |
| CTE (ppm/K)[7] | 14 | 20 | 5.8 |
| Breakdown Voltage (kV/mil) | 0.5 | 6...7 | >1 |
| Thermal conductivity (W/m·K) | 0.27 | 0.12 | 3 |
| Mass density (g/cm$^3$) | 1.85 | 1.42 | 3.1 |
| Radiation length, min/max (% $X/X_0$)[8] | 0.007/0.13 | 0.009/0.25 | 0.035/0.102 |
| Tensile strength (MPa)[9] | 275 | 230 | 320 |
| Young's Modulus (GPa) | 21 | 2.5...4 | 152 |

**Table 4.14.:** Comparison of properties of different substrate materials collated from [191], [184], [192], [189], [190], [187], [188], [193] and [23].
[1] Typically 60 % $SiO_2$ and 40 % epoxy.
[2] *DuPont* Pyralux AP.
[3] *DuPont* DP 951.
[4] Thickness for one layer tape obtained after firing process.
[5] Value for electro deposited copper plating; non-standard process.
[6] Identical wet-processing technology for FR4 and Kapton substrates.
[7] In the plane of the substrate plate unless the CTE is isotropical.
[8] Calculated for minimum available dielectric and conductor thicknesses; min/max values for dielectric only and dielectric with full conductor coverage of two layers, respectively.
[9] Measured at 25 °C.

single components is encountered, the simple additivity of the fractional radiation lengths in Equation (4.36) may hold under certain circumstances only. Those caveats are, although not exhaustingly, considered along a discussion about the validity of *Bragg's* additivity rule in Appendix B.

From the selected materials listed above, first parameter validations were undertaken with thin layer prototype PCBs based on Kapton-polyimide since this material is offered as standard choice for thin carriers. A short comprehension of the prototype evolution is given in the following paragraphs.

**Flex-Prototype 1** A first PCB was made on *DuPont* Pyralux–AP 9121 base material with laminated 36 µm copper layer. The laminated material has the advantage that no additional adhesive layer exists between dielectric core and metal layer. A meandric impedance test structure was laid out on one layer representing a single ended transmission line with characteristic impedance of 27 Ω and trace width 300 µm as illustrated in Figure 4.52. For the derivation of micro-stripline geometry and the related characteristic impedance in great detail and further particulars of high frequency circuit design the reader is referred to e.g. [192, 194, 195]. The relation between trace width and strip-line impedance for the given material is obtained from the manufacturer (Figure 4.53). The low characteristic transmission impedance of $Z = 27\,\Omega$ was pragmatically anticipated by choosing the lowest possible trace width. Wider traces would result in even lower impedances. To match the commonly used transmission line impedance of
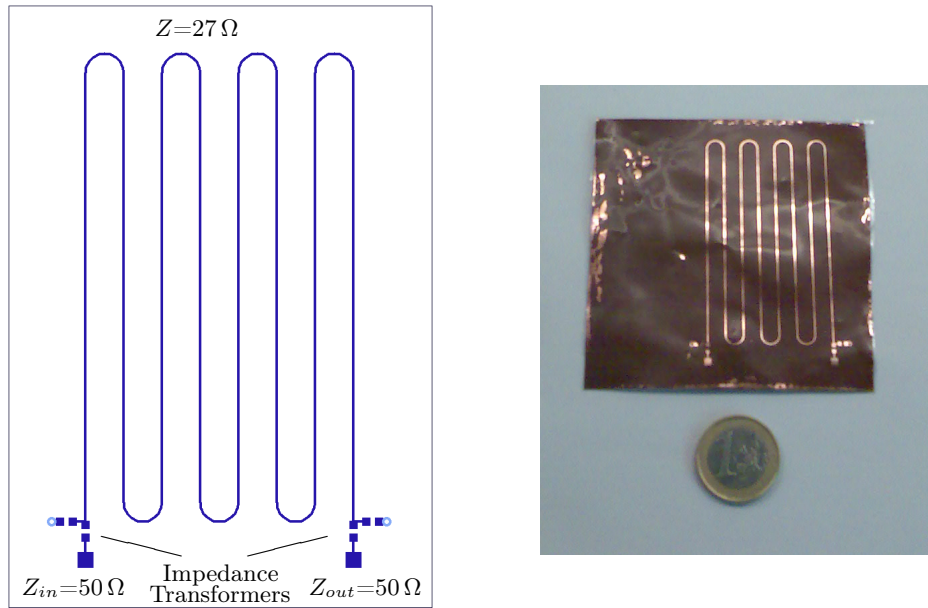
**Figure 4.52.:** Flex prototype № 1. Impedance measurement test structure with transmission micro-stripline and resistive impedance transformers (left) and photo of the PCB after wet processing (right).

$50\,\Omega$ additional impedance transformers to/from the transmission line to the input and output pads are foreseen using simple resistive voltage dividers.
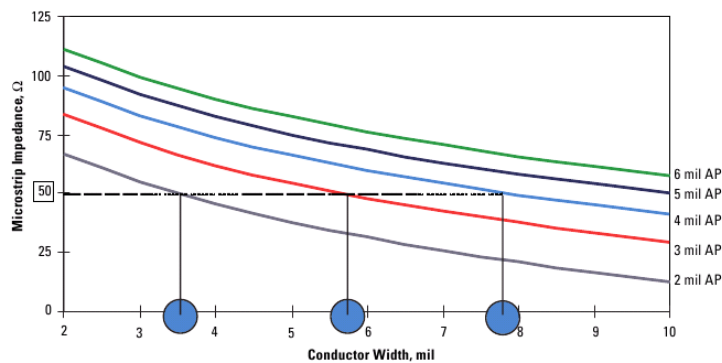


**Figure 4.53.:** Nomogram for determining the design trace width for given dielectric thickness and required characteristic impedance [188].

The transmission behavior was analyzed with a setup consisting of a tunable signal generator and a logarithmic power detector. Comparison of the transmitted or reflected power with the emitted power of the generator allows to draw conclusions about the signal attenuation at the line output in dependence of the frequency. Figure 4.54 illustrates a such obtained measurement of the insertion loss of the prototype structure. The measured bandwidth can be determined to $\approx 400\,\text{MHz}$ (3 db) and roughly $650\,\text{MHz}$ at 6 db attenuation. The dip near $100\,\text{MHz}$ corresponds to a resonance on the length of the signal line due to a mismatch of
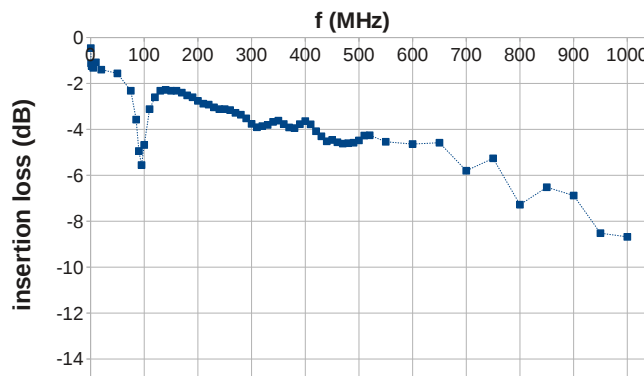
**Figure 4.54.:** Measured insertion loss of the transmission line structure (flex prototype № 1). The dip at $\simeq 100\,\text{MHz}$ results from a resonance along the line length due to a mismatch of the line's characteristic impedance to the design value (see text) and can be used to validate the permittivity of the material.

the exact line impedance and the termination impedance. The discrepancy can be explained with a lack of accuracy in the utilized etching process. Without doubt, trace widths with a much higher precision may be obtained from professional processing techniques. However, the inaccurate etching process used for this prototype PCB created the slight mismatch in the transmission impedance which is useful for determining the resonance frequency of the standing wave on the line and thus permits validation of the material dielectric constant. The usable transmission bandwidth is expected to be higher for a perfectly matched line.

**Flex-Prototype 2 - Single FE carrier PCBs**   The second generation of flex prototypes was laid out on $20\,\mu\text{m}$ thick kapton carrier with double sided electrical structures. A huge variety of designs and test structures had been implemented like single- and multi-FE fan-out combs for different front-end ASICs, various signal cables and single-FE carrier PCBs with included sensor fan-out structures. Furthermore, the feasibility of the adaptor routing between sensor pitch and front-end input pitch utilizing standard processes of PCB fabrication should be verified. Figure 4.55 shows such a single-FE flex PCB for an n-XYTER front-end. The input pads on the right hand side are laid out in a staggered configuration of two rows (pitch $130\,\mu\text{m}$) which connect to the double row output pad interface of the sensor with commensurate pitch. The FE input pitch in this case is $50\,\mu\text{m}$. A 4-fold staggering of pads on the PCB achieves this dense input pattern without violating processing design rules or bonding limitations. First inspections and electrical tests conducted by the manufacturer confirmed that all specified design parameters were met. Further evaluations are pending.

For the final hybrid carrier PCB a two layer layout on kapton-polyimide, as the second generation prototype was laid out already, is foreseen following the design recommendations of [196, 197] with the parameters given in Table 4.14. The value of radiation length for the compound material is in general very low but may peak up to ca. $0.25\,\%$ $X/X_0$ locally, when copper traces or larger areas on both sides overlap. The large difference of the CTE between kapton and silicon and possibly arising mechanical stresses on the mounted assembly
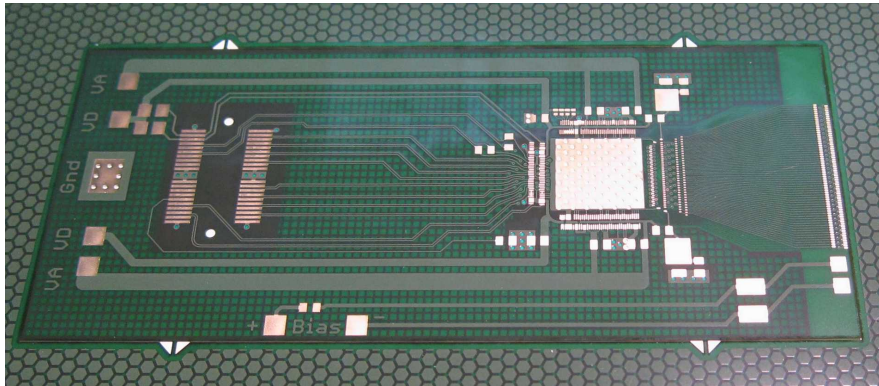
**Figure 4.55.:** Photograph of a single FE flex PCB prototype. Input pads for the wire-bonding connections to the sensor with specified pitch of 130 μm are seen at the right hand side. The FE chip position is supported by a thermally conducting copper pad with a large number of thermal through holes (vias). FE signals are routed to a high density connector to be placed on the left side. Power and potential connections are on the far left side. Pads close to the front-end position belong to mandatory ceramic blocking capacitors. Due to the low thickness of the material the bluish underlay pad lettering shines through the material in the upper part of the photograph.

still remains an open issue. A controlled tempering procedure is therefore suggested for the assembled building blocks.

The fan-out routing of the default 130 μm pitch structure to the front-end pitch can be processed by standard PCB manufacturing techniques as verified with the second generation prototype described above. Figure 4.56 shows a layout study for connection to multiple n-XYTER front-end ASICs. The bonding pads at the top edge are placed in two staggered rows at the sensor read-out pitch of 130 μm. Channels connecting to the upper pad row are routed through micro vias to the back side of the PCB and guided back again to the top side near the corresponding bonding pad for the connection to the FE. This scheme allows a collision-free routing of all 128 channels from the sensor interface toward the FE input perimeter. Technical feasibility of this concept has been demonstrated with the second prototyping run as well.

The next step is the interconnection of this thin kapton flex to the sensor by directly glueing the PCB with an overlap of 6.7 mm onto the sensor such that the innermost AC-pads of the sensor and the bonding pads on the flex-PCB face each other at equal pitches. The staggered pad rows then can be connected via straight bonding wires thus alleviating the fine-pitch wire-bonding process.

### 4.5.3.  Floating Channels

The prototype sensors originating from the CIS01-prototyping run possess an incommensurate number of channels wrt. the number of 128 channels per front-end chip. One reason for this mismatch arises from the originally intended read-out pitch of 65 μm requiring 7 FEs for the long sensor side read-out which was changed to an "every-other channel" read-out scheme with similar spacial resolution figures but a reduced density of read-out electronics by a factor of two eventually at a later time during the design process. However, adoption to the modified read-out condition would require either larger sensors yielding a commensurate number of $n \cdot 128$ channels with a natural number of $n$ front-ends or the increase of channels from 896
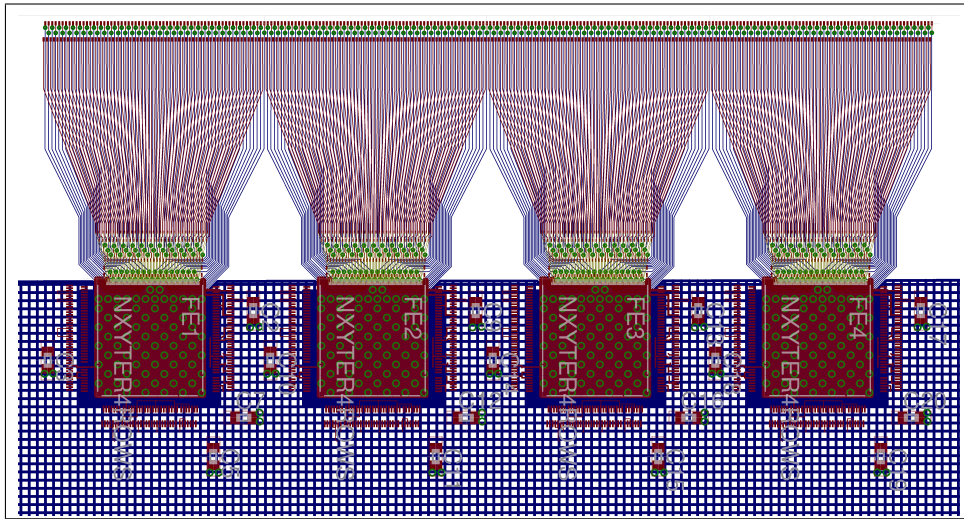
**Figure 4.56.:** Layout of fan-in adaptor structure of the readout flex PCB. At the upper edge two rows of pads are foreseen for wire bonding to the sensor at a pitch of 130 µm. The PCB is glued upon the sensor with an overlap of ca. 6 mm. The back-end part of the front-end chips (lower part) is not routed yet in this scheme.

to 1024 keeping the sensor dimensions constant and thus changing the read-out pitch from 130 µm to 113.75 µm, provided an every-other strip read-out scheme. Latter option is seen preferable over a change in sensor dimensions since a subsequent complete redesign of the barrel layer configuration and positions shall be avoided. On the other hand, the current sensor design yields a total number of 896 $p$-side strips. With every second channel connected for read-out, this leaves a number of 448 front-end channels which is, as emphasized above, an incommensurate amount of 3.5 FE entities á 128 channels. Assuming connection of the entire set of $p$-side channels to 4 FE-chips a number of 64 FE-channels remains unconnected (beside the already accounted intermediate channels present at sensor pitch of 65 µm and read-out pitch of 130 µm). Those floating channels could in principle facilitate the noise characterization by connecting them to different input capacitances represented by stubs with varying lengths. Some of those stubs might as well be implemented as traces running in parallel to the fan-in routes.

## 4.6. Powering Scheme

### 4.6.1. Power Domains and Ground References

The supply of operating voltages to the strip modules has to be carefully planned under consideration of the full power domain extents. As it was shown earlier in this thesis the $p$-side and $n$-side read-out electronics of the sensor modules have to be operated without potential reference to each other nor to the sensor bias. This scheme remedies the problem of common mode variations by uncontrolled high ground return currents or spikes but its practical realization is challenging since a coupling between different potential domains must be avoided under all circumstances. Moreover, a good ground reference rail must be provided along the supply lines for each module acting as safety ground. A plan of the anticipated potential domains is given in Figure 4.57. First of all the depletion of the sensor is ensured by
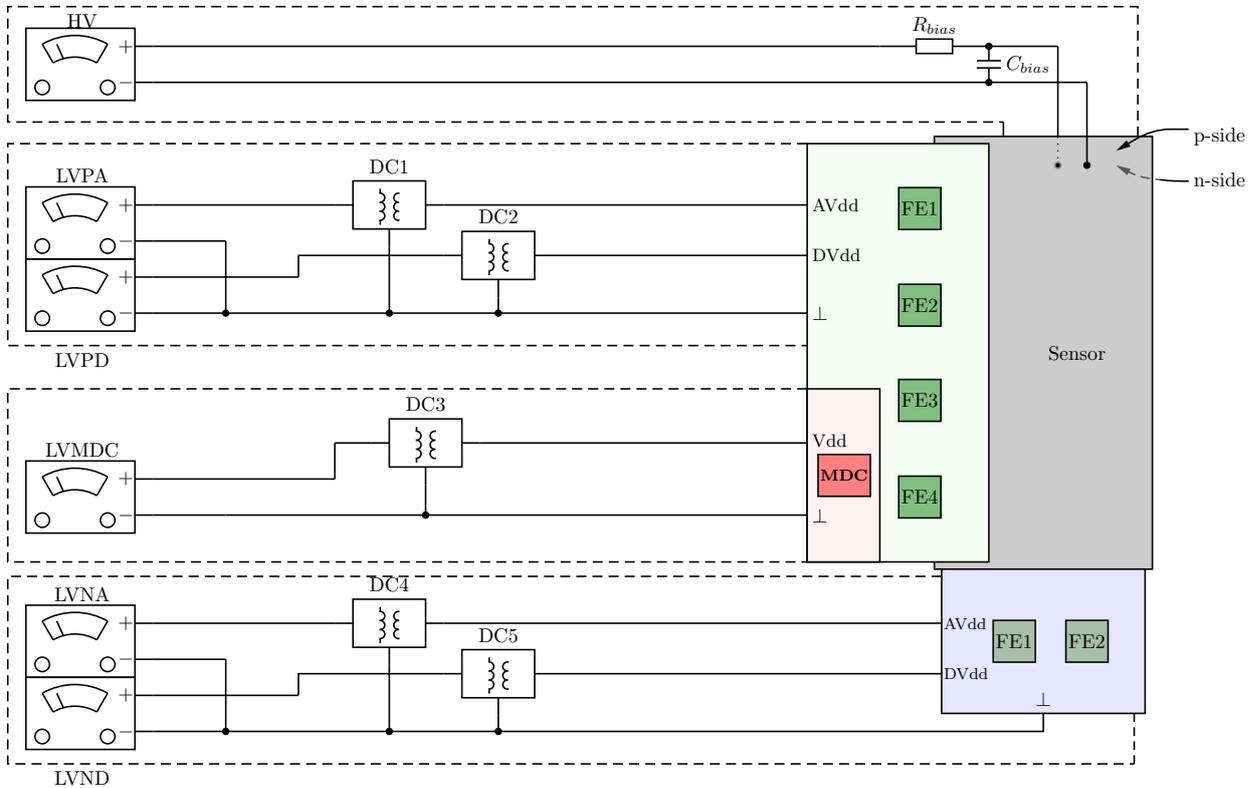


**Figure 4.57.:** Connection scheme of supply voltages and ground reference domains of a single sensor-module entity.

the connection to bias supply voltage (denoted HV) through the low pass filter combination $R_{bias}C_{bias}$. Supply voltages for the read-out electronics are routed independently to the $p$-side and $n$-side read-out flex-PCBs, respectively. The front-end ASICs require separate supply voltages for their analog and digital parts. DC-DC-converters placed as close as possible to the MVD generate these voltages (1.5 V) from higher raw voltages provided from external voltage sources denoted as LVxx to compensate for the voltage drop along the supply lines from the voltage sources until the DC-DC-converters. The converters are assumed to have a common ground reference on both input and output side. The cable length from power supplies to the converter devices is not critical and may amount to several dozens of meters

depending on the excess voltage wrt. the minimum operating voltage of the DC-DC-converters. A more thorough discussion on specific converter prototypes is enrolled later in this section. Beside the need for floating power supplies for the front-end operating voltages of both sensor-side read-out electronics, the introduction of a separate power domain is suggested for the supply of the MDC ASIC (reddish section in Figure 4.57). As a result, any feedback of interference acting on the long signal lines between MDC-output and the following stage as well as interference on the MDC ground reference (which both act as antennae) is effectively inhibited at the cost of an additional power supply and a separate supply path for each module. The signal connections between the front-end outputs of either sensor-side electronics and the MDC input is accomplished through the isolated coupling introduced in Section 4.4. The physical connection from the $n$-side flex-PCB to the MDC sitting at the $p$-side flex requires an additional cable which carries the differential links of those front-ends to the MDC.

## 4.6.2.  Power Budget

The foreseen powering scheme of the strip detector modules contains separate low voltage supply paths for the $n$-side, $p$-side and MDC readout electronics, respectively since the front-end electronics on either side and the MDC are operated without galvanic reference to a common ground in a floating regime. This avoids high parasitic currents in the case of breakdown of the thin insulation barrier between $n$-side implants and metalization (pinholes) of the sensors, which would otherwise result in the loss of the complete sensor. Thus a total of five independent low voltages (including one analog and one digital voltage for either sensor side FEs) and four high voltages for each sensor bias have to be supplied. The low voltage paths are connected with sense feedback to compensate for the voltage drop on the cables behind the DC-DC-converters. Assuming a maximum of 1 W power dissipation per front-end at operating voltages of 1.5 V the values given in Table 4.15 can be estimated for the maximum supply current on the low voltage lines on the basis of available data or comparisons to similar architectures [35,171,180,198]. The numbers are collective maximum load currents for one module entity, i.e. a complete hybridized 4-sensor structure. The voltage supplies of equivalent domains for $p$-side-FEs and MDC are fed from common rails per module. The $n$-side-FEs are to be supplied separately since each $n$-side FE supply voltage is superimposed on the individual sensor bias potentials.

The current drawn on the bias voltage lines is negligible even with the maximum applied irradiation dose at the end of the $\overline{\mathsf{P}}$ANDA lifetime and amounts to at most 2 mA per sensor (cf. Section 4.2.6). Sensing lines are thus not required for this supply but a good filtering with very low cutoff frequencies is mandatory on the module level as illustrated in Figure 4.57.

|  | $p$-side | | $n$-side | | MDC |
|---|---|---|---|---|---|
|  | AVDD | DVDD | AVDD | DVDD | VDD |
| Current / Sensor Entity (A) | 2.2 | 1.2 | 1.1 | 0.6 | 0.25 |
| Current / Module (A) | 8.8 | 4.8 | 4×1.1 | 4×0.6 | 1.0 |

**Table 4.15.:** Estimated currents drawn on the electronics power supply for each sensor entity and per module separated by the corresponding voltage of the module supply.

### 4.6.3. DC-DC Converters

The power supplied to the sensor modules is subject to a certain inevitable loss due to thermal dissipation. In order to avoid a significant loss due to the finite cable series resistances, the voltage should be as high as possible minimizing the current in the cable and as a consequence the voltage drop along the cable length. This implies that the available total power can be transformed without loss into a current-voltage product with lower voltage, i.e. the voltage required at the load site. This is not possible with linear voltage regulators since these devices simply dissipate the product of the voltage difference (between in- and output) and the current into heat. An almost power-accurate conversion on the other hand can be achieved by switched voltage regulators with an active power load feedback. Such devices chop the input voltage at a fixed frequency in the range of $100\,\text{kHz} \dots 10\,\text{MHz}$ with a variable pulse width modulation which regulates the output power. The energy is stored in a large reactance (inductivity or capacitor) and smoothed by a low pass filter. The closed feedback loop assures a stable output voltage under varying load conditions.

Commercially available switching regulators almost exclusively make use of a magnetical energy storage in form of coils with high-permeative cores. High power conversion efficiencies in excess of $\approx 90\,\%$ are achievable in this way [199]. However, function of those magnetically operated converters ceases in even moderate magnetic fields since the saturation of the coil core-materials and the resulting significant drop of inductance usually shifts the operating point of the converter out of functional range.

The *CERN* DC-DC Converter group introduced a design of a power converter showing a high efficiency of $\approx 85\,\%$ (at $2\,\text{A}$ load current) optimized for operation in strong magnetic fields and low noise emission [200]. Further key parameters of the SM01C DC-DC converter are comprehended in Table 4.16. Modified versions of those converters with an output voltage

| Property | Value |
|---|---|
| input voltage range | $7 \dots 15\,\text{V}$ |
| max. output current | $5\,\text{A}$ |
| output voltage | $2.5\,\text{V}$ @ $1\,\text{A}$ |
| | $2.4\,\text{V}$ @ $5\,\text{A}$ |
| efficiency | $85\,\%$ @ $2\,\text{A}$ |
| | $75\,\%$ @ $5\,\text{A}$ |
| size (l×w×h) | $28.4 \times 13.5 \times 10\,\text{mm}^3$ |

**Table 4.16.:** Properties of SM01C DC-DC Converter [201].

of $1.5\,\text{V}$ are proposed to supply the power to the DSSD modules as close as possible to the MVD. However, the limited available space inside the MVD-volume permits the closest possible placement behind the backward end cap connection panel seen toward the upstream direction. Therefore the operation of commercial devices placed outside the magnet yoke is conceivable as well.

## 4.7. Cooling

Operation of the MVD dissipates thermal power in the order of $1\,\mathrm{W/cm^2}$ at maximum as specified by [35]. In order to take out the introduced heat energy active cooling of the entire MVD renders therefore mandatory. Initial estimates settled for a system based on the one used for the ALICE silicon detector with a water circulation using $18\,°\mathrm{C}$ feed temperature working in under-pressure mode [202]. In this regime water from a reservoir situated at a level above the MVD is guided through the cooling system and drained into a second reservoir at lower ground. The height difference sets the "under-pressure", i.e. the difference from the ambient air pressure which forces the water into the lower reservoir. Figure 4.58 illustrates the cooling pipe routing through two elements of the strip barrel. The pipes embedded inside the
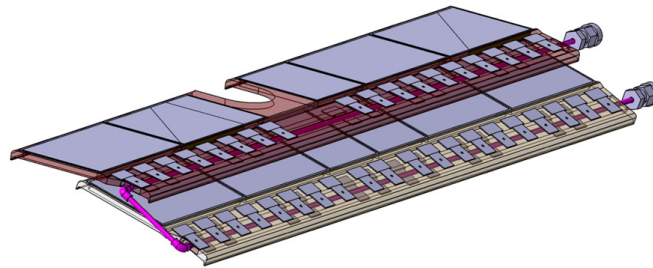


**Figure 4.58.:** Cooling connections to the strip barrel super modules illustrated for two chained modules. The cooling pipes are embedded inside the carbon-foam body of the module carrier frames running directly underneath the front-end chips [148].

carbon foam of the module carrier frames consist of nickel-cobalt alloy with $2\,\mathrm{mm}$ diameter and $80\,\mathrm{\mu m}$ wall thickness. Flow inlets and outlets at the end of the modules are connected to external pipe-loops by means of sleeves made of thermoplastic resin material in order to daisy-chain all the modules from a half-barrel. A test bench with a module prototype structure equipped with power resistors equal in size and power dissipation to the planned front-ends was setup in Turin. Measurement results indicate that the temperature of the barrel modules under full operation can be kept below $35\,°\mathrm{C}$ provided improved contact area between the cooling pipe and the front-end chip bulk. Moreover, the obtained results are consistent with simulations [203].

The temperatures at different locations on the modules should be monitored constantly using PT100/PT1000 or NTC thermo-sensors in order to identify problems of the cooling system or malfunctions of front-end electronics. In this case the system can safely be shut down without causing further damage. An additional temperature sensor is foreseen to be attached directly to the strip sensor. Its temperature strongly influences the leakage current following the relation [93]

$$I_L \propto T^2 \exp\left(-\frac{E_g}{2kT}\right) \tag{4.37}$$

where $E_g = 1.12\,\mathrm{eV}$ is the bandgap energy of silicon and $k$ *Boltzmann*'s constant. Evaluating this relation for two different temperatures yields a doubling of the leakage current when the temperature rises from $30\,°\mathrm{C}$ to $40\,°\mathrm{C}$. Figure 4.59 shows the interdependence measured during

a long acquisition period for an ITC01-type detector. The temperature swing is due to ambient temperature changes during this time. The leakage current doubles within a temperature rise of roughly 8 Kelvin thus exceeding the expected slope. In order to prevent excessive
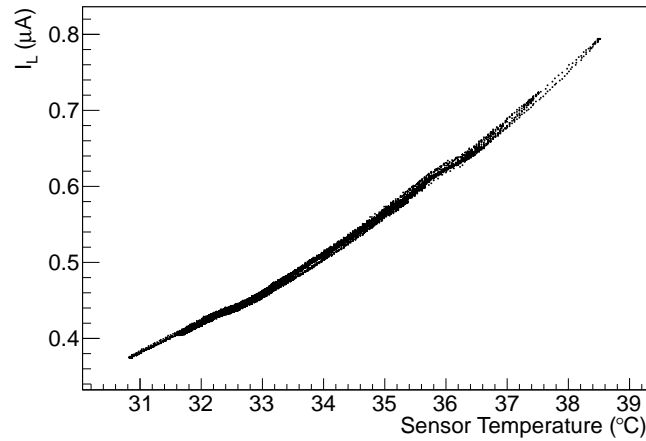


**Figure 4.59.:** Leakage current of strip sensor ITC01 vs. ambient temperature.

leakage currents or even self-heating of the sensors due to significant power dissipation a cooling of sensors is necessary. Provided that the dissipated heat from the front-end electronics is transported off the module and the specified temperature constraints are met, a forced airflow through the MVD volume should sufficiently keep the sensor temperatures within safe operating range.

# Chapter 5.

# Conclusions

A conceptual design for single DSSD sensor and front-end electronics modules for the barrel part of the $\overline{\mathsf{P}}$ANDA MVD was introduced in the preceding chapters. The mechanical configuration was identified through extensive physics-driven simulations by [88, 89], whereas read-out scheme, implemented preprocessing algorithms and proposed hardware layout are rooted in experiences made with prototypes scrutinized so far.

The following list of topics shall review results, conclusions or points that are required to be further addressed in future labor.

**Sensors:** Evaluation of prototype sensor performance yielded results within the expected range. However, several issues were found to be noteworthy and deserve further attention. A number of prototype sensors from ITC/irst and CiS have been partly or entirely characterized as reported in sections 3.2 and 4.2. The explicitly measured capacitances for strip-to-backside, strip-to-neighbor and metal coupling of the more recent prototypes CIS01 agree well with the values predicted by models or compared with typical values for similar sensors obtained from literature. For the S1-sensors a load capacitance presented to the preamplifier inputs can thus be estimated from Table 4.3 to yield

$$C_{strip}(p) = 9.8 \pm 0.2 \, \text{pF}$$

for the $p$-side strips ($l = 33.315 \, \text{mm}$) and

$$C_{strip}(n) = 17.1 \pm 0.4 \, \text{pF}$$

for the $n$-side strips ($l = 58.275 \, \text{mm}$). Note that the determined measurement errors do not reflect the fluctuations among different strips of the same sensor or among different sensors.

The sensors analyzed so far are punch-through biased devices. Experience with poly-silicon biased sensors on the other hand has not been collected yet. Noise analyses of sensor and sensor/FE systems based on the available sensors (which exclusively exhibit punch-through biasing) yielded noise figures which compromise the minimum envisaged SNR of 10 (see Table 4.5) toward the end of the $\overline{\mathsf{P}}$ANDA operation assuming a total accumulated radiation dose of $10^{14} \, \text{cm}^{-2}$ n. eq. as reported in Table 5.1. The affected region of the strip tracker is limited to the very forward part of the MVD where the actual fluence actually peaks at the specified maximum $10^{14} \, \text{n}_{1\text{MeV eq}} \, \text{cm}^{-2}$. Moreover, *Lutz* [204] states, that the additional noise contribution attributed to the punch-through biasing mechanism may not be as high as the leakage current shot noise but a somewhat smaller value due to single-electron correlations similar to the reduced thermal noise in MOSFETs (see Section 4.3.3.3, paragraph "Noise Analysis" in

| irradiation dose | | biasing technology | |
|---|---|---|---|
| ($n_{1\text{MeV eq}}\,\text{cm}^{-2}$) | | poly-silicon | punch-through |
| | $t_{\text{opt}}$ (ns) | 292 | 272 |
| 0 | $\text{ENC}_{\text{min}}$ ($e$) | 670 | 694 |
| | SNR | 30.6 | 29.5 |
| | $t_{\text{opt}}$ (ns) | 58 | 41 |
| $5 \cdot 10^{13}$ | $\text{ENC}_{\text{min}}$ ($e$) | 1806 | 2132 |
| | SNR | 11.4 | 9.6 |
| | $t_{\text{opt}}$ (ns) | 41 | 29 |
| $1 \cdot 10^{14}$ | $\text{ENC}_{\text{min}}$ ($e$) | 2143 | 2536 |
| | SNR | 9.6 | 8.1 |

**Table 5.1.:** Summarized minimum achievable ENC values and optimum shaping time constants in dependence of the accumulated radiation dose for poly-silicon and punch-through biasing schemes.

this thesis). The impact of the leakage current shot noise originating from the two different biasing technologies on the noise performance of the sensor-FE combination therefore needs further empirical investigation.

Analysis of the single cluster hit resolution at orthogonal passage of particles through the sensor showed general correspondence between simulations and measurements (Section 3.3.6). The charge sharing behavior between strip electrodes is well understood that assumptions about the shape of the $\eta$-$x$-function lead to experimentally verified descriptions of $\eta$-distributions and consequently to the expected RMS hit resolutions. Latter imply a similar accuracy for DSSD read-out with and without intermediate floating strip at 65 μm strip pitch as discussed in Section 4.2.5. Evaluation of the dependence of spacial resolution on the SNR as reported in Table 4.4 indicated a deterioration from $16\,\mu\text{m}_{\text{rms}}$ for 65 μm read-out pitch to $25\,\mu\text{m}_{\text{rms}}$ for 130 μm every-other read-out scheme provided a worst-case SNR of 10.

Radiation hardness of CIS01 prototype sensors was verified mainly through irradiation with low energetic protons. Measurement of leakage currents and bulk stray capacitances ascertained a normal depletion behavior and expected leakages up to equivalent fluences of $1 \cdot 10^{14}\ n_{1\text{MeV eq}}\,\text{cm}^{-2}$ (Section 4.2.6). However, the charge collection behavior of irradiated sensors could not be evaluated yet. Further investigations are recommended here.

**Front-end Electronics:**   Key parameters and design requirements have been formulated for the read-out front-end electronics of the MVD silicon strip tracker. Noise calculations have been undertaken to demonstrate the influence of different noise sources on the performance of the sensor-FE combination. Several points in the design of the preamplifier stage that deserve further consideration for optimization efforts wrt. noise and signal-to-noise performance were discussed in Section 4.3.3.3. Impact of the implementation of a ToT-stage as analog-to-digital converter on charge signal resolution and noise was given consideration as well.

The architecture of a module data concentrator (MDC) ASIC was introduced in Section 4.4. Basic preprocessing of front-end data outputs as well as higher level feature extraction procedures to be implemented and data transmission schemes are investigated. The problem of sustaining the synchronicity with increasing latencies in the read-out chain was brought into focus and simple relations for the estimation of maximum ring-buffer lengths in dependence of time-stamping and transmission clocks were introduced and thoroughly discussed.

**DSSD barrel modules:** The construction of barrel modules for the MVD strip tracking section as it is currently conceived is subject of Section 4.5. A hybrid assembly integrating sensor, front-end electronics and electrical connections as well as prototyping steps taken so far were presented and a scheme for power distribution and potential isolation between power domains proposed. Fabrication of first thin flex-PCB prototypes was engaged, assembly of those prototypes is currently processed by the time of the conclusion of this thesis.

**Calculation of displacement damage in compound materials** as described in detail in Appendix B was included into this thesis since displacement damage cross sections were found to be difficult to obtain for materials other than those with a large industrial or instrumental significant importance such as silicon. The electrical properties of ceramic capacitors used in the assembly of the front-end modules within the MVD will have to be verified to sustain the local radiation doses. The dielectric of those capacitors is usually composed of a barium-titanate ceramic ($BaTiO_3$), more seldom of a lead-zirconate-titanate compound ($Pb(Zr,Ti)O_3$) whose displacement cross sections could not be found in literature surveys. However, several program codes and algorithms exist that calculate the desired cross sections yielding lesser or higher accuracies. For an incomplete overview refer to [210, 213, 215–217, 219]. Those programs and codes are either difficult to obtain or simply not executable on recent workstations. A detailed derivation of a simplified procedure is therefore given in Appendix B together with the calculated damage cross sections of silicon and $BaTiO_3$. Cross sections for other compounds should be easily inferred following the indicated guide.

# Appendix A.

# Results of Tracking–Station Measurements

Several beam time campaigns with large amounts of acquired data from a silicon strip tracking telescope (described in detail in Refs. [205, 206]) have been evaluated in this thesis wrt. mainly cluster energy loss statistics. In this Appendix energy loss plots for each sensor plane with the fitted parametrization discussed in Section 3.3.7 and tables summarizing the fit parameters are found that could not or were not intended to be placed within the main body of the document. Furthermore, the internal calibration procedure of the APV25-based sensor read-out for galvanically isolated channels is indicated as reference.

## A.1. *DESY* Beamtime

| Sensor Index | Doping Type | MPV ($\mathrm{k}e$) | $\sigma_L$ ($\mathrm{k}e$) | $\sigma_G$ ($\mathrm{k}e$) | SNR |
|---|---|---|---|---|---|
| 0 | p | 21.98(1) | 1.728(1) | 2.239(2) | 37.0 |
|   | n | 22.30(1) | 1.783(1) | 2.334(2) | 27.1 |
| 1a | p | 21.89(1) | 1.713(1) | 2.045(2) | 43.7 |
| 1b | p | 21.91(1) | 1.680(1) | 2.167(2) | 41.1 |
| 2a | p | 22.01(1) | 1.680(1) | 2.086(2) | 42.3 |
| 2b | p | 21.97(1) | 1.738(1) | 2.137(2) | 41.0 |
| 3 | n | 21.98(1) | 1.632(1) | 3.271(2) | 25.7 |
|   | p | 23.92(1) | 1.919(2) | 2.991(5) | 37.4 |

**Table A.1.:** Summarized energy loss fit parameters of *DESY* beamtime data sets.

## A.2. Jülich III Beamtime @ *COSY*

In this beam time campaign 4 sensors with entirely double sided read-out have been used. Sensor nr. 3 was connected with its $n$-side read-out galvanically isolated. As a consequence the linear relation between charge and ADC counts was not given any more as seen in Figure A.2(b) in comparison to the almost perfect linear calibration of a DC-coupled channel (Figure A.2(a)). A remedying parametrization was introduced for AC coupled readout electronics using a combined approach of two linear functions with different slopes, i.e.

$$q_1 = p_0 \cdot \mathrm{ADC}$$

| | |
|---|---|
| (a) | (b) |
| (c) | (d) |
| (e) | (f) |
| (g) | (h) |
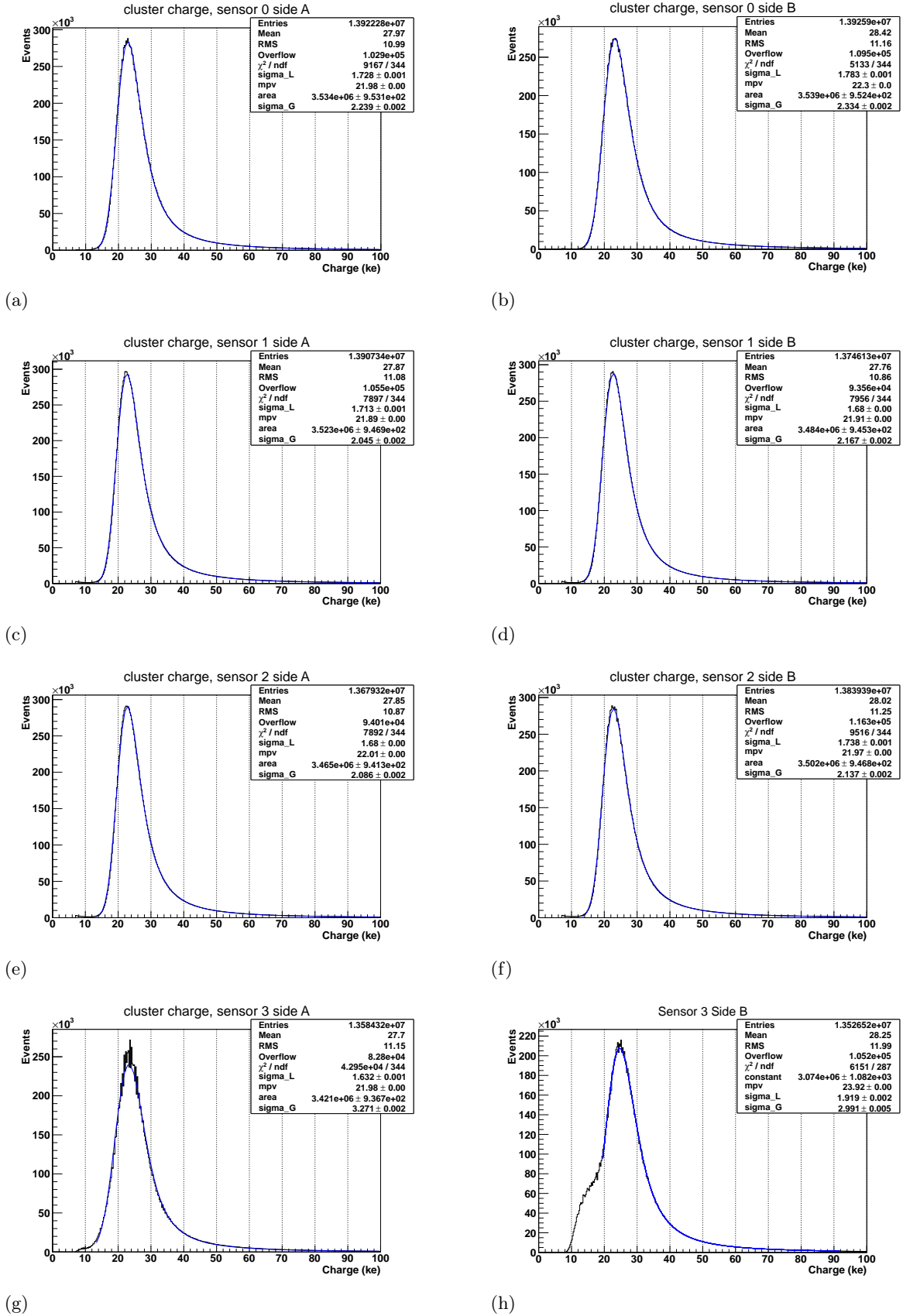
**Figure A.1.:** Cluster energy loss plots of each sensitive layer of the tracking telescope for *DESY* beamtime data sets. The sequence of the sensors follows the numbering (0...3) and the position in the beam in downstream direction.

and

$$q_2 = p_1 \cdot \text{ADC} + p_2$$

with the two slope parameters $p_0$, $p_1$ and the intercept $p_2$. A smooth transition at the mutual intercept point can be arranged by bridging the two straight lines by

$$\frac{1}{q} = \frac{1}{q_1} + \frac{1}{q_2}.$$

The resulting parametrization describes the calibration due to internal charge injection sufficiently well as seen in Figure A.2(b). The ENC of the AC-coupled sensor channels appears to be estimated correctly (last 3 front-ends in Figure A.2(c), compared to the DC-coupled $n$-side read-out of sensor 0, i.e. the first 3 front-ends) while the large ENC fluctuations among the channels of the $p$-side of sensor 3 are not explained yet.
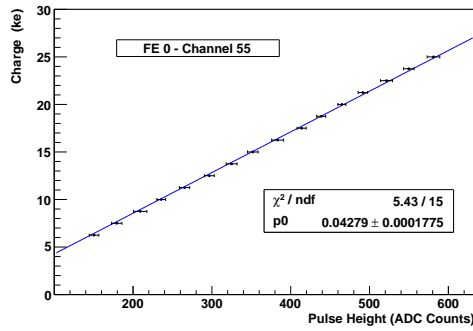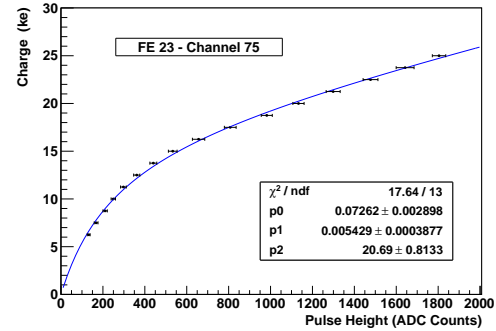


(a)                                                                                              (b)
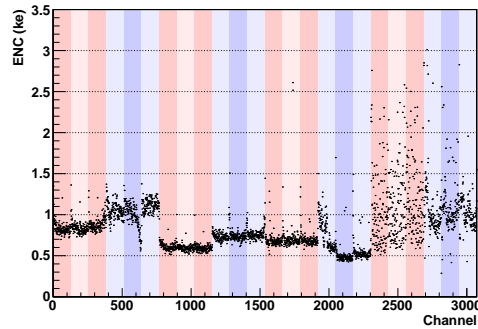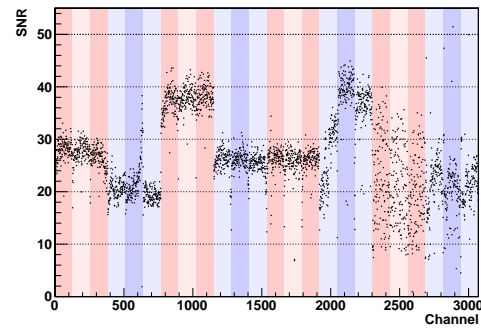
(c)                                                                                              (d)

**Figure A.2.:** Internal calibration of DC-coupled sensor channels (a), internal calibration of AC-coupled channel with combined dual-slope parametrization (b), reconstructed ENC (c) and SNR (d).
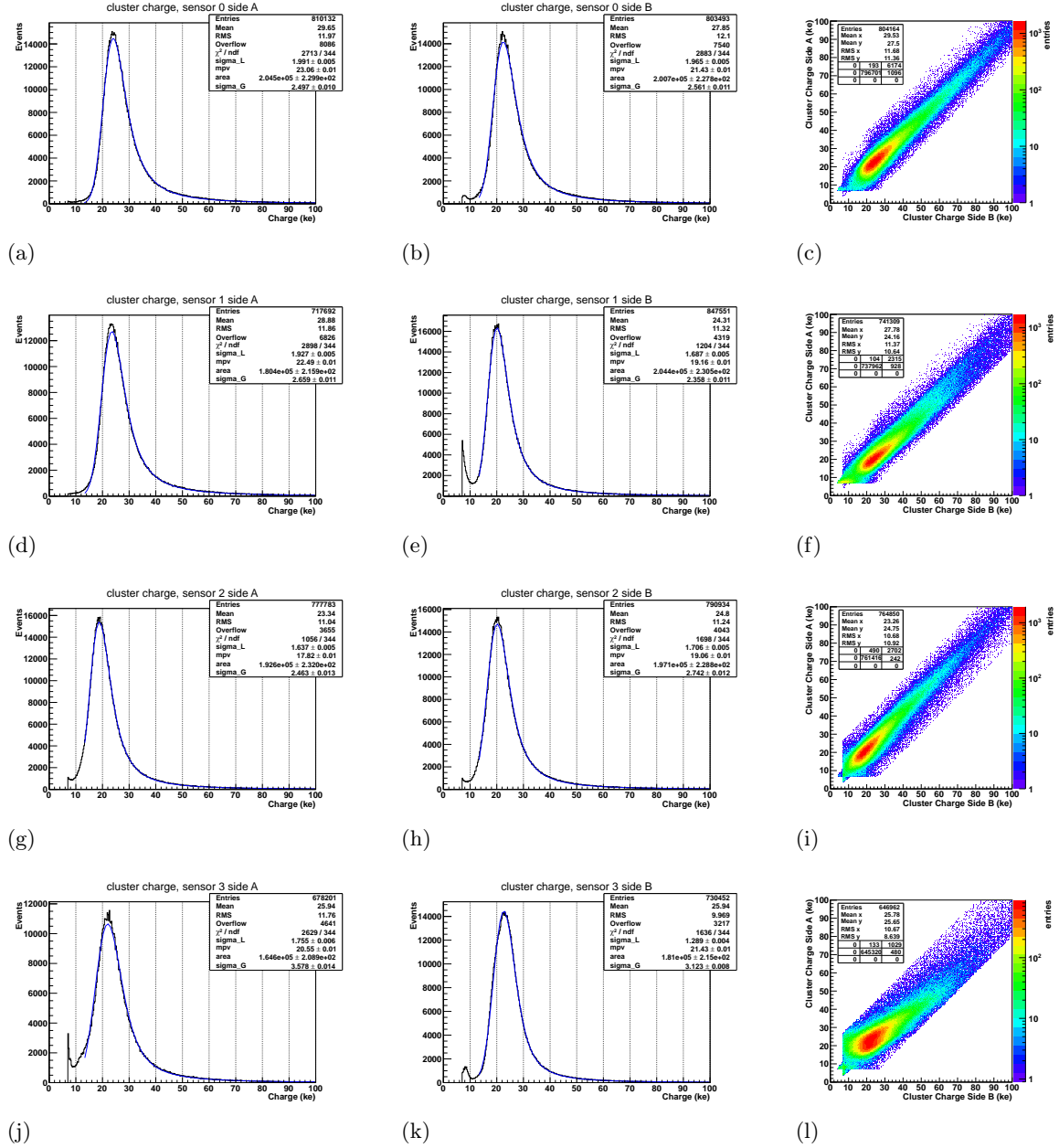
**Figure A.3.:** Cluster energy loss plots of each sensitive layer of the tracking telescope for *COSY* beamtime data (left and central columns) and cluster charge correlations between top and bottom side (right column). The sequence of the sensors follows the numbering (0...3) and the position in the beam in downstream direction.

| Sensor Index | Doping Type | MPV ($\mathrm{k}e$) | $\sigma_L$ ($\mathrm{k}e$) | $\sigma_G$ ($\mathrm{k}e$) | SNR |
|---|---|---|---|---|---|
| 0 | p | 23.06(1) | 1.991(5) | 2.497(11) | 26.6 |
|   | n | 21.43(1) | 1.965(5) | 2.561(11) | 20.0 |
| 1 | p | 22.49(1) | 1.927(5) | 2.659(11) | 37.2 |
|   | n | 19.16(1) | 1.687(5) | 2.358(11) | 25.4 |
| 2 | n | 17.82(1) | 1.637(5) | 2.463(13) | 26.0 |
|   | p | 19.06(1) | 1.706(5) | 2.742(12) | 33.6 |
| 3 | p | 20.55(1) | 1.755(6) | 3.578(14) | 21.2 |
|   | n | 21.43(1) | 1.289(4) | 3.123(8) | 21.4 |

**Table A.2.:** Summarized energy loss fit parameters of *COSY* beamtime data sets.

# Appendix B.

# Calculation of Displacement Damage and Equivalent Fluence

## B.1. Equivalent Fluence Calculation

The effective rate of interactions in a material due to incident neutrons under consideration of the displacement damage (NIEL) is obtained by

$$D = \int\limits_0^\infty \Phi_n(E)\sigma_{displ}(E)\mathrm{d}E \tag{B.1}$$

once the neutron spectral fluence $\Phi_n(E)$ and the material specific displacement damage cross section $\sigma_{displ}(E)$ are known. It is in some cases more convenient to indicate this damage rate $D$ as equivalent rate that would be evident for a monochromatic stream of neutrons at a well defined energy. Eqn. (B.1) is therefore referred to the displacement cross section at this energy. By convention, the reference cross section is chosen at a neutron kinetic energy of 1 MeV [125]. The equivalent damage rate then is

$$\Phi_{\mathrm{eq}} = \frac{\int\limits_0^\infty \Phi_n(E)\sigma_{displ}(E)\mathrm{d}E}{\sigma_{displ}(1\,\mathrm{MeV})}. \tag{B.2}$$

Note, that $\Phi_{\mathrm{eq}}$ is a fluence by units but it should not be mixed up with the initial neutron fluence $\Phi_n$. It can be interpreted as a fluence of actually with the material interacting neutrons[1], whereas $\Phi_n$ states the fluence of total neutrons crossing the same cross section.

## B.2. Displacement Damage of Neutrons in Material

The effect of non-ionizing damage is associated with the displacement of lattice atoms by knock-on collisions from impinging particles with kinetic energy $T$. Depending on the latter, the primary knock-on atom (PKA) of the absorber may have sufficient energy itself to trigger secondary collisions. Furthermore, the momentum transfer of each collision depends on the mass ratio of projectile and target. A chain of possible cascade collisions ensues at sufficiently high PKA momenta. Each knocked-on lattice atom on the other hand may deposit part or

---

[1] This is a mere simplified interpretation since the knocked-on lattice atoms contribute to the displacement cross section as well.

all of its energy into ionization of other atoms described by the *Bethe-Bloch* formalism. This contribution is consequently not available for displacements. The calculation of both, the ionizing and the displacement energy loss of each stage in the collision cascade is therefore mandatory for the determination of the displacement damage inflicted to the material.

### B.2.1. Electronic Stopping Power of PKA-Ions in Material

The *Bethe-Bloch* description of the mean electronic energy loss in matter was introduced in Section 2.3 and is valid for higher kinetic energies with $E > 200 \, \text{keV/amu}$. The low energy regime on the other hand is well covered by *Lindhard*'s theory of electronic stopping of ions [207]:

$$S_{Lindhard} = \frac{1}{N}\left(\frac{dE}{dx}\right) = 8\pi e^2 a_0 \frac{Z_1^{\frac{7}{6}} Z_2}{\left(Z_1^{\frac{2}{3}} + Z_2^{\frac{2}{3}}\right)^{\frac{3}{2}}} \frac{v}{v_0} \tag{B.3}$$

with $v$ the velocity of the projectile, $N$ the atomic density of the target material, $Z_1$, $Z_2$ the charge numbers of the projectile and the target material, respectively, $a_0 = 0.529 \, \text{Å}$, $v_0 = \frac{e^2}{\hbar}$ *Bohr*'s velocity and $e$ the charge of the electron. This formula is valid for incident velocities obeying $v/v_0 < 1$ which corresponds to PKA energies of $E < 25 \, \text{keV/amu}$ [111].

For higher energies ($v/v0 \gg 1$) the discussed formalism of *Bethe-Bloch* yields a correct estimate of the stopping power [108, 109]:

$$S_{Bethe-Bloch} = \frac{1}{N}\left(\frac{dE}{dx}\right) = 2\pi Z_{eff}^2 Z_2 e^4 \left(\frac{A_1 u}{m_e c^2}\right) \frac{1}{E} \ln\left(\frac{4E}{\left(\frac{A_1 u}{m_e c^2}\right)\bar{I}}\right) \tag{B.4}$$

with $A_1$ being the mass number of the projectile, $u$ the atomic mass unit, $m_e$ the electron mass, $c$ the speed of light in vacuum and $\bar{I} \approx 16 \cdot Z_2^{0.9}$ the mean excitation energy of the target atoms. The effective charge $Z_{eff}$ of the impinging particle accounts for the energy-dependent mean number of stripped electrons and can be approximated e.g. by the *Thomas-Fermi*-Model:

$$\frac{Z_{eff}}{Z_1} = 1 - \exp\left(-\frac{v}{v_0 Z^{\frac{2}{3}}}\right)$$

The two stopping power regimes can then be combined in order to sustain validity in the intermediate region. The *Bethe-Bloch* curve should be extended toward smaller energies by linear extrapolation beneath the point of maximum ionization for this purpose. *Biersack* and *Haggmark* suggested the following bridging procedure [208]:

$$S_{combined}^{-1} = S_{Lindhard}^{-1} + S_{Bethe-Bloch}^{-1} \tag{B.5}$$

The so obtained combined stopping power is an adequate approximation for cases when the mass and charge numbers of projectile and target species do not differ radically. This is especially true for the recoil particles in surrounding matter of the same specie.

## B.2.2. Inter-Atomic Potentials

*Lindhard* and *Winterbon* indicated power law functions to remedy the fairly complex description of shielded nuclear potentials by approximations in a broad range of energy transfers (compare to the poor descriptions of other semiclassic models as e.g. the *Thomas-Fermi* potential ansatz). These approximation functions usually have to be matched over several power laws to comply with the physically motivated models. However, the simplest approach of the inverse power law potential turned out to be in good agreement with latter ones provided using three different inter-matching energy regimes [207, 209]:

$$\sigma(E,T)\mathrm{d}T = C_m E^{-m} T^{-1-m}\mathrm{d}T \tag{B.6}$$

with

$$C_m = \frac{\pi}{2}\lambda_m a^2 \left(\frac{A_1}{A_2}\right)^2 \left(\frac{2Z_1 Z_2 e^2}{a}\right)^{2m}$$

and

$$a = \frac{0.4683}{\sqrt{Z_1^{2/3} + Z_2^{2/3}}}.$$

The choice of the values for $m$ and $\lambda_m$ depends on the reduced energy defined as

$$\epsilon = \frac{Ea}{Z_1 Z_2 e^2}\frac{A_2}{A_1 + A_2}$$

and can be obtained from table B.1.

| energy regime | $m$ | $\lambda_m$ |
|:---:|:---:|:---:|
| $\epsilon \leq 0.0234$ | 0 | 24 |
| $0.0234 < \epsilon \leq 0.369$ | $^1/_3$ | 1.309 |
| $0.369 < \epsilon \leq 12.0$ | $^1/_2$ | 0.327 |
| $\epsilon > 12.0$ | 1 | 0.5 |

**Table B.1.:** Power potential constants used for the approximation of inter-atomic potentials spanning several energy regimes (see text). Values taken from [210].

## B.2.3. Calculation of Damage Functions

The displacement of lattice atoms is understood as a removal of that atom from its lattice site by transfer of kinetic energy by the impinging particle. The primary knock-on atom usually has a very limited free pathlength such that its energy is transferred rapidly to other lattice atoms in secondary collisions and a collision cascade emerges [126]. Since each atom of the target material is bound to the lattice, a projectile needs to transfer a minimum energy in order to displace that atom. *Kinchin & Pease* first proposed a very simple model to parameterize the number of displaced atoms in a cascade triggered by a projectile of initial kinetic energy $T$ [211]:

$$\nu_{FP} = 0.8\frac{E^*(T)}{2\langle E_d\rangle} \tag{B.7}$$

where $E^*(T)$ is the fraction of kinetic energy deposited in nuclear displacement rather than electronic excitation. In the *Kinchin & Pease* model $E^*(T)$ can simply be chosen as the kinetic energy as a very coarse approximation, whereas $E^*(T)$ takes a more complex shape described by several potential laws in the formulation of *Torrens, Robinson* and *Norgett* (NRT-model) [212].

A different approach that describes the displacement cascade in form of an analytical equation for the conservation of the number of displacements vs. energy (subsequently called the *displacement function*) was first discussed by *Lindhard* [207]. The conservation equation given in this reference can be transformed by linear estimation of the energy transfer to the electrons from the slope of the displacement function (see ref. [210] for details) into the differential equation

$$S_e \frac{\mathrm{d}\nu(E)}{\mathrm{d}E} = \int_0^E \left[ \Gamma\big(T - E_d\big)\big(1 + \nu(T)\big) + \Gamma\big(E - T - E_d\big)\nu(E - T) - \nu(E) \right]$$
$$\times \sigma_{nucl}(E, T)\mathrm{d}T \tag{B.8}$$

where $\Gamma(x)$ is the unit step function, $S_e$ the electronic stopping power of the PKA in medium, $E_d$ the displacement threshold for removing the specific target atom from its lattice position and $\sigma_{nucl}(E, T)$ the differential nuclear scattering cross section of the PKA with atoms of the same species. Equation (B.8) is an integral-differential equation in the target function $\nu(E)$ and can be solved numerically by application of e.g. the *Runge-Kutta* method combined with a simple quadrature algorithm to tackle the integration.

Once the displacement function $\nu(E)$ is known, the total displacement cross section can be defined as

$$\sigma_{displ}(E_n) = \frac{4\pi\sigma_{el}(E_n)}{E_n \Lambda_{nA}} \int_0^{E_n \Lambda_{nA}} (\nu(E) + 1)\,\Gamma\left(E - E_d\right)\mathrm{d}E$$
$$+ \sum_{k=\text{all channels}} 2\pi \int_{E_{min}}^{E_{max}} \Lambda_{BA}\sigma_k(E_n, \Theta) \left|\frac{\mathrm{d}\cos\Theta}{\mathrm{d}E}\right| (\nu(E) + 1)\,\mathrm{d}E \tag{B.9}$$

with $\Lambda_{12} = \frac{4A_1 A_2}{(A_1 + A_2)^2}$ the energy transfer efficiency between particle 1 and 2, indices $n$ and $A$ for the neutron and the PKA-nucleus, respectively, index $B = A + 1 - x$ for the PKA-nucleus resulting from $(n, x)$ nuclear reaction, $\sigma_{el}(E)$ the total neutron elastic cross section and $\sigma_k(E_n, \Theta)$ the differential neutron scattering cross section of the material in nuclear (non-elastic) channel $k$ and $\Theta$ the scattering angle in the laboratory system. The first term in eqn. (B.9) represents the displacement damage caused by elastically recoiling PKAs while the second part accounts for PKAs produced by non-elastic collisions creating recoils which differ in their mass number from the bulk material such as $(n, \gamma)$ or $(n, \alpha)$ processes. This term holds also true for the inelastic $(n, n')$ as well as $(n, p)$-processes since they can be seen as a neutron disintegration process with a production of a neutron (proton) in the final state thus leaving the nucleus unaltered after de-excitation, i.e. $B = A$.

The contributions to the total displacement cross section from different reaction channels are presented in Figure B.1 for $^{28}$Si as target material. For this material the threshold energy for displacements is $E_d = 21\,\mathrm{eV}$ (see table B.2). Due to the energy transfer efficiency of
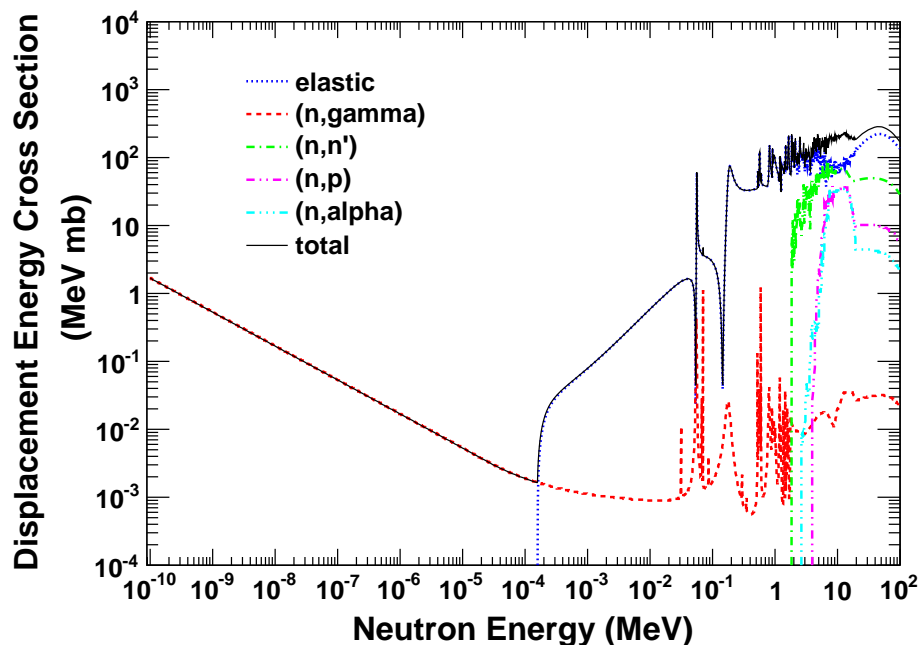
**Figure B.1.:** Contributions to the total damage energy cross section for $^{28}$Si. Below displacement threshold $E_d$ the (n,$\gamma$)-cross section (dashed) determines the total cross section. Beyond this energy up to ca. 2 MeV the figure is dominated by the elastic contribution (dotted). At higher energies channels for inelastic excitation of the target nucleus (dashed-dotted), proton production (dashed-2×dotted) and alpha production (dashed-3×dotted) as well as production of heavier hadrons or higher $Q$-values (not shown) open.

neutrons incident on Si-nuclei of $\Lambda_{nSi} \approx 0.13$, the minimum kinetic neutron energy required for displacing a lattice atom amounts to ca. 160 eV. Below this threshold energy the total cross section is determined exclusively by (n, $\gamma$)-reactions. The $Q$-values of this channel are usually high, thus allowing a thermal neutron to produce a recoiling PKA with kinetic energy above the displacement threshold. Other non-elastic channels do contribute to the total cross section only at higher neutron energies above several MeV, while the intermediate region, i.e. from displacement threshold up to the opening of the production channels, the total cross section is dominated by the elastic energy transfer from the neutron to the PKA.

## B.2.4.  Displacement Damage of Neutrons and Recoils in Compounds

The methods shown above are commonly used for the calculation of displacement damage in homogenous materials consisting of only a single atomic type of lattice atoms. For the often encountered case of a mixture of different materials, i.e. different nuclear species, the PKA as well as each element in the following displacement chain can appear to be of any type of nuclei contained in the target material. The knocked-on particle experiences electronic stopping in the surrounding composite material as already described above, but this time the calculation of stopping power has to take into account the material composition. Assuming homogenous mixture, *Bragg's Additivity Rule* applies:

$$S_e = \frac{\sum\limits_i A_i N_i S_{e,i}}{\sum\limits_i A_i N_i} \tag{B.10}$$

with the mass numbers $A_i$, atomic densities $N_i$ and stopping powers $S_{e,i}$ of material components $i$.

The calculation of the damage function following equation (B.9) in case of multi-atomic compounds expands into a system of coupled integral-differential equations (see also *Parkin & Coulter* [213] or *Ghoniem & Huang* [210])):

$$S_{e,i}\frac{\mathrm{d}\nu_{ij}(E)}{\mathrm{d}E} = \sum_k f_k \int\limits_0^{\Lambda_{ik}E} \left[\Gamma(T - E_{d,k})(\delta_{kj} + \nu_{kj}(T)) + \Gamma(E - T - \frac{E_{d,j}}{\Lambda_{ij}})\nu_{ij}(E - T) - \nu_{ij}(E)\right]$$
$$\times\, \sigma_{nucl,ik}(E,T)\mathrm{d}T \tag{B.11}$$

with $S_{e,i}$ the electronic stopping power of a PKA of type $i$ incident on the compound, $f_k$ the fraction of atomic density of the component within the compound, $E_{d,i}$ the displacement energy threshold of a lattice atom of material type $i$, $\sigma_{nucl,ij}(E,T)$ the differential nuclear scattering cross section between nuclei of species $i$ and $j$.

The monoatomic displacement cross section (B.9) can now be extended to account for the type of PKA of species $i$ and $j$ incident on lattice atoms of type $i$ and $j$, respectively to form the partial displacement cross section:

$$\sigma_{part,ij}(E_n) = \frac{4\pi\sigma_{el,i}(E_n)}{E_n \Lambda_{ni}} \int\limits_0^{E_n \Lambda_{ni}} (\nu_{ij}(E) + \delta_{ij})\,\Gamma\left(E - E_{d,i}\right)\mathrm{d}E$$
$$+ \sum_{k=\text{all channels}} 2\pi \int\limits_{E_{min}}^{E_{max}} \frac{\Lambda_{Bj}}{\Lambda_{ij}}\sigma_{k,i}(E_n, \Theta)\left|\frac{\mathrm{d}\cos\Theta}{\mathrm{d}E}\right|(\nu_{ij}(E) + \delta_{ij})\,\mathrm{d}E \tag{B.12}$$

where $\sigma_{el,i}$ is the integral elastic neutron scattering cross section of material $i$, $\sigma_{k,i}(E_n, \Theta)$ the differential neutron scattering cross section of material $i$ in nuclear (non-elastic) channel $k$.

$(n, \gamma)$ **reactions:**  For the $(n, \gamma)$ nuclear channel the transferred energy can be estimated from the $Q$-value of the reaction $Q_{\gamma,i}$ and the momentum transfer of the collision assuming a non-coherent addition of the according recoil momenta:

$$E = \frac{En}{A_i + 1} + \frac{Q_{\gamma,i}^2}{2(A_i + 1)u} + \sqrt{\frac{Q_{\gamma,i}^2 E_n}{u}}\cos\Theta$$

This is a rough approximation assuming that the $\gamma$-de-excitation takes place in one or a low number of steps. Furthermore both the initial recoil process and the $\gamma$-de-excitation are seen as non-superimposed processes, which means that the half lives of the recoiling nuclei in average should be larger than the typical stopping time of those nuclei in the surrounding matter. The minimum and maximum transferred energies are then given by

$$E_{min/max} = \frac{En}{A_i + 1} + \frac{Q_{\gamma,i}^2}{2(A_i + 1)u} \mp \sqrt{\frac{Q_{\gamma,i}^2 E_n}{u}}$$

and

$$\left| \frac{\mathrm{d}\cos\Theta}{\mathrm{d}E} \right| = \sqrt{\frac{u}{Q^2 E_n}}.$$

$(n, x)$ **reactions:** $(x = n', p, d, \alpha$ etc.) The minimum and maximum transferred energies in case of nuclear reaction channels with massive particles in the final state can be given as

$$E_{min/max} = \frac{B_i E_n}{(A_i + 1)^2} + \left( \frac{A_i E_n}{A_i + 1} - Q_{x,i} \right) \left( 1 + \frac{B_i}{x} \right)^{-1}$$
$$\mp \frac{2}{A_i + 1} \sqrt{\left( \frac{A_i E_n^2}{A_i + 1} - Q_{x,i} E_n \right) \left( \frac{1}{x} + \frac{1}{B_i} \right)^{-1}}$$

as well as

$$\left| \frac{\mathrm{d}\cos\Theta}{\mathrm{d}E} \right| = \frac{A_i + 1}{2} \sqrt{\left( \frac{1}{x} + \frac{1}{B_i} \right) \left( \frac{A_i E_n^2}{A_i + 1} - Q_{x,i} E_n \right)^{-1}}$$

with $B_i = A_i + 1 - x$ as the resulting mass number of the target nucleus after the reaction.

The in this way obtained integration boundaries as well as the elimination of the $\Theta$-dependence allows the transition from differential cross sections to integral neutron cross sections which can be pulled out of the integral in eqn. (B.12). The remaining simple integration may be carried out numerically with high precision since the function $\nu_{ij}(E)$ is continuous. The integral neutron cross sections required in above calculations are taken entirely from the ENDF/B-VII.1 library [214].

The fractional displacement cross section for lattice specie $i$ is

$$\sigma_{displ,i}(E_n) = f_i \sum_k P_{nk} \cdot \sigma_{part,ki}(E_n) \tag{B.13}$$

where $P_{ni} = \dfrac{N_i \sigma_{tot,i}(E_n)}{\sum_l N_l \sigma_{tot,l}(E_n)}$ corresponds to the probability that a neutron hits a nucleus of type $i$ and $\sigma_{tot,i}$ is the total microscopic neutron cross section of nuclide $i$. Note that the denominator of the expression for $P_{ni}$ is equivalent to the total macroscopic neutron cross section of the compound. On the other hand, the probability that a PKA collides with specie $i$ is simply expressed in terms of the fraction of atomic density $f_i$ of that specie inside the compound.

Finally, the total displacement cross section of the compound material is simply the summation of the fractional lattice cross sections:

$$\sigma_{displ}(E_n) = \sum_i \sigma_{displ,i}(E_n). \tag{B.14}$$

In Figure B.3 the partial displacement cross sections weighted with the probability $P_{ni}$ to encounter a collision of a neutron with a PKA of type $i$ are shown for the BaTiO$_3$ compound with the most abundant nuclide of the respective components, i.e. $^{138}$Ba, $^{48}$Ti and $^{16}$O (compare with table B.2). The following figures (B.4, B.5) were calculated taking into account the most abundant five isotopes of barium, five isotopes of titanium and the single nuclide $^{16}$O. Since all combinations of recoils and targets have to be considered in the damage

function computation, a total of $(5+5+1)^2=121$ coupled integral-differential equations had to be solved. In figure B.4, a comparison of the damage cross sections of the BaTiO$_3$-compound (dotted) with each of its constituents (Ba: dashed-dotted, Ti: dashed-2×dotted, O: dashed-3×dotted) with the full consideration of the isotopic content is drawn. Additionally, the cross section that accounts to a simple addition only of the single constituents according to their molecular fraction within the compound is presented (dashed trace). The computed displacement cross section of the BaTiO$_3$-compound with the full consideration of the nuclide mixture is separately presented again in Figure B.5. Finally, the displacement cross section for the natural (elemental) mixture of silicon was calculated as reported in Figure B.6.
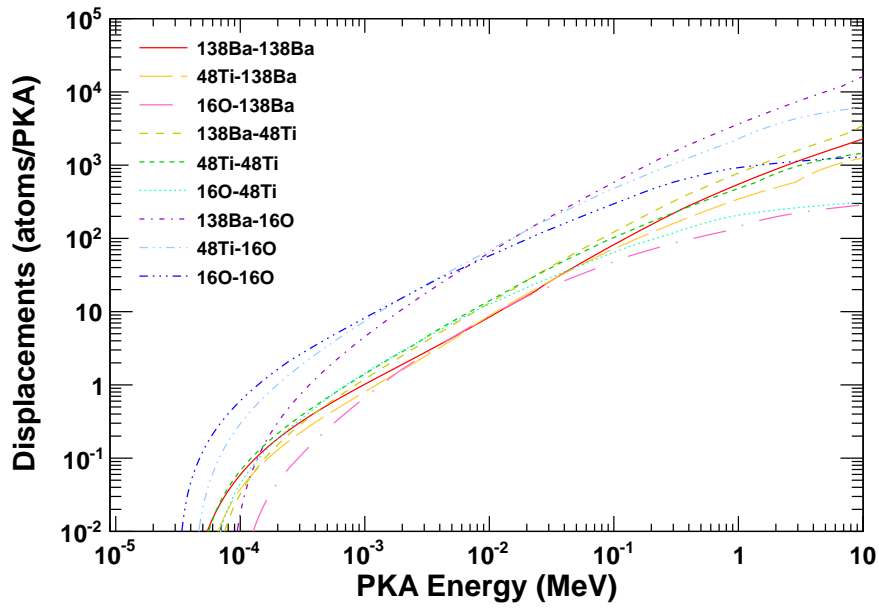


**Figure B.2.:** Displacement functions for BaTiO$_3$ compound considering the most significant nuclide specie only for barium, titanium and oxygen, respectively. Each possible combination of recoil PKA incident on different target nuclei introduces different displacement damage depending on the displacement threshold energies, the atomic density of the target specie, the electronic stopping power of the recoil in the compound and the nuclear scattering cross section between the recoil and the specific target atom.
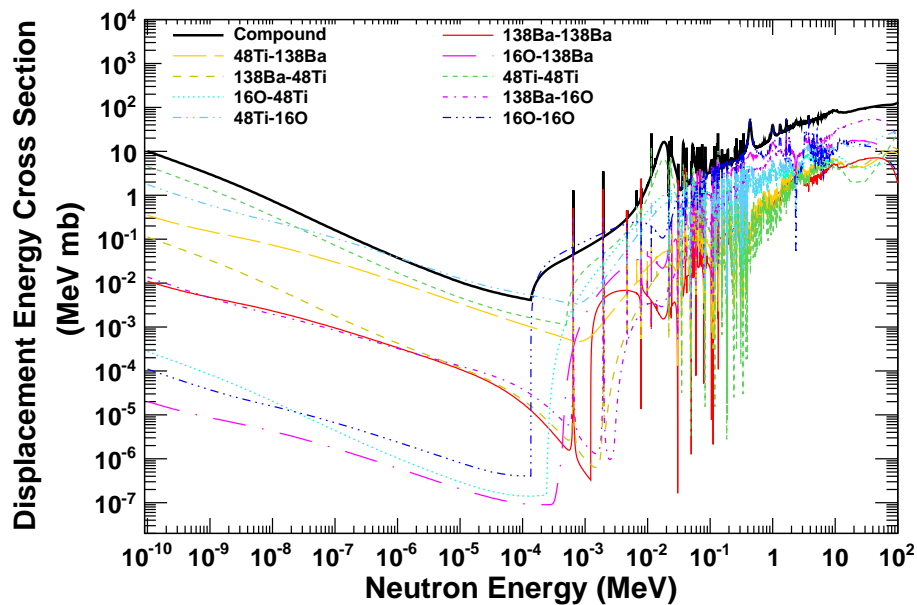
**Figure B.3.:** Partial displacement damage energy cross section for BaTiO$_3$ compound calculated for the most abundant nuclide species of barium, titanium and oxygen, respectively.
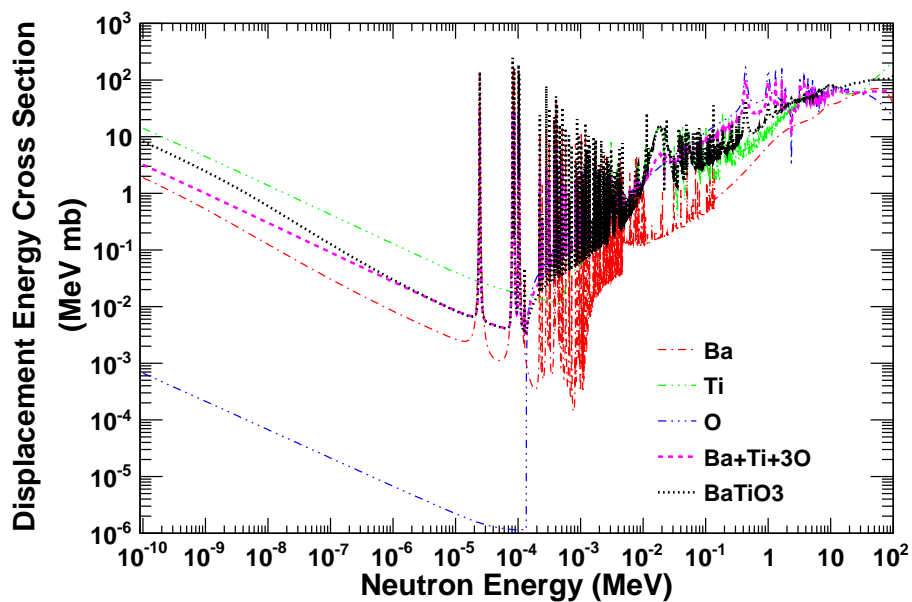


**Figure B.4.:** Displacement damage energy cross sections for BaTiO$_3$ compound and its constituents. The total cross section (dotted) is compared with the cross section that would result from simple addition of the cross sections of the single constituents (dashed).
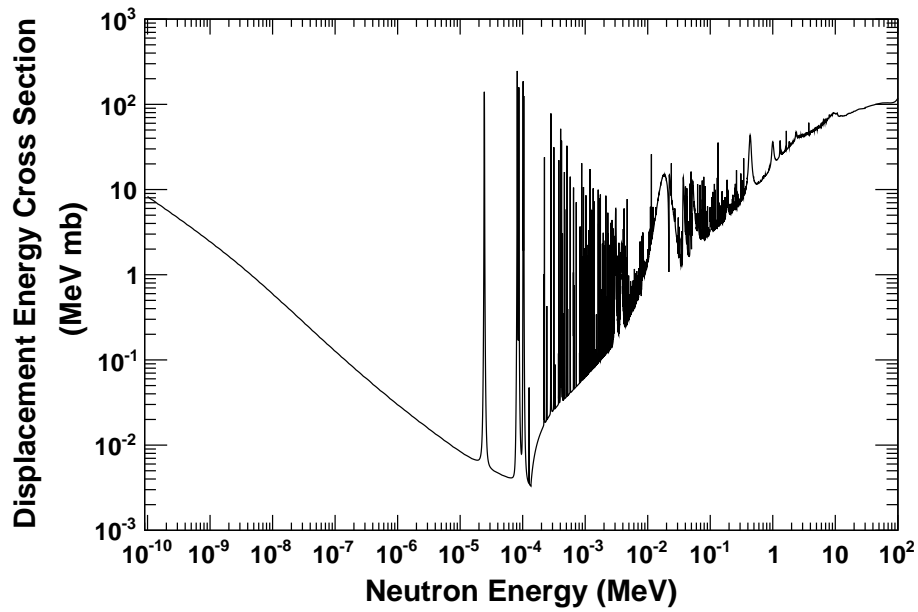
**Figure B.5.:** Total displacement damage energy cross section for $BaTiO_3$ compound calculated for the most abundant nuclide species (5 Ba-isotopes, 5 Ti-isotopes and $^{16}O$).
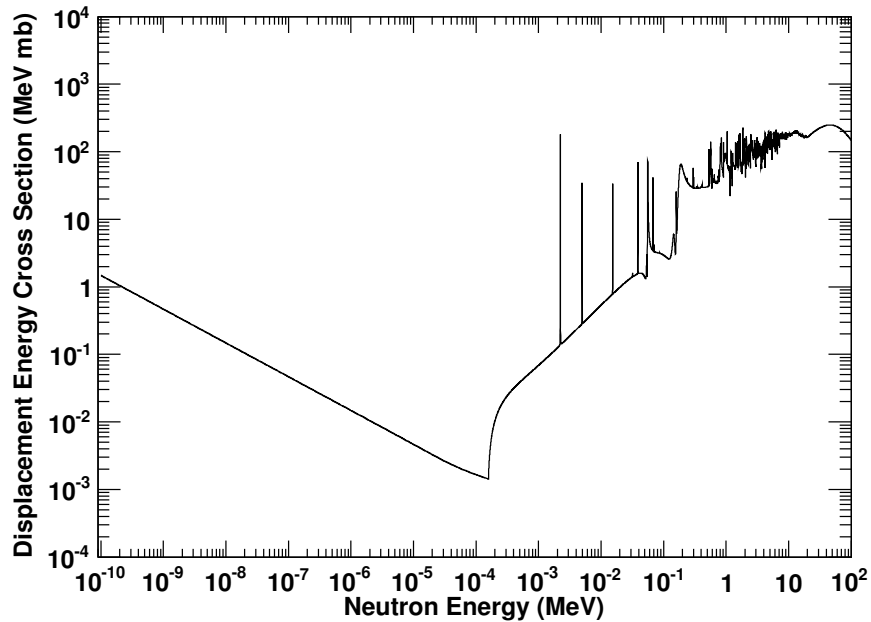


**Figure B.6.:** Total displacement damage energy cross section for elemental Si compound (92.2 % $^{28}Si$, 4.7 % $^{29}Si$ and 3.1 % $^{30}Si$).

## B.3. Nuclide Properties

The computation of the displacement damage cross sections for compounds requires the precise knowledge of fraction, nuclide content and nuclide properties of each material component. Since those information have to be gathered from a largely scattered set of literature and databases, the inclusion of compiled data for some selected species considered in the calculations earlier in this section seemed advisable also with regard to follow-up studies. Elemental abundances, displacement thresholds, and nuclear $Q$-values for oxygen, silicon, barium and titanium are listed in Table B.2.

| nuclide | elemental abundance | displacement threshold $E_d$ (eV) | nuclear $Q$-Values (MeV)[5] | | |
|---|---|---|---|---|---|
| | | | $(n, \gamma)$ | $(n, p)$ | $(n, \alpha)$ |
| $^{16}_{8}$O | $\approx 100\,\%$ | 30 [215] | 4.1446 | -9.6368 | -2.2143 |
| $_{14}$Si | | $20^1$, $24^2$, $18^3$ | | | |
| $^{28}$Si | 92.2 % | | 8.474 | -3.86 | -2.65 |
| $^{29}$Si | 4.7 % | | 10.61 | -2.899 | -0.0347 |
| $^{30}$Si | 3.1 % | | 6.592 | -7.752 | -4.20 |
| $_{56}$Ba | | $35^4$ | | | |
| $^{138}$Ba | 71.7 % | | 4.7234 | -4.5932 | 3.8802 |
| $^{137}$Ba | 11.2 % | | 8.61139 | -0.39053 | 6.0462 |
| $^{136}$Ba | 7.9 % | | 6.89839 | -1.76554 | 4.4102 |
| $^{135}$Ba | 6.6 % | | 9.10739 | 0.577454 | 7.07019 |
| $^{134}$Ba | 2.4 % | | 6.97339 | -1.27654 | 5.10720 |
| $^{130}$Ba | 0.1 % | | | | |
| $^{132}$Ba | 0.1 % | | | | |
| $_{22}$Ti | | 40 [215] | | | |
| $^{48}$Ti | 73.8 % | | 8.1424 | -3.20810 | -2.03140 |
| $^{46}$Ti | 8.0 % | | 8.8774 | -1.58493 | -0.0800498 |
| $^{47}$Ti | 7.3 % | | 11.6274 | 0.1823 | 2.18115 |
| $^{49}$Ti | 5.5 % | | 10.9394 | -1.22283 | 0.22745 |
| $^{50}$Ti | 5.4 % | | 6.37239 | -6.10612 | -3.44385 |

**Table B.2.:** Naturally occurring stable isotopes of selected elements with their elemental nuclide abundances and displacement thresholds. For each nuclide, the nuclear reaction $Q$-values of the first three significant reaction channels relevant at energies up to 20 MeV are specified. These values are used for the computation of the damage energy cross sections in this appendix.
[1] Average of collected values [130, 131].
[2] Measured value obtained from displacements with electrons [216].
[3] Molecular-Dynamics (MD) calculations [217].
[4] Value for Ba taken from systematic measurements of constituent displacement thresholds for $YBa_2Cu_3O_7$ high-$T_C$ superconductor [218].
[5] Values taken from [214].

# Appendix C.

# Neutron Irradiation of Ceramic Capacitors

In order to scrutinize the radiation damage effects on the utilized components inside the $\overline{\text{P}}$ANDA-MVD, several batches of ceramic capacitors were irradiated at the nuclear research reactor facility in Delft [220]. This Reactor is a water moderated pool bed reactor and thus comprises a spectrum of mainly thermal neutrons with kinetic energies below $10\,\text{eV}$. The displacement energy cross section in this range is usually low, since only $(n, \gamma)$ channels can be activated. However, at huge fluences the faster neutron part of the spectrum may not be negligible any more and, moreover, the large $Q$-values of the $(n, \gamma)$-reactions allow recoil energies sufficiently large to trigger secondary displacement cascades. The calculation of the actual displacement damage therefore requires the knowledge of the primary neutron spectrum and of the displacement cross section of the target material. Former is usually measured and supplied by the irradiation site while latter can be calculated using the algorithm given in Appendix B.

## C.1. Irradiation and Capacitance Measurements

As a starting point ceramic capacitors were chosen for irradiation. One reason for this selection is the relatively simple construction, although the precise material composition is often not sufficiently known or even unknown. Since the application of these capacitors (beside other very few commercially available components) is mandatory in the construction of the front-end electronics carrier (see section 4.5), detailed knowledge about their properties, particularly the material composition and the radiation tolerance is required.

Different types and sizes of ceramic capacitors were irradiated for 10 hours with the flux given in table C.1. The irradiation goods are encased inside a plastic cartouche (Figure C.1)

| Energy Regime | kinetic Energy | flux ($\text{cm}^{-2}\,\text{s}^{-1}$) | fluence @ $10\,\text{h}$ ($\text{cm}^{-2}$) |
|:---:|:---:|:---:|:---:|
| thermal | $< 0.5\,\text{eV}$ | $5 \cdot 10^{12}$ | $1.8 \cdot 10^{17}$ |
| epithermal | $0.5\,\text{eV}\dots 1\,\text{keV}$ | $1 \cdot 10^{12}$ | $3.6 \cdot 10^{16}$ |
| fast | $1\,\text{keV}\dots 10\,\text{MeV}$ | $3 \cdot 10^{11}$ | $1.08 \cdot 10^{16}$ |

**Table C.1.:** Neutron flux values during sample irradiation at the reactor facility in Delft for three energy regimes taken from [220].

which gets delivered to the reactor core by a pneumatic system. After the end of the irradiation interval the cartouche is extracted and left alone until the fast activation decayed and limiting values for transportation are obeyed. The displacement damage cross section for the dielectric material of the ceramic capacitors, namely barium-titanate ($BaTiO_3$) is calculated

**Figure C.1.:** Photograph of the irradiation sample cartouche. The cartouche itself consists of polyethylene to withstand the high neutron flux in the reactor core during irradiation. It is injected into the core pneumatically via a pipe system and remains at a defined position until the end of the dose application.

and reported in Appendix B. Together with the supplied neutron spectrum at the irradiation site (Figure C.3) a total displacement damage rate of

$$D = 7.09 \cdot 10^{17} \, \text{MeV mb cm}^{-2}$$

was calculated. The damage cross section for the BaTiO$_3$ compound and 1 MeV neutrons is retrieved from the calculations in Appendix B and yields $\sigma_{displ,\text{BaTiO}_3}(1 \, \text{MeV}) \approx 26 \, \text{MeV mb}$. Thus the displacement damage referenced to this value in analogy to the indication for silicon obtains the 1 MeV neutron equivalent fluence of

$$\Phi_{\text{eq}} = 2.73 \cdot 10^{16} \, \text{n}_{1\text{MeV eq}} \, \text{cm}^{-2}.$$

The capacitance of all samples was determined after the irradiation with an LCR-meter fixture. An independent group of capacitors retrieved from the same production lot was taken as reference. Each group contained between 5 and 10 capacitors for each type. The average value of the measured capacitances of each set for the three capacitor types is reported in Table C.2. The measurement error is considered negligible whereas the standard deviation within each group is indicated as error interval. Details about the measurement setup are documented in [221]. The raw values are corrected for the dual series capacitance used for coupling to the LCR-meter. It can be noted that the nominal capacitance did not change

| capacitor type | capacitance (nF) | |
| --- | --- | --- |
| | no irradiation | irradiated sample |
| 0603 X7R | $103.1^{\pm 2.0}_{\pm 10.0}$ | $109.8^{\pm 1.5}_{\pm 10.0}$ |
| 0402 X7R | $106.1^{\pm 3.0}_{\pm 10.0}$ | $103.1^{\pm 3.5}_{\pm 10.0}$ |
| 0201 X5R | $99.5^{\pm 6.0}_{\pm 10.0}$ | $74.7^{\pm 5.0}_{\pm 10.0}$ |

**Table C.2.:** Measured average capacitances of ceramic capacitors (nominal value 100 nF) irradiated with equivalent fluence of $\Phi_{\text{eq}} = 2.73 \cdot 10^{16} \, \text{n}_{1\text{MeV eq}} \, \text{cm}^{-2}$ and average capacitance measured for the reference group.

significantly for the larger package sizes after the irradiation. In fact, the 0603 capacitors appear to exhibit a somewhat higher capacitance. It must be remembered, though, that each value was obtained from independent sets of capacitors. The fluctuations of the average values are thus reconcilable with the tolerance of 10 % indicated by the manufacturer. This tolerance referred to the nominal value of 100 nF is stated together with the sample's standard deviation.

From each set one capacitor was arbitrarily chosen and subjected to a destructive break-down voltage measurement. The actually registered voltage breakdowns appeared for each tested sample far beyond the specified maximum operating voltage.

## C.2. Neutron Activation Analysis (NAA)

The huge abundance of thermal and epithermal neutrons in uranium-235 fission reactor environments activates the target nuclei, i.e. the capture of a thermal neutron generates a nuclide with a new mass number:

$$n + {}^{Z}_{N}A \rightarrow {}^{Z}_{N+1}(A+1)^* \tag{C.1}$$

The new nucleus ${}^{Z}(A+1)$ is usually unstable and is left in an excited state after the capture (except for nuclides that lead again to a stable configuration, as for ex. $^{28}$Si, $^{29}$Si and $^{30}$Si). The excited nucleus de-excites almost promptly under emission of a photon to the ground state[1]. The remaining nucleus subsequently decays (mostly through $\beta^{\pm}$ reactions) into a new nuclide:

$$\begin{aligned}
{}^{Z}_{N+1}(A+1) &\rightarrow {}^{Z-1}_{N+2}(A+1)^* + e^+ + \nu_e \\
&\rightarrow {}^{Z+1}_{N}(A+1)^* + e^- + \bar{\nu}_e
\end{aligned} \tag{C.2}$$
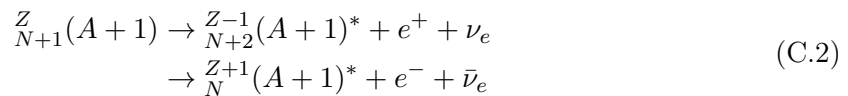
where the first branch is taken by nuclides with neutron excess while the second one leads proton-rich nuclei toward the valley of stability in the nuclide chart. The remaining nucleus now de-excites into its ground state

$$_{N'}^{Z'}A'^* \rightarrow {}^{Z'}_{N'}A' + \gamma \tag{C.3}$$

under emission of a photon. Analysis of the spectrum of all these post-transmutation de-excitation photons is domain of the Neutron Activation Analysis (NAA). The NAA may give a more detailed insight in a) the compound composition and b) the de-excitation behavior of the activated material.

A $\gamma$-spectrum recorded ca. 5 days after the irradiation of one of the irradiated ceramic capacitors is reported in Figure C.2 showing a large number of lines with high activities. Identification of lines and association to the originating nuclides is accomplished with e.g. [222]. The spectrum exhibits strong activations of barium while the other main constituents of the dielectric, titanium and oxygen, leave no traces in NAA spectra due to the fast decay times of the activated nuclei or too low activation cross sections. Gamma energies, half-lifes and neutron activation cross sections of several relevant nuclides are summarized in Table C.3. For the application in the sensitive volume of the MVD the abundance of activatable materials must be kept as low as possible. Therefore, the utilization of ceramic capacitors with a low content of silver and gold is recommended since those elements have exceedingly high activation cross sections.

---

[1]Except for some nuclides which remain in a long-lived excited (isomeric) state as for example $^{110m}$Ag.
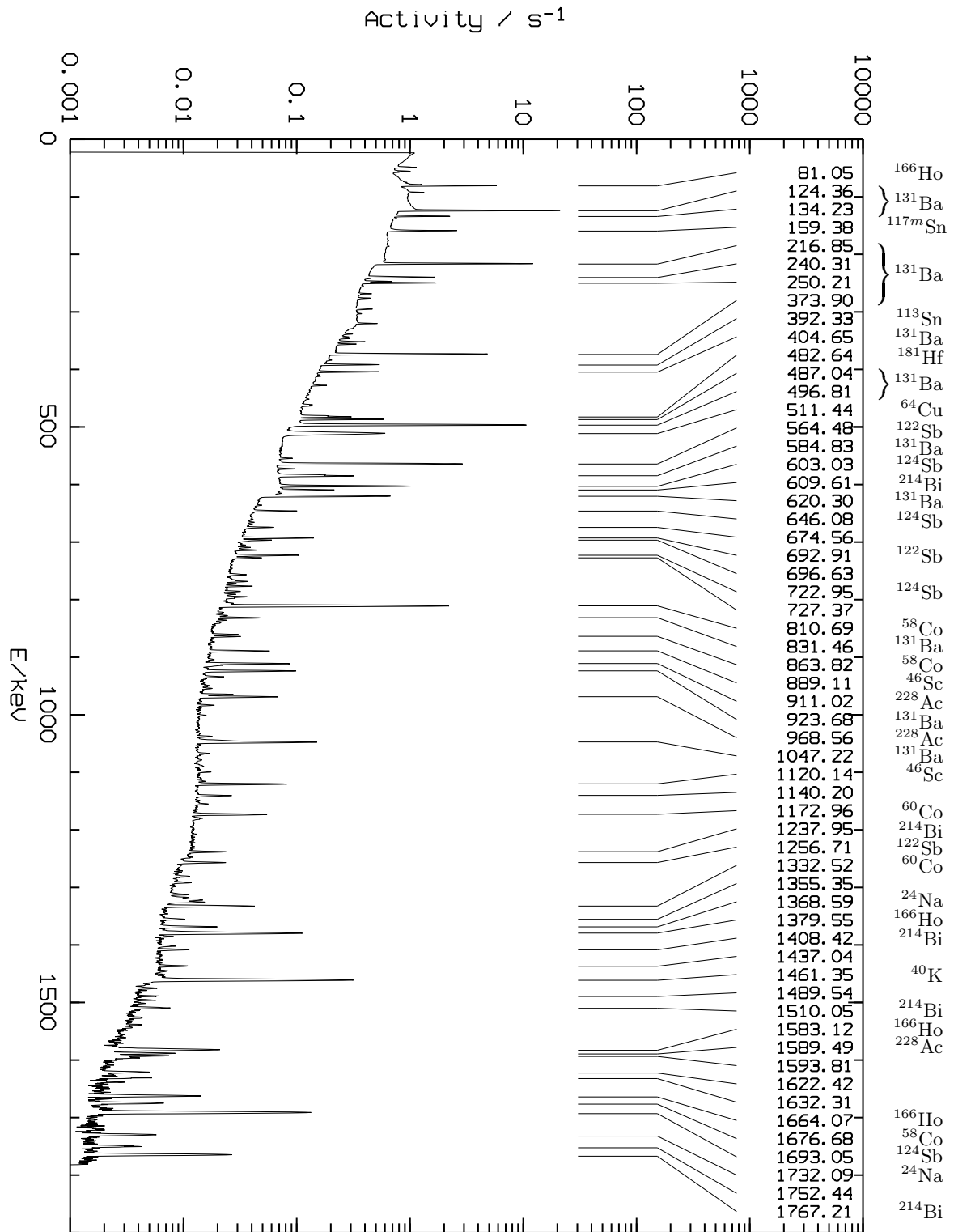
**Figure C.2.:** $\gamma$-spectrum of neutron activated ceramic capacitor, type X7R.
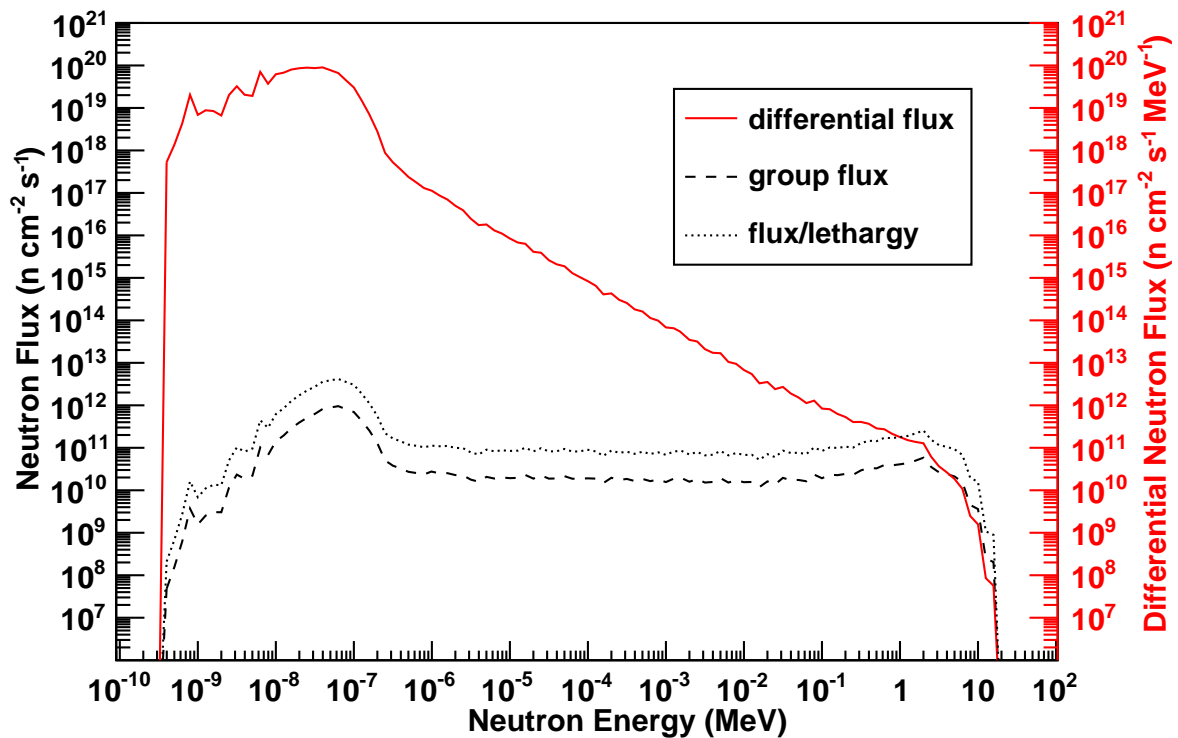
**Figure C.3.:** Neutron spectrum of irradiation facility BPx at the fission reactor in Delft (supplied by [223]) in three different representations. The flux per energy (solid line, right hand scale) often gives a biased picture at very low energies. Therefore a more practical representation is achieved by specifying the flux per energy interval, or group flux (dashed line, left scale) which is defined as the differential flux multiplied with the energy interval. In order to avoid a distorted view when the energy intervals are not equally distributed, the differential flux is multiplied with the center-energy of the groups instead (dotted, left scale). This representation is often referred to as lethargy plot or flux per unit lethargy.

## C.3. $\gamma$-Emission Lines of Selected Nuclides

**Table C.3.:** Selected nuclides relevant for Neutron Activation Analysis (NAA). The thermal neutron capture cross sections are given only for the mother nuclides of nuclei generated by a thermal $(n,\gamma)$-process (marked with "NTH"), while the generating decay process or decay chain is outlined for naturally occurring emitters. Values shown in columns 1 through 4 were taken from *Erdtmann & Soyka* [222] whereas cross sections originate from the ENDF/B-VII.1-catalog [214].

| Nuclide | $T_{1/2}$ | strongest $\gamma-$emissions (keV) | Generating Process | thermal neutron capture cross section $\sigma_{n,th}$ (barn) |
|---|---|---|---|---|
| $^{131}$Ba | 11.5 d | 496.32 123.80 216.09 373.26 249.44 | NTH $^{130}$Ba | 8.68 |
| $^{198}$Au | 2.70 d | 411.80 | NTH $^{197}$Au | 98.7 |
| $^{110m}$Ag | 249.76 d | 657.72 884.65 937.45 1384.24 763.92 706.65 1504.95 677.58 | NTH $^{109}$Ag | 91.1 |
| $^{51}$Cr | 27.8 d | 320.1 | NTH $^{50}$Cr | 15.9 |
| $^{40}$K | $1.248\cdot10^9$ y | 1460.82 | nat. | |
| $^{214}$Bi | 19.9 m | 609.32 1764.49 1120.29 1238.12 768.36 1407.99 1509.21 | nat. $\beta^-$ $^{214}$Pb Uranium-Radium-Chain | |
| $^{214}$Pb | 26.8 m | 351.93 295.22 77.11 | nat. Uranium-Radium-Chain | |
| $^{228}$Ac | 6.15 h | 911.20 968.97 338.32 | nat. Thorium-Chain | |
| $^{181}$Hf | 42.39 d | 482.18 133.02 345.93 | NTH $^{180}$Hf | 13.0 |
| $^{122}$Sb | 2.72 d | 564.08 672.76 | NTH $^{121}$Sb | 5.77 |
| $^{113}$Sn | 115.09 d | 391.71 | NTH $^{112}$Sn | 0.85 |
| $^{115}$Sn | | | NTH $^{114}$Sn | 0.13 |

<div align="center">**Table C.3.:** (continued)</div>

| Nuclide | $T_{1/2}$ | strongest $\gamma-$emissions (keV) | Generating Process | thermal neutron capture cross section $\sigma_{\mathrm{n,th}}$ (barn) |
|---|---|---|---|---|
| $^{117m}$Sn | 13.6 d | 158.56 156.02 | NTH $^{116}$Sn | 0.13 |
| $^{166}$Ho | 26.82 h | 80.58 1379.44 49.13 55.67 | NTH $^{165}$Ho | 64.7 |

# Appendix D.

# Abbreviations

AC . . . . . . . . . . . . . . Alternating Current; often referred to other observables than current thus meaning 'Alternating Mode'

ADC . . . . . . . . . . . . Analog-to-Digital Converter

ASIC . . . . . . . . . . . . Application Specific Integrated Circuit

BR . . . . . . . . . . . . . . Branching Ratio

CCE . . . . . . . . . . . . Charge Collection Efficiency

CEU . . . . . . . . . . . . Column End Unit

CLK . . . . . . . . . . . . Clock (signal)

CM . . . . . . . . . . . . . . Common Mode

COG . . . . . . . . . . . . Center of Gravity

COSY . . . . . . . . . . . Cooler Synchrotron

CPLD . . . . . . . . . . . Configurable Programmable Logic Device

CPU . . . . . . . . . . . . Central Processing Unit

CR-RC . . . . . . . . . . Combination of series capacitance, parallel resistance, series resistance and parallel capacitance forming a passive bandpass filter

CRC . . . . . . . . . . . . Cyclic Redundancy Check

CSA . . . . . . . . . . . . . Charge Sensitive Preamplifier

CTE . . . . . . . . . . . . Coefficient of Temperature Expansion

DAC . . . . . . . . . . . . Digital-to-Analog Converter

DAQ . . . . . . . . . . . . Data Acquisition

DC . . . . . . . . . . . . . . Direct Current; often referred to other observables than current thus meaning 'Constant Mode'

DPA, dpa . . . . . . . Displacement per Atom

DSP . . . . . . . . . . . . . Digital Signal Processing

DSSD . . . . . . . . . . . Double sided Silicon Strip Detector

DUT . . . . . . . . . . . . Device under Test

ELSA . . . . . . . . . . . Elektronen-Stretcher Anlage

EMC . . . . . . . . . . . . Electromagnetic Calorimeter

EMI . . . . . . . . . . . . . Electromagnetic Interference

ENC . . . . . . . . . . . . Equivalent Noise Charge

EoC . . . . . . . . . . . . . End of Column (for pixel front-ends) End of Channel-Set (for strip front-ends)

EoE . . . . . . . . . . . . . End of Event

ESR . . . . . . . . . . . . . Equivalent Series Resistance

EVC . . . . . . . . . . . . Event Complete

FAIR . . . . . . . . . . . Facility for Anti-Proton and Ion Research

FE . . . . . . . . . . . . . . Front-end

| | |
|---|---|
| FET . . . . . . . . . . . . . | Field Effect Transistor |
| FF . . . . . . . . . . . . . . | Flip-Flop |
| FIFO . . . . . . . . . . . | First In, First Out |
| FPGA . . . . . . . . . . | Field Programmable Gate Array |
| FZ . . . . . . . . . . . . . . | Floating Zone |
| HDL . . . . . . . . . . . . | Hardware Description Language |
| HESR . . . . . . . . . . . | High Energy Storage Ring |
| HEP . . . . . . . . . . . . . | High Energy Physics |
| HRB . . . . . . . . . . . . | Hit Ring-Buffer |
| HV . . . . . . . . . . . . . . | High Voltage |
| I$^2$C, I2C . . . . . . . . | Inter-IC Communication Bus |
| IC . . . . . . . . . . . . . . . | Integrated Circuit |
| IP . . . . . . . . . . . . . . . | Interaction Point |
| KERMA . . . . . . . . . | Kinetic Energy Released in Matter |
| LCR-Meter . . . . . . | Device for Measurement of Inductance, Capacitance and Resistance |
| LE . . . . . . . . . . . . . . | Leading Edge |
| LSB . . . . . . . . . . . . . | Least Significant Bit |
| LTCC . . . . . . . . . . | Low Temperature Co-Fired Ceramics |
| LUT . . . . . . . . . . . . | Look-Up Table |
| LV . . . . . . . . . . . . . . | Low Voltage |
| LVDS . . . . . . . . . . | Low Voltage Differential Signalling |
| MC . . . . . . . . . . . . . | Monte-Carlo |
| MDC[1] . . . . . . . . . . | Mini Drift Chamber |
| MDC[2] . . . . . . . . . . | Module Data Concentrator |
| MIP, m.i.p. . . . . . . | Minimum Ionizing Particle |
| MOS . . . . . . . . . . . . | Metal Oxide - Semiconductor junction |
| MPV . . . . . . . . . . . | Most Probable Value |
| MSB . . . . . . . . . . . | Most Significant Bit |
| MVD . . . . . . . . . . . | Micro Vertex Detector |
| NAA . . . . . . . . . . . . | Neutron Activation Analysis |
| NIEL . . . . . . . . . . . | Non-Ionizing Energy Loss |
| NIM . . . . . . . . . . . . | Nuclear Instrumentation Module |
| $\overline{\text{P}}$ANDA . . . . . . . . . | (Anti)-Proton Annihilations at Darmstadt |
| PCB . . . . . . . . . . . . . | Printed Circuit Board |
| PKA . . . . . . . . . . . . | Primary knock-on Atom |
| PLL . . . . . . . . . . . . . | Phase-Locked Loop |
| PMT . . . . . . . . . . . | Photo Multiplier Tube |
| QA . . . . . . . . . . . . . . | Quality Assurance |
| RC . . . . . . . . . . . . . . | Combination of series resistance and parallel capacitance forming a passive lowpass filter with $3\,\text{dB}$ roll-off |
| RICH . . . . . . . . . . . | Ring Image Cherenkov Detector |
| RMS . . . . . . . . . . . . | Root Mean Square |
| R/O, RO . . . . . . . . | Readout |
| ROL . . . . . . . . . . . . | Readout Latency |
| ROP . . . . . . . . . . . . | Readout Pointer |
| SEU . . . . . . . . . . . . . | Single Event Upset |

---

[1] Referring to a drift detector system.
[2] Referring to an application specific IC.

SKA . . . . . . . . . . . . . Secondary knock-on Atom
SLVS . . . . . . . . . . . . Scalable Low-Voltage Signaling
SMD . . . . . . . . . . . Surface Mount Device
SNR . . . . . . . . . . . . Signal-to-Noise Ratio
SPI . . . . . . . . . . . . . . Serial Peripheral Interface
SR . . . . . . . . . . . . . . Shift Register
STT . . . . . . . . . . . . . Straw Tube Tracker
TE . . . . . . . . . . . . . . Trailing Edge
TID . . . . . . . . . . . . . Total Ionizing Dose
ToA . . . . . . . . . . . . . Time of Arrival
ToF . . . . . . . . . . . . . Time of Flight
ToT . . . . . . . . . . . . . Time over Threshold
TS . . . . . . . . . . . . . . Time Stamp
TSC . . . . . . . . . . . . . Time Stamp Counter
VLSI . . . . . . . . . . . . Very Large Scale Integration
VME . . . . . . . . . . . . Versa Module European (ANSI/IEEE 1014); a universal
bus system originating from VERSAbus standard

# References

[1] E. Rutherford, "LXXIX. The scattering of $\alpha$ and $\beta$ particles by matter and the structure of the atom," *Philosophical Magazine Series 6*, vol. 21, no. 125, pp. 669–688, 1911.

[2] N. Bohr, "On the Constitution of Atoms and Molecules," *Philosophical Magazine Series 6*, vol. 26, p. 1 ff, 1913.

[3] E. Rutherford, "LI. Collision of $\alpha$ particles with light atoms I-IV," *Philosophical Magazine Series 6*, vol. 37, no. 222, p. 537 ff, 1919.

[4] W. Bothe and H. Becker, "Eine Kern-$\gamma$-Strahlung bei leichten Elementen," *Naturwissenschaften*, vol. 18, pp. 705–705, Aug. 1930.

[5] W. Bothe and H. Becker, "Künstliche Erregung von Kern-$\gamma$-Strahlen," *Zeitschrift fur Physik*, vol. 66, pp. 289–306, May 1930.

[6] I. Joliot-Curie and F. Joliot-Curie, "Projections d'atomes par les rayons très pénétrants excités dans les noyaux légers," *Comptes rendus hebdomadaires des séances de l'Académie des sciences*, vol. 194, p. 876 ff, 1932.

[7] J. Chadwick, "Possible Existence of a Neutron," *Nature*, vol. 129, p. 312, Feb. 1932.

[8] W. Heisenberg, "Über den Bau der Atomkerne. II," *Zeitschrift für Physik A Hadrons and Nuclei*, vol. 78, pp. 156–164, 1932. 10.1007/BF01337585.

[9] W. Heisenberg, "Über den Bau der Atomkerne. III," *Zeitschrift für Physik A Hadrons and Nuclei*, vol. 80, pp. 587–596, 1933. 10.1007/BF01335696.

[10] C. F. v. Weizsäcker, "Zur Theorie der Kernmassen," *Zeitschrift für Physik A Hadrons and Nuclei*, vol. 96, pp. 431–458, 1935. 10.1007/BF01337700.

[11] H. Yukawa, "On the interaction of elementary particles," *Proc.Phys.Math.Soc.Jap.*, vol. 17, pp. 48–57, 1935.

[12] C. Lattes, G. Occhialini, and C. Powell, "Observations on the Tracks of Slow Mesons in Photographic Emulsions. 1," *Nature*, vol. 160, pp. 453–456, 1947.

[13] C. Lattes, G. Occhialini, and C. Powell, "Observations on the Tracks of Slow Mesons in Photographic Emulsions. 2," *Nature*, vol. 160, pp. 486–492, 1947.

[14] R. Frisch and O. Stern, "Über die magnetische Ablenkung von Wasserstoffmolekülen und das magnetische Moment des Protons. I and II," *Zeitschrift für Physik A Hadrons and Nuclei*, vol. 85, p. 4 ff, 1933. 10.1007/BF01330773.

[15] L. W. Alvarez and F. Bloch, "A Quantitative Determination of the Neutron Moment in Absolute Nuclear Magnetons," *Phys.Rev.*, vol. 57, pp. 111–122, 1940.

[16] M. Gell-Mann, "The Eightfold Way: A Theory of strong interaction symmetry," 1961.

[17] S. Glashow and M. Gell-Mann, "Gauge Theories of Vector Particles," *Annals Phys.*, vol. 15, pp. 437–460, 1961.

[18] M. Gell-Mann, "Symmetries of baryons and mesons," *Phys.Rev.*, vol. 125, pp. 1067–1084, 1962.

[19] M. Gell-Mann, "A schematic model of baryons and mesons," *Physics Letters*, vol. 8, no. 3, pp. 214 – 215, 1964.

[20] M. Gell-Mann and Y. Ne'eman, "The Eightfold way: a review with a collection of reprints," 1964.

[21] G. Zweig, "An SU(3) model for strong interaction symmetry and its breaking," 1964.

[22] R. Feynman, M. Gell-Mann, and G. Zweig, "Group U(6) x U(6) generated by current components," *Phys.Rev.Lett.*, vol. 13, pp. 678–680, 1964.

[23] K. Nakamura (Particle Data Group) *et al.*, "Review of Particle Physics," *J. Phys. G*, vol. 37, pp. 1+, 2010.

[24] H. Fritzsch and M. Gell-Mann, "Current algebra: Quarks and what else?," *eConf*, vol. C720906V2, pp. 135–165, 1972.

[25] W. A. Bardeen, H. Fritzsch, and M. Gell-Mann, "Light cone current algebra, pi0 decay, and e+ e- annihilation," 1972.

[26] Povh, Rith, and Zetsche, *Einführung in die Kernphysik*. Springer Verlag, 1996.

[27] K. Gottfried and V. Weisskopf, *Concepts of Particle Physics*. Concepts of Particle Physics, Oxford University Press, USA, 1986.

[28] D. J. E. Callaway and A. Rahman, "Microcanonical Ensemble Formulation of Lattice Gauge Theory," *Physical Review Letters*, vol. 49, pp. 613–616, Aug. 1982.

[29] D. H. Perkins, *Introduction to High Energy Physics*. Cambridge University Press, $4^{th}$ ed., 2000.

[30] W. Cottingham and D. Greenwood, *An Introduction to the Standard Model of Particle Physics*. Cambridge University Press, 1998.

[31] T. Barnes, "Update on Charmonium Theory," *AIP Conf.Proc.*, vol. 1257, pp. 11–18, 2010.

[32] A. Donnachie, "Low-energy hadronic physics," *Physics Reports*, vol. 403–404, no. 0, pp. 281 – 301, 2004. CERN - the second 25 years.

[33] M. Kotulla *et al.*, "Strong interaction studies with antiprotons. Letter of intent for PANDA (Antiproton Annihilations at Darmstadt)," 2004.

[34] R. Maier, D. Prasuhn, R. Stassen, H. Stockhorst, C. Dimopoulou, *et al.*, "Stochastic Cooling Developments for HESR at FAIR," *Conf.Proc.*, vol. C1205201, pp. 388–390, 2012.

[35] PANDA Collaboration, *Technical Design Report for the Micro-Vertex Detector (MVD)*, 2012. arXiv:1207.6581; http://www-panda.gsi.de.

[36] M. Lutz *et al.*, "Physics Performance Report for PANDA: Strong Interaction Studies with Antiprotons," 2009. arXiv:0903.3905.

[37] K.-T. Brinkmann, P. Gianotti, and I. Lehmann, "Exploring the Mysteries of Strong Interactions – The PANDA Experiment," *Nucl. Phys. News*, vol. 16, 2005.

[38] J. Ritman, "The PANDA detector at the GSI-FAIR project," *Int.J.Mod.Phys.*, vol. A20, pp. 567–569, 2005.

[39] K. Peters, "Charmonium and exotic hadrons at PANDA," *Int.J.Mod.Phys.*, vol. A20, pp. 570–577, 2005.

[40] K. Brinkmann, "PANDA at the GSI future facility," *Nucl.Instrum.Meth.*, vol. A549, pp. 146–152, 2005.

[41] K. Brinkmann, "Physics with the PANDA detector at FAIR," *Nucl.Phys.*, vol. A790, pp. 75–80, 2007.

[42] I. Lehmann, "Physics Programme of PANDA at FAIR," pp. 408–410, 2009.

[43] J. Messchendorp, "A systematic study of the strong interaction with PANDA," *PoS*, vol. EPS-HEP2009, p. 083, 2009.

[44] P. Gianotti, "The PANDA experiment at FAIR," *Nucl.Phys.*, vol. A835, pp. 96–101, 2010.

[45] A. Gillitzer, "Strong interaction physics with PANDA," *Int.J.Mod.Phys.*, vol. A26, pp. 523–528, 2011.

[46] T. Würschig, "Charm spectroscopy at the PANDA experiment," *AIP Conf.Proc.*, vol. 1441, pp. 329–331, 2012.

[47] K. Seth, "Experimental review of charmonium spectroscopy," *The European Physical Journal A - Hadrons and Nuclei*, vol. 18, pp. 563–565, 2003. 10.1140/epja/i2002-10284-4.

[48] PANDA Collaboration, *Technical Progress Report*, 2005. http://www-panda.gsi.de.

[49] T. Barnes and S. Olsen, "Chapter 14 charmonium spectroscopy," *International Journal of Modern Physics A*, vol. 24, no. supp01, pp. 305–325, 2009.

[50] S.-K. Choi, S. L. Olsen, K. Abe, T. Abe, I. Adachi, B. S. Ahn, H. Aihara, K. Akai, M. Akatsu, M. Akemoto, Y. Asano, T. Aso, V. Aulchenko, T. Aushev, A. M. Bakich, Y. Ban, S. Banerjee, A. Bondar, A. Bozek, M. Bračko, J. Brodzicka, T. E. Browder, P. Chang, Y. Chao, K.-F. Chen, B. G. Cheon, R. Chistov, Y. Choi, Y. K. Choi, M. Danilov, L. Y. Dong, A. Drutskoy, S. Eidelman, V. Eiges, J. Flanagan, C. Fukunaga, K. Furukawa, N. Gabyshev, T. Gershon, B. Golob, H. Guler, R. Guo, C. Hagner, F. Handa, T. Hara, N. C. Hastings, H. Hayashii, M. Hazumi, L. Hinz, Y. Hoshi, W.-S. Hou, Y. B. Hsiung, H.-C. Huang, T. Iijima, K. Inami, A. Ishikawa, R. Itoh, M. Iwasaki, Y. Iwasaki, J. H. Kang, S. U. Kataoka, N. Katayama, H. Kawai, T. Kawasaki, H. Kichimi, E. Kikutani, H. J. Kim, H. Kim, J. H. Kim, S. K. Kim, K. Kinoshita, H. Koiso, P. Koppenburg, S. Korpar, P. Križan, P. Krokovny, S. Kumar, A. Kuzmin, J. S. Lange, G. Leder, S. H. Lee, T. Lesiak, S.-W. Lin, D. Liventsev, J. MacNaughton, G. Majumder, F. Mandl, D. Marlow, T. Matsumoto, S. Michizono, T. Mimashi, W. Mitaroff, K. Miyabayashi, H. Miyake, D. Mohapatra, G. R. Moloney, T. Nagamine, Y. Nagasaka, T. Nakadaira, T. T. Nakamura, M. Nakao, Z. Natkaniec, S. Nishida, O. Nitoh, T. Nozaki, S. Ogawa, Y. Ogawa, K. Ohmi, Y. Ohnishi, T. Ohshima, N. Ohuchi, K. Oide, T. Okabe, S. Okuno, W. Ostrowicz, H. Ozaki, H. Palka, H. Park, N. Parslow, L. E. Piilonen, H. Sagawa, S. Saitoh, Y. Sakai, T. R. Sarangi, M. Satapathy, A. Satpathy, O. Schneider, A. J. Schwartz, S. Semenov, K. Senyo, R. Seuster, M. E.

Sevior, H. Shibuya, T. Shidara, B. Shwartz, V. Sidorov, N. Soni, S. Stanič, M. Starič, A. Sugiyama, T. Sumiyoshi, S. Suzuki, F. Takasaki, K. Tamai, N. Tamura, M. Tanaka, M. Tawada, G. N. Taylor, Y. Teramoto, T. Tomura, K. Trabelsi, T. Tsukamoto, S. Uehara, K. Ueno, Y. Unno, S. Uno, G. Varner, K. E. Varvell, C. C. Wang, C. H. Wang, J. G. Wang, Y. Watanabe, E. Won, B. D. Yabsley, Y. Yamada, A. Yamaguchi, Y. Yamashita, H. Yanai, H. Yang, J. Ying, M. Yoshida, C. C. Zhang, Z. P. Zhang, and D. Žontar, "Observation of a narrow charmoniumlike state in exclusive $B^{\pm} \to K^{\pm}\pi^{+}\pi^{-}J/\psi$ decays," *Phys. Rev. Lett.*, vol. 91, p. 262001, Dec 2003.

[51] J. S. Lange, M. Galuska, T. Gessler, W. Kühn, S. Kunze, *et al.*, "Prospects for X(3872) Detection at Panda," *AIP Conf.Proc.*, vol. 1374, pp. 549–552, 2011.

[52] R. L. Jaffe, "Perhaps a Stable Dihyperon," *Phys.Rev.Lett.*, vol. 38, pp. 195–198, 1977.

[53] The E896 Collaboration, H. Caines, S. Albergo, R. Bellwied, M. Bennett, D. Boemi, B. Bonner, Z. Caccia, W. Christie, G. Cinà, S. Costa, H. Crawford, M. Cronqvist, R. Debbe, J. Engelage, I. Flores, L. Greiner, T. Hallman, G. Hoffman, H. Huang, T. J. Humanic, G. Igo, A. Insolia, P. Jensen, E. Judd, K. Kainz, M. Kaplan, S. Kelly, I. Kotov, G. Kunde, P. Lindstrom, T. Ljubicic, W. Llope, G. L. Curto, R. Longacre, D. Lynn, L. Madansky, N. Mahzeh, Z. Milosevich, J. T. Mitchell, J. Mitchell, S. Nehmeh, C. Nociforo, S. Paganis, S. U. Pandey, R. Potenza, E. Platner, P. Riley, D. Russ, A. Saulys, J. Schambach, J. Sheen, C. Stokley, E. Sugarbaker, J. Takahashi, J. Tang, A. Tratner, S. Trentalange, A. Tricomi, C. Tull, C. Tuvè, J. Whitfield, and K. Wilson, "An update on the strangeness production measurements and H 0 di-baryon search as performed by the AGS experiment 896," *Journal of Physics G: Nuclear and Particle Physics*, vol. 27, no. 3, p. 311, 2001.

[54] F. Weber, "Strangeness in neutron stars," *Journal of Physics G: Nuclear and Particle Physics*, vol. 27, no. 3, p. 465, 2001.

[55] K. J. Juge, J. Kuti, and C. Morningstar, "Fine structure of the qcd string spectrum," *Phys. Rev. Lett.*, vol. 90, p. 161601, Apr 2003.

[56] C. J. Morningstar and M. Peardon, "Glueball spectrum from an anisotropic lattice study," *Phys. Rev. D*, vol. 60, p. 034509, Jul 1999.

[57] W. I. Eshraim, S. Janowski, F. Giacosa, and D. H. Rischke, "Decay of the pseudoscalar glueball into scalar and pseudoscalar mesons," 2012.

[58] K. Peters, "Charmonium and exotic hadrons at PANDA," *Int.J.Mod.Phys.*, vol. E16, pp. 919–924, 2007.

[59] W. Weise, "Nuclear aspects of chiral symmetry," *Nuclear Physics A*, vol. 553, no. 0, pp. 59 – 72, 1993.

[60] S. Leupold, V. Metag, and U. Mosel, "Hadrons in strongly interacting matter," *International Journal of Modern Physics E*, vol. 19, no. 02, pp. 147–224, 2010.

[61] J. Schaffner-Bielich, "Effect of in-medium properties on heavy-ion collisions," *Journal of Physics G: Nuclear and Particle Physics*, vol. 27, no. 3, p. 337, 2001.

[62] M. Strikman, "QCD with and in nuclei: Color transparency and short-range correlations in nuclei: Theory, observations, directions for further studies," *Nucl.Phys.*, vol. A827, pp. 240C–245C, 2009.

[63] O. Hartmann, "Hadron properties in the nuclear medium: The PANDA program with anti-p A reactions," *Int.J.Mod.Phys.*, vol. A22, pp. 578–581, 2007.

[64] J. Pochodzalla, "Future hypernuclear physics at MAMI-C and PANDA-GSI," *Nucl.Phys.*, vol. A754, pp. 430–442, 2005.

[65] A. Sokolov, A. Gillitzer, and J. Ritman, "Physics with open charm mesons at PANDA," *AIP Conf.Proc.*, vol. 796, pp. 63–68, 2005.

[66] E. Tomasi-Gustafsson, "Form factor measurements with bar PANDA at FAIR," *Chin.Phys.*, vol. C34, pp. 863–868, 2010.

[67] M. Anselmino, M. Boglione, U. D'Alesio, S. Melis, F. Murgia, *et al.*, "Sivers effect in Drell-Yan processes," *Phys.Rev.*, vol. D79, p. 054010, 2009.

[68] F. Maas, "Electromagnetic form factors in the time like domain," *Nucl.Phys.Proc.Suppl.*, vol. 181-182, pp. 45–50, 2008.

[69] M. Sudol, M. Mora Espi, E. Becheva, J. Boucher, T. Hennino, *et al.*, "Feasibility studies of the time-like proton electromagnetic form factor measurements with PANDA at FAIR," *Eur.Phys.J.*, vol. A44, pp. 373–384, 2010.

[70] S. Brodsky, "Novel QCD Physics at $\overline{\mathsf{P}}$ANDA," June 2012. XLI. PANDA Collaboration Meeting, Evanston/IL, USA.

[71] $\overline{\mathsf{P}}$ANDA Collaboration. Project Homepage, Oct. 2012. http://www-panda.gsi.de.

[72] A. Khoukaz, "Internal targets for the PANDA experiment," *PoS*, vol. STORI11, p. 036, 2011.

[73] W. Erni *et al.*, "Technical Design Report for the PANDA Solenoid and Dipole Spectrometer Magnets," 2009.

[74] T. Würschig, S. Bianco, R. Jäkel, R. Kliemt, M. Mertens, *et al.*, "Contribution of the MVD to the charm spectroscopy at PANDA," *Nucl.Phys.Proc.Suppl.*, vol. 210-211, pp. 269–272, 2011.

[75] T. Stockmanns, "A high rate, low radiation length Micro-Vertex-Detector for the PANDA experiment," *Nucl.Instrum.Meth.*, vol. A650, pp. 64–67, 2011.

[76] D. Calvo, "Triggerless and low mass micro vertex detector for the PANDA experiment," *Nucl.Phys.Proc.Suppl.*, vol. 215, pp. 192–194, 2011.

[77] D. Calvo, P. De Remigis, S. Martoiu, A. Rivetti, and R. Wheadon, "TOPIX: The first prototype of pixel readout for PANDA experiment," *Nucl.Instrum.Meth.*, vol. A596, pp. 96–99, 2008.

[78] D. Calvo, P. De Remigis, T. Kugathasan, G. Mazza, M. Mignone, A. Rivetti, S. Salerno, T. Stockmanns, and R. Wheadon, "A silicon pixel readout ASIC in CMOS 0.13 $\mu$m for the PANDA microvertex detector," *Nuclear Science Symposium Conference Record*, vol. NSS '08, IEEE, 2008.

[79] G. Mazza, D. Calvo, P. De Remigis, T. Kugathasan, M. Mignone, *et al.*, "A CMOS 0.13-mu m silicon pixel detector readout ASIC for the PANDA experiment," *JINST*, vol. 7, p. C02015, 2012.

[80] A. Potenza, "Design of High Dynamic Range Front-End Electronics for Particle Detectors in a 0.13 μm CMOS Technology," Master's thesis, Università degli Studi di Torino, Oct. 2009.

[81] D. Calvo, P. De Remigis, F. Osmic, P. Riedler, G. Stefanini, *et al.*, "Thinned epitaxial silicon hybrid pixel sensors for the PANDA experiment," *Nucl.Instrum.Meth.*, vol. A594, pp. 29–32, 2008.

[82] $\overline{\mathsf{P}}$ANDA Collaboration, "Technical Design Report for the: PANDA Straw Tube Tracker," 2012.

[83] C. Schwarz, "Development of the PANDA barrel DIRC," *JINST*, vol. 4, p. P12016, 2009.

[84] K. Föhl, I. Brodski, M. Düren, A. Hayrapetyan, P. Koch, *et al.*, "The focussing light guide disc DIRC design," *JINST*, vol. 4, p. P11026, 2009.

[85] "Technical Design Report for PANDA Electromagnetic Calorimeter (EMC)," 2008.

[86] T. Randriamalala, *Conceptual Design of the $\overline{\mathsf{P}}$ANDA Luminosity Monitor and Reconstruction Strategy to Measure the Width of the $X(3872)$ State.* PhD thesis, Ruhr-Universität Bochum, 2011.

[87] J. S. Lange, D. Jin, D. Kirschner, A. Kopp, W. Kühn, *et al.*, "Plans for PANDA Online Computing," *JINST*, vol. 4, p. P11001, 2009.

[88] T. Würschig, *Design Optimization of the PANDA Micro-Vertex-Detector for high performance spectroscopy in the charm quark sector.* PhD thesis, Universität Bonn, 2011.

[89] R. Jäkel, *Resolution Studies for the Micro-Vertex-Detector of the PANDA Experiment and the Reconstruction of Charmed Mesons for Specific Hadronic Channels.* PhD thesis, Technische Universität Dresden, 2009.

[90] F. Hügging, "Radiation Damage Estimation for the PANDA Micro-Vertex-Detector." PANDA Collaboration Meeting, GSI Darmstadt, Dec. 2005.

[91] F. Sauli, ed., *Instrumentation in High Energy Physics.* World Scientific Publishing Co.Pte.Ltd., 2$^{nd}$ ed., 1993.

[92] G. Lutz, *Semiconductor Radiation Detectors: Device Physics.* Accelerator Physics, Springer, 1999.

[93] H. Spieler, *Semiconductor Detector Systems.* Series on Semiconductor Science and Technology, Oxford University Press, 2005.

[94] C. Kittel, *Introduction to solid state physics.* Wiley & Sons, New York, 8$^{th}$ ed., 2005.

[95] S. Sze and K. Ng, *Physics of Semiconductor Devices.* Wiley-Interscience publication, John Wiley & Sons, 2006.

[96] F. Scholze, H. Rabus, and G. Ulm, "Mean energy required to produce an electron-hole pair in silicon for photons of energies between 50 and 1500 eV," *J. Appl. Phys.*, vol. 84, pp. 2926 – 2939, 1998.

[97] R. Pehl, F. Goulding, D. Landis, and M. Lenzlinger, "Accurate determination of the ionization energy in semiconductor detectors," *Nuclear Instruments and Methods*, vol. 59, no. 1, pp. 45 – 55, 1968.

[98] "Semiconductor Characteristics and Properties Database." on-line collection from IOFFE Physico-Technical Institute, St. Petersburg, Russia, 2001. http://www.ioffe.rssi.ru/SVA/NSM/; last visited in October 2012.

[99] C. Klein, "Bandgap Dependence and Related Features of Radiation Ionization Energies in Semiconductors," *J. Appl. Phys.*, vol. 39, no. 4, pp. 2029 – 2038, 1968.

[100] A. Owens and A. Peacock, "Compound semiconductor radiation detectors," *Nuclear Instruments and Methods in Physics Research Section A: Accelerators, Spectrometers, Detectors and Associated Equipment*, vol. 531, no. 1–2, pp. 18 – 37, 2004. Proceedings of the 5th International Workshop on Radiation Imaging Detectors.

[101] U. Fano, "Ionization yield of radiations. ii. the fluctuations of the number of ions," *Phys. Rev.*, vol. 72, pp. 26–29, Jul 1947.

[102] A. B. Sproul and M. A. Green, "Improved value for the silicon intrinsic carrier concentration from 275 to 375 K," *J. Appl. Phys.*, vol. 70, pp. 846 – 872, 1991.

[103] V. Eremin, J. Bohm, S. Roe, G. Ruggiero, and P. Weilhammer, "The charge collection in single side silicon microstrip detectors," *Nuclear Instruments and Methods in Physics Research Section A: Accelerators, Spectrometers, Detectors and Associated Equipment*, vol. 500, no. 1–3, pp. 121 – 132, 2003.

[104] V. Radeka, "Semiconductor position-sensitive detectors," *Nuclear Instruments and Methods in Physics Research Section A: Accelerators, Spectrometers, Detectors and Associated Equipment*, vol. 226, no. 1, pp. 209 – 218, 1984.

[105] J. Ponpon, "Semiconductor detectors for 2d x-ray imaging," *Nuclear Instruments and Methods in Physics Research Section A: Accelerators, Spectrometers, Detectors and Associated Equipment*, vol. 551, no. 1, pp. 15 – 26, 2005. Proceedings of the E-MRS Fall Meeting 2004, Symposium D – Applications of Linear and Area Detectors for X-Ray and Neutron Diffraction and Spectroscopy.

[106] J. Kemmer and G. Lutz, "Concepts for simplification of strip detector design and production," *Nuclear Instruments and Methods in Physics Research Section A: Accelerators, Spectrometers, Detectors and Associated Equipment*, vol. 326, no. 1–2, pp. 209 – 213, 1993.

[107] N. Bohr, "LX. On the decrease of velocity of swiftly moving electrified particles in passing through matter," *Philosophical Magazine Series 6*, vol. 30, no. 178, pp. 581–612, 1915.

[108] H. Bethe, "Zur Theorie des Durchgangs schneller Korpuskularstrahlen durch Materie," *Annalen der Physik*, vol. 397, no. 3, pp. 325–400, 1930.

[109] F. Bloch, "Zur Bremsung rasch bewegter Teilchen beim Durchgang durch Materie," *Annalen der Physik*, vol. 408, no. 3, pp. 285–320, 1933.

[110] U. Fano, "Penetration of protons, alpha particles, and mesons," *Annual Review of Nuclear Science*, vol. 13, no. 1, pp. 1–66, 1963.

[111] J. Ziegler, "Stopping of energetic light ions in elemental matter," *J. Appl. Phys.*, vol. 85, no. 3, pp. 1249 – 1272, 1999.

[112] W. R. Leo, *Techniques for Nuclear and Particle Physics Experiments*. Springer Berlin Heidelberg New York, $2^{nd}$ ed., 1994.

[113] L. D. Landau, ed., *On the Energy Loss of Fast Particles by Ionization*, (Oxford), Pergamon Press, 1965. Collected Papers of L.D.Landau.

[114] P. V. Vavilov, "Ionization Losses of High-Energy Heavy Particles," *Soviet Physics JETP*, vol. 5, 1957.

[115] J. Paul, "The rate of energy loss and intrinsic resolution of silicon detectors," *Nuclear Instruments and Methods*, vol. 94, no. 2, pp. 275 – 283, 1971.

[116] H. Bichsel, "Energy loss and ionization of fast charged particles in a 20 µm silicon detector," *Nuclear Instruments and Methods in Physics Research Section A: Accelerators, Spectrometers, Detectors and Associated Equipment*, vol. 235, no. 1, pp. 174 – 179, 1985.

[117] H. Bichsel, "Straggling in thin silicon detectors," *Rev. Mod. Phys.*, vol. 60, pp. 663–699, Jul 1988.

[118] J. Bak, A. Burenkov, J. Petersen, E. Uggerhøj, S. Møller, and P. Siffert, "Large departures from Landau distributions for high-energy particles traversing thin Si and Ge targets," *Nuclear Physics B*, vol. 288, no. 0, pp. 681 – 716, 1987.

[119] S. Hancock, F. James, J. Movchet, P. G. Rancoita, and L. VanRossum, "Energy loss and energy straggling of protons and pions in the momentum range 0.7 to 115 gev/ $c$," *Phys. Rev. A*, vol. 28, pp. 615–620, Aug 1983.

[120] K. Akimov, "Energy losses of fast charged particles in thin silicon detectors," *Nuclear Instruments and Methods in Physics Research Section B: Beam Interactions with Materials and Atoms*, vol. 83, no. 1–2, pp. 62 – 64, 1993.

[121] G. Hall, "Ionisation energy losses of highly relativistic charged particles in thin silicon layers," *Nuclear Instruments and Methods in Physics Research*, vol. 220, no. 2–3, pp. 356 – 362, 1984.

[122] "Space Radiation Effects on Microelectronics," course presented by the Radiation Effects Group, NASA Jet Propulsion Laboratory, Mar. 2002. available online at http://parts.jpl.nasa.gov/docs/Radcrs_Final.pdf; visited in October 2012.

[123] A. Vasilescu and G. Lindström, "Displacement damage in silicon." on-line compilation, Aug. 2000. http://sesam.desy.de/members/gunnar/Si-dfuncs.html; last visited in October 2012.

[124] American Society for Testing and Materials (ASTM), *ASTM Standard E722: Standard Practice for Characterizing Neutron Fluence Spectra in Terms of an Equivalent Monoenergetic Neutron Fluence for Radiation-Hardness Testing of Electronics*, 2009. ASTM E722-09e1.

[125] American Society for Testing and Materials (ASTM), *ASTM Standard E1854: Standard Practice for Ensuring Test Consistency in Neutron-Induced Displacement Damage of Electronic Parts*, 2007. ASTM E1854-07.

[126] J. Srour, C. Marshall, and P. Marshall, "Review of displacement damage effects in silicon devices," *Nuclear Science, IEEE Transactions on*, vol. 50, pp. 653 – 670, june 2003.

[127] Rose Collaboration (RD48), *Third RD48 Status Report*, Dec. 1999. Available online at http://rd48.web.cern.ch/RD48/; visited on July 5th, 2011.

[128] A. Vasilescu, "Fluence normalization based on the NIEL scaling hypothesis," in *Proceedings of the 3rd ROSE Workshop on Radiation Hardening of Silicon Detectors*, (DESY Hamburg, Germany), February 12—14 1998. DESY-PROCEEDINGS-1998-02.

[129] M. Moll, E. Fretwurst, and G. Lindström, "Leakage current of hadron irradiated silicon detectors – material dependence," *Nucl. Instr. Meth.*, vol. A426, no. 1, pp. 87–93, 1999.

[130] M. Huhtinen, "Simulation of non-ionising energy loss and defect formation in silicon," *Nuclear Instruments and Methods*, vol. A 491, pp. 194–215, 2002.

[131] G. Messenger, "A summary review of displacement damage from high energy radiation in silicon semiconductors and semiconductor devices," *Nuclear Science, IEEE Transactions on*, vol. 39, pp. 468 –473, jun 1992.

[132] L. Jones, *APV25-S1 – User Guide*. RAL, Sept. 2001. Version 2.2.

[133] E. Messomo, *Radiation and Temperature Effects on the APV25 Readout Chip for the CMS Tracker*. PhD thesis, Imperial College London, Nov. 2002.

[134] D. Betta *et al.*, "Development of a fabrication technology for double-sided AC-coupled silicon microstrip detectors," *Nucl. Instr. Meth.*, vol. A 460, pp. 306–315, 2001.

[135] J. B. Johnson, "Thermal agitation of electricity in conductors," *Phys. Rev.*, vol. 32, pp. 97–109, Jul 1928.

[136] H. Nyquist, "Thermal agitation of electric charge in conductors," *Phys. Rev.*, vol. 32, pp. 110–113, Jul 1928.

[137] G. Giacomini, *Noise Characterization of Silicon Strip Detectors*. PhD thesis, Università degli Studi di Trieste, 2008.

[138] J. Kraus, *Radio astronomy*. McGraw-Hill, 1966.

[139] E. Barberis, N. Cartiglia, J. Dann, T. Dubbs, K. Noble, K. O'Shaughnessy, J. Rahn, H.-W. Sadrozinski, R. Wichmann, T. Ohsugi, Y. Unno, H. Miyata, N. Tamura, and K. Yamamoto, "Analysis of capacitance measurements on silicon microstrip detectors," *Nuclear Science, IEEE Transactions on*, vol. 41, pp. 785 –790, aug 1994.

[140] M. Friedl, T. Bauer, and M. Krammer, "A simple model of charge collection in silicon detectors," *Nuclear Instruments and Methods in Physics Research A*, vol. 461, pp. 192–196, 2001.

[141] E. Belau, R. Klanner, G. Lutz, E. Neugebauer, H. Seebrunner, A. Wylie, T. Böhringer, L. Hubbeling, P. Weilhammer, J. Kemmer, U. Kötz, and M. Riebesell, "Charge collection in silicon strip detectors," *Nuclear Instruments and Methods in Physics Research*, vol. 214, no. 2–3, pp. 253 – 260, 1983.

[142] G. Bashindzhagyan and N. Korotkova, "Determining the position of an ionizing particle in a system of silicon microstrip detectors," *Instruments and Experimental Techniques*, vol. 49, pp. 331–341, 2006. 10.1134/S0020441206030055.

[143] G. Bashindzhagyan and N. Korotkova, "The use of capacitive charge division in silicon microstrip detectors," *Instruments and Experimental Techniques*, vol. 49, pp. 318–330, 2006. 10.1134/S0020441206030043.

[144] C. Piemonte. private communication, 2006. ITC/Irst Trento.

[145] G.-F. D. Betta, M. Boscardin, L. Bosisio, I. Rachevskaia, M. Zen, and N. Zorzi, "Development of a fabrication technology for double-sided ac-coupled silicon microstrip detectors," *Nuclear Instruments and Methods in Physics Research Section A: Accelerators, Spectrometers, Detectors and Associated Equipment*, vol. 460, no. 2–3, pp. 306 – 315, 2001.

[146] J. W. Motz, H. A. Olsen, and H. W. Koch, "Pair production by photons," *Rev. Mod. Phys.*, vol. 41, pp. 581–639, Oct 1969.

[147] E. L. Hart, G. Cocconi, V. T. Cocconi, and J. M. Sellen, "Electron Pair Production in

the Field of the Proton and in the Field of the Electron by Photons of Energy from 10 Mev to 1 Bev," *Phys. Rev.*, vol. 115, pp. 678–686, Aug 1959.

[148] T. Würschig, July 2012. private communication.

[149] CiS Forschungsinstitut für Mikrosensorik und Photovoltaik GmbH. http://www.cismst.de, Oct. 2011.

[150] "ST2819A Precision LCR Meter," operation manual, Sourcetronic, Nov. 2007.

[151] Philips Semiconductors, *BB131 VHF variable capacitance diode Datasheet*, Feb. 2004. p. 4.

[152] T. McDonald, M. Soldano, A. Murray, and T. Avram, "Power MOSFET Avalanche Design Guidelines," Application Note AN-1005, International Rectifier, 2004. Available online at http://www.irf.com; visited on July 4th, 2011.

[153] G. Hall, D. Vitè, and R. Wheadon, "Calculation of the geometrical capacitance of silicon microstrip structures using a variational approach," *Nuclear Instruments and Methods in Physics Research Section A: Accelerators, Spectrometers, Detectors and Associated Equipment*, vol. 326, no. 1–2, pp. 228 – 233, 1993.

[154] K. Yamamoto, K. Yamamura, K. Saito, M. Konmura, M. Nakamura, and K. Niwa, "A study on the interstrip capacitance of double-sided silicon strip detectors," *Nuclear Instruments and Methods in Physics Research Section A: Accelerators, Spectrometers, Detectors and Associated Equipment*, vol. 326, no. 1–2, pp. 222 – 227, 1993.

[155] N. Bruner, M. Frautschi, M. Hoeferkamp, and S. Seidel, "Characterization procedures for double-sided silicon microstrip detectors," *Nuclear Instruments and Methods in Physics Research Section A: Accelerators, Spectrometers, Detectors and Associated Equipment*, vol. 362, no. 2–3, pp. 315 – 337, 1995.

[156] M. Frautschi, M. Hoeferkamp, and S. Seidel, "Capacitance measurements of double-sided silicon microstrip detectors," *Nuclear Instruments and Methods in Physics Research Section A: Accelerators, Spectrometers, Detectors and Associated Equipment*, vol. 378, no. 1–2, pp. 284 – 296, 1996.

[157] R. Yarema, J. Hoff, A. Mekkaoui, M. Manghisoni, V. Re, P. Manfredi, L. Ratti, and V. Speziali, "Fermilab Silicon Strip Readout Chip for BTeV," *IEEE Trans. Nucl. Sci.*, vol. 52, no. 3, pp. 799–804, 2005.

[158] A. Voronin, D. Karmanov, M. Merkin, and S. Rogozhin, "First Results in Studying the Readout Electronics of the Silicon Tracking System for Upgrading the CLAS12 Experiment," *Instruments and Experimental Techniques*, vol. 53, no. 6, pp. 805–811, 2010.

[159] L. Fabbri *et al.*, "The high rate data acquisition system for the SLIM5 beam test," *Nuclear Instruments and Methods in Physics Research A, pp. 321-323*, vol. 617, pp. 321–323, 2010.

[160] C. J. Schmitt *et al.*, *The n-XYTER Reference Manual.* n-XYTER Project, GSI Darmstadt, Sept. 2009. document version 1.50 (Draft).

[161] A. Brogna, S. Buzzetti, W. Dabrowski, T. Fiutowski, B. Gebauer, M. Klein, C. Schmidt, H. Soltveit, R. Szczygiel, and U. Trunk, "N-XYTER, a CMOS read-out ASIC for high

resolution time and amplitude measurements on high rate multi-channel counting mode neutron detectors," *Nuclear Instruments and Methods in Physics Research A*, vol. 568, no. 1, pp. 301–308, 2006.

[162] C. Bozzi, V. Carassiti, A. Ramusino, S. Dittongo, M. Folegani, L. Piemontese, B. Abbott, A. Breon, A. Clark, S. Dow, Q. Fan, F. Goozen, C. Hernikl, A. Karcher, L. Kerth, I. Kipnis, S. Kluth, G. Lynch, M. Levi, P. Luft, L. Luo, M. Nyman, M. Pedrali-Noy, N. Roe, G. Zizka, D. Roberts, J. Schieck, D. Barni, E. Brenna, I. Defendi, A. Forti, D. Giugni, F. Lanni, F. Palombo, V. Vaniev, A. Leona, E. Mandelli, P. Manfredi, A. Perazzo, V. Re, C. Angelini, G. Batignani, S. Bettarini, M. Bondioli, F. Bosi, G. Calderini, M. Carpinelli, F. Dutra, F. Forti, D. Gagliardi, M. Giorgi, A. Lusiani, P. Mammini, M. Morganti, F. Morsani, E. Paoloni, A. Profeti, M. Rama, G. Rampino, G. Rizzo, F. Sandrelli, G. Simi, G. Triggiani, S. Tritto, R. Vitale, P. Burchat, C. Cheng, D. Kirkby, T. Meyer, C. Roat, M. Bona, F. Bianchi, F. Daudo, B. Girolamo, D. Gamba, G. Giraudo, P. Grosso, A. Romero, A. Smol, P. Trapani, D. Zanin, L. Bosisio, G. Ricca, L. Lanceri, A. Pompili, P. Poropat, M. Prest, C. Rastelli, E. Vallazza, G. Vuagnin, C. Hast, E. Potter, V. Sharma, S. Burke, D. Callahan, C. Campagnari, B. Dahmes, A. Eppich, D. Hale, K. Hall, P. Hart, N. Kuznetsova, S. Kyre, S. Levy, O. Long, J. May, J. Richman, W. Verkerke, M. Witherell, J. Beringer, A. Eisner, A. Frey, A. Grillo, M. Grothe, R. Johnson, W. Kroeger, W. Lockman, T. Pulliam, W. Rowe, R. Schmitz, A. Seiden, E. Spencer, M. Turri, M. Wilder, E. Charles, P. Elmer, J. Nielsen, W. Orejudos, I. Scott, J. Walsh, and H. Zobernig, "The BaBar Silicon Vertex Tracker," *Nuclear Instruments and Methods in Physics Research Section A: Accelerators, Spectrometers, Detectors and Associated Equipment*, vol. 461, no. 1–3, pp. 162 – 167, 2001. 8th Pisa Meeting on Advanced Detectors.

[163] P. Manfredi, L. Ratti, V. Re, N. Roe, and V. Speziali, "Noise limits of AToM, a128 channel CMOS readout chip in applications with room temperature high granularity detectors," *Nuclear Instruments and Methods in Physics Research Section A: Accelerators, Spectrometers, Detectors and Associated Equipment*, vol. 458, no. 1–2, pp. 382 – 391, 2001. Proc. 11th Inbt. Workshop on Room Temperature Semiconductor X- and Gamma-Ray Detectors and Associated Electronics.

[164] Ref. [88], Table 6.6, p.156.

[165] JEDEC, *Scalable Low-Voltage Signaling for 400 mV (SLVS-400)*, Oct. 2001. (JESD8-13).

[166] M. Bucher, D. Kazazis, D. Binkley, D. Foty, and Y. Papananos, "Analysis of Transconductances at All Levels of Inversion in Deep Submicron CMOS," in *Proceedings of the 9th IEEE Conference on Electronics, Circuits and Systems (ICECS 2000)*, vol. III, (Dubrovnik, Croatia), pp. 1183–1186, Sept. 2011.

[167] H. Spieler, "Front-end electronics and trigger systems—status and challenges," *Nuclear Instruments and Methods in Physics Research Section A: Accelerators, Spectrometers, Detectors and Associated Equipment*, vol. 581, no. 1–2, pp. 65 – 79, 2007. VCI 2007 - Proceedings of the 11th International Vienna Conference on Instrumentation.

[168] Ref. [133], pp.82-84.

[169] W. Dabrowski *et al.*, "Noise measurements on radiation-hardened CMOS transistors," in *Conference Record of the 1991 IEEE Nuclear Science Symposium and Medical Imaging Conference*, (Santa Fe, New Mexico), Nov. 2-9 1991.

[170] Ref. [93], p. 300 f.

[171] H.-G. Zaunick, *Erweiterung einer Teststation für Pixelfrontends und Charakterisierung eines FE-I-Chips.* Diploma thesis, Technische Universität Dresden, 2006.

[172] I. Perić, L. Blanquart, G. Comes, P. Denes, K. Einsweiler, P. Fischer, E. Mandelli, and G. Meddeler, "The FEI3 readout chip for the ATLAS pixel detector," *Nuclear Instruments and Methods in Physics Research Section A: Accelerators, Spectrometers, Detectors and Associated Equipment*, vol. 565, no. 1, pp. 178 – 187, 2006. Proceedings of the International Workshop on Semiconductor Pixel Detectors for Particles and Imaging PIXEL 2005.

[173] P. Moreira *et al.*, "The GBT Project," in *Proceedings of the Topical Workshop on electronics for particle physics*, (Paris, France), pp. 342–346, Sept 21-25 2009.

[174] G. Mazza. private communication, 2012.

[175] P. Moreira *et al.*, *The GBTX link interface ASIC.* GBT Project, Nov. 2011. Draft V1.7.

[176] S. Rice, "Mathematical analysis of random noise," *Bell System Technical Journal*, vol. 23, no. 3, pp. 282 – 332, 1944.

[177] S. Rice, "Mathematical analysis of random noise," *Bell System Technical Journal*, vol. 24, no. 1, pp. 46 – 156, 1945.

[178] H. Spieler, "Introduction to Radiation Detectors and Electronics." lecture notes, UC Berkeley, 1999. http://www-physics.lbl.gov/~spieler/physics_198_notes_1999/.

[179] K. Koop, "FPGA-basierte Auslese von Silizium-Streifen-Detektoren." Diploma Thesis, Universität Bonn, 2009, available online at http://panda.hiskp.uni-bonn.de/files/Diplomarbeit_Koop.pdf.

[180] H. Sohlbach, "Readout controller design for the MVD Si-strip sensors," March 2011. XXXVI. PANDA Collaboration Meeting.

[181] A. X. Widmer and P. A. Franaszek, "A DC-Balanced, Partitioned-Block, 8B/10B Transmission Code," *IBM Journal of Research and Development*, vol. 27, pp. 440 –451, sept. 1983.

[182] A. X. Widmer, "DC balanced 7B/8B, 9B/10B, and partitioned DC balanced 12B/14B, 17B/20B, and 16B/18B transmission codes." Patent, Sept. 2003. US 6,614,369 B1.

[183] DDWG, *Digital Visual Interface (DVI) specification reference*, Apr. 1999. contains TMDS specification.

[184] A. Djordjevič, R. Biljič, V. Likar-Smiljanič, and T. Sarkar, "Wideband Frequency-Domain Characterization of FR-4 and Time-Domain Causality," *IEEE Transactions on Electromagnetic Compatibility*, vol. 43, pp. 662–667, Nov. 2001.

[185] M. Tavlet, A. Fontaine, and H. Schönbacher, *Compilation of radiation damage test data, pt.2. Index des resultats d'essais de radioresistance, t.2; 2nd ed.* Geneva: CERN, 1998.

[186] D. Severin, W. Ensinger, T. Seidl, and C. Trautmann, "Radiation hardness of kapton exposed to swift heavy ions," GSI Scientific Report, Gesellschaft für Schwerionenforschung, Darmstadt, 2008.

[187] DuPont, *General Specifications of Kapton Polyimide Films*, June 2010. Available online at http://www2.dupont.com/Kapton/en_US/; visited on July 3rd, 2011.

[188] DuPont, *Pyralux AP Technical Data Sheet*, Sept. 2011. Available online at http://www2.dupont.com/Pyralux/en_US/products/laminate/AP/pyralux_ap.html; visited on February 2nd, 2011.

[189] Y. Imanaka, *Multilayered Low Temperature Cofired Ceramics (LTCC) Technology*. Berlin: Springer, May 2008.

[190] L. J. Golonka, "Technology and applications of Low Temperature Cofired Ceramic (LTCC) based sensors and microsystems," *Bulletin of the Polish Academy of Sciences: Technical Sciences*, vol. 54, no. 2, pp. 221–231, 2006.

[191] M. Jawitz, *Printed circuit board materials handbook*. Electronic packaging and interconnection series, McGraw-Hill, 1997.

[192] E. Fooks and R. Zakarevičius, *Microwave Engineering Using Microstrip Circuits*. Prentice Hall, 1990.

[193] C. Livermore and J. Voldman, "Material Property Database." on-line collection, Mar. 2004. http://www.mit.edu/~6.777/matprops/matprops.htm, visited in January 2012.

[194] C. Bowick, *RF Circuit Design*. Newnes, $2^{nd}$ ed., 2007.

[195] J. Ardizzoni, "A Practical Guide to High-Speed Printed-Circuit-Board Layout," *Analog Dialogue*, vol. 39-09, Sept. 2005.

[196] IPC, *Generic Standard on Printed Board Design*, May 2003. IPC Standard 2221A.

[197] IPC, *Sectional design standard for flexible printed boards*, Nov. 2011. IPC Standard 2223C.

[198] K. Einsweiler, *ATLAS On-Detector Electronics Architecture*, 2003. Draft V3.0.

[199] P. Horowitz and W. Hill, *The Art of Electronics*. Cambridge University Press, 1989.

[200] G. Blanchot *et al.*, "Low noise DC to DC converters for the sLHC experiments," *Journal of Instrumentation*, vol. 5, Dec. 2010.

[201] G. Blanchot *et al.*, *SM01c DC/DC Converter*. CERN DC/DC Converter Project, Nov. 2011. Datasheet V1.

[202] A. Pepato, G. Anelli, F. Antinori, A. Badalà, M. Burns, G. Bruno, I. Cali, M. Campbell, M. Caselle, S. Ceresa, P. Chocula, M. Cinausero, J. Conrad, R. Dima, D. Elia, D. Fabris, R. Fini, E. Fioretto, L. Garizzo, S. Kapusta, A. Kluge, M. Krivda, V. Lenti, F. Librizzi, M. Lunardon, D. Maniero, V. Manzari, S. Martini, D. Mazzaro, M. Morel, S. Moretto, F. Osmic, G. Pappalardo, V. Paticchio, G. Prete, A. Pulvirenti, P. Riedler, F. Riggi, L. Sandor, R. Santoro, F. Scarlassara, G. Segato, F. Soramel, G. Stefanini, C. T. de Matos, M. Turcato, R. Turrisi, L. Vannucci, G. Viesti, and T. Virgili, "The mechanics and cooling system of the alice silicon pixel detector," *Nuclear Instruments and Methods in Physics Research Section A: Accelerators, Spectrometers, Detectors and Associated Equipment*, vol. 565, no. 1, pp. 6 – 12, 2006. Proceedings of the International Workshop on Semiconductor Pixel Detectors for Particles and Imaging – PIXEL 2005.

[203] G. Giraudo, "MVD updates on mechanics and cooling," June 2010. XXXII. PANDA Collaboration Meeting.

[204] Ref. [92], p. 221 f., section 7.8.2, paragraph "Noise with Punch-Through Biasing".

[205] S. Bianco, M. Becker, K.-T. Brinkmann, R. Kliemt, K. Koop, R. Schnell, T. Würschig, and H.-G. Zaunick, "Measurement with a Si-strip telescope," in *Proceedings of the 10th International Conference on Large Scale Applications and Radiation Hardness of Semiconductor Detectors*, (Firenze, Italy), July 6-8 2011.

[206] M. Becker, S. Bianco, K.-T. Brinkmann, R. Kliemt, K. Koop, R. Schnell, T. Würschig, and H.-G. Zaunick, "Commisioning of a multi-purpose Silicon-strip beam telescope." in preparation, 2012.

[207] J. Lindhard and M. Scharff, "Energy Dissipation by Ions in the kev Region," *Phys. Rev.*, vol. 124, pp. 128–130, Oct 1961.

[208] J. Biersack and L. Haggmark, "A Monte Carlo computer program for the transport of energetic ions in amorphous targets," *Nuclear Instruments and Methods*, vol. 174, no. 1–2, pp. 257–269, 1980.

[209] K. Winterbon, P. Sigmund, and J. Sanders, "Spatial distribution of energy deposited by atomic particles in elastic collisions," *Mat. Fys. Medd. Dan. Vid. Selsk.*, vol. 37, pp. 1–73, 1970.

[210] H. Hanchen and N. Ghoniem, "Neutron displacement damage cross sections for SiC," *Journal of Nuclear Materials*, vol. 199, no. 3, pp. 221 – 230, 1993.

[211] G. H. Kinchin and R. S. Pease, "The displacement of atoms in solids by radiation," *Reports on Progress in Physics*, vol. 18, no. 1, p. 1, 1955.

[212] M. Norgett, M. Robinson, and I. Torrens, "A proposed method of calculating displacement dose rates," *Nuclear Engineering and Design*, vol. 33, no. 1, pp. 50 – 54, 1975.

[213] D. Parkin and C. Coulter, "Displacement functions for diatomic materials," *Journal of Nuclear Materials*, vol. 85–86, Part 1, no. 0, pp. 611 – 615, 1979.

[214] M. Chadwick, M. Herman, P. Obložinský, *et al.*, "ENDF/B-VII.1 Nuclear Data for Science and Technology: Cross Sections, Covariances, Fission Product Yields and Decay Data," *Nuclear Data Sheets*, vol. 112, no. 12, pp. 2887 – 2996, 2011. Special Issue on ENDF/B-VII.1 Library.

[215] L. R. Greenwood and R. K. Smither, "SPECTER: Neutron Damage Calculations for Materials Irradiation," tech. rep., Argonne National Laboratory, Argonne, Illinois 60439, Jan. 1985. ANL/FPP/TM-197.

[216] P. L. F. Hemment and P. R. C. Stevens in *Atomic Collision Phenomena in Solids* (D. W. Palmer, M. W. Thompson, and P. D. Townsend, eds.), p. 280, Amsterdam: North-Holland, 1970.

[217] L. A. Miller, D. K. Brice, A. K. Prinja, and S. T. Picraux, "Displacement-threshold energies in Si calculated by molecular dynamics," *Phys. Rev. B*, vol. 49, pp. 16953–16964, Jun 1994.

[218] V. Kirsanov, N. Musin, and H. Shamarina, "Displacement threshold energy in high-temperature superconductors. II. Thresholds for O, Ba and Y in YBa2Cu3O7," *Physics Letters A*, vol. 171, no. 3–4, pp. 223 – 233, 1992.

[219] S. Watts, "Overview of radiation damage in silicon detectors — models and defect engineering," *Nuclear Instruments and Methods in Physics Research Section A: Accelerators,*

*Spectrometers, Detectors and Associated Equipment*, vol. 386, no. 1, pp. 149 – 155, 1997. Proceedings of the 5th International Workshop on Vertex Detectors.

[220] Reactor Instituut Delft, *Hoger Onderwijs Reactor (HOR)*, 2011. Available online at http://tnw.home.tudelft.nl/en/cooperation/facilities/reactor-instituut-delft/; visited on december 20th, 2011.

[221] D. Deermann, "Charakterisierung von Siliziumstreifendetektoren." Diploma Thesis, Universität Bonn, 2011, available online at http://panda.hiskp.uni-bonn.de/files/Diplomarbeit_Dariusch.pdf.

[222] G. Erdtmann and W. Soyka, *Die $\gamma$-Linien der Radionuklide.* Kernforschungsanlage Jülich, $2^{nd}$ ed., 1974.

[223] M. Blauuw. private communication, Dec. 2011. Reactor Institute Delft.

# List of Figures

# List of Tables

# Acknowledgements